UNIVERSIDAD COMPLUTENSE DE MADRID
FACULTAD DE CIENCIAS FÍSICAS

TESIS DOCTORAL

Subwavelength metamaterials for high-performance photonic microdevices
Metamateriales sub-longitud de onda para microdispositivos fotónicos de altas prestaciones

MEMORIA PARA OPTAR AL GRADO DE DOCTOR

PRESENTADA POR

David González Andrade

DIRECTOR

Aitor Villafranca Velasco
Pedro Corredera Guillén

To my grandmother María

and my grandfather Bartolo

Acknowledgements

First of all, I would like to express my deepest gratitude to Dr. Aitor Villafranca Velasco who gave me the opportunity to begin this research journey more than three years ago. Aitor has always been a substantial support since I entered the Institute of Optics and working with him, I have not only grown professionally but also personally. Thank you very much Aitor for your full confidence in me, for believing in all my ideas and for guiding me throughout this tough process. I would also like to thank Dr. Pedro Corredera Guillén for all his advice and the scientific knowledge he shared with me during these three years. I really admire the ease with which you have always explained to me the concepts of optics. Thank you Pedro for always being there if necessary and for all the great moments we shared during the coffee breaks.

My special thanks also go to Dr. Juan Diego Ania Castañón for welcoming me into his research group and for his support with all the bureaucratic procedures. I also want to thank all my colleagues of the Nonlinear Dynamics and Fiber Optics group: José Luis de Miguel, Conchi Pulido, Juan Galindo and José María Soto. A special mention goes to Alaine, who has been by my side since I started this journey. She is a very hardworking person with whom I am glad to have shared all our sorrows and joys during our PhD. My heartfelt thanks for all your support during these years.

In this time, I have also had the pleasure to work with many brilliant people without whom this thesis would not have been possible. I would like to thank Prof. Gonzalo Wangüemert Pérez for initiating me into the world of research, for his full dedication and unlimited support. I also want to thank Prof. Íñigo Molina Fernández, who opened the doors of his group every time I needed to characterize the fabricated devices. I am also thankful to Dr. Alejandro Ortega Moñux, Dr. Robert Halir, Dr. José de Oliva Rubio and José Manuel Luque González for the fruitful discussions.

I have also had the opportunity to work at the Centre de Nanosciences et de Nanotechnologies (C2N) for six months. I would like to express my sincere thanks to Dr. Carlos Alonso Ramos Ramos and Prof. Laurent Vivien for this unique opportunity. Additionally, I truly appreciate the patience and the advice of Dr. Elena Durán Valdeiglesias, who taught me how to characterize my first photonic chip. It has been an honor to work together with the entire MINAPHOT team and during the time I have spent there it has been like my second home. I want to specially thank Prof. Delphine Marris Morini, Prof. Eric Cassan, Dr. Mathias Berciano, Xavier Le Roux, Christian Lafforgue and Dr. Diego Pérez Galacho from C2N, as well as Dr. Sylvain Guerber, Nathalie Vulliet, Dr. Sébastien Cremer, Dr. Stephane Monfray and Dr. Frédéric Boeuf from STMicroelectronics.

I would also like to mention other excellent researchers with whom I have had the pleasure to work with during a short research stay of two months in Canada. I am extremely thankful to Dr. Pavel Cheben for the human quality with which he hosted me in Ottawa. Thank you Pavel for always finding time to discuss about the papers and for teaching me that perfection is the final goal. I would also like to acknowledge Prof. Lawrence R. Chen and his entire group from McGill University during the time I spent in Montreal.

On the financial side, I would like to acknowledge the support from the Spanish Ministry of Science, Innovation and Universities (formerly Ministry of Economy and Competitiveness) through grants TEC2015-71127-C2-1-R (FPI scholarship BES-2016-077798) and RTI2018-097957-B-C33, the Community of Madrid through grants S2013/MIT-2790 and S2018/NMT-4326, the EMPIR program through grant JRP-i22 14IND13 Photind and the Horizon 2020 research and innovation program through the Marie Sklodowska-Curie grant 734331. I would also like to express my sincere gratitude to Alcyon Photonics S.L. for its financial and, above all, human support without which it would not have been possible to achieve some of the results of this thesis.

Finally, I would like to dedicate these last lines to thank my family and my loved ones for all the help and support they have provided me during these years. I do not have enough words to express my gratitude to my parents Maribel and Mariano. I deeply appreciate all your advices and sacrifices, without which I would not have been able to accomplish this thesis. Also, I want to express my thanks to my sister Cristina, my grandmother María and my uncle Miguel for their unwavering trust in me. Last but not least, my deepest gratitude goes to Aida, who has taught me that dreams can come true if you have the courage to pursue them. Thank you for being there every time I needed to talk, for your patience and especially for understanding me in difficult times.

Table of Contents

List of acronyms

BOX	Buried Oxide
C2N	Centre de Nanosciences et de Nanotechnologies
CMOS	Complementary Metal-Oxide-Semiconductor
CSIC	Spanish National Research Council
CVD	Chemical Vapour Deposition
CWDM	Coarse Wavelength-Division-Multiplexing
DBR	Distributed Bragg Reflector (laser)
DC	Duty Cycle
DFB	Distributed Feedback (laser)
DEMUX	Demultiplexer
DWDM	Dense Wavelength-Division-Multiplexing
E-beam	Electron-beam (lithography)
EL	Excess Loss
EME	Eigenmode Expansion (method)
EMT	Effective Medium Theory
ER	Extinction Ratio
FDE	Finite Difference Eigenmode (solver)
FDTD	Finite-Difference Time-Domain (method)
FEM	Finite Element Method
FSR	Free Spectral Range
FT	Fourier Transform

GFP	Group IV Photonics
IB	Imbalance
ICP-RIE	Inductively Coupled Plasma – Reactive Ion Etching (process)
IL	Insertion loss
IO	Institute of Optics “Daza de Valdés”
IoT	Internet of Things
IR	Infrared
LIDAR	Light Detection And Ranging
MDM	Mode-Division Multiplexing
MEMS	Micro Electromechanical Systems
MINAPHOT	Micro and Nano-Photonics devices on silicon platform
MIR	Mid-Infrared
MMI	Multimode Interference
MUX	Multiplexer
MZI	Mach-Zehnder Interferometer
NRC	National Research Council of Canada
ODL	Optical Delay Line
OTDM	Optical Time-Division Multiplexing
PCT	Patent Cooperation Treaty
PDM	Polarization-Division Multiplexing
PE	Phase Error
PECVD	Plasma Enhanced Chemical Vapour Deposition
PIC	Photonic Integrated Circuit
PM	Polarization Maintaining (fiber)
PMMA	Polymethyl Methacrylate

PS	Phase Shifter
SDM	Space-Division Multiplexing
SEM	Scanning Electron Microscope (image)
SHFT	Spatial Heterodyne Fourier Transform
SiN	Silicon Nitride
SWG	Subwavelength Grating
SOI	Silicon-On-Insulator
TE	Transverse Electric
TM	Transverse Magnetic
UMA	University of Malaga
UV	Ultraviolet
WDM	Wavelength-Division Multiplexing
XT	Crosstalk (inter-mode)

Abstract: Subwavelength metamaterials for high-performance photonic microdevices

INTRODUCTION AND OBJECTIVES

Photonics has become of paramount importance in many areas of our everyday life owing to its inherent potential to develop not only telecom and datacom solutions, but also many other applications such as metrology [DeMiguel'18], energy generation and saving [Polman'12, Miller'17], spectrometry [Velasco'13a], sensing [Rodríguez-Barrios'10], medicine [Morgner'00] and industrial manufacturing [Malinauskas'16], to name a few. Particularly, integrated optics has attracted increasing industrial attention and scientific efforts to implement photonic integrated circuits (PICs) capable of tackling all abovementioned tasks in compact and efficient systems.

Among all the available materials, silicon photonics leverages the maturity of the fabrication techniques reached by the microelectronics industry, enabling cost-effective mass production [Chen'18]. Different material platforms with a high refractive index contrast have been proposed for silicon photonics to achieve higher integration levels and perform more complex functions in a single chip, such as silicon-on-insulator (SOI) and silicon nitride (Si_3N_4, commonly simplified to SiN). The increased integration capacity of silicon photonics has enabled to tackle one of our greatest technological challenges: global data traffic inside data centers. Besides short-range optical interconnects for telecom and datacom applications, the progress in silicon photonics also encompasses many other untapped applications that are being explored by academia and industry: absorption spectroscopy and bio-sensing [Herrero-Bermello'17, Wangüemert-Pérez'19], light detection and ranging (LIDAR) [Poulton'17a], quantum computing [Harris'16], microwave and terahertz photonics [Marpaung'19, Harter'18], nonlinear optics [Leuthold'10], and many others.

However, the performance of any on-chip application is determined by two factors: its top-level design, which is specific for each application; and the performance of its constituent elements, which in a significant part is common to all applications, as they share many fundamental building blocks, such as couplers, multiplexers, splitters, polarization controllers, etc. Standard building blocks available in photonic design kits are often rudimentary and present limited performances (bandwidth, losses, crosstalk, etc.), hindering the access of end-application designers to the technology. This is mainly caused by the high index contrast, high birefringence and elevated thermal dependence of silicon waveguides, as well as by fabrication limitations with stringent minimum feature size. Therefore, it is of utmost importance to develop new fundamental building blocks that address these core challenges and provide the foundation for a new generation of high-performance on-chip applications. In this way, the main objective of this thesis is the design and characterization of key building blocks with high performance and large fabrication tolerances for next generation silicon photonic integrated circuits. To overcome the inherent limitations posed by the material platform original and novel structures based on nano-scale features have been proposed and experimentally demonstrated, including subwavelength grating (SWG) metamaterial and slot waveguides.

RESULTS OF THE RESEARCH

During the development of the present thesis, significant advances have been reported in the fields of mode-division multiplexing, passive phase shifting and optical beam splitting. The design and characterization of these photonic devices has resulted in the following contributions:

- A broadband and compact mode converter and multiplexer/demultiplexer (MUX/DEMUX) based on a subwavelength engineered multimode interference (MMI) coupler has been designed, fabricated and characterized for the SOI platform. In addition to the SWG MMI, this device consists of a 90° phase shifter (PS) and a symmetric Y-junction. SWG metamaterial waveguides have been exploited to control the dispersion of the higher-order modes propagated through the multimode section of the MMI, and therefore, to reduce the wavelength-dependent losses of conventional MMIs [Halir’16]. A complete MUX-DEMUX link was fabricated, exhibiting insertion loss lower than 1.3 dB and crosstalk better than -15.3 dB for both multiplexed modes over a broad 145 nm wavelength range (1.495 – 1.64 µm). This flat low-loss response is achieved for a single MUX/DEMUX footprint of only 38.6 µm × 3.7 µm.
- The unique properties of SWG metamaterial waveguides have been leveraged to substantially improve both the performance and the fabrication tolerances of state-of-the-art passive PSs based on equal-length waveguides. The limitations of passive phase shifters have been theoretically studied and a 90° PS has been designed and implemented for the SOI platform, showing

a simulated phase error below ±1.7° within an unprecedented 400 nm bandwidth. This flat spectral response is maintained for over- and under-etching errors of ±20 nm. The device was fabricated and measurements were carried out showing an excellent agreement with simulations predictions. A phase slope of 63°/µm was measured over a 145 nm bandwidth (1.495 – 1.64 µm) for conventional tapered PSs, whereas the proposed asymmetric SWG PS yielded an almost flat phase slope of only 16°/µm within the same bandwidth.

- A novel design strategy to implement high-performance beam splitters has been proposed based on modal- and symmetry-engineering of a slot waveguide. Hence, any mode-beating behaviour that limits the operation of other conventional beam splitters such as directional couplers and MMIs is circumvented, whereas the symmetric output transition ensures equal power splitting in a polarization- and wavelength-agnostic fashion like symmetric Y-junctions. The proposed beam splitter was fabricated using SOI wafers and measurements demonstrated low loss and imbalance of less than 1 dB for both polarizations and a bandwidth exceeding 390 nm. This remarkable performance was also measured for beam splitters in which artificial fabrication errors of ±25nm were introduced, demonstrating the robustness of the design.
- The splitter was thoroughly redesigned for SiN platform applying the same design strategy. This device was fabricated at the facilities of ST Crolles with an excess loss and imbalance below 0.62 dB and 0.6 dB, respectively, for both TE and TM polarization in an ultra-broad 420 nm wavelength range, making it one of the SiN beam splitters with broadest bandwidth.

CONCLUSIONS

The results reported in this thesis provide novel building blocks with very high performance based on subwavelength metamaterials, paving the way for next generation of high-performance on-chip applications. Since all the developed devices perform fundamental operations in integrated photonics, they can be employed in a wide range of applications such as high capacity optical interconnects, microwave and terahertz photonics, microspectrometers, quantum computing, LIDAR and biochemical sensing.

Resumen: Metamateriales sub-longitud de onda para microdispositivos fotónicos de altas prestaciones

INTRODUCCIÓN Y OBJETIVOS

La fotónica ha adquirido una importancia fundamental en muchos ámbitos de nuestra vida cotidiana debido a su potencial intrínseco para desarrollar soluciones no sólo en el campo de las telecomunicaciones y las interconexiones de corto alcance, sino también en otras muchas áreas como la metrología [DeMiguel'18], la generación de energía [Polman'12, Miller'17], la espectrometría [Velasco'13a], la detección [Rodríguez-Barrios'10], la medicina [Morgner'00] y la fabricación industrial [Malinauskas'16]. En particular, la óptica integrada ha atraído tanto la atención de la industria como los esfuerzos científicos para implementar circuitos fotónicos integrados (PICs, *Photonic Integrated Circuits*) capaces de abordar todas las tareas mencionadas anteriormente en sistemas compactos y eficientes.

Entre todos los materiales disponibles, la fotónica de silicio aprovecha la madurez de las técnicas de fabricación alcanzadas por la industria de la microelectrónica, permitiendo una producción en masa rentable [Chen'18]. Para maximizar su densidad de integración y poder realizar funciones más complejas en un único chip, diferentes plataformas materiales con un alto contraste de índice de refracción se han propuesto, como por ejemplo las plataformas de silicio sobre aislante (SOI, *Silicon-On-Insulator*) y de nitruro de silicio (Si_3N_4, comúnmente simplificada a SiN, *Silicon Nitride*). Esta mayor densidad de integración ha permitido abordar uno de nuestros mayores desafíos tecnológicos hasta la fecha: el tráfico de datos global dentro de los centros de datos. Además de las interconexiones ópticas de corto alcance, el progreso de la fotónica de silicio también comprende muchas otras aplicaciones inexploradas que están siendo estudiadas en el ámbito académico e industrial como, por ejemplo, la espectroscopía de absorción y biodetección [Herrero-Bermello'17, Wangüemert-Pérez'19], LIDAR (*Light Detection And Ranging*) [Poulton'17a], computación cuántica [Harris'16], fotónica de microondas y terahercios [Marpaung'19, Harter'18], óptica no lineal [Leuthold'10], y muchas otras.

Sin embargo, el rendimiento de cualquiera de estas aplicaciones está determinado por dos factores: su diseño de alto nivel, que es específico para cada aplicación; y el rendimiento de sus componentes, que suele ser común a todas las aplicaciones, ya que comparten bloques fundamentales como acopladores, multiplexores, divisores, controladores de polarización, etc. Los componentes estándar que se encuentran disponibles en los kits de diseño fotónico presentan a menudo prestaciones limitadas (en ancho de banda, pérdidas, diafonía, etc.), dificultando el acceso de los diseñadores de aplicaciones finales a esta tecnología. Dichas limitaciones se deben principalmente al alto contraste de índice, la alta birrefringencia y la elevada dependencia térmica de las guías de ondas de silicio, así como a las restricciones de fabricación. Por lo tanto, es de suma importancia desarrollar nuevos componentes básicos que aborden estos desafíos y proporcionen la base para una nueva generación de aplicaciones en chip de alto rendimiento. El objetivo principal de esta tesis es, por tanto, el diseño y caracterización de dispositivos con altas prestaciones y buenas tolerancias de fabricación para la próxima generación de PICs. Para superar las limitaciones inherentes planteadas por la plataforma material, se han propuesto y demostrado experimentalmente dispositivos originales y novedosos basados en estructuras de escala nanométrica, incluyendo metamateriales de rejillas sub-longitud de onda (SWG, *Subwavelength Grating*) y guías de onda de ranura.

RESULTADOS DE LA INVESTIGACIÓN

Durante el desarrollo de la presente tesis, se han realizado contribuciones significativas en los campos de la multiplexación por división modal, desfasadores pasivos y divisores de haz ópticos. El diseño y caracterización de dichos dispositivos fotónicos ha dado lugar a las siguientes aportaciones:

- Se ha diseñado, fabricado y caracterizado un convertidor y multiplexor de modos compacto y de banda ancha (MUX/DEMUX, *Multiplexer/ Demultiplexer*) basado en un acoplador de interferencia multimodal (MMI, *Multimode Interference*) implementado con guías de onda SWG. Además del SWG MMI, este dispositivo consta de un desfasador (PS, *Phase Shifter*) de 90° y una unión en Y simétrica. Las guías de ondas metamateriales SWG se han explotado para controlar la dispersión de los modos de orden superior propagados a través de la sección multimodo del MMI y, por lo tanto, para reducir las pérdidas dependientes de la longitud de onda de los MMIs convencionales [Halir'16]. Un enlace MUX-DEMUX completo fue fabricado, presentando pérdidas de inserción inferiores a 1.3 dB y una diafonía mejor que

-15.3 dB para los dos modos multiplexados en un rango de longitud de onda de 145 nm (1.495 – 1.64 µm). Esta respuesta plana de bajas pérdidas se logra para unas dimensiones de tan sólo 38.6 µm × 3.7 µm.

- Las extraordinarias virtudes de las guías de ondas metamateriales SWG también se han aprovechado para mejorar sustancialmente el rendimiento y las tolerancias de fabricación de los PSs pasivos del estado de la técnica basados en guías de ondas de igual longitud. Las limitaciones de los PSs pasivos se han estudiado teóricamente y se ha diseñado e implementado un PS de 90° para la plataforma de SOI. Las simulaciones muestran un error de fase menor de ±1.7° para un ancho de banda sin precedentes de 400 nm. Esta respuesta espectral plana se mantiene para errores de sobregrabado y subgrabado de ±20 nm. El dispositivo fue fabricado y las medidas realizadas mostraron una excelente concordancia con las predicciones de las simulaciones. Para los PSs basados en guías de onda trapezoidales se midió una pendiente de fase de 63°/µm en un ancho de banda de 145 nm (1.495 – 1.64 µm), mientras que el SWG PS propuesto mostraba una pendiente de fase casi plana de solo 16°/µm dentro del mismo ancho de banda.
- Una estrategia de diseño novedosa ha sido propuesta para la implementación de divisores de haz de alto rendimiento basados en ingeniería modal y de simetría en una guía de onda de ranura. De esta forma, se evita cualquier batido de modos dependiente de la longitud de onda que típicamente limita el funcionamiento de otros divisores de haz convencionales, como los acopladores direccionales y los MMIs. La transición de salida simétrica, además, garantiza una división de potencia equitativa en los puertos de salida, independientemente de la polarización y de la longitud de onda. El divisor de haz propuesto se fabricó utilizando obleas de SOI y las mediciones demostraron pérdidas y desbalanceo menores a 1 dB para ambas polarizaciones en un ancho de banda superior a 390 nm. Estas notables prestaciones se mantuvieron incluso para divisores de haz en los que se introdujeron errores de fabricación artificiales de ±25 nm, demostrando la robustez de nuestro diseño.
- El divisor de haz fue completamente rediseñado para la plataforma de SiN aplicando la misma estrategia de diseño. Este dispositivo fue fabricado en las instalaciones de STMicroelectronics. Las pérdidas y desbalanceos medidas eran menores de 0.62 dB y 0.6 dB, respectivamente, para las polarizaciones TE y TM en un rango de longitud de onda excediendo los 420 nm, siendo uno de los divisores de haz demostrados en SiN con mayor ancho de banda.

CONCLUSIONES

En conclusión, los resultados alcanzados en la presente tesis doctoral han proporcionado nuevos componentes fundamentales de muy altas prestaciones gracias a la tecnología SWG, allanando el camino a la próxima generación de aplicaciones en chip de alto rendimiento. Dado que todos los dispositivos desarrollados realizan operaciones básicas de la fotónica integrada, se pueden utilizar en una amplia gama de aplicaciones como interconexiones ópticas de alta capacidad, fotónica de microondas y terahercios, microespectrómetros, computación cuántica, LIDAR y detección bioquímica.

I

Introduction

The present thesis covers the design, optimization and experimental demonstration of novel high-performance photonic integrated devices based on subwavelength metamaterials. These developments have been the result of national and international collaborations between the Spanish National Research Council (CSIC) - Institute of Optics “Daza de Valdés” (IO) and other renowned institutions such as the University of Malaga (UMA), the Centre de Nanosciences et de Nanotechnologies (C2N) and the National Research Council of Canada (NRC). This opening chapter provides context for these findings, in terms of technology, applications and objectives.

In section 1.1, the evolution of photonics is overviewed, focusing primarily in integrated optics. The scientific and industrial relevance of silicon photonics as an enabling technology for the development of multi-purpose integrated circuits is presented in section 1.2. Finally, the objectives and organization of the document are described in section 1.3.

1.1. Evolution of photonics: from the laser to the chip

The term photonics was originally coined in the late 1960s to designate a new emerging field related to the generation, detection and manipulation of light. However, the origin of photonics can be traced back to the invention of the first operating laser by Theodore H. Maiman in 1960 [Maiman'60]. This breakthrough entailed an increasing interest in the field, which only one year later led to the theoretical demonstration that a laser beam could be directed by means of a glass fiber [Snitzer'61]. The major problem that hindered glass fibers for long-haul data transmission was its high propagation loss. This challenge was not solved until 1966, when Charles K. Kao and George A. Hockham showed that attenuation could be decreased to about 20 dB/km by reducing the iron impurity concentration, and subsequently, the high particle scattering losses [Kao'66]. Optical communications experienced a quantum leap from that moment, owing to the reduced latency and the increased data transmission capacity offered by dielectric fibers compared to other transmission media based on copper pairs or coaxial cables.

Integrated optics would emerge only a few years later, leveraging all the benefits provided by optical fibers in terms of latency, bandwidth capacity and isolation, and bringing them to the chip scale. In 1969 Stewart E. Miller proposed the first photonic integrated circuit (PIC) on a single substrate for signal processing and communications [Miller'69]. In his paper, Miller outlined the potential of dielectric waveguides to guide a laser beam and discussed the possibility of implementing the circuitry for an integrated laser. Among the advantages of integrated optics, he already mentioned acoustic, thermal and mechanical isolation facilitated by the circuit miniaturization, in addition to low power consumption. Other devices such as phase modulators, hybrid couplers and frequency-selective filters were also described in detail, laying the groundwork for contemporary integrated optics.

Nowadays, photonics has become of paramount importance in many areas of our everyday life. While optical fibers are the highways of backbone and access communication networks [Lam'16], integrated optics has already replace conventional copper interconnects in data centers to overcome capacity and energy consumption bottlenecks of electronics [Liu'10, Tatum'15]. Furthermore, photonics has recently been considered as a Key Enabling Technology under the H2020 program of the European Commission, confirming its potential to develop not only telecom and datacom solutions, but also many other applications such as metrology [DeMiguel'18], energy generation and saving [Polman'12, Miller'17], spectrometry [Velasco'13a], sensing [Rodríguez-Barrios'10], medicine [Morgner'00] and industrial manufacturing

[Malinauskas’16], to name a few. Particularly, integrated optics has attracted increasing industrial attention and scientific efforts to implement PICs capable of tackling all abovementioned tasks in compact and efficient systems.

In order to address these challenges, several materials with different advantages and limitations have been employed for the development and fabrication of PICs, among which the following stand out:

- Lithium niobate ($LiNbO_3$) is a synthetic crystal (i.e. it cannot be found in nature) with remarkable electro-optic and second-order nonlinear optical effects. Therefore, this material has been primarily used for the implementation of active components, e. g. high speed electro-optical modulators or integrated lasers [Poberaj’12]. Its main drawback is that the integration of lithium niobate components with other elements on the same substrate is still challenging, although some solutions have recently appeared to overcome this problem [Baets’19].
- Group III-V materials include combinations of elements such as indium (In), gallium (Ga), aluminium (Al), phosphorus (P) and arsenic (As), among others. These elements can be used to create binary and ternary material alloys, e. g. indium phosphide (InP), gallium arsenide (GaAs), indium gallium arsenide (InGaAs), which have been extensively used in photonics. For example, InP has enabled the integration of both active and passive components on a single chip, such as laser, modulators, photodetectors, waveguides and couplers [Zhao’19], and is considered as a promising candidate to replace integrated circuits based on lithium niobate. Nevertheless, InP waveguides present higher propagation loss than other waveguides based on group IV materials [DAgostino’15] and their fabrication requires specialized facilities that increase the overall production cost.
- Group IV elements comprise silicon (Si), tin (Sn), germanium (Ge), carbon (C) and lead (Pb). Silicon photonics was first proposed in the mid-1980s in order to avoid complex binary and ternary alloys of III-V materials [Soref’86]. Silicon was most used for datacom applications because of its minimal dispersion at the 1.3 µm wavelength region and the compatibility of PICs with optical fiber. Additionally, Si waveguides present low propagation loss at the second (1.31 µm wavelength) and third (1.55 µm wavelength) telecommunication windows, and the possibility of monolithic integration of electronic and photonic devices. Nevertheless, silicon inherently presents

poor quality for light emission and detection due to its indirect band gap. To overcome this constraint other group IV-based materials like Ge have been explored, successfully demonstrating lasers, modulators and photodetectors [Camacho-Aguilera'12, Liu'08, Vivien'09] that can be monolithically integrated with other silicon-based components. This convergence between silicon photonics and other group IV-based materials is also known as group IV photonics (GFP).

These material platforms have enabled remarkable achievements both in traditional communication applications [Liang'16] and in new optical frontiers, such as microwave an terahertz photonics [Marpaung'19, Harter'18, Tait'17], integrated frequency combs [Gaeta'19, Kippenberg'11], biochemical sensors [Juan-Colás'16, Wang'14a], LIDAR systems [Poulton'17a], or chips for microsatellites and microdrones [Jalali'06, Thomson'16, Vivien'16]. Ultimately, integrated photonics provide an untapped miniaturization potential that will greatly impact our world in the following years.

1.2. Applications and challenges of silicon photonics

Among all materials mentioned in the previous section, silicon has been the heart of modern microelectronics industry due to its unique nature as a semiconductor. Although it is rarely found as pure element in earth's crust, it can be obtained from silica, which is one of the most abundant compounds. As the manufacturing process of silicon wafers with a great purity is also affordable and efficient, the cost of fabricating electronic integrated circuits is reasonably economical. These compelling reasons have made silicon an engaging material that has been intensively developed in the microelectronics industry in recent decades.

One of the key advantages of silicon photonics is its leverage of the maturity of the fabrication techniques reached by the microelectronics industry, enabling cost-effective mass production [Chen'18]. Silicon-based PICs are compatible with complementary metal-oxide-semiconductor (CMOS) lithography processes and, consequently, can be monolithically integrated with CMOS electronics. Different material platforms have been proposed for silicon photonics hitherto, being their refractive index contrast (Δn) between the waveguide and cladding the key parameter for determining the integration density of photonics devices on the wafer. For example, the first silicon photonics waveguides presented a low refractive index contrast and were based on silicon on doped silicon [Soref'86], greatly limiting integration capacity. Material technology rapidly evolved towards high refractive index contrast platforms, such as silicon-on-insulator (SOI) and silicon nitride (Si_3N_4, commonly simplified to SiN), in order to achieve higher integration levels and perform more complex functions in a single chip. Since then, silicon photonics has undergone a fast-paced evolution driven mainly by the interest in optical interconnects for short-range communications links in the one meter to 10 km range [Miller'09, Vlasov'12].

The increased integration capacity of silicon photonics has enabled to tackle one of our greatest technological challenges: global data traffic. Internet traffic inside data centers is steadily growing worldwide, owing to two major factors. On the one hand, the number of devices connected to the internet is expanding as a result of 5G communications and Internet of Things (IoT) paradigms; while, on the other hand, there is an increasing demand for new services like big data, streaming and cloud computing that require massive data management. Figure 1.1 shows the annual internet traffic growth inside data centers from 2010 to 2018 and the forecast until 2021. In addition to exceeding the threshold of 20 zettabytes (1 zettabyte = 10^{21} bytes) in 2021, it is estimated that 95% of all this internet traffic will have a cloud nature and will be generated not only by humans but in large part by machine and automated devices [Cisco'18]. Not only the growth of global data traffic follows an exponential trend, also energy consumption of data centers does so. Hence, data center operators aim to reduce more than tenfold the energy required to transmit a single bit in the near future, reducing economic costs as well as their environmental footprint [Cheng'18]. In this imminent scenario of huge demand for broader bandwidth and faster data rates, it is crucial to harness the full potential of silicon photonics to improve both performance and energy consumption in intra- and inter-chip connections of data centers.

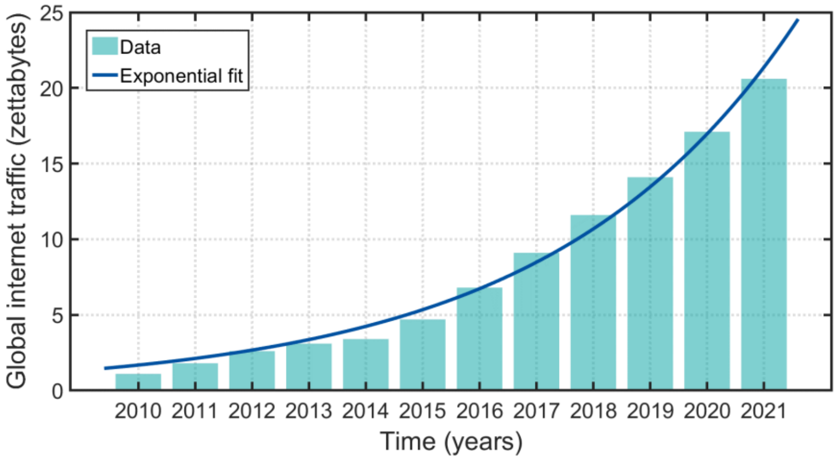

Figure 1.1. *Global internet traffic inside data centers as a function of time reported by Cisco Global Cloud Index white paper [Cisco'18].*

1.2.1. Advanced multiplexing technologies for optical interconnects

In order to cope with this enormous capacity demand, silicon-based optical interconnects are evolving through advanced multiplexing technologies that allow the simultaneous transmission and reception of multiple data channels through the same waveguide. These multiplexing technologies comprise:

- Wavelength-division multiplexing (WDM) is one of the most used multiplexing technologies, leveraging the intrinsic high-bandwidth density of silicon photonics to carry different data channels at different wavelengths [Lee'08]. Depending on the wavelength or frequency spacing between channels, two different alternatives can be distinguished. For dense WDM (DWDM) the space between frequency carriers is usually less than 200 GHz (~1.6 nm at the wavelength of 1550 nm) [Liu'19a], resulting in tens of channels multiplexed in the wavelength domain. For example, a silicon integrated receiver with an aggregate data rate of 1 Tb/s (40 WDM channels × 25 Gb/s) has already been demonstrated by using DWDM [Feng'13]. Since each channel requires one laser source tuned at a given wavelength, all the lasers must be carefully aligned and stabilized with the complexity and cost that this entails [Dai'14]. A more attractive approach is coarse WDM (CWDM), with a broader spacing between channels (20 nm) that allows to relax these requirements and reduce power consumption [Driscoll'18].
- Polarization-division multiplexing (PDM) employs two orthogonal polarization states of light-waves to double the number of channels for a single wavelength [Doerr'10]. For instance, two sets of solutions are obtained by solving Maxwell's equations in rectangular waveguides that are typically used for silicon photonics: quasi transverse electric (quasi-TE) modes with horizontal or in-plane polarization and quasi transverse magnetic (quasi-TM) modes with vertical or out-of-plane polarization. Notice that optical axes are defined in integrated optics by the chip plane. PDM has been demonstrated together with different modulation schemes [Dong'12, Dong'13] or WDM [Chen'15a] in order to increase the overall aggregated bandwidth for silicon optical interconnects.
- Optical time-division multiplexing (OTDM) is another essential multiplexing technology to multiply the overall transmission capacity of silicon optical interconnects [Aboketaf'10]. In OTDM, different data channels are transmitted through a waveguide at the same wavelength but interleaved at different time slots, i.e. the main data stream consists of time-

multiplexed streams retrieved from each input data channel. By way of illustration, optical demultiplexing of a 1.28 Tb/s data signal has been demonstrated by means of nano-engineered silicon waveguides [Ji’10], whereas a 640 Gb/s OTDM signal has been successfully generated using silicon microring resonators [Ding’11].

- Space-division multiplexing (SDM) aims to further increase capacity of WDM, PDM and OTDM technologies. This solution relies on placing several physical channels that are spatially distributed on the chip. Therefore, it is necessary to use in parallel as many waveguides and photonic components as additional spatial channels are desired [Song’15]. For this reason, the footprints of SDM-PICs are dramatically large and waveguide crossing are often necessary, incrementing the layout complexity.
- Mode-division multiplexing (MDM) has recently emerged with the development of high refractive index contrast platforms that allow efficient mode-selective manipulation [Li’18a]. As the name implies, MDM is based on several spatial eigenmodes (or simply modes) supported by a multimode waveguide. It is important to highlight that eigenmodes are the solutions for the propagation of light-waves inside a waveguide with a certain geometry, obtained by solving Maxwell’s equations. These eigenmodes form an orthogonal space of functions which means that interference between them does not occur [Dändliker’00]. As a consequence, each data channel can be spatially encoded in a specific mode of the multimode waveguide, being the capacity increase directly proportional to the total number of modes used.

Among all these multiplexing technologies, WDM, PDM and OTDM are three mature and well-developed solutions that are already being used in optical interconnects. Conversely, SDM and MDM are two promising candidates that have recently emerged and are not intended to replace WDM, PDM and OTDM, but to complement them by adding new degrees of orthogonality to further increase capacity. In particular, MDM is focusing much attention because it maintains the level of integration and avoids the losses related to waveguide crossings required in SDM.

1.2.2. Applications beyond optical interconnects

Besides short-range optical interconnects for telecom and datacom applications, the progress in silicon photonics also encompasses many other untapped applications that are being explored by academia and industry. Absorption spectroscopy and bio-sensing applications benefit from high refractive index contrast platforms for compact and high-resolution sensors [Herrero-Bermello’17, Wangüemert-Pérez’19]. These devices can be used in handheld analysers, microdrones for environmental monitoring in hazardous areas, and even in microsatellites; replacing classic Fourier transform (FT) spectrometers based on moving mirrors with spatial heterodyne FT (SHFT) microspectrometers that avoid any difficulty of aligning moving parts [Florjańczyk’07]. Health-related aspects can also be monitored using biochemical sensors that perform medical analyses on lab-on-a-chip solutions [Estevez’12, Wang’14a].

Silicon photonics is also present in the automotive sector with optical phased arrays used as transmitters and receivers in integrated chips for light detection and ranging (LIDAR), i.e. for simultaneous distance and velocity measurements by illuminating objects with a laser light and measuring the reflected light [Poulton’17a]. Other LIDAR applications include 3D object recognition, aerial terrain mapping and atmospheric study (pollution, gas composition, meteorology, to name a few).

Other recently proposed cutting-edge applications comprise quantum computing [Harris’16], radio-over-fiber systems [Vacondio’10], microwave and terahertz photonics [Marpaung’19, Harter’18], nonlinear optics [Leuthold’10], long wavelength integrated photonics in mid-infrared (MIR) [Soref’10], integrated frequency combs [Kippenberg’11] and many others.

The importance of silicon photonics is further supported by the recent economic analyses, placing the value of the silicon photonics market around 700 million dollars in 2018 with a compound annual growth rate of more than 20% for the period from 2018 to 2023 [ReportsnReports’18]. This economic growth is mainly driven by optical interconnects in data centers, however, non-data center applications mentioned above are expected to grow to an impressive value of 300 million dollars in 2025 [YoléDevelopment’16].

1.2.3. The challenge ahead

However, in order to reach its full potential, silicon photonics needs to overcome a series of challenges which currently slow down both their scientific impact and industrial applicability. The performance of any on-chip application is determined by two factors: its top-level design, which is specific for each application; and the performance of its constituent elements, which in a significant part is common to all applications, as they share many fundamental building blocks, such as couplers, multiplexers, splitters, polarization controllers, etc.

Standard building blocks currently available in photonic design kits are often rudimentary and present limited performances (bandwidth, losses, crosstalk, etc), hindering the access of end-application designers to the technology. This is mainly caused by the inherent properties of silicon waveguides, as well as by fabrication limitations. On the material front, the same high index contrast that enables the integration capacity of silicon photonics also results in a high birefringence, challenging dispersion profiles and elevated thermal dependence. Fabrication technology also presents stringent minimum feature size limitations. The combination of both material properties and foundry limitations also results in a very high sensitivity to fabrication errors (i.e. small deviations from nominal design result in sharp performance degradation).

It is therefore of paramount importance to develop new fundamental building blocks that address these core challenges and provide the foundation for a new generation of high-performance on-chip applications.

1.3. Objectives and organization of this thesis

1.3.1. Main objectives and content overview

The framework described in the previous sections reveals that silicon photonics has been postulated as a promising technology to develop numerous applications in an efficient and compact manner. While it seems that the sweet spot for large-scale manufacturing process has been found, there is still much room for improvement in the performance of the fundamental components. The main objective of this thesis is the design and characterization of key building blocks with high performance and large fabrication tolerances for next generation silicon photonic integrated circuits. To overcome the inherent limitations posed by the material platform, mainly SOI in this thesis (see Appendix A for a full description of the material platforms), original and novel structures based on nano-scale features have been proposed and experimentally demonstrated, including subwavelength grating (SWG) metamaterial and slot waveguides.

The work conducted during this thesis is graphically outlined in Fig. 1.2, highlighting the three main building blocks that articulate the present document (namely a broadband mode converter and multiplexer/demultiplexer, an ultra-broadband nanophotonic phase shifter, and an ultra-broadband dual-polarization beam splitter). A brief synopsis for each block is presented hereunder.

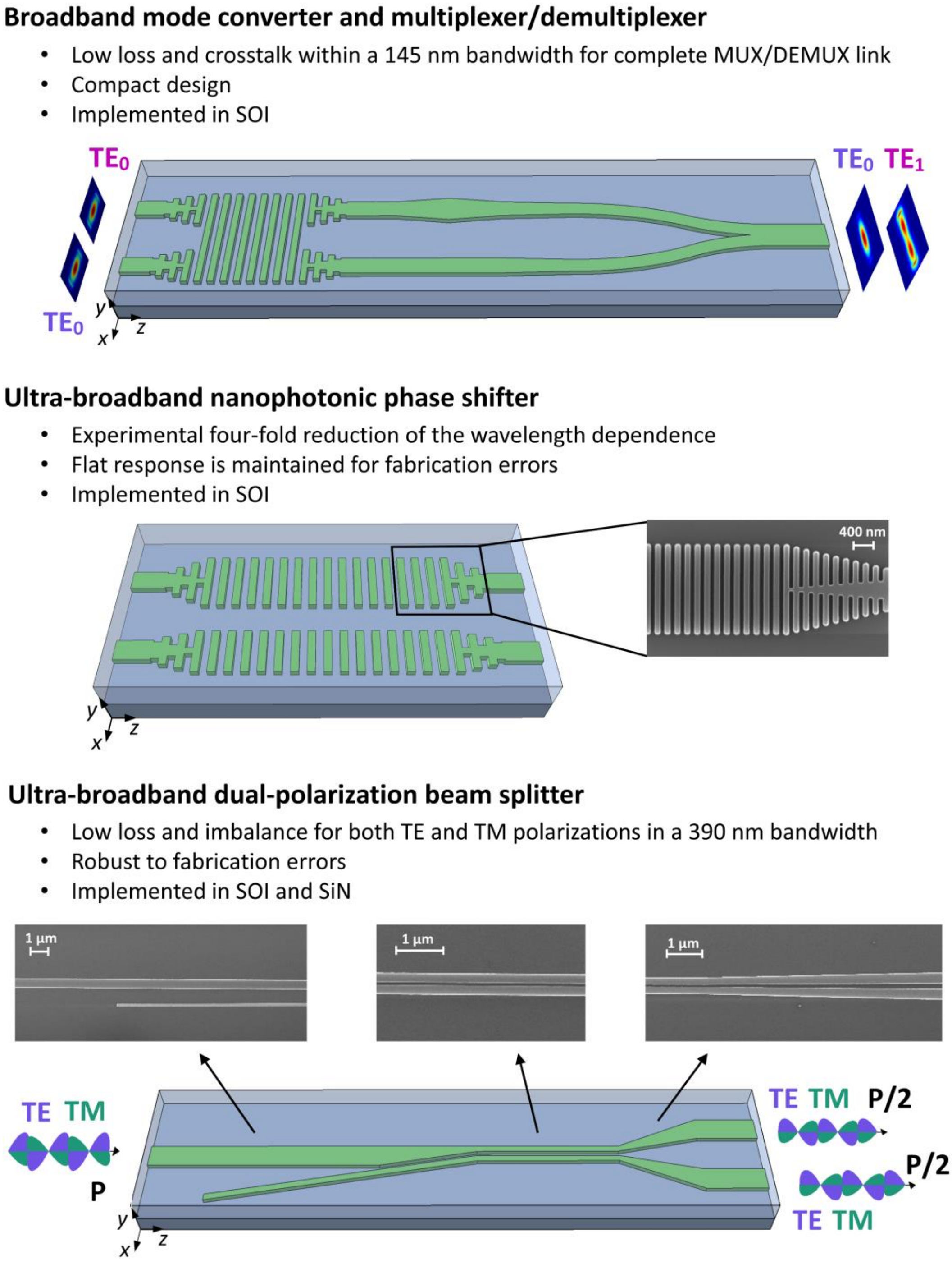

Broadband mode converter and multiplexer/demultiplexer

- Low loss and crosstalk within a 145 nm bandwidth for complete MUX/DEMUX link
- Compact design
- Implemented in SOI

Ultra-broadband nanophotonic phase shifter

- Experimental four-fold reduction of the wavelength dependence
- Flat response is maintained for fabrication errors
- Implemented in SOI

Ultra-broadband dual-polarization beam splitter

- Low loss and imbalance for both TE and TM polarizations in a 390 nm bandwidth
- Robust to fabrication errors
- Implemented in SOI and SiN

Figure 1.2. *Graphical overview of the work conducted in this thesis.*

Broadband mode converter and multiplexer/demultiplexer

Advanced multiplexing technologies enabled by silicon photonics have increased the capacity of optical interconnects satisfying the ever-growing capacity demand for telecom and datacom applications. Mode-division multiplexing has recently focused the attention of the research community to add an additional orthogonal degree to already existing optical communications systems based on WDM and PDM [Luo'14, Wang'14b]. One of the key elements to perform MDM is the mode converter and multiplexer/demultiplexer (MUX/DEMUX). As the name implies, this component performs two different functions. Working as MUX, it converts the fundamental modes into other higher-order modes and combines them into a single multimode waveguide. Conversely working as DEMUX, higher-order modes are converted into fundamental modes and at the same time separated into different physical single-mode waveguides. Several mode MUX/DEMUX have been proposed to date; however, these architectures are intrinsically narrowband solutions due to their physical operation principle or present relative wide bandwidths at the cost of long lengths and stringent fabrication tolerances [Li'18a].

One of the goals of this thesis is to overcome these constraints by implementing a compact and broadband mode MUX/DEMUX based on a subwavelength engineered multimode interference (MMI) device, a 90° phase shifter (PS) and a symmetric Y-junction. Here, SWG metamaterial waveguides have been exploited to control the dispersion of the higher-order modes propagated through the multimode section of the MMI, and therefore, to reduce the wavelength-dependent losses of conventional MMIs [Halir'16]. The device has been designed and fabricated in the SOI platform displaying a compact footprint of only $38.6 \times 3.7\ \mu m^2$. Experimental demonstration of a passive MUX/DEMUX based on an MMI has been carried out for the first time. A complete MUX-DEMUX link (i.e. two devices in back-to-back configuration) exhibits insertion loss below 1.3 dB (0.65 dB per device) and crosstalk better than -15.3 dB for both TE_0 and TE_1 modes within a broad bandwidth of 145 nm. This device has been developed in collaboration with Alcyon Photonics S.L., the University of Malaga and the National Research Council of Canada.

Ultra-broadband nanophotonic phase shifter

Optical phase shifters are essential components in a wide range of applications, including telecom and datacom, sensing and quantum computing [Hillerkuss'10, Knill'01]. These devices can be classified into two groups, active phase shifters and passive phase shifters. The biggest difference between them is that active phase shifters leverage different physical effects to dynamically tune their wavelength response (i.e. change their optical path) [Harris'14, Soref'87], while in passive phase shifters the response is static (i.e. it cannot be tuned) [Morrissey'15]. Active phase shifters have focused most scientific efforts as they are used for the implementation of modulators, switches or tunable filters [Reed'10, VanCampenhout'09, Djordjevic'11]. On the other hand, very little progress has been made in passive phase shifters that are currently becoming more important for arbitrary-ratio power splitters [Cherchi'14] and in the MDM field [Yi'14], as stated previously.

In collaboration with the UMA and the NRC, the limitations of passive phase shifters have been theoretically studied, and an ultra-broadband solution has been proposed harnessing both anisotropy and dispersion engineering of two SWG waveguides with the same length. A 90° phase shifter has been designed and implemented for the SOI platform. Simulation results predict a phase error below ±1.7° within an unprecedented 400 nm bandwidth. Furthermore, the flat response is maintained for fabrication errors up to ±20 nm. In order to measure the spectral response of the fabricated phase shifters a novel method has been presented. Experimental results show a four-fold reduction of the wavelength dependence compared to conventional counterparts.

Ultra-broadband dual-polarization beam splitter

Another essential building block in integrated optics are power splitters, also named beam splitters. These devices can be found in a myriad of applications in addition to telecom and datacom, such as sensing, spectroscopy and LIDAR [Dong'14, Estevez'12, Poulton'17a, Velasco'13b], to name a few. Since the beginning of integrated optics, optical beam splitters have been intensively studied and many different beam splitting architectures have been reported for the SOI platform. However, these devices suffer either from narrow bandwidths, single-polarization operation or tight fabrication tolerances. The narrowband behaviour stems from the strong modal dispersion of SOI waveguides, whereas the single-mode operation arises from the high birefringence between TE and TM polarizations. High-performance beam splitters meeting those requirements are still sought for next-generation PICs.

In this context, a design methodology has been developed that can be used for both the SOI and SiN platforms. The design, fabrication and measurement process has been carried out in collaboration with the Centre de Nanosciences et de Nanotechnologies and the NRC. The proposed beam splitter is based on a modal engineered slot waveguide. Excess loss and imbalance of less than 1 dB have been demonstrated in the SOI platform for both polarizations and a bandwidth exceeding 390 nm. This high performance is maintained even in the presence of fabrication errors of up to ±25 nm. Finally, the splitter was thoroughly redesigned for SiN platform, achieving excess loss and imbalance below 0.7 dB for both TE and TM polarization in an outstanding 420 nm wavelength range.

1.3.2. Document organization

The structure of this thesis is divided into the following six chapters. Chapter II provides the theoretical basis of periodic waveguides, with special emphasis on subwavelength metamaterial structures. The fundamentals and applications are reviewed in detail since they will serve as foundation for the design of the devices in subsequent chapters.

Chapter III is devoted to the design and characterization of a broadband mode multiplexer/demultiplexer in the SOI platform. First, the state of the art is reviewed the and principle of operation of the proposed device is discussed in detail. Subsequently, the optimization of the design performed for the device fabrication is explained and the broadband experimental characterization is presented.

Chapter IV is dedicated to the proposed SWG phase shifter. Limitations of state-of-the-art passive phase shifters based on waveguides of the same length are studied. The use of metamaterial SWG waveguides to mitigate wavelength dependence is presented and applied to the design of an ultra-broadband phase shifter. Fabrication and characterization of the novel device is then described, including theoretical and experimental comparison of other state-of-the-art phase shifters.

In Chapter V, the design of an ultra-broadband dual-polarization beam splitter is carried out for both the SOI and SiN platforms. The design is detailed first for the SOI platform and the experimental results are presented. Next, the consequences of moving from SOI to SiN are explained, the modifications made in the design are specified and the characterization results are shown.

Finally, Chapter VI summarizes the conclusions obtained from this thesis and potential future work lines.

Bibliography is found at the end of the document.

II

Fundamentals of subwavelength grating waveguides

Periodic structures have attracted the interest of scientists since the end of the nineteenth century, when it was already known that the behaviour of the waves propagating through the periodic medium depends on the aspect ratio between the periodicity and the operating wavelength. In this chapter, the principle of operation of periodic waveguides is reviewed, with special emphasis on the subwavelength case. Section 2.1 provides a brief historical introduction, where the Floquet-Bloch theorem is presented and applied to periodic waveguides. In section 2.2, the 3D problem is reduced to a one-dimensional stratified medium with analytical solution. However, this approach is not complete, therefore, in section 2.3 each operating regime of periodic waveguides is explained in detail. Finally, section 2.4 reviews some essential applications of SWG waveguides. The potential of this technology for the development of high-performance PICs is also succinctly discussed in this section.

2.1. Introduction to periodic structures

The propagation of waves through a medium endowed with a periodic structure was already studied by Lord Rayleigh at the end of the XIX century [Rayleigh’87]. In his seminal paper, Rayleigh explained the reflection of a train of progressive waves incident to a laminated medium with periodic variations and concluded that partial reflexions occur in phase when the period of the structure is approximately the half of the wavelength of the incident waves. In this way, reflections interfere constructively, resulting in a strong back reflection of the wave propagated through the periodic medium. Only one year later, Hertz made use of a network of wires distributed periodically to filter radio waves depending on their polarization [Hertz’88]. In his experiment, the period of the network was much smaller than the wavelength of radio waves, thus, modifying the electromagnetic properties of the transmission medium whereby radio waves were propagated according to the network orientation. These two dissimilar applications only show an apex of the importance that periodic structures would acquire in the following decades.

Along the XX century, periodic structures were intensively investigated for application in various areas such as optical multilayers [Muchmore’48], slow wave propagation in microwave tubes and optical waveguides [Field’49, Oliner’59], antennas [Thomas’57] and wave propagation in time-space periodic media [Cassedy’63], to name a few. More recently periodic thin-film dielectric waveguides have been used in integrated optics for the development of distributed feedback (DFB) and distributed Bragg reflector (DBR) lasers [Wang’74], optical reflection filters [Flanders’74], mode converters [Kuhn’71] and surface grating couplers [Harris’72]. The extreme versatility demonstrated by periodic waveguides stems from the radically different behaviours that can be achieved depending on the relation between the structure period and the wavelength of the propagated wave, as detailed in the following sections.

Fundamentals of periodic waveguides can be analysed using the Floquet-Bloch theory, which owes its name to the French mathematician Gaston Floquet and the Swiss physicist Felix Bloch. In 1883, Floquet found the solution to the problem of a linear differential equation with periodic coefficients [Floquet’83]. Bloch generalized these results many years later when he studied the propagation of electrons in a periodic crystal structure [Bloch’28]. The solution of the wave function reached by Bloch are called Bloch waves, which would lay the basis for energy band and solid state theories [Simon’13].

Far from conducting an exhaustive mathematical development of electromagnetic waves propagating through periodic waveguides, the present introductory section aims to give a more comprehensive analysis to the propagation behaviour in periodic waveguides. To this effect, it is fundamental to introduce the Floquet-Bloch theorem [Davison'96].

Consider a second-order differential equation with periodic coefficients $P(z)$ with period Λ, i.e. $P(z \pm \Lambda) = P(z)$, and a stationary state $\xi(z)$:

$$\frac{d^2\xi(z)}{dz^2} + P(z)\xi(z) = 0. \tag{2.1}$$

The solution to this type of differential equation is given by the Floquet-Bloch theorem and can be expressed as a linear combination of functions of the form

$$\xi(z) = e^{jkz}u(z), \tag{2.2}$$

in which $u(z)$ is a periodic function that satisfies $u(z \pm \Lambda) = u(z)$ and k is a constant to be determined.

One of the most important conclusions that can be drawn from the Floquet-Bloch theory is the electromagnetic field solution that is propagated through a periodic waveguide. Figure 2.1 shows a schematic view of a periodic waveguide with a segmented core along the z direction. In addition to the waveguide width and thickness, two new parameters define the structure of a periodic waveguide, namely the spatial repetition interval or pitch (Λ) and the duty cycle ($\mathrm{DC} = a/\Lambda$), where a is the length of each core segment within a period. The refractive index of the structure varies periodically in the z axis, which can be mathematically expressed as

$$n(x,y,z) = n(x,y,z \pm \Lambda), \tag{2.3}$$

where Λ is the spatial period or pitch, and z is the direction of propagation.

Considering the propagation of an electromagnetic wave in the z direction, i.e. lengthwise to the periodic waveguide, the field solution, $\vec{E}(x,y,z)$, can be expressed as the product of two functions as the Floquet-Bloch theorem states:

$$\vec{E}(x,y,z) = \vec{E}_B(x,y,z)e^{-\gamma_B z}, \tag{2.4}$$

where γ_B is the complex propagation constant and $\vec{E}_B(x,y,z)$ is periodic in the z direction with a period Λ:

$$\vec{E}_B(x,y,z)=\vec{E}_B(x,y,z\pm\Lambda). \tag{2.5}$$

It should be noted that the electric field component has been selected here as an example, but the same procedure can be applied to the magnetic field component. In addition, the temporal dependence $e^{j\omega t}$ is assumed throughout the thesis for clarity in the notation.

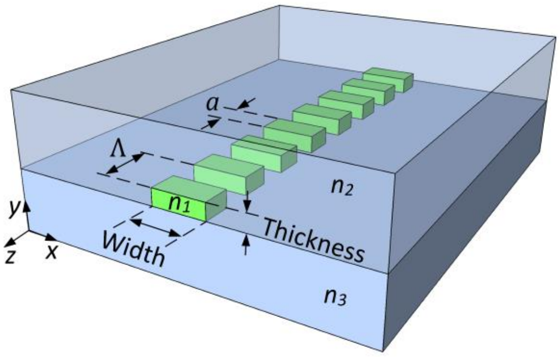

Figure 2.1. *Schematic of a periodic waveguide consisting of a segmented core with refractive index n_1 (in green), an upper cladding layer with refractive index n_2 and a lower layer n_3. The structure presents a period Λ and a duty cycle of a/Λ.*

The field described in Eq. (2.4) is known as the Floquet-Bloch mode of the periodic waveguide and can be understood as a generalization of the modes propagated through a conventional, i.e. non-periodic, waveguide (see Fig. A.1 of Appendix A). Nevertheless, the main difference with conventional waveguide modes is that the Floquet-Bloch mode profile is not constant along the direction of propagation, but is repeated with the same period as the periodic waveguide. The transmission characteristics are given by the exponential function and the complex propagation constant that can be broken down into real and imaginary parts:

$$\gamma_B=\alpha_B+j\beta_B, \tag{2.6}$$

where α_B is the attenuation constant and β_B is the phase constant (also known as propagation constant). The attenuation constant is directly related to the propagation loss per unit length, while the phase constant indicates the phase change experienced by the Floquet-Bloch mode as it propagates along the periodic waveguide. It is important to mention that the definition of the phase throughout this thesis is $\Phi =$

$-\beta_B z$. Similar to conventional waveguide modes, the complex effective index of the Floquet-Bloch mode can be defined as follows

$$n_{eff,B} = -j\frac{\gamma_B}{k_0} = \frac{\beta_B}{k_0} - j\frac{\alpha_B}{k_0} = n_{eff,B,r} + jn_{eff,B,i}. \tag{2.7}$$

Here, k_0 is the vacuum wavenumber, i.e. $k_0 = 2\pi/\lambda$, and $n_{eff,B,r}$ and $n_{eff,B,i}$ are the real and imaginary parts of the complex effective index, respectively. It is important to note that through the thesis the term “effective index” (without mentioning the word complex) refers to $n_{eff,B,r}$.

2.2. Periodic stratified medium

Although the modes of a periodic waveguide have been defined using the Floquet-Bloch theorem, there are no analytical solutions to describe the behaviour of a 3D periodic waveguide. However, a simplified approach based on a stratified medium can be used for this purpose, which consists in reducing the problem to a single dimension. In such a way, the periodic structure is infinitely extended in the z and x directions. Figure 2.2 shows an example of a stratified medium based on an arrangement of different dielectric materials with refractive indexes n_1 and n_2 alternated periodically along the z axis with a pitch Λ and DC $= a/\Lambda$.

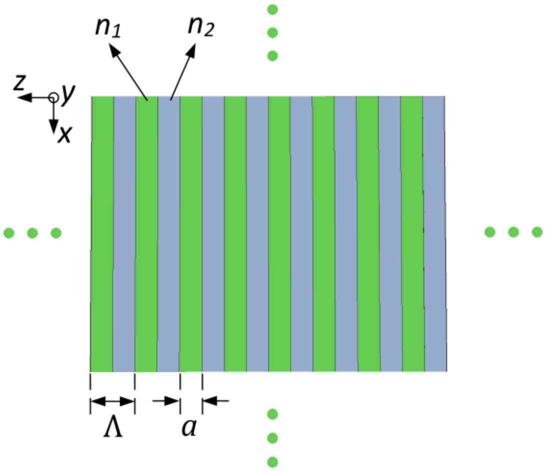

Figure 2.2. *Top view of a two-layer stratified medium that extends indefinitely in both x and z directions. The two layers with refractive indexes* n_1 *and* n_2 *are repeated periodically along the z axis with a period Λ and a duty cycle a/Λ.*

The behavior of a Floquet-Bloch mode with normal incidence to the interface of the layers (propagation along the z axis) was already studied in 1977 [Ye'77]. Analytical solutions were obtained by applying the Floquet-Bloch theorem to a periodically stratified medium, obtaining two different operating regimes depending on the relationship between the wavelength of the mode and pitch of the structure:

- Propagation of Floquet-Bloch modes, where the complex propagation constant is a pure imaginary number, i.e. $\alpha_B = 0$. Therefore, the Floquet-Bloch mode propagates throughout the periodic medium without radiation or reflection losses. The condition that needs to be fulfilled to operate in this regime is given by the following expression:

$$\beta_B = \frac{2\pi}{\lambda} n_{eff,B,r} < \frac{\pi}{\Lambda}, \tag{2.8}$$

- Forbidden bands of the periodic medium, where the Floquet-Bloch mode is evanescent and, thus, the complex propagation constant presents a real part. i.e. $\alpha_B \neq 0$. The Floquet-Bloch mode propagated along the periodic medium in the z axis is reflected in the opposite direction since the Bragg condition is fulfilled:

$$\gamma_B = \alpha_B + j\frac{2\pi}{\lambda} n_{eff,B,r} = \alpha_B + j\frac{m\pi}{\Lambda}, \tag{2.9}$$

  where m is an integer indicating the m^{th} region of Bragg. The wavelength range at which the previous condition is satisfied is also known as photonic bandgap in the field of photonic crystals.

2.3. Operating principle of periodic waveguides

The operation of a 3D periodic waveguide also depends on different factors such as the material platform and the geometry of the waveguide, although to a lesser extent than the ratio between the pitch of the waveguide and the wavelength of the Floquet-Bloch mode. Most experiments with periodic waveguides working in the transmission and reflection regimes have demonstrated to follow the same behaviour as described in the previous section 2.2 [Halir'15]. Notwithstanding, the principle of operation of periodic waveguides can be sorted into three different regimes: radiation, reflection (or Bragg) and diffraction-less transmission (or subwavelength), as shown in Fig. 2.3.

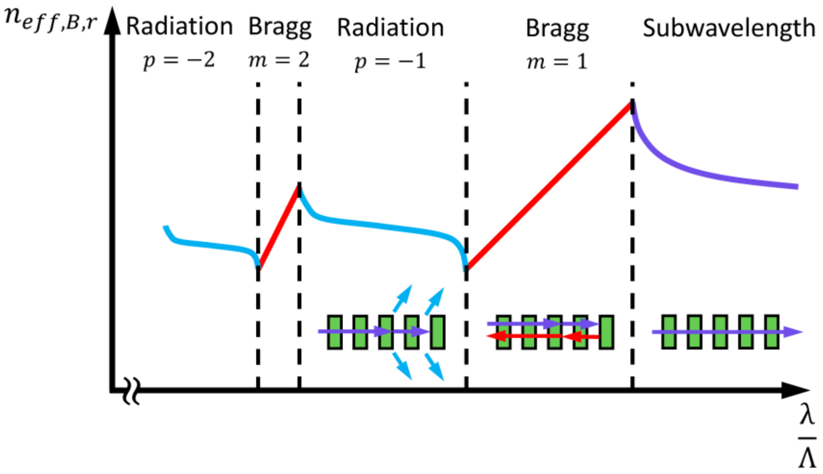

Figure 2.3. *Real part of the Floquet-Bloch refractive index as a function of the wavelength-to-pitch ratio. Second-order radiation and Bragg reflection regimes are shown as an example of the distribution followed by higher-order operation bands. The operation of periodic waveguides is schematically represented for the subwavelength regime and first-order radiation and Bragg reflection. This graph has been adapted from [Halir'15].*

Since the study of a periodic stratified medium developed by Yeh *et al.* [Ye'77] is a 1D approach, it does not consider the possibility of the modes being radiated to the upper cladding or the lower layer. For the sake of providing an insightful overview of all operation regimes of a periodic waveguide, diffractive effects are explained in detail in this section. In addition, a deeper approach will be carried out on the transmission of Floquet-Bloch modes through periodic waveguides and their forbidden bands.

2.3.1. Radiation regime

In the radiation regime, the light propagated through a periodic waveguide (or grating) is diffracted. For consistency with the nomenclature used in section 2.1, the mathematical development will be carried out for the electric field component though the procedure is also valid for the magnetic field component. In practice, the field distribution of the Floquet-Bloch mode supported by the periodic structure can be considered invariant in the x direction [Tamir'77] (see Fig. 2.4):

$$\vec{E}(y,z)=\vec{E}_B(y,z)e^{-\gamma_B z}. \qquad \textbf{(2.10)}$$

Since the mode profile $\vec{E}_B(y,z)$ is a periodic function in the z dimension with a period Λ, it can be expressed as a Fourier series expansion:

$$\vec{E}_B(y,z)=\sum_p \psi_B^{(p)}(y)e^{jp\frac{2\pi}{\Lambda}z}, \tag{2.11}$$

where $\psi_B^{(p)}(y)$ is the field distribution along the y axis and p is an integer that stands for the harmonic order. Replacing the Floquet Bloch mode profile, $\vec{E}_B(y,z)$, with its Fourier series expansion, Eq. (2.10) can be rewritten as

$$\vec{E}(y,z)=\sum_p \psi_B^{(p)}(y)e^{\gamma_B^{(p)}z}. \tag{2.12}$$

Here, $\gamma_B^{(p)}$ is the complex propagation constant of the harmonic of order p, whose real and imaginary parts are

$$\gamma_B^{(p)}=\alpha_B+j\beta_B^{(p)}. \tag{2.13}$$

As can be inferred from Eq. (2.13), all harmonics of the Floquet-Bloch mode share the same attenuation constant, whereas the phase constant presents different values for each harmonic

$$\beta_B^{(p)}=\beta_B+p\frac{2\pi}{\Lambda}. \tag{2.14}$$

Figure 2.4 shows the phase matching condition for the diffraction of a Floquet-Bloch harmonic with phase constant $\beta_B^{(p)}$. For the sake of clarity, only radiation towards the upper cladding is represented.

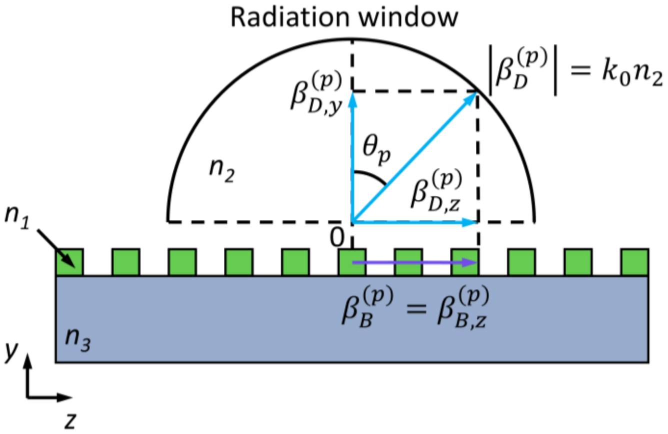

Figure 2.4. *Schematic of the upper radiation window of a diffraction grating (side view). The harmonic of order p supported by the periodic waveguide with phase constant* $\beta_B^{(p)}$ *is radiated to the upper cladding since the phase matching condition* $\beta_{B,z}^{(p)}=\beta_{D,z}^{(p)}$ *is satisfied at a given angle* θ_p.

The radiation window is a semicircle of radius equal to $k_0 n_2$ since the upper cladding supports manifold plane waves defined by the following phase constant

$$\beta_D^{(p)} = \beta_{D,z}^{(p)} + \beta_{D,y}^{(p)} = k_0 n_2 \left[\sin\left(\theta_p\right) + \cos\left(\theta_p\right)\right], \tag{2.15}$$

where θ_p is the radiation angle (defined with respect to the vertical) for the diffracted harmonic of order p, and $\beta_{D,z}^{(p)}$ and $\beta_{D,y}^{(p)}$ are the components of the diffraction phase constant in the z and the y axes, respectively.

If the phase constant of the Floquet-Bloch harmonic matches the longitudinal component of the diffraction phase constant, i.e. $\beta_{B,z}^{(p)} = \beta_{D,z}^{(p)}$, the harmonic will be radiated towards the upper cladding. This expression can be rewritten as follows, yielding the grating equation

$$\frac{2\pi}{\lambda} n_{eff,B,r} + p\frac{2\pi}{\Lambda} = k_0 n_2 \sin\left(\theta_p\right), \tag{2.16}$$

$$n_{eff,B,r} + p\frac{\lambda}{\Lambda} = n_2 \sin\left(\theta_p\right). \tag{2.17}$$

To work in the radiation regime and satisfy the equality of Eq. (2.17), two requirements must be met. First, the angle θ_p must be real; and second, only harmonics with a negative order, i.e. $p < 0$, can be radiated by the grating since $n_{eff,B,r} > n_2$. Taking into consideration both requirements, Eq. (2.17) leads to

$$\left| n_{eff,B,r} + p\frac{\lambda}{\Lambda} \right| \le n_2, \tag{2.18}$$

and the upper and lower limits of the grating period to radiate the p^{th} harmonic at a particular wavelength are, respectively,

$$\Lambda_{\max} = \frac{p\lambda}{-n_{eff,B,r} + n_2}, \tag{2.19}$$

$$\Lambda_{\min} = \frac{-p\lambda}{n_{eff,B,r} + n_2}. \tag{2.20}$$

The pitch interval defined by Eqs. (2.19) and (2.20) for the p^{th} harmonic can partially overlap with the interval of the following harmonic of order $p + 1$. Hence, gratings can diffract one or more harmonics depending on the design parameters.

This radiation regime occurs between two consecutive Bragg regions and is typically exploited in integrated optics by surface grating couplers in order to couple the light into an optical fiber and vice versa [Taillaert'02]. Owing to their versatility and ease for integration into any position of the chip surface, diffraction gratings have become essential components in silicon photonics for fiber-chip light coupling [Alonso-Ramos'14, Benedikovic'17, Sánchez-Postigo'16], avoiding the large mismatch of size and refractive index between waveguides and optical fiber modes. Nevertheless, other applications have also been explored, including beam splitters [Yang'11], wavelength duplexers [Roelkens'07], polarization beam splitters [Tang'09], biosensors [Wei'08] and optical spectrometers [Chaganti'06].

Operation of most surface grating couplers relies on a single beam radiation to couple the light from the chip into the optical fiber (or vice versa). Note that each diffraction order is radiated with a different angle given by Eq. (2.17) and the optical fiber can only be aligned to one of them. Figure 2.5 shows a 3D representation of a grating coupler (panel a) and the equivalent 2D model (panel b). The original 3D design problem can be simplified to the 2D side view problem because the width of the grating coupler (W_{GC}) tend to be very wide compared to the operating wavelength, and consequently, the structure can be considered as invariant in the x direction [Tamir'77].

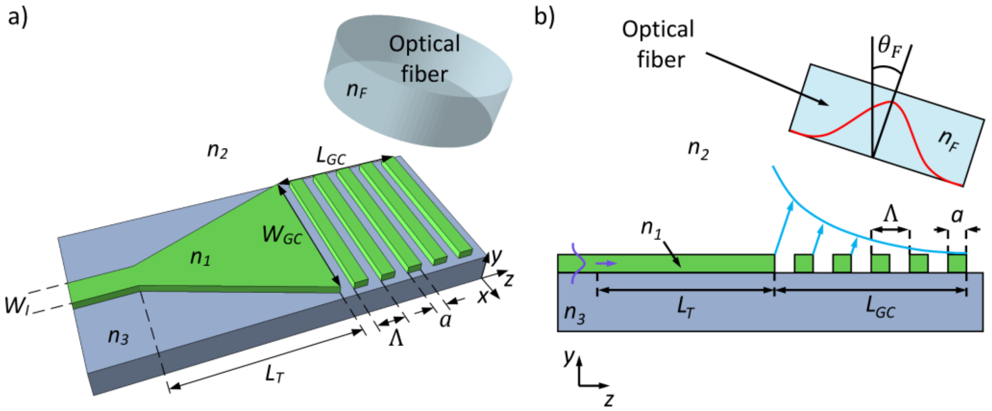

Figure 2.5. *(a) 3D view of a conventional surface grating coupler used to couple light from the chip into an optical fiber or vice versa. A tapered transition of length* L_T *is required to connect the interconnection waveguide (width* W_I*) with the grating coupler (width* W_{GC}*). (b) 2D model of the same grating coupler (side view). The fundamental modes of the interconnection waveguide and the optical fiber are depicted in purple and red, respectively. The field radiated by the grating coupler (in blue) follows an exponential distribution.*

The mismatch between the width of the interconnection waveguide (W_I) and the width of the grating coupler requires the integration of an adiabatic taper, whose length (L_T) is designed to minimize the transmission loss. On the other hand, the periodic section consists of an arrangement of different alternating materials with refractive indexes n_1 and n_2 repeated periodically. Both the duty cycle and the pitch determine the length of each segment, i.e. $a = \mathrm{DC} \cdot \Lambda$ for core segments (in green) and $\Lambda - a$ for the upper cladding segments (in white). The width and the total length (number of periods) of the grating are designed to maximize the overlap between the radiated field with exponential distribution (in blue) and the fundamental mode of the optical fiber with Gaussian distribution (in red). It should be noted that the optical fiber is placed above the grating coupler with a certain tilt angle, θ_F, which is the same as the angle of the beam radiated from the grating, as previously described.

2.3.2. Bragg reflection regime

The reflection regime of a periodic waveguide is also denoted as Bragg regime, inheriting the name from the study conducted by Bragg on X-rays reflected by crystal structures [Bragg'13]. As previously outlined for a stratified medium, a periodic waveguide with a period equal to a multiple of half the wavelength propagating through the structure is said to satisfy the Bragg condition. This expression can be rewritten for the convenience of the reader as

$$\Lambda = \frac{m\lambda}{2n_{eff,B,r}}, \tag{2.21}$$

with m integer and $n_{eff,B,r}$ being the real part of the complex effective index of the Floquet-Bloch mode. The wavelength at which Bragg's condition is met is also referred to as Bragg wavelength.

The behaviour of waveguide Bragg gratings can be explained analytically by another form of the grating equation [Loewen'97]. For reflection to occur, the phase constant of the Floquet-Bloch mode propagating in the z direction must match the backward-propagating Floquet-Bloch mode (rather than the diffraction phase constant). This phase-matching condition is given by

$$\frac{2\pi}{\lambda} n_{eff,B,r} + p\frac{2\pi}{\Lambda} = -\frac{2\pi}{\lambda} n_{eff,B,r}, \tag{2.22}$$

where the minus sign comes from the opposite direction of propagation ($-z$) and the change of variables $p = -m$ must be considered to deduce Eq. (2.21).

An example of an integrated Bragg filter based on this principle is schematically shown in Figs. 2.6a (3D view) and 2.6b (side view). The device is based on a periodic refractive index modulation along the z direction with a pitch that fulfils the Bragg condition of Eq. (2.21). The length of the Bragg grating (L_{BG}) is typically designed to be long enough in order to avoid light transmission at the Bragg resonant wavelength. In this case, the light propagating in the z direction (represented in purple in Fig. 2.6b) is back-reflected at each discontinuity of the periodic segments until all the incident light is mirrored in the opposite direction (in red). An intuitive way to understand this operating principle is to consider reflected light as a set of waves added in phase (that is, constructively, since the pitch is a multiple of half the wavelength in the medium), causing strong reflections in the counterpropagating direction.

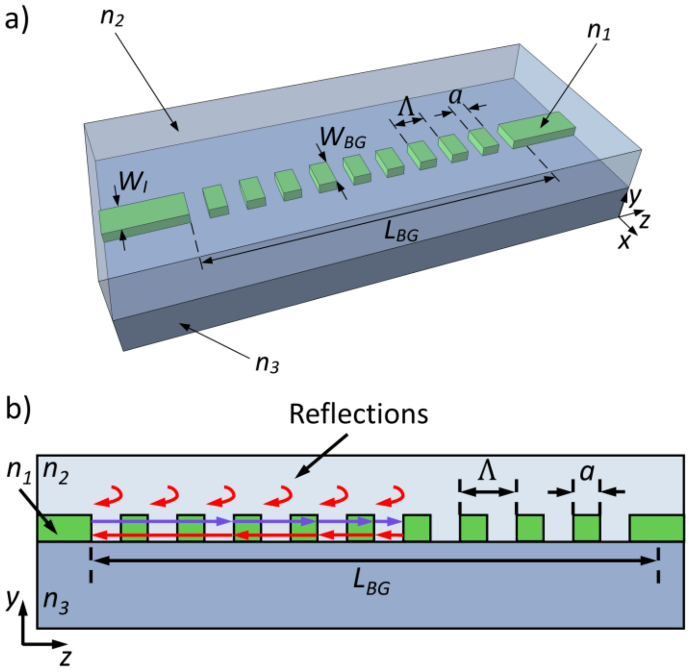

Figure 2.6. *(a) 3D view and (b) 2D side view of a waveguide Bragg grating. The light propagated in the z direction (represented in purple) is reflected in the opposite direction (in red) since reflections at each discontinuity of the periodic segments interfere constructively.*

Bragg gratings have been widely used for datacom as narrowband reflection filters [Boeuf’15], sensing due to the high sensitivity of the Bragg resonant wavelength to temperature and refractive index variations [Passaro’08], and signal processing [Zhang’18]. Furthermore, novel high-rejection Bragg grating filters have been proposed recently with great prospects for on-chip pump rejection [Pérez-Galacho’17], nonlinear optics and quantum photonics [Oser’19].

Notice that although photonic crystals are also based on the forbidden bands of periodic structures, their principle of operation is completely different compared to waveguide Bragg gratings. Photonic crystal devices present defects in the periodic structure that enables forward propagation of light, i.e. the light injected into the photonic crystal structure is not reflected to the counterpropagating direction [Birner'01]. On this account, photonic crystals are out of the scope of the present thesis.

2.3.3. Subwavelength diffraction-less regime

The name of subwavelength regime arises from the much shorter periodicity of the structure compared to the light wavelength, enabling the suppression of diffractive and reflective effects studied in the preceding sections. Specifically, the pitch must be shorter than half the wavelength of the light propagating through the structure, this means below the condition imposed by the first Bragg regime, which can be rewritten from Eq. (2.8) as

$$\Lambda < \frac{\lambda}{2n_{eff,B,r}}. \tag{2.23}$$

where $\lambda/n_{eff,B,r}$ is the wavelength of light propagating along the structure.

It is important to mention that diffraction-less propagation has recently been demonstrated above the first Bragg regime with longer period values by judiciously designing the waveguide geometry (thickness and width). This solution facilitates fabrication requirements due to the larger feature sizes, but the region lies very close to both radiation and Bragg regimes [Alonso-Ramos'19]. Despite the potential of light propagation through long-period gratings, this thesis is focused on the design and characterization of high-performance devices working in the subwavelength regime using nano-scale features.

An SWG waveguide is composed of different dielectric materials that alternate at a scale much smaller than the operating wavelength. This periodic structure suppresses diffraction effects and can be modeled as a homogeneous metamaterial, i.e. as a non-periodic equivalent material whose optical properties can be tailored by modifying the geometrical design parameters [Rytov'56, Yariv'77]. Figures 2.7a and 2.7b show a 3D schematic of a canonical SWG waveguide and a 3D view of the equivalent material, respectively. This strategy of modeling the subwavelength structure as an equivalent homogeneous medium described by distinct refractive indexes is known as the homogenization theory or effective medium theory (EMT).

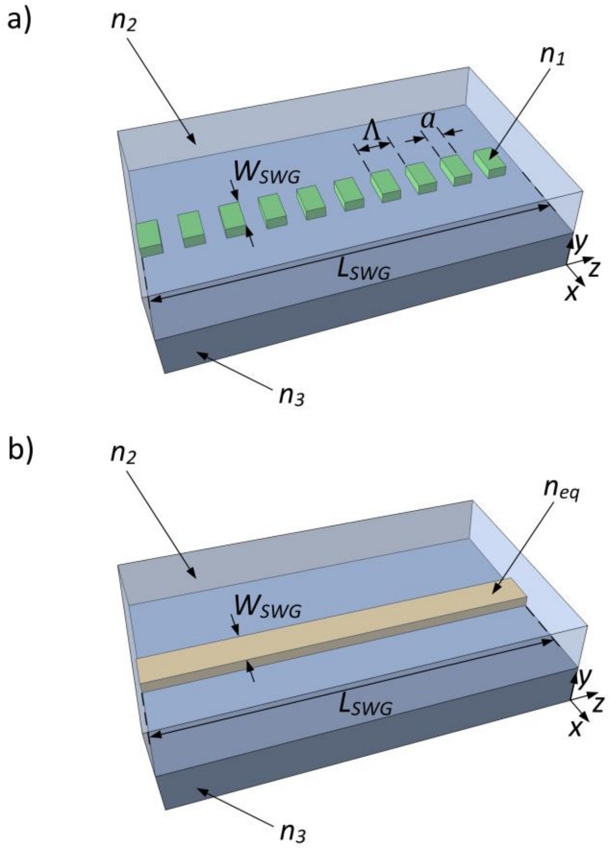

Figure 2.7. *(a) 3D view of a subwavelength grating waveguide. (b) 3D view of the equivalent homogeneous metamaterial.*

Rytov was one of the pioneers in studying the electromagnetic properties at the macroscopic level of a finely stratified medium, i.e. $\Lambda \ll \lambda$, and he established approximate equations to define the equivalent homogeneous material

$$n_{xx}^2 \approx \mathrm{DC} \cdot n_1^2 + (1 - \mathrm{DC}) \cdot n_2^2, \tag{2.24}$$

$$\frac{1}{n_{zz}^2} \approx \mathrm{DC} \cdot \frac{1}{n_1^2} + (1 - \mathrm{DC}) \cdot \frac{1}{n_2^2}, \tag{2.25}$$

where n_{xx} and n_{zz} are the refractive indexes of the equivalent medium for light polarized along the x and z directions, respectively. The refractive indexes n_1 and n_2 correspond to the different materials used for the guiding and the cladding layers, respectively. Since both indexes must be greater than the unity, n_{xx} is always greater than n_{zz} for a DC within the range (0, 1) [Halir'15]. n_{xx} and n_{zz} can be modified by varying the DC, enabling control over the refractive index of the equivalent homogeneous material, and subsequently, the confinement of the modes that propagate through the structure.

A direct consequence that can be deduced from Eqs. (2.24) and (2.25) is the inherent anisotropy of the equivalent homogeneous medium, even though the materials that constitute the periodic stratified medium are isotropic. In Rytov's words, the inhomogeneous isotropic medium behaves like a homogeneous but anisotropic medium [Rytov'56]. Furthermore, this equivalent anisotropic medium is birefringent since the physical property that differs for the x and z axes is the refractive index, i.e. anisotropy is exposed as a change of the refractive index according to the axis considered for light propagation.

The inherent anisotropic behavior due to the birefringence of SWG waveguides can also be modeled as a uniaxial crystal [Saleh'91, Gu'96]. This means as an optical transmission medium described by a refractive index tensor $\mathbf{n_{eq}} = \mathrm{diag}[n_{xx}, n_{xx}, n_{zz}]$, according to the coordinate system defined in Fig. 2.7. The refractive index in the x and y directions have the same value and are called the ordinary or slow axes, since a higher refractive index (remember from Rytov's formulas that $n_{xx} > n_{zz}$) implies a lower phase velocity of the light propagating in these directions. Conversely, the z axis is the extraordinary or fast axis, and subsequently the optic axis. It should be noted that in crystal optics the optic axis corresponds by definition to the extraordinary axis, which can be fast or slow depending of the values of the refractive index in the x, y and z directions.

The approximations shown above for the refractive indexes of the anisotropic material [see Eqs. (2.24) and (2.25)] are a zero-order approximation and are only valid for the quasi-static limit, $\Lambda/\lambda \rightarrow 0$ [Rytov'56, Haggans'93]. This region is within the subwavelength regime and is also known as deep subwavelength regime. By way of illustration, a periodic silicon waveguide can be considered to operate in the deep subwavelength regime when its period is below 100 nm at the wavelength of 1.55 µm [Halir'18]. Although this requirement implies minimum feature sizes at the limit of electron-beam (e-beam) lithography (i.e. below 50 nm), there is a transition zone between the deep subwavelength regime and the first Bragg regimen where the light propagates without radiation or reflection losses but Rytov's expressions are no longer accurate [Cheben'18]. This region, i.e. $\Lambda \approx 200$ nm is the main regime that will be exploited in the present thesis for the development of high-performance nanophotonic devices. Some previous state-of-the-art applications of this regime can be found in the following section.

2.4. Applications of subwavelength grating waveguides

Since the first demonstration of a silicon waveguide with a core segmented at a scale substantially smaller than the wavelength [Cheben'06], SWG waveguides have attracted increasing attention for the development of high-performance PICs. This interest in SWG metamaterial waveguides has also resulted from the refinements in fabrication techniques [Cheben'18], allowing minimum feature sizes slightly below 100 nm and, consequently, minimum periods of ~200 nm for an SWG waveguide with $\mathrm{DC} = 0.5$. In the last decade countless devices engineered with SWG metamaterials have been proposed for various applications such as fiber-chip edge coupling [Cheben'06, Cheben'10, Cheben'15], apodization of surface grating couplers [Halir'10, Benedikovic'15], polarization beam splitting [Herrero-Bermello'19a], polarization conversion [Xiong'14], ultra-broadband beam splitting and MDM [Halir'16, González-Andrade'18], sensing [Wangüemert-Pérez'14] and spectral filtering [Čtyroký'18], among many others.

Applications of SWG waveguides can be divided mainly into three groups, depending on the property exploited for their design: refractive index engineering, dispersion engineering and anisotropy engineering. Each of these groups is explained in the following subsections, where the operation principle of a particular device will be described by way of example.

2.4.1. Refractive index engineering

One of the main capabilities of SWG waveguides is to control the refractive index of the equivalent metamaterial. According to Rytov's equations, the equivalent refractive indexes n_{xx} and n_{zz} can be synthesized between the refractive indexes of the guiding layer, n_1, and the upper cladding, n_2, by adjusting its geometrical properties (mainly the duty cycle). This additional degree of freedom in the design opens new paths to engineer the refractive index of the metamaterial and, at the same time, the effective index of the Floquet-Bloch mode propagating through the structure.

As an example, refractive index engineering has been leveraged in silicon photonics for the implementation of high-performance fiber-chip edge couplers [Cheben'06, Cheben'10, Cheben'15]. Figure 2.8a shows the first generation of these SWG mode converters [Cheben'06]. The Floquet-Bloch mode of the SWG waveguide is engineered to match the effective index and size of the fundamental mode of an optical fiber. To this effect, the duty cycle is progressively modified along the propagation direction z, precisely controlling the Floquet-Bloch mode size and effective index.

Figures 2.8b and 2.8c show scanning electron microscope (SEM) images of an optimized version of the SWG mode converter [Cheben'15]. This device presents an ultra-high coupling efficiency of 0.32 dB for both TE and TM polarizations within the 1.48 – 1.58 μm wavelength range. Moreover, IBM researchers have recently shown that scalable and cost-effective photonic chip packaging is possible using fiber-chip edge couplers based on SWG waveguides [Barwicz'16]. Owing to the low loss, negligible polarization dependence and broad band operation, refractive index engineered SWG couplers have become basic building blocks in silicon photonic circuits.

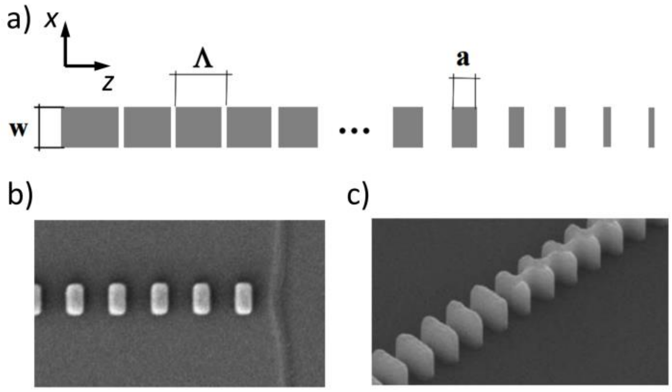

Figure 2.8. *(a) Top view of the first generation SWG fiber-chip edge coupler. Reference: [Cheben'06]. Scanning electron microscope images of (b) the optimized SWG nanophotonic coupler and (c) an intermediate section of the transition between SWG and silicon wire waveguide. Reference [Cheben'15].*

Other integrated devices based on refractive index engineering include crossings [Bock'10], apodized surface grating couplers [Halir'10, Benedikovic'15], antireflective structures [Schmid'07], evanescent field sensors [Wangüemert-Pérez'14, Flueckiger'16] and polarization management devices [Xiong'14].

2.4.2. Dispersion engineering

The chromatic dispersion of SWG metamaterial waveguides, understood as the wavelength dependence of the effective index of the Floquet-Bloch mode, is determined by the wavelength-to-pitch ratio of the periodic structure. In the deep subwavelength regime, the chromatic dispersion is virtually insignificant (see Fig. 2.3) and the main contribution to dispersion comes from the material dispersion of its constituents. When the SWG waveguide operates in the transition region towards the

Bragg regime, chromatic dispersion becomes apparent and contributes to the overall dispersion.

The dispersion properties of SWG waveguides working in the transition region were first exploited by Halir *et al.* demonstrating by simulation a directional coupler with a broad operation bandwidth [Halir’12]. Figure 2.9a shows the geometry and the principle of operation of this directional coupler. When the fundamental mode is injected through one of the coupler arms, the even and odd supermodes are excited. The beat length of these modes is given by

$$L_{\pi}(\lambda)=\frac{\lambda}{2\left(n_{eff,r,1}(\lambda)-n_{eff,r,2}(\lambda)\right)}, \tag{2.26}$$

where $n_{eff,r,1}(\lambda)$ and $n_{eff,r,2}(\lambda)$ are the real part of the effective indexes of even and odd supermodes, respectively. From Eq. (2.26), it is clear that the beat length depends on the wavelength. However, it can be engineered to be approximately flat for judiciously chosen Λ and DC as shown in Fig. 2.9b. The odd supermode is asymmetric and variations in the SWG region between waveguides have little impact, while the even supermode does perceive those changes. This enables to modify the wavelength dependence of the even supermode effective index to be approximately equal to the wavelength dependence of the odd supermode effective index, i.e. $dn_{eff,r,1}/d\lambda \approx dn_{eff,r,2}/d\lambda$.

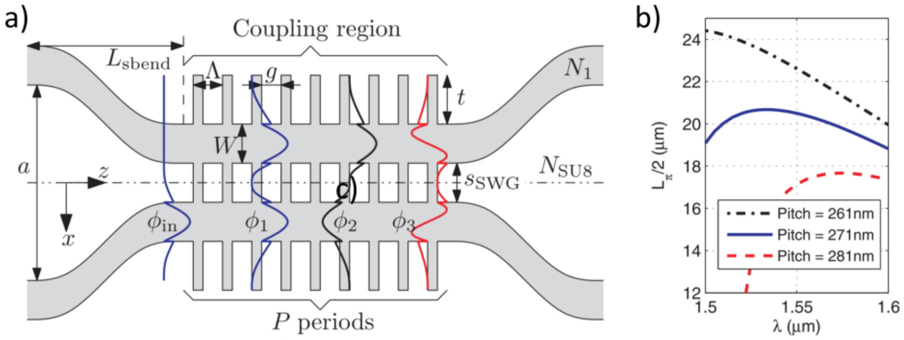

Figure 2.9. *(a) Schematic and principle of operation of a subwavelength engineered directional coupler. (b) Half the beat length as a function of the wavelength represented for different pitch values. Reference: [Halir’12].*

Simulation of this first proposal presented a length of 19.2 µm and a power imbalance between the output arms below 0.6 dB for a 100 nm bandwidth [Halir’12]. Fabrication of a similar directional coupler based on this concept was carried out in 220-nm-thick SOI wafers a few years later [Wang’16a]. Experimental demonstration showed a power imbalance below ±0.7 dB over a broad bandwidth of 100 nm, thus, verifying that dispersion engineering can be used to design broadband power splitters. Other integrated devices based on dispersion engineering include ultra-broadband MMI couplers [Halir’16], focusing grating couplers [Zhong’14] and mode MUX/DEMUX [Jafari’17, González-Andrade’18].

2.4.3. Anisotropy engineering

Inherent anisotropy of SWG waveguides can be combined with dispersion engineering in order to mitigate the wavelength dependence posed by conventional MMIs [Halir’16]. Since subwavelength engineered MMIs are part of the mode converter and MUX/DEMUX developed in the present thesis, its operation will be detailed in the corresponding chapter.

Nevertheless, a novel approach to control anisotropy in SWG metamaterial waveguides by tilting the grating segments has been recently proposed [Luque-González’18]. Simulations and experimental results show that a tilted SWG structure within the $x - z$ plane induces a significative effective index variation for TE-polarized modes, whereas this effect is 20 times smaller for TM-polarized light. Mathematically, the rotation of the segments at an angle θ_r on the y axis consists of the product of the refractive index tensor $\mathbf{n_{eq}}$ by a rotation matrix, $\mathbf{R}(\theta_r)$, resulting in the following non-diagonal refractive index tensor $\tilde{\mathbf{n}}_{\mathbf{eq}}$

$$\mathbf{n}_{\mathbf{eq}}\left(\theta_r\right) = \mathbf{R}^{-1}\left(\theta_r\right)\mathbf{n}_{\mathbf{eq}}\mathbf{R}\left(\theta_r\right) = \begin{bmatrix} n_{xx}\left(\theta_r\right) & 0 & n_{xz}\left(\theta_r\right) \\ 0 & n_{yy}\left(\theta_r\right) & 0 \\ n_{xz}\left(\theta_r\right) & 0 & n_{zz}\left(\theta_r\right) \end{bmatrix}, \tag{2.27}$$

where the matrix elements are

$$\begin{aligned} n_{xx}\left(\theta_r\right) &= n_{xx}^2 \cos^2\left(\theta_r\right) + n_{zz}^2 \sin^2\left(\theta_r\right), \\ n_{yy}\left(\theta_r\right) &= n_{yy}^2 = n_{xx}^2, \\ n_{zz}\left(\theta_r\right) &= n_{xx}^2 \sin^2\left(\theta_r\right) + n_{zz}^2 \cos^2\left(\theta_r\right), \\ n_{xz}\left(\theta_r\right) &= \left(n_{zz}^2 - n_{xx}^2\right)\sin\left(\theta_r\right)\cos\left(\theta_r\right). \end{aligned} \tag{2.28}$$

One can observe from Eq. (2.28) that $\tilde{n}_{xx}(\theta_r)$, $\tilde{n}_{yy}(\theta_r)$, $\tilde{n}_{zz}(\theta_r)$ and $\tilde{n}_{xz}(\theta_r)$ vary depending on the tilt angle of the grating segments. Accordingly, fundamental TE and TM modes propagating along the structure in the z direction are affected differently by the tilt angle. In the case of the TE-polarized mode (electric field polarized in the x

direction), the refractive index of the equivalent medium is given by $\tilde{n}_{xx}(\theta_r)$. On the other hand, the TM-polarized mode (electric field polarized in the y direction) is hardly affected by the rotation of the segments, since the refractive index of the equivalent medium is given by $\tilde{n}_{yy}(\theta_r) = n_{xx}^2$.

Figure 2.10 shows a 3D schematic of a tilted SWG waveguide, along with the effective index of the TE and TM fundamental modes of a 550-nm-wide by 300-nm-thick silicon SWG waveguide as a function of the tilt angle (for a fixed pitch of 220 nm and a 50% duty cycle). The same effective index for both modes is achieved at a tilt angle of ~48°, yielding a zero-birefringence behaviour [Herrero-Bermello'19b]. According to simulations, this polarization-independent behaviour is maintained in the 1.5 – 1.6 µm wavelength range, showing a negligible birefringence of $6 \cdot 10^{-3}$. This principle has been further exploited in an integrated polarization splitter based on an MMI with tilted SWG [Herrero-Bermello'19a]. Device length was reduced under 100 µm, with an enhanced bandwidth of more than 128 nm for insertion losses below 1 dB and extinction ratio above 20 dB.

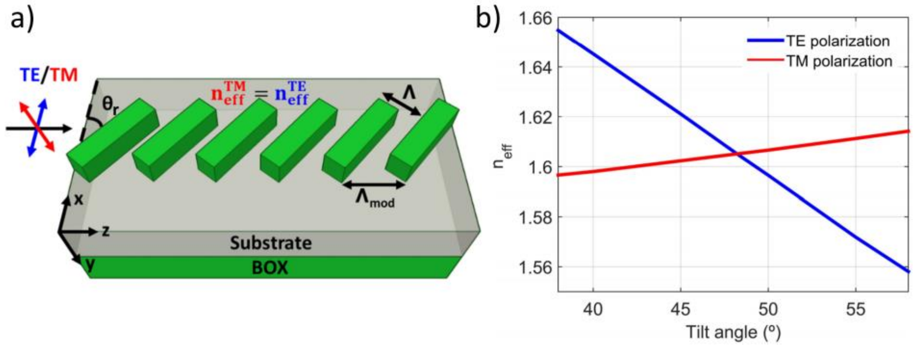

Figure 2.10. *(a) Schematic of a tilted SWG metamaterial waveguide with zero birefringence for TE and TM polarizations. (b) Effective index of the fundamental TE and TM modes as a function of the tilt angle. The zero-birefringence point is achieved for ~48°. Reference: [Herrero-Bermello'19b].*

2.4.4. Untapped potential

As showcased by the previous examples, subwavelength structures are experiencing a fast-pace growth due to the versatility provided by the additional degrees of freedom in the design. Although still in a relatively early research stage, SWG metamaterials can be currently considered as a fundamental tool for the design of high-performance PICs. Refractive index, dispersion and anisotropy engineering have allowed the development of photonic devices with features that would be difficult or impossible to achieve with conventional waveguides, and provide remarkable prospects for the implementation of polarization-independent devices, high-capacity optical communications or transformation optics [Cheben'18]. Furthermore, new large-volume fabrication processes with more accurate lithographic resolutions, like immersion [Jeong'13] or extreme-ultraviolet (UV) lithography [Wagner'10] are opening promising prospects for SWG-metamaterial-based structures to be commercially exploited.

In the present tesis, this still untapped potential is applied to a new generation of high-performance silicon photonic devices, including a broadband mode converter and multiplexer/demultiplexer, and ultra-broadband nanophotonic phase shifter, and an ultra-broadband dual-polarization beam splitter.

III

Ultra-broadband mode converter and multiplexer/demultiplexer

The exponential growth of global Internet traffic in data centers requires new multiplexing technologies such as mode-division multiplexing to further increase the capacity of optical interconnects. The mode converter and multiplexer/demultiplexer is a key element in MDM systems in order to transform and combine the fundamental modes into higher-order modes and vice versa. This chapter is devoted to the development of a novel broadband and compact mode converter and MUX/DEMUX integrated in a silicon chip. Section 3.1 is an introduction to mode-division multiplexing aimed at the SOI platform. The architecture of the proposed device and its operation are detailed in section 3.2, while its design is carried out in section 3.3. The first experimental results and design optimization can be found in section 3.4. The final experimental results are shown in section 3.5 and conclusions are summarized in section 3.6.

3.1. Introduction to mode-division multiplexing

Mode-division multiplexing was proposed for optical fibers in 1982 to increase the aggregated bandwidth by transmitting independent signals encoded in different spatial modes [Berdagué'82]. Notwithstanding, it was not until a few years ago that MDM attracted the interest of both scientific and industrial communities as an enabling technology to further expand the capacity of inter- and intra-chip communications while maintaining the same level of integration [Kawaguchi'02, Lee'03, Greenberg'05, Bagheri'09]. Mode-division multiplexing technology relies on the orthogonality of the field profiles between the guided modes supported by a multimode optical waveguide [Dändliker'00]. Each of these modes can be used as an independent communication channel to transmit different information at the same wavelength, i.e. the information is encoded in the different spatial modes supported by the multimode waveguide. Ideally, fundamental and higher-order modes are propagated through the multimode waveguide without a power coupling between them; however, in real scenarios perturbations in the waveguide lead to inter-mode crosstalk (XT) [Williams'19].

A complete MDM system comprises several components to handle and arbitrarily route the multimode waveguide throughout the chip [Zhou'19], such as multimode waveguide bends [Gabrielli'12, Sun'17, Xu'18a], switches [Stern'15, Xiong'17, Sun'18], crossing [Xu'18b, Li'18b, Liu'19b] and mode splitters [Luo'16, Xu'16, Chang'18a]. However, mode conversion (i.e. transforming a signal between modes of different orders) and mode multiplexing (i.e. combining modes of different orders into a single waveguide) remain the essential challenges at the core of any MDM system. These two tasks can be implemented jointly or separately, depending on the design of the involved building blocks. That is, there are mode converters [Leuthold'98, Ohana'14, Chen'15b, Linh'19], mode multiplexers [Dorin'14, Pérez-Galacho'15], and a third group of devices that perform both operations simultaneously, namely the mode converter and MUX/DEMUX [Driscoll'13, Xing'13a, Ding'13, Li'14]. The device developed in this thesis belongs to this group and, therefore, the rest of this chapter is mainly focused on this kind of devices.

Figure 3.1 shows an example of an on-chip MDM link formed by two mode converters and MUX/DEMUXs, in which the total capacity is tripled (three multiplexed modes). In contrast to the WDM technology where multiplexing is performed for different wavelengths, in MDM technology the wavelength of the multiplexed/demultiplexed modes is the same (λ_i), which significantly reduces the system complexity since only a single laser source is required. Alternatively, both

WDM and MDM can be combined in a single system further enhancing the link capacity.

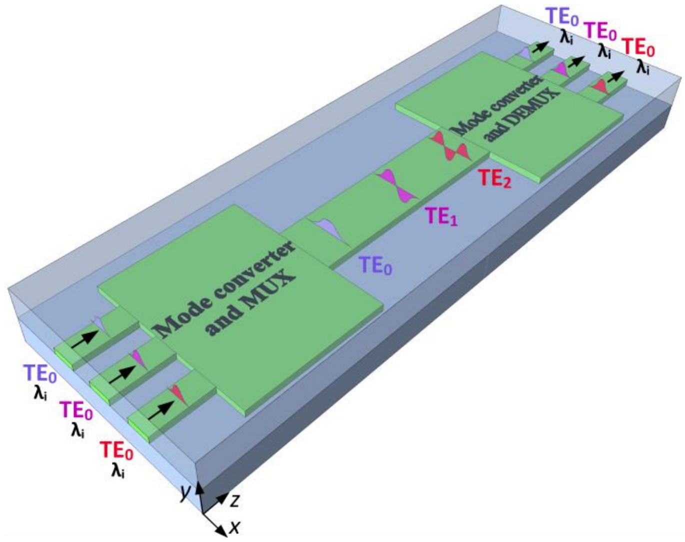

Figure 3.1. *Schematic of a three-mode MDM link composed of two mode converters and multiplexer/demultiplexers and a multimode waveguide, which supports the fundamental (in purple), first-order (in magenta) and second-order (in red) modes.*

In this case, three fundamental modes at the same wavelength are injected into the mode converter and MUX, which is responsible for transforming and coupling them into the multimode waveguide as the fundamental (in purple), first-order mode (in magenta) and second-order modes (in red). After propagating through the multimode waveguide (ideally without power coupling between them), the opposite process is performed by the mode converter and DEMUX, and each of the modes in the multimode waveguide is transformed back into the fundamental mode and coupled to the corresponding single-mode waveguide. It should be noted that the complete MDM link only requires the design of a single device, the mode converter and MUX/DEMUX. The same example using independent mode converters and mode MUX/DEMUX would require at least the design of three devices (a mode converter for each higher-order mode and one mode MUX/DEMUX), increasing the overall complexity of the MDM link.

The number of mode converters and MUX/DEMUXs reported in the last decade has experienced a soaring growth as an indication of the relevance that MDM is acquiring in silicon photonics [Li’18a]. Several architectures have been proposed to perform mode conversion and multiplexing/demultiplexing simultaneously (see Fig. 3.2), each with its strengths and limitations depending on the physical operation principle on which they are based: mode evolution, evanescent coupling or multimode interference.

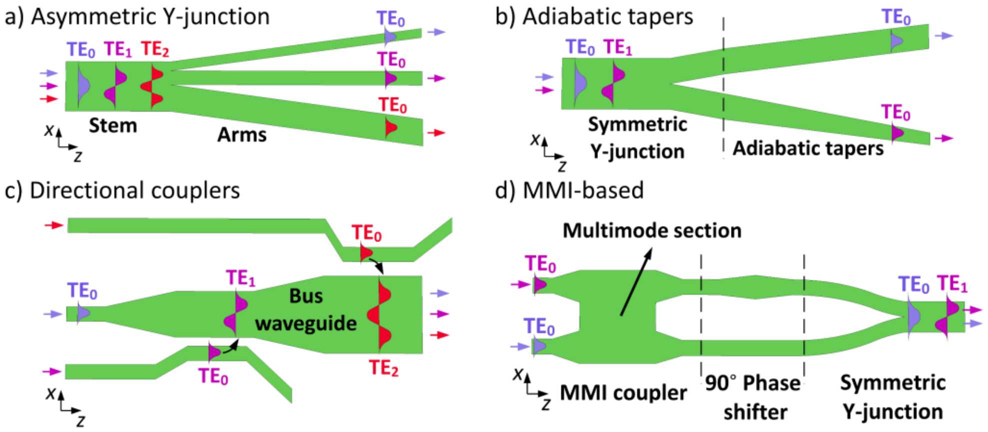

Figure 3.2. *Examples of state-of-the-art mode converters and MUX/DEMUXs. (a) Asymmetric Y-junctions and (b) adiabatic tapers rely on the mode evolution principle. (c) Directional couplers exploit evanescent coupling between narrow and wide waveguides and (d) multimode-interference-based devices induce phase shifts between multiple arms.*

Asymmetric Y-junctions were one of the first mode converters and MUX/DEMUXs studied for dielectric thin-film waveguides [Yajima'73, Burns'75], with an example shown in Fig. 3.2a. Their principle of operation relies on mode evolution, thereby fundamental and higher-order modes supported by the multimode waveguide (also denoted as stem in symmetric and asymmetric Y-junctions) are adiabatically coupled to each single-mode arm and converted into the fundamental mode [Riesen'12]. Consequently, asymmetric Y-junctions are based on adiabatic structures, leading to long lengths but also to broad operating bandwidths. The performance of these devices is typically hindered by the limited resolution of fabrication processes, i.e. a tip between the arms is generated after fabrication, which degrades the performance in terms of losses, crosstalk and bandwidth [Driscoll'13, Li'18c]. The design of asymmetric Y-junctions can be further optimized by using shortcuts to adiabaticity, reducing the lengths required for the adiabatic transition [Martínez-Garaot'14].

Other mode converters and MUX/DEMUXs based on the mode-evolution principle rely on adiabatic tapers (see Fig. 3.2b as an example) [Xing'13a, Sun'16a, Zhang'17, Xu'19]. Since the working principle is the same as in asymmetric Y-junctions, these devices also exhibit large footprint (lengths longer than 300 µm) and broad bandwidths; however, fabrication tolerances are improved compared to asymmetric Y-junctions [Xing'13a, Sun'16a].

Evanescent coupling can be applied to mode converters and MUX/DEMUXs which comprise a coupling region with two asymmetric waveguides, such as ring resonators, asymmetric directional couplers and contra-directional couplers [Dorin'14, Dai'13, Qiu'13]. Figure 3.2c shows a three-mode asymmetric directional coupler by way of illustration. In this case, the principle of operation relies on the phase matching condition between the fundamental mode of the single-mode waveguide and the corresponding higher-order mode of the multimode waveguide (also named bus waveguide). The advantages of this architecture are the ease of scalability to higher-order modes and the compact footprints. Nevertheless, these devices are intrinsically narrowband and present stringent fabrication tolerances since the coupling depends exponentially on the gap between single-mode and multimode waveguides [Chrostowski'15]. To overcome these limitations, directional couplers based on tapered waveguides have been proposed, significantly improving both tolerances to fabrication errors and bandwidths [Ding'13, Pan'15, Wang'15, Sun'16b, Guo'17, Li'17, Dai'18].

The multimode-interference-based mode converter and MUX/DEMUX build upon the Talbot effect of a multimode waveguide, i.e. single or multiple images of the input field are formed at different lengths of the multimode waveguide and multiport couplers with a certain amplitude and phase relation between the output ports can be achieved [Soldano'95]. Combining this MMI coupler with other elements, such as phase shifters and symmetric Y-junctions (see Fig. 3.2d as an example), it is possible to perform mode conversion and multiplexing/demultiplexing [Kawaguchi'02, Uematsu'12, Li'14, Han'15, Xiao'18]. Architecture of Fig. 3.2d is the starting point of the proposed mode converter and MUX/DEMUX and will be explained in detail in the following section.

Finally, other devices based on inverse design have also been proposed with compact dimensions. However, experimental bandwidths are limited to less than 100 nm, layouts for fabrication are intricate and require minimum feature sizes below 90 nm [Frellsen'16, Chang'18b].

3.2. Architecture and principle of operation

Mode converters and MUX/DEMUXs based on MMI couplers usually comprise several components, being the performance of the entire architecture restricted by the most limiting constituent. As an example, the architecture shown in Fig. 3.2d is based on three different passive devices: a 2×2 MMI coupler, a 90° phase shifter and a symmetric Y-junction. Theoretically, both the 90° PS and the symmetric Y-junction present low losses over a broad bandwidth, whereas the MMI coupler is intrinsically limited by the beat length between the fundamental and first-order mode in the multimode section [Soldano'95]:

$$L_\pi(\lambda)=\frac{\lambda}{2\left(n_{eff,r,0}(\lambda)-n_{eff,r,1}(\lambda)\right)}, \tag{3.1}$$

where λ is the wavelength and $n_{eff,r,0}(\lambda)$ and $n_{eff,r,1}(\lambda)$ are the real part of the effective indexes of the fundamental and first-order modes in the multimode section, respectively. Since the 2×2 MMI coupler is designed to reproduce the input field in two-fold images at a specific wavelength, i.e. $L_{MMI} = 3L_\pi/2$ for general interference and $L_{MMI} = L_\pi/2$ for paired interference, its performance deteriorates when detuning from the design wavelength. This results from the fact that self-images are formed at different positions for each wavelength (see wavelength dependence of Eq. (3.1)). Therefore, conventional MMIs limit the overall performance of this architecture, which could be improved by an alternative MMI solution with a less wavelength-dependent response.

Recently, Halir *et al.* from the UMA and the NRC proposed an ultra-broadband 2×2 MMI coupler working for TE polarization, which leverages the inherent anisotropy and dispersion properties of SWG waveguides to mitigate the wavelength dependence of the beat length [Halir'16]. The mode converter and MUX/DEMUX proposed in this thesis replaces the conventional MMI with a subwavelength engineered MMI to overcome the bandwidth restrictions and improve the performance of the complete architecture. Figure 3.3 shows a top view of the schematic of the proposed mode converter and MUX/DEMUX working for TE polarization based on an SWG MMI (instead of the conventional MMI), a 90° PS and a symmetric Y-junction.

The operation principle of the SWG MMI is the same as its conventional counterpart, however the beat length of this SWG MMI is now given by the following expression [Halir'16]:

$$L_\pi(\lambda)\approx\frac{4W_e}{3\lambda}\frac{n_{zz}^2}{n_{xx}}, \tag{3.2}$$

where W_e is the effective width of the multimode section, which is assumed to be invariant with wavelength, and n_{xx} and n_{zz} are the refractive indexes of the equivalent medium in the x and z directions as described in section 2.3.3. The term n_{zz}^2/n_{xx} can be engineered to be proportional to λ by judiciously designing the period and the duty cycle of the SWG waveguide. Hence, the wavelength dependence of Eq. (3.2) can be mitigated and the SWG MMI can operate in a broader bandwidth than the conventional MMI based on non-periodic waveguides.

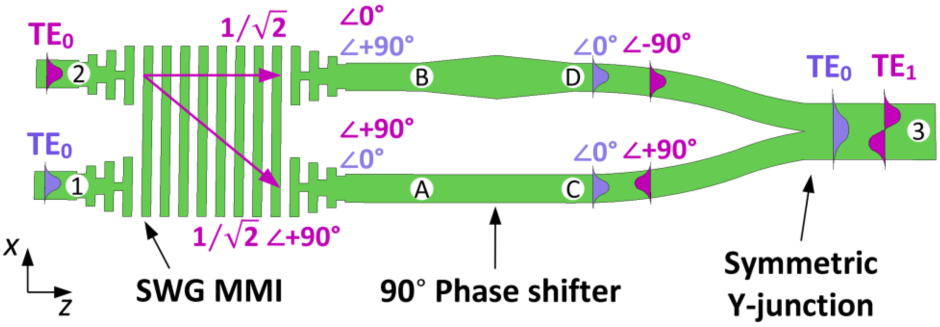

Figure 3.3. *Proposed mode converter and MUX/DEMUX based on a subwavelength engineered MMI, a 90° phase shifter and a symmetric Y-junction. Note that the term* $1/\sqrt{2}$ *corresponds to the amplitude of the transmission parameter of a 2×2 MMI considering the input and output fields of the optical signal.*

The optical PS can be easily implemented on-chip by means of two parallel waveguides of the same length, in which one varies its width along the direction of propagation z and the other maintains a constant width. Two trapezoidal tapers placed in back-to-back configuration increase or decrease the waveguide width of the upper PS arm, delaying or advancing the mode propagated through this arm compared to the mode propagated through the straight waveguide. The phase shifts introduced by the upper and lower arms of the PS are, respectively:

$$\Phi_{\mathrm{DB}}(\lambda) = -\int_0^{L_{PS}} \beta_U(z,\lambda)\,\mathrm{d}z, \tag{3.3}$$

$$\Phi_{\mathrm{CA}}(\lambda) = -\beta_L(\lambda)L_{PS}, \tag{3.4}$$

where $\beta_U(\lambda)$ is the phase constant of the fundamental mode propagating through the upper arm of the PS, $\beta_L(\lambda)$ is the phase constant of the fundamental mode propagating through the lower arm of the PS, and L_{PS} is the length of the phase shifter. The phase shift between both fundamental modes is therefore:

$$\Delta\Phi(\lambda) = \Phi_{\mathrm{CA}}(\lambda) - \Phi_{\mathrm{DB}}(\lambda). \tag{3.5}$$

It is important to mention that following this definition, the phase shift between the arms of the PS is positive ($\Delta\Phi(\lambda) > 0$) when the width of the tapers increases, since the mode propagating through the upper arm has a greater propagation constant compared to the mode propagating through the straight waveguide. Conversely, when the width of the tapers decreases, the phase difference between the arms is negative ($\Delta\Phi(\lambda) < 0$) since the propagation constant of the mode in the upper PS arm is lower than the propagation constant of the mode propagating through the straight waveguide.

Finally, the symmetric Y-junction comprises two S-bends (arms) and a multimode waveguide (stem) in order to combine both arms of the PS into a single multimode waveguide. It should be noted that the width of the Y-junction stem must be wide enough to support both the fundamental and the first-order modes.

The principle of operation of the proposed two-mode converter and MUX/DEMUX is described below for MUX and DEMUX operations:

- MUX operation: the fundamental mode injected through port 1 (in purple) is evenly divided by the SWG MMI in amplitude, but a phase difference is induced at the output ports $\Delta\Phi_{\mathrm{AB}} = \Phi_{\mathrm{A}} - \Phi_{\mathrm{B}} = -90°$. The PS delays the mode propagated through the upper arm +90° with respect to the mode propagated through the lower arm, resulting in two in-phase TE_0 modes (total phase shift of 0°). These two in-phase modes are coupled and transformed by the symmetric Y-junction into the fundamental mode of the multimode waveguide (port 3). On the other hand, the fundamental mode injected through port 2 (in magenta) is also evenly divided by the SWG MMI in amplitude but the phase difference between output ports A and B is now $\Delta\Phi_{\mathrm{AB}} = \Phi_{\mathrm{A}} - \Phi_{\mathrm{B}} = +90°$. Since the PS delays the mode propagated through the upper arm an additional +90° with respect to the mode propagated through the lower arm, two out-of-phase TE_0 modes (180° phase shift) are obtained in the arms of the symmetric Y-junction, which are coupled to the multimode waveguide (port 3) as the first-order mode.
- DEMUX operation: when the TE_0 mode is injected through port 3 (in purple), it is equally split by the symmetric Y-junction in two in-phase TE_0 modes (0° phase shift). A +90° is induced after the PS section between the lower and upper arms, resulting in the fundamental mode being coupled to port 1 of the SWG MMI. When the TE_1 mode is injected through port 3, the symmetric Y-junction equally splits the TE_1 mode in two out-of-phase TE_0 modes (180° phase shift). After the PS section, the phase difference between MMI inputs results in the fundamental mode being coupled to port 2.

3.3. Device design

The design of the proposed mode converter and MUX/DEMUX is described in this section considering 220-nm-thick silicon waveguides deposited on a BOX layer and surrounded by a SiO_2 upper cladding. The wavelength range covered by the design ranges from 1.4 μm to 1.7 μm, with a central wavelength of 1.55 μm. Interconnection waveguides with a typical 500-nm-width were originally selected to connect the different components (SWG MMI, 90° PS and symmetric Y-junction), being single mode at the central wavelength but multimode at wavelengths close to 1.4 μm. However, residual higher-order modes are weakly confined and can be radiated in a straightforward way using waveguide bends with small radii. The design of each individual component can be found in the following subsections, optimized for TE polarization.

3.3.1. SWG MMI

Figure 3.4 shows the schematic of a 2×2 SWG MMI and its physical design parameters. This device comprises two distinct parts, the SWG tapers and the SWG multimode section. The former ensures that the transition between non-periodic interconnection waveguides (width W_I) and SWG access waveguides (width W_A) is performed adiabatically, whereas the latter is designed to optimize the bandwidth performance by judiciously designing the parameters of the SWG multimode waveguide.

Design parameters of the 2×2 SWG MMI were taken from [Halir'16] to take advantage from the previous design carried out by the UMA and the NRC that successfully demonstrated an ultra-broad bandwidth in excess of 300 nm. First, the SWG multimode section is designed to mitigate the wavelength dependence of the beat length. In order to prevent fabrication issues related to the minimum feature sizes, the duty cycle is set to 50% to maximize the lengths of both silicon and silicon dioxide segments. Several pitch values are then considered and an almost flat beat length $L_\pi \approx 10\ \mu\text{m}$ is achieved for $\Lambda = 190\ \text{nm}$. Since the SWG MMI coupler relies on general interference, the length of the SWG multimode section is $L_{MMI} = 3L_\pi/2 \approx 15\ \mu\text{m}$, which results in a number of periods of $P_{MMI} = L_{MMI}/\Lambda \approx 79$ periods. Since the widths of the access and interconnection waveguides are $W_A = 1.7\ \mu\text{m}$ and $W_I = 0.5\ \mu\text{m}$, respectively, an SWG taper length of $L_T = 5.7\ \mu\text{m}$ ($P_T = 30$ periods) is found to adiabatically adjust the effective index of the mode in the non-periodic waveguide to the effective index of the Floquet-Bloch mode in the access waveguide.

Additionally, the gap between access waveguides is designed to avoid any power coupling, resulting in $G = 0.3$ µm. Once the preliminary design of the SWG MMI coupler is achieved, the length L_{MMI} and the width W_{MMI} of the multimode section are optimized by iterative 3D finite-difference time-domain (FDTD) simulations, yielding optimized values of $L_{MMI} = 14.06$ µm ($P_{MMI} = 74$ periods) and $W_{MMI} = 3.25$ µm.

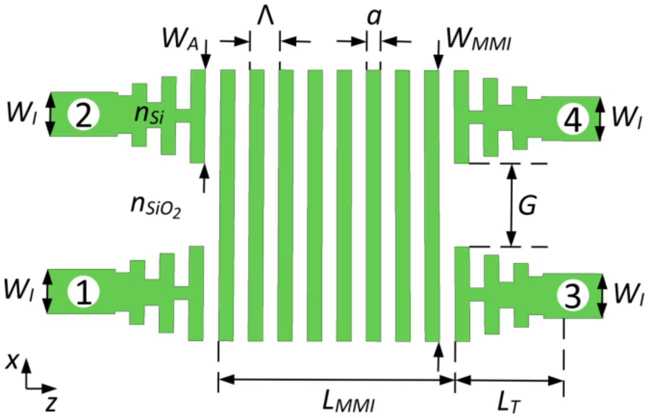

Figure 3.4. *Schematic of an SWG MMI consisting of a multimode section (width W_{MMI} and length L_{MMI}) and SWG tapers (length L_T), which perform an adiabatic transition between the non-periodic interconnection waveguides (width W_I) and the periodic access waveguides (width W_A).*

In order to compare the performance of the proposed mode converter and MUX/DEMUX with a conventional counterpart, a conventional MMI was also designed, based upon the parameters also included in [Halir'16]. In this case, all dimensions of the SWG MMI coupler are maintained, except the length of the multimode section and the length of the tapers, which increase up to $L_{MMI,Conv} = 38.5$ µm and $L_{T,Conv} = 6$ µm, respectively. The final dimensions of the conventional and SWG MMIs designed are summarized in Table 3.1.

Conventional and SWG MMIs with the abovementioned physical parameters were simulated via 3D FDTD [FullWAVE'19] to verify their performance. It should be noted that simulations carried out for the SWG MMI include 60-nm-thick air gaps between the silicon segments of the SWG waveguides, since it is known that for this design the trenches between two silicon segments are not completely filled by the SiO_2 cladding during the fabrication [Halir'16].

Table 3.1. *Geometrical parameters of the conventional and SWG MMIs designs.*

Component	Parameter	Definition	Value
SWG MMI	Λ	Period	190 nm
	DC	Duty cycle	50%
	W_I	Input width	500 nm
	W_A	Access width	1.7 µm
	W_{MMI}	MMI width	3.25 µm
	G	Gap	300 nm
	L_T	Taper length	5.7 µm (30 periods)
	L_{MMI}	MMI length	14.06 µm (74 periods)
Conventional MMI	$W_{I,Conv}$	Input width	500 nm
	$W_{A,Conv}$	Access width	1.7 µm
	$W_{MMI,Conv}$	MMI width	3.25 µm
	G_{Conv}	Gap	300 nm
	$L_{T,Conv}$	Taper length	6 µm
	$L_{MMI,Conv}$	MMI length	38.5 µm

The typical figures of merit for MMI couplers are defined hereunder using the scattering parameters (also denoted as S-parameters) associated to the input port 1 and output ports 3 and 4, i.e. S_{31} and S_{41}, respectively:

- Excess loss ($\mathrm{EL_{MMI}}$): is the total optical power at the output ports 3 and 4 with respect to the optical power injected at the input port 1. Ideally, EL = 0 dB.

$$\mathrm{EL_{MMI}} = -10\log\left(\left|S_{31}\right|^2 + \left|S_{41}\right|^2\right). \quad \textbf{(3.6)}$$

- Imbalance (IB_{MMI}): is the optical power difference between output ports 3 and 4 when light is injected through the input port 1. Ideally, $IB = 0$ dB.

$$IB_{MMI} = 10\log\left(\left|S_{31}\right|^2 / \left|S_{41}\right|^2\right). \tag{3.7}$$

- Phase error (PE_{MMI}): is the deviation of the phase difference between the waves of the output ports 3 and 4 when light is injected through the input port 1. Ideally, $PE_{MMI} = 0°$.

$$PE_{MMI} = \angle\left(\frac{S_{31}}{S_{41}}\right) + 90°. \tag{3.8}$$

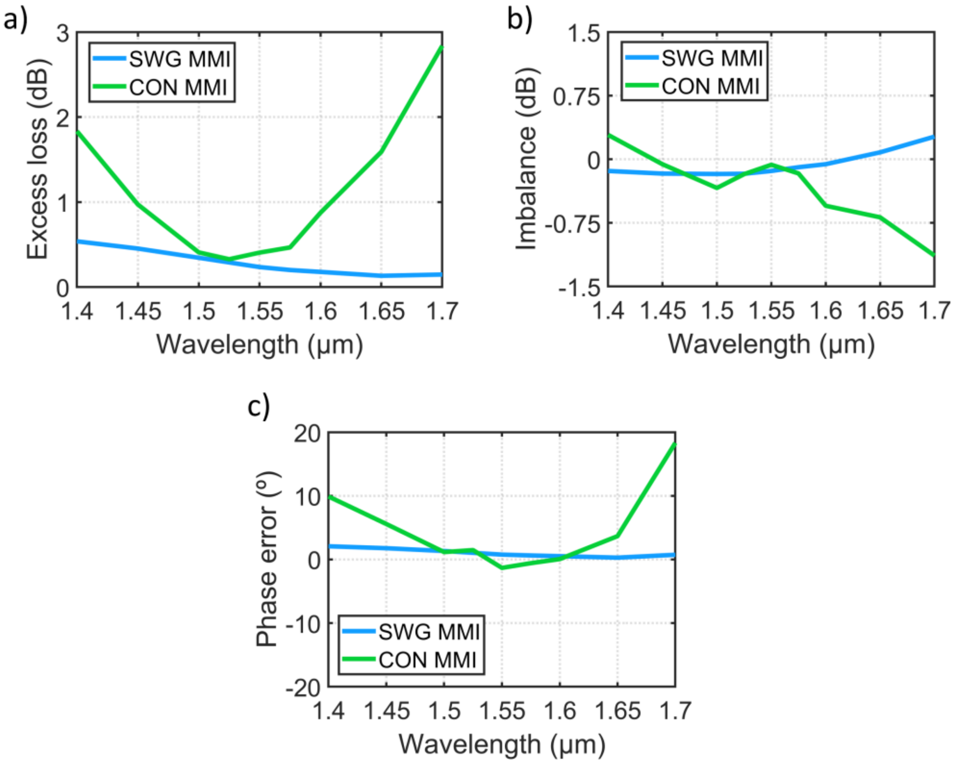

Figure 3.5. *Simulated (a) excess loss, (b) imbalance and (c) phase error as a function of the wavelength calculated for the SWG MMI (in blue) and the conventional MMI (in green).*

Figure 3.5 shows the simulated performance of the designed SWG MMI (represented in blue) and the conventional MMI (in green). Degradation of excess loss (see Fig. 3.5a) and phase error (see Fig. 3.5c) when detuning from the design wavelength at $\lambda = 1.55$ μm greatly limits the bandwidth of the conventional MMI. The subwavelength engineered MMI presents instead an almost flat response, exhibiting excess loss lower than 0.54 dB, imbalance better than 0.27 dB and phase error under 2° within the simulated 300 nm wavelength range.

3.3.2. 90° phase shifter

Schematic and physical design parameters of the 90° PS are represented in Fig. 3.6a. For this phase shifting structure, only the width (W_{PS}) and length (L_{PS}) of the trapezoidal tapers must be selected, since the width of the straight waveguide is given by the width of the interconnection waveguides, i.e. $W_I = 500$ nm. Note that the target 90° phase shift can be achieved by many different combinations of W_{PS} and L_{PS}. Nevertheless, we set $W_{PS} = 700$ nm to ensure that the width increment, $\Delta W = W_{PS} - W_I = 200$ nm, is at least twice the minimum feature size of e-beam technology. The distance between both arms is determined by the MMI, $D = G + (W_A - W_I) = 1.5$ µm.

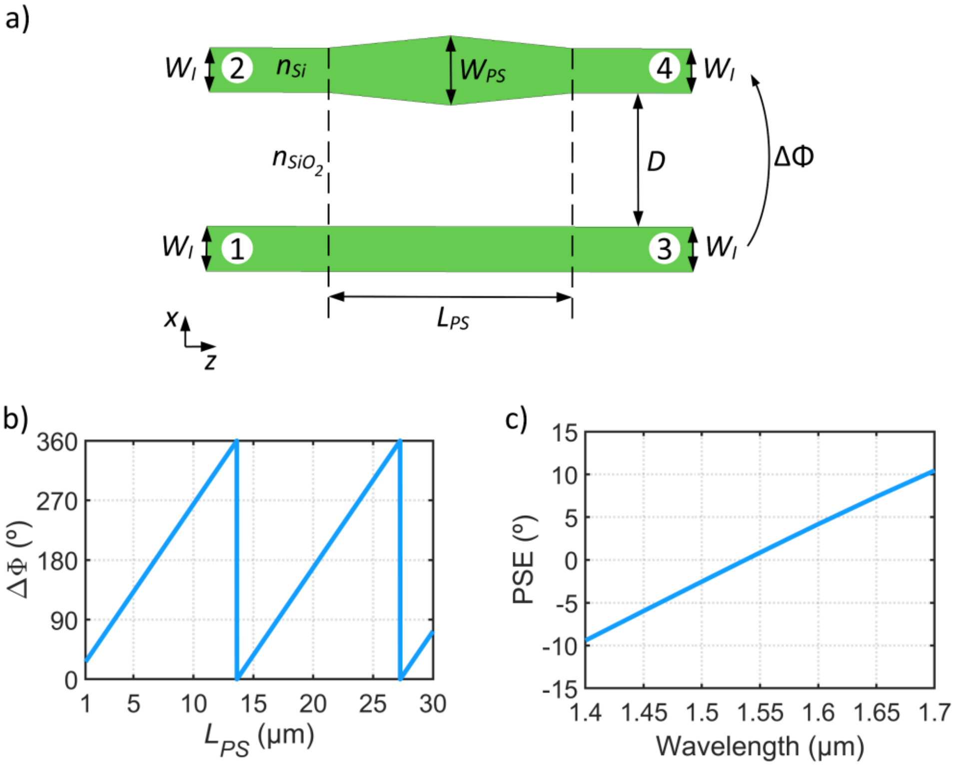

Figure 3.6. *(a) Schematic of the 90° phase shifter based on two parallel waveguides of the same length L_{PS}. The upper arm includes two tapers in back-to-back to increase the width to W_{PS}, whereas the width of the lower arm remains unaltered. (b) Phase difference between the lower and the upper arm of the PS as a function of its length. (c) Phase shift error of the designed PS (L_{PS} = 3.41 µm) as a function of the wavelength.*

The design of the length L_{PS} was carried out via finite element method (FEM) [FemSIM'19], calculating the effective index of the fundamental mode for different waveguide widths at $\lambda = 1.55$ µm and performing the analytical calculation of Eq. (3.5). The phase difference between the lower and upper arms of the PS is shown in Fig. 3.6b. In order to reduce the wavelength dependence of the PS response and achieve a compact PS, a length of $L_{PS} = 3.41$ µm is selected.

The performance of the designed PS can be quantified by defining a figure of merit similar to the phase error of MMI couplers:

- Phase shift error (PSE): is defined as the phase deviation from the target phase shift. Ideally, PE $= 0°$.

$$\mathrm{PSE}{=}\angle\left(\frac{S_{31}}{S_{42}}\right)-90° = \Delta\Phi(\lambda)-90°, \qquad \textbf{(3.9)}$$

where $\Delta\Phi(\lambda)$ is the phase shift induced between the lower and upper arms of the PS as stated in Eq. (3.5), and the target phase shift is 90° for this design.

Figure 3.6c shows the PSE of the designed phase shifter as a function of the wavelength obtained through 3D FDTD simulations. The maximum PSE is only 11° within the 1.4 – 1.7 µm wavelength range. This value is much smaller than the phase deviation introduced by the conventional MMI at the edges of the band considered for the design (i.e. $< 20°$), thus confirming that the conventional MMI is the most limiting constituent of the mode converter and MUX/DEMUX.

3.3.3. Symmetric Y-junction

The schematic of the symmetric Y-junction together with its geometric parameters is shown in Fig. 3.7a. Both the width and the separation of the Y-junction arms are established by the design of the previous components, i.e. $W_I = 500$ nm and $D = 1.5$ µm. In addition, the stem width is $2W_I = 1$ µm, which supports the fundamental and the first-order modes. Therefore, the design of the symmetric Y-junction is limited to selecting the type of S-bends used and the length of the arms L_Y that minimize losses and ensure a compact footprint.

We chose arc shaped S-bends and performed 3D FDTD simulations [FullWAVE'19] sweeping the angle θ_Y to obtain the excess losses at $\lambda = 1.55$ µm when injecting TE_0 and TE_1 modes through the stem, i.e. port 1 (see Fig. 3.7b). Note that sweeping the angle θ_Y implies to change the length of the arms L_Y since the distance between them D is fixed. The figures of merit used for the symmetric Y-junction are $\mathrm{EL_Y}$ and $\mathrm{IB_Y}$, defined equivalently as for MMI couplers but for a three-port device:

$$\mathrm{EL_Y} = -10\log\left(\left|S_{21}\right|^2 + \left|S_{31}\right|^2\right), \tag{3.10}$$

$$\mathrm{IB_Y} = 10\log\left(\left|S_{21}\right|^2 / \left|S_{31}\right|^2\right). \tag{3.11}$$

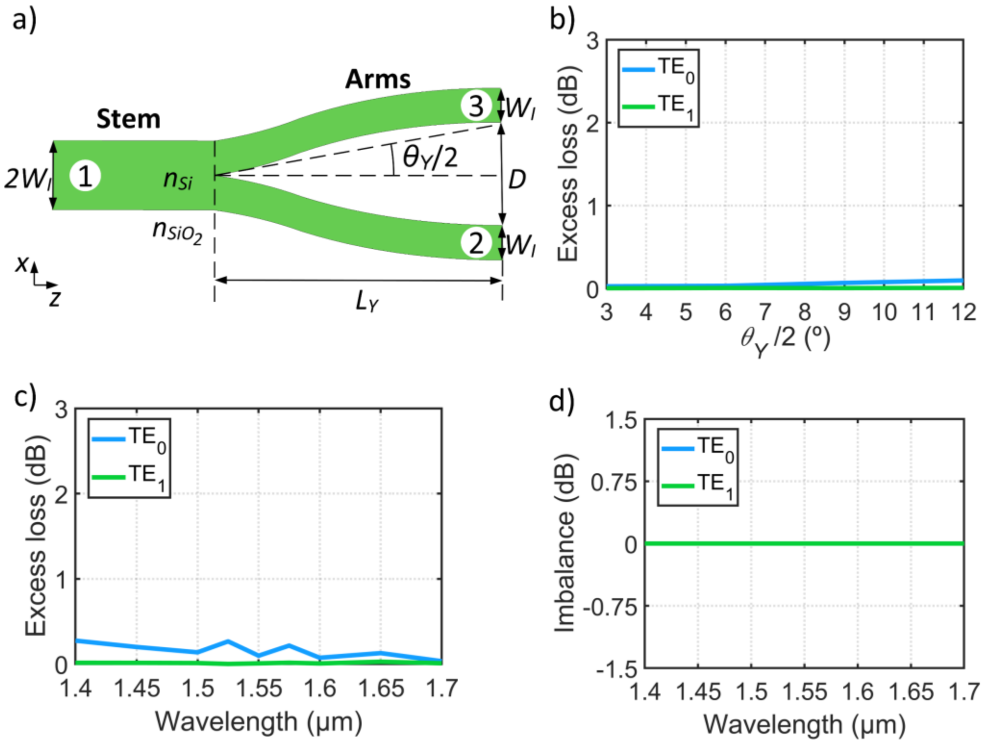

Figure 3.7. *(a) Schematic of the symmetric Y-junction based on arc shaped S-bends. (b) Excess loss as a function of half the angle between the arms of the Y-junction when the fundamental (in blue) and the first-order (in green) modes are launched through port 1 at λ=1.55 μm. (c) Excess loss and (d) imbalance of the designed Y-junction with $\theta_Y/2$ = 12° as a function of the wavelength. Green and blue curves correspond, respectively, to TE_0 and TE_1 modes injected through the stem (port 1). It should be noted that the green curve is on top of the blue curve.*

As it can be observed, excess losses for TE_1 mode are hardly affected by the angle due to the odd symmetry of the field profile of the TE_1 mode, which presents a null at the tip. The TE_0 mode does show greater losses as the angle between the arms grows, i.e. the length decreases, since its field profile presents even symmetry. An angle

$\theta_Y/2 = 12°$ was chosen in order to obtain a design with losses below 0.1 dB, resulting in a length of $L_Y = 7.14$ µm.

Excess loss and imbalance for the designed Y-junction are shown in Figs. 3.7c and 3.7d, respectively. Excess loss for TE_0 mode is below 0.3 dB within the entire simulated wavelength range, whereas negligible values under 0.03 dB are attained for TE_1 mode. Regarding the imbalance, both modes present an almost ideal performance near 0 dB thanks to the structural symmetry of the symmetric Y-junction (see Fig. 3.7d).

3.3.4. Simulation results of the complete device

Owing to the small mesh required to properly simulate the PS, simulation of the complete mode converter and MUX/DEMUX is time-consuming and resource-intensive. Therefore, the response of the complete mode converter and MUX/DEMUX was obtained by using the S-parameter matrices previously calculated via 3D FDTD for the design of each component [FullWAVE'19]. Elements of these matrices were calculated by the simulator as a correlation with the corresponding mode at the specific input/output port, thereby power from undesired higher-order modes was not considered due to the mode orthogonality. S-parameter matrices of the MMI, the PS and the symmetric Y-junction were concatenated by means of an in-house tool of the UMA to obtain the S-parameter matrix of the proposed mode converter and MUX/DEMUX and its conventional counterpart.

Typical figures of merit for the mode converter and MUX/DEMUX comprise insertion loss ($\mathrm{IL_{MUX}}$ or $\mathrm{IL_{DEMUX}}$) and crosstalk ($\mathrm{XT_{MUX}}$ or $\mathrm{XT_{DEMUX}}$), which can be described in different ways for MUX and DEMUX operation using the S-parameters for each input/output port and the corresponding modes (see Fig. 3.3):

- For MUX operation, insertion loss is the optical power transferred to the desired mode at output port 3 relative to the input optical power at port 1 or port 2. For example, when the fundamental mode is launched through port 1, insertion loss corresponds to the optical power transferred to the fundamental mode in port 3 (the multimode waveguide). On the other hand, when the fundamental mode is launched through port 2, insertion loss corresponds to the optical power transferred to the first-order mode in port 3. Mathematically, it can be expressed as:

$$\mathrm{IL_{MUX,0}} = -10\log\left(\left|S_{31\_00}\right|^2\right) \text{ (for input port 1),} \qquad \textbf{(3.12)}$$

$$\mathrm{IL}_{\mathrm{MUX},1} = -10\log\left(\left|S_{32\_10}\right|^2\right) \text{ (for input port 2),} \quad \textbf{(3.13)}$$

where the first two indexes stand for the output and input port, respectively, and the last two indexes for the corresponding order of the mode at each port. In this way, S_{31_00} is the S-parameter associated to the fundamental mode of the input port 1 and the fundamental mode of the output port 3; and S_{32_10} is the S-parameter associated to the fundamental mode of the input port 2 and the first-order mode of the output port 3.

Crosstalk is defined as the optical power difference between undesired and desired modes at the output port 3:

$$\mathrm{XT}_{\mathrm{MUX},0} = 10\log\left(\left|S_{31\_10}\right|^2 \Big/ \left|S_{31\_00}\right|^2\right) \text{ (for input port 1),} \quad \textbf{(3.14)}$$

$$\mathrm{XT}_{\mathrm{MUX},1} = 10\log\left(\left|S_{32\_00}\right|^2 \Big/ \left|S_{32\_10}\right|^2\right) \text{ (for input port 2),} \quad \textbf{(3.15)}$$

here, S_{31_10} is the S-parameter associated to the fundamental mode of the input port 1 and the first-order mode of the output port 3; and S_{32_00} is the S-parameter associated to the fundamental mode of the input port 2 and the fundamental mode of the output port 3.

- Similarly, for DEMUX operation insertion loss is the optical power transferred to the desired output port (port 1 or port 2) relative to the input optical power at port 3. When the fundamental mode is launched through port 3, insertion loss corresponds to the optical power transferred to the fundamental mode in port 1; whereas when the first-order mode is launched through port 3, insertion loss corresponds to the optical power transferred to the fundamental mode in port 2:

$$\mathrm{IL}_{\mathrm{DEMUX},0} = -10\log\left(\left|S_{13\_00}\right|^2\right) \text{ (for input } \mathrm{TE}_0\text{),} \quad \textbf{(3.16)}$$

$$\mathrm{IL}_{\mathrm{DEMUX},1} = -10\log\left(\left|S_{23\_01}\right|^2\right) \text{ (for input } \mathrm{TE}_1\text{),} \quad \textbf{(3.17)}$$

where S_{13_00} is the S-parameter associated to the fundamental mode of the input port 3 and the fundamental mode of the output port 1; and S_{23_01} is the S-parameter associated to the first-order mode of the input port 3 and the fundamental mode of the output port 2.

Working as a DEMUX, the crosstalk is the power difference between undesired and desired ports:

$$\mathrm{XT}_{\mathrm{DEMUX},0} = 10\log\left(\left|S_{23\_00}\right|^2 \Big/ \left|S_{13\_00}\right|^2\right) \text{ (for input TE}_0\text{)}, \qquad \textbf{(3.18)}$$

$$\mathrm{XT}_{\mathrm{DEMUX},1} = 10\log\left(\left|S_{13\_01}\right|^2 \Big/ \left|S_{23\_01}\right|^2\right) \text{ (for input TE}_1\text{)}, \qquad \textbf{(3.19)}$$

here, S_{13_01} is the S-parameter associated to the first-order mode of the input port 3 and the fundamental mode of the output port 1; and S_{23_00} is the S-parameter associated to the fundamental mode of the input port 3 and the fundamental mode of the output port 2.

Final performance of the proposed mode converter and MUX/DEMUX and its conventional counterpart based on a non-periodic MMI is shown in Fig. 3.8 with solid and dashed lines, respectively. Figures 3.8a and 3.8c correspond to MUX operation, whereas DEMUX operation is represented in Figs. 3.8b and 3.8d. Note that the spectral response of both devices is practically the same for both MUX and DEMUX operation since the imbalance of the MMIs is close to zero and the losses of the PS and of the symmetric Y-junction are negligible.

Insertion losses of the mode converter and MUX/DEMUX based on SWG structures are as low as 0.84 dB (solid blue curve) and 0.61 dB (solid green curve) within the simulated 300 nm wavelength range for MUX and DEMUX operation, whereas crosstalk is better than -20 dB (solid blue curve) and -20.1 dB (solid green curve) for the same wavelength range and also both operations. Minima of the crosstalk curves are shifted 25 nm as a consequence of small phase deviations introduced by the SWG MMI and the PS.

Regarding the conventional mode converter and MUX/DEMUX, insertion losses increase up to 3.2 dB (blue curve) and 2.9 dB (green curve), and crosstalk values deteriorate to -15.5 dB (blue curve) and -11.8 dB (green curve) considering the same 1.4 – 1.7 μm wavelength range and the worst performance between MUX and DEMUX operation. There is a wavelength region around $\lambda \approx 1.45$ μm for which the phase error introduced by the conventional MMI is counterbalanced by the phase error of the PS (see Figs. 3.5c and 3.6c), resulting in low crosstalk values. However, this phase compensation is unlikely to occur at the same wavelength in fabricated devices since fabrication errors not only affect losses, but also phase errors of both the MMI and the PS. In addition, to achieve insertion losses below 0.84 dB for the conventional mode converter and MUX/DEMUX, the bandwidth must be reduced to just 100 nm

(1.455 – 1.555 µm), confirming that the conventional MMI seriously limits the performance of the entire architecture.

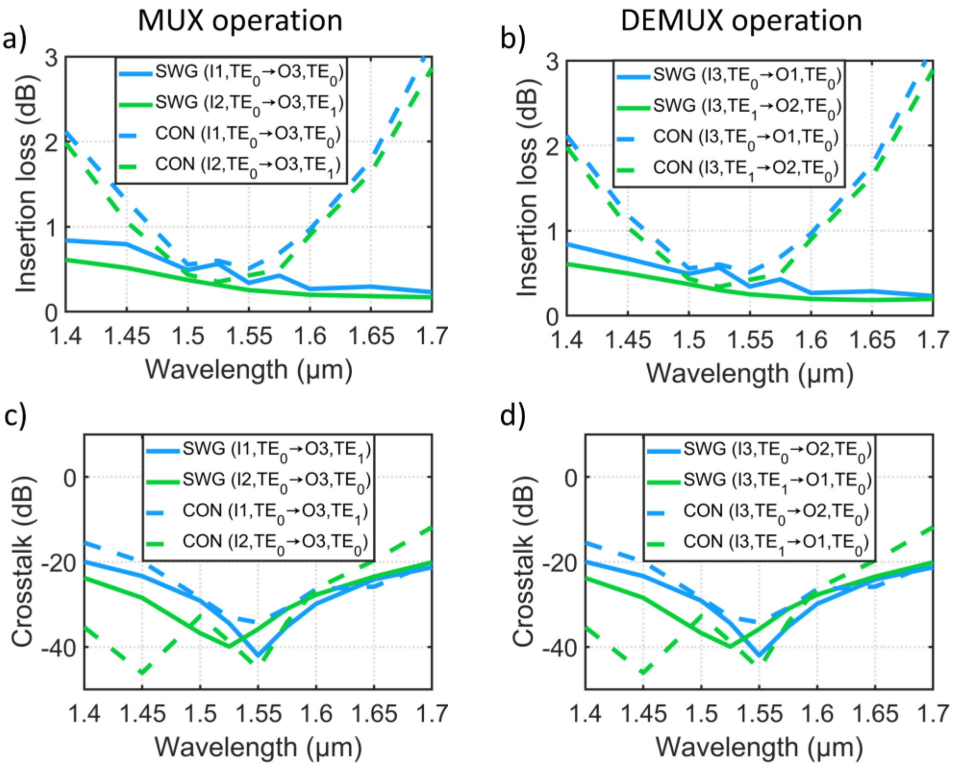

Figure 3.8. *Simulated performance of the proposed SWG mode converter and MUX/DEMUX (solid lines) compared to its conventional counterpart (dashed lines). (a) Insertion loss and (c) crosstalk of both devices working as a MUX is represented in the first column, i.e. from input ports 1 (I1) and 2 (I2) to the output port 3 (O3). (b) Insertion loss and (d) crosstalk of both devices working as a DEMUX is represented in the second column, i.e. from input port 3 (I3) to the output ports 1 (O1) and 2 (O2).*

The simulated field distribution of the proposed SWG mode converter and MUX/DEMUX is represented in Fig. 3.9 at the wavelengths of 1.4 µm, 1.55 µm and 1.7 µm when the fundamental and the first-order modes are injected through the multimode waveguide (DEMUX operation). At shorter wavelengths (see Figs. 3.9a and 3.9b), interconnection waveguides are no longer single-mode and little excitation of the TE_1 mode originates some ripples that are greater for TE_0 mode than for TE_1 mode as a result of the Y-junction tip. This effect is not a problem for isolated MUX or DEMUX since TE_1 mode can be straightforwardly radiated, but excitation of higher-order modes must be taken into consideration for the fabrication of an MDM link as will be discussed in the following sections. Nevertheless, an almost ideal performance is achieved for TE_0 and TE_1 modes at $\lambda = 1.55$ µm and $\lambda = 1.7$ µm.

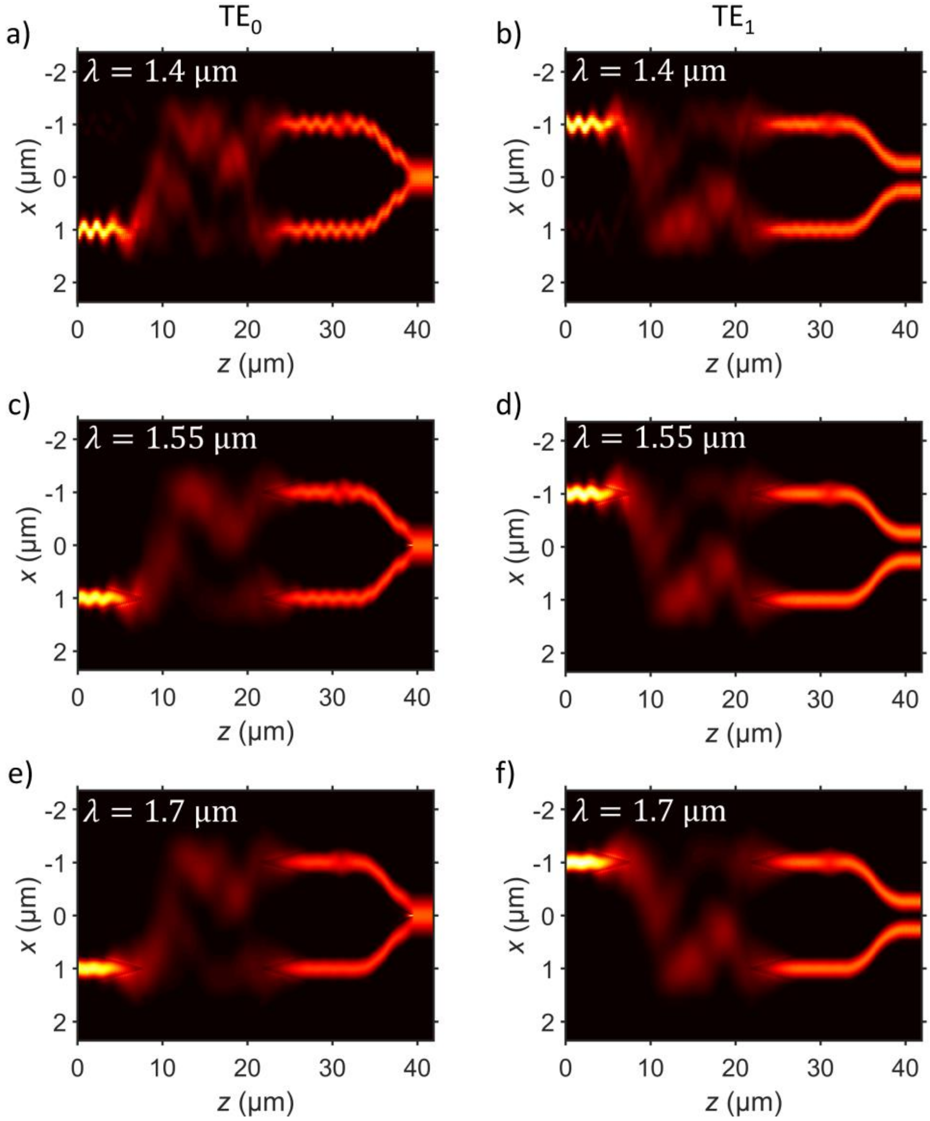

Figure 3.9. *Simulated field distribution of the mode converter and MUX/DEMUX when the fundamental mode is launched through port 3 at the wavelengths of (a) 1.4 µm, (c) 1.55 µm and (e) 1.7 µm; and when the firs-order mode is launched through port 3 at the wavelengths of (b) 1.4 µm, (d) 1.55 µm and (f) 1.7 µm.*

Last but not least, tolerances to fabrication errors were studied at the design wavelength $\lambda = 1.55$ µm following the same approach of concatenation of S-parameter matrices. Typical over- and under-etching errors during the fabrication process result in variations in the transverse and longitudinal directions. Hence, absolute width variations of $\Delta\delta$ were considered and the duty cycle was varied accordingly for the SWG MMI to perform a reliable study, i.e. $\mathrm{DC} = (a + \Delta\delta)/\Lambda$. Figure 3.10 shows the performance degradation for fabrication errors of up to $\Delta\delta = \pm 40$ nm. The proposed mode converter and MUX/DEMUX tolerate deviations of ±20 nm, yielding insertion loss and crosstalk below 0.8 and -19.5 dB, respectively.

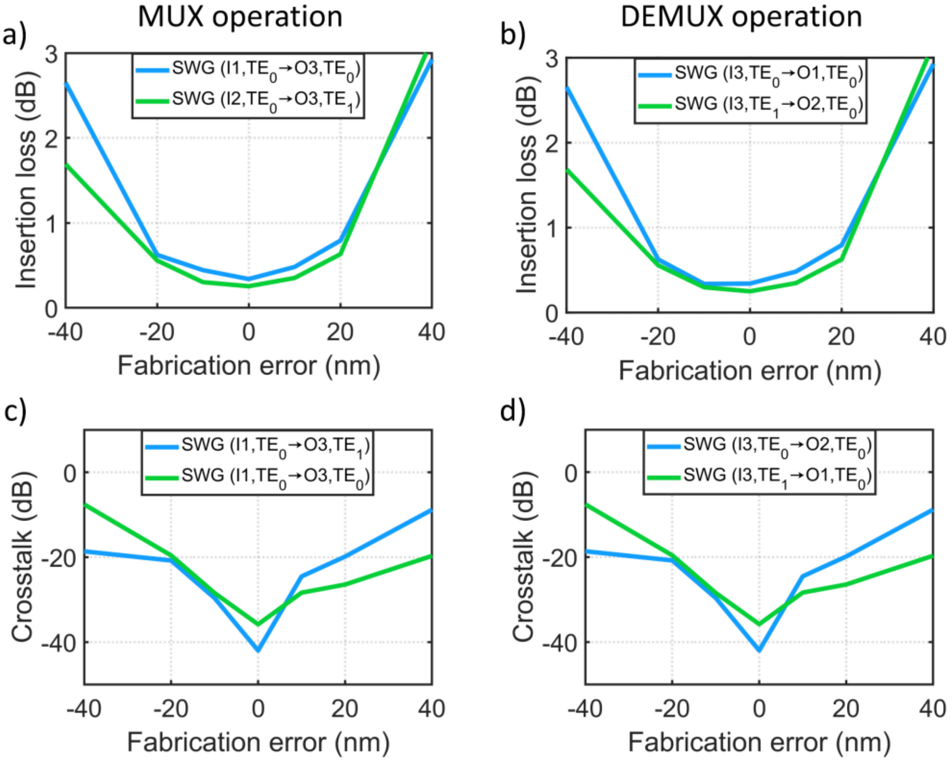

Figure 3.10. *Tolerance to fabrication errors of the proposed SWG mode converter and MUX/DEMUX at λ=1.55 µm. (a) Insertion loss and (c) crosstalk working as a MUX is represented in the first column, i.e. from input ports 1 (I1) and 2 (I2) to the output port 3 (O3). (b) Insertion loss and (d) crosstalk working as a DEMUX is represented in the second column, i.e. from input port 3 (I3) to the output ports 1 (O1) and 2 (O2).*

3.4. First experimental results and design optimization

The fabrication of the proposed mode converter and MUX/DEMUX was first carried out in collaboration with the NRC and the UMA at the facilities of the University of Washington [Washington'19]. This section aims to describe the test structures used for the characterization of the device and the challenges faced for the demonstration of a complete MUX-DEMUX link. Analysis of the experimental results raise important conclusions for further design optimization.

3.4.1. Test structures and fabrication

Selection of the test structures used for the characterization of the mode converter and MUX/DEMUX is not straightforward and must be defined before fabrication. As discussed in the previous sections, characterization of MUX and DEMUX operation implies either the detection or the injection of the first-order mode in the multimode waveguide. Although it is possible to perform mode conversion from TE_0 to TE_1 mode or vice versa, state-of-the-art mode converters have a narrow bandwidth compared to the 300 nm bandwidth of the proposed device, which impedes full device characterization. Furthermore, measurement complexity would increase since a precise independent characterization of the mode converter would be required.

Alternatively, two different test structures were used to verify the formation of the fundamental and first-order modes in the multimode waveguide, and to quantify device performance (see Fig. 3.11). The first test structure consists of a single device working as a mode converter and MUX (see Fig. 3.11a), whereas the second test structure is a complete MDM link formed by two mode converters and MUX/DEMUXs in back-to-back configuration (see Fig. 3.11b). Notwithstanding, other auxiliary test structures, such as a mode converter and DEMUX with the multimode waveguide fed by a TE_0 mode converter (adiabatic taper), were also included to extract relevant information from the device performance.

It is well known that the length of the multimode waveguide in a MUX-DEMUX link impacts on the crosstalk spectrum [Driscoll'13, Sun'16a, Williams'19]. This effect was studied by means of a circuit model considering transmission parameters as depicted in Fig. 3.11c. In this way, the response of both MUX and DEMUX is defined by the following expressions, respectively:

$$\begin{bmatrix} M0 \\ M1 \end{bmatrix} = \begin{bmatrix} a & b \\ c & d \end{bmatrix} \cdot \begin{bmatrix} I1 \\ I2 \end{bmatrix}, \tag{3.20}$$

$$\begin{bmatrix} O3 \\ O4 \end{bmatrix} = \begin{bmatrix} e & f \\ g & h \end{bmatrix} \cdot \begin{bmatrix} M0 \\ M1 \end{bmatrix}, \tag{3.21}$$

here, the transmission parameters of the MUX are given by the matrix elements a, b, c and d, whereas the transmission parameters of the DEMUX are e, f, g and h. The complex amplitudes at input ports 1 and 2 and output ports 3 and 4 are, respectively,

I_1, I_2, O_3 and O_4. Similarly, M_0 and M_1 are the complex amplitudes of the fundamental and first-order modes in the multimode waveguide.

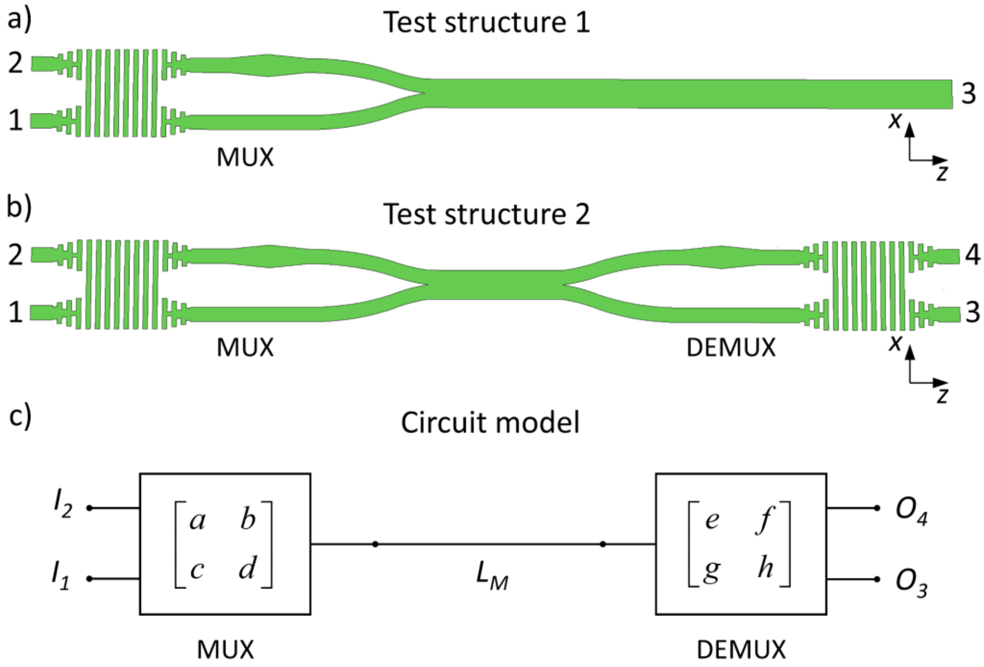

Figure 3.11. *Schematic of the main test structures used for the characterization of the proposed mode converter and MUX/DEMUX. (a) Device working in MUX configuration and (b) MUX-DEMUX link. (c) Representation of the circuit model of the MUX-DEMUX link using transmission parameters.*

The behaviour of the complete MUX-DEMUX link can be mathematically expressed as:

$$\begin{bmatrix} O3 \\ O4 \end{bmatrix} = \begin{bmatrix} e & f \\ g & h \end{bmatrix} \cdot \begin{bmatrix} e^{-j\beta_0 L_M} & 0 \\ 0 & e^{-j\beta_1 L_M} \end{bmatrix} \cdot \begin{bmatrix} a & b \\ c & d \end{bmatrix} \cdot \begin{bmatrix} I1 \\ I2 \end{bmatrix}, \qquad \textbf{(3.22)}$$

where β_0 and β_1 are the propagation constants of the fundamental and first-order modes propagating along the multimode waveguide of length L_M. When the fundamental mode is launched through port 1, i.e. $I_1 = 1$ and $I_2 = 0$, equation (3.22) is simplified to:

$$\begin{bmatrix} O3 \\ O4 \end{bmatrix} = e^{-j\beta_0 L_M} \cdot \begin{bmatrix} e & f \\ g & h \end{bmatrix} \cdot \begin{bmatrix} a \\ ce^{-j\Delta\beta L_M} \end{bmatrix} = e^{-j\beta_0 L_M} \cdot \begin{bmatrix} ea + fce^{-j\Delta\beta L_M} \\ ga + hce^{-j\Delta\beta L_M} \end{bmatrix}, \qquad \textbf{(3.23)}$$

with $\Delta\beta = \beta_1 - \beta_0$. For the architecture under study in this chapter, it holds that $|a|^2, |d|^2 \gg |b|^2, |c|^2$ and $|e|^2, |h|^2 \gg |f|^2, |g|^2$. Hence, variations in the crosstalk spectrum are mainly given by the intensity at the output port 4:

$$O4 = e^{-j\beta_0 L_M}\left(ga + hce^{-j\Delta\beta L_M}\right), \tag{3.24}$$

$$\begin{aligned} |O4|^2 = {} & |g|^2|a|^2 + |h|^2|c|^2 + \\ & + 2|g||a||h||c|\cos\left(\Delta\beta L_M - \varphi_h - \varphi_c + \varphi_g + \varphi_a\right), \end{aligned} \tag{3.25}$$

where each complex amplitude has been broken down into magnitude and phase, i.e. $a = |a|e^{j\varphi_a}$. The first argument in the cosine is the difference between propagation constants of the first two modes interfering in the multimode waveguide. This term depends on the wavelength and the length of the multimode waveguide L_M. The second argument stands for the difference in phase between two interfering signals: $\varphi_g + \varphi_a$ for the signal following the path $I_1 \rightarrow \mathrm{TE}_0 \rightarrow O_4$, and $\varphi_h + \varphi_c$ for the signal following the path $I_1 \rightarrow \mathrm{TE}_1 \rightarrow O_4$. Note that these results are equivalent to the demonstration recently made by Williams *et al.* [Williams'19].

For a sufficient long multimode waveguide, the free spectral range (FSR) is approximately:

$$\mathrm{FSR} \approx \frac{\lambda^2}{\Delta n_g L_M} = \frac{\lambda^2}{\left(n_{g,1} - n_{g,0}\right)L_M}, \tag{3.26}$$

where $n_{g,0}$ and $n_{g,1}$ are the group index of the fundamental and first-order modes in the multimode waveguide and can be calculated as $n_g(\lambda) = n_{eff,r}(\lambda) - \lambda dn_{eff,r}(\lambda)/d\lambda$.

Once the influence of the multimode waveguide length on the MUX-DEMUX link was determined, the length L_M was chosen to achieve an FSR below 10 nm at the wavelength of $\lambda = 1.55$ µm. The group index difference between the first two modes supported by the 1-µm-wide multimode waveguide is $\Delta n_g \approx 0.454$, thereby a length $L_M > 530$ µm is obtained from Eq. (3.26). To ensure that the FSR is less than 10 nm, a length of $L_M = 600$ µm was finally chosen.

A Visual Basic library developed by the UMA was used to draw the mask in AutoCAD. Different design variations were included with variations in the number of periods of the SWG MMI and the length of the PS. Moreover, some MUX-DEMUX links with the conventional MMI were also included for the sake of operation verification. The samples were fabricated using SOI wafers with a standard thickness of 220 nm for the Si layer and a 3-µm-thick BOX. Although the standard thickness for the BOX layer is currently 2 µm, at the time of fabrication (i.e. year 2017), the University of Washington was using SOI wafers with a BOX of 3 µm. The patterns were defined using the e-beam system at the University of Washington [Washington'19] and the subsequent etching process was also performed at the same facilities. Finally, a silicon dioxide upper cladding of 3 µm was deposited to protect the devices.

3.4.2. Analysis of results and design optimization

Measurements of the test structures presented in the previous section were carried out in the laboratories of the UMA using a setup as schematically shown in Fig. 3.12. A tunable laser from the former Agilent Technologies operating in the 1.495 – 1.64 µm wavelength range was employed to couple linearly polarized light from a customized polarization maintaining (PM) lensed fiber to the chip via high-performance SWG fiber-chip edge couplers [Cheben'06, Cheben'10, Cheben'15]. The PM lensed fiber was mounted on a fiber rotator to align the optical fiber axis to the chip x axis, i.e. in-plane or TE polarization. The chip was placed on a holder and two motorized nano-positioning stages at the input and output were used to precisely align the PM lensed optical fiber and the microscope objective to the chip waveguides, respectively. The output light beam from the chip was collected with a 40x achromatic microscope objective and filtered with a Glan-Thomson calcite polarizer mounted on a precision rotation stage. A broadband dielectric mirror in a folding frame allowed to direct the filtered light beam either to an infrared (IR) camera or to a germanium photodetector with an operating wavelength range from 0.78 µm to 1.8 µm, which was connected to a digital power meter.

First, the proposed mode converter and MUX/DEMUX based on an SWG MMI was measured using the test structure 1 to verify the formation of the fundamental and first-order modes in the multimode waveguide. The profile of the modes was captured with the IR camera at three different wavelengths: 1.495 µm, 1.55 µm and 1.64 µm (see Fig. 3.13). Light injected through the input port 1 generates the fundamental mode in the multimode waveguide (port 3 of Fig. 3.11a), while light injected through the input port 2 generates the first-order mode. Therefore, the operation as mode converter and MUX is successfully demonstrated over a broad bandwidth of 145 nm.

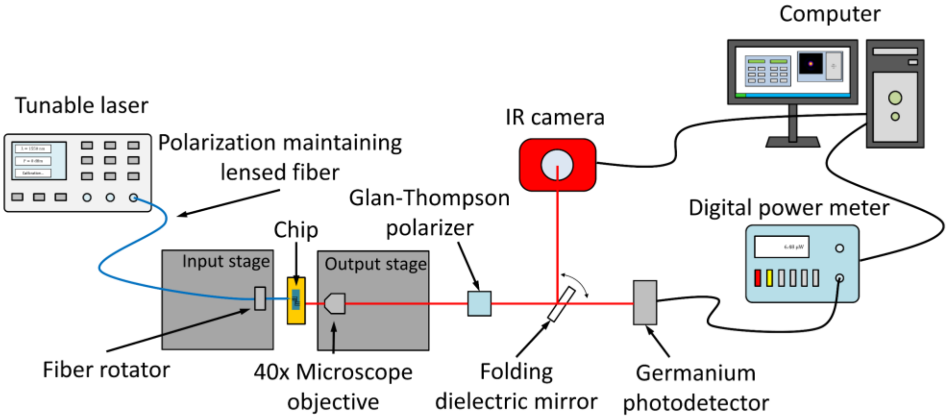

Figure 3.12. *Schematic of the measurement setup used to characterize the mode converter and MUX/DEMUX.*

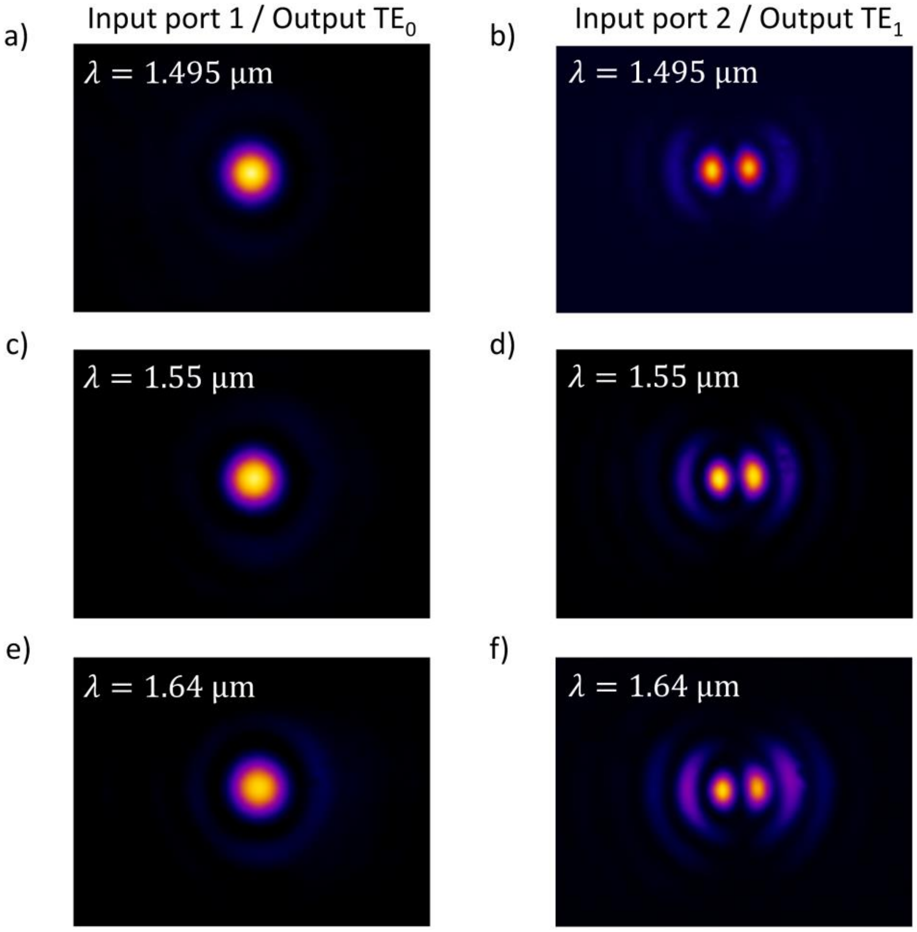

Figure 3.13. *Mode profiles imaged with an IR camera when the fundamental mode is injected through the input port 1 at the wavelengths of (a) 1.495 µm, (c) 1.55 µm and (e) 1.64 µm; and through the input port 2 at the wavelengths of (b) 1.495 µm, (d) 1.55 µm and (f) 1.64 µm.*

The complete MUX-DEMUX link was measured afterwards. Light was first coupled to one of the input ports and power measurements at the output ports 3 and 4 were performed sequentially. Insertion loss and crosstalk obtained for the MUX-DEMUX link based on an SWG MMI and its conventional counterpart are depicted in Fig. 3.14. As it can be observed, insertion losses present ripples with a maximum amplitude of ~5 dB when the fundamental mode is injected through the input port 1 (blue curves), i.e. the fundamental mode is generated in the multimode waveguide. By contrast, when the fundamental mode is injected through port 2 and the first-order mode is generated in the multimode waveguide, the spectral response presents no ripples (green curves).

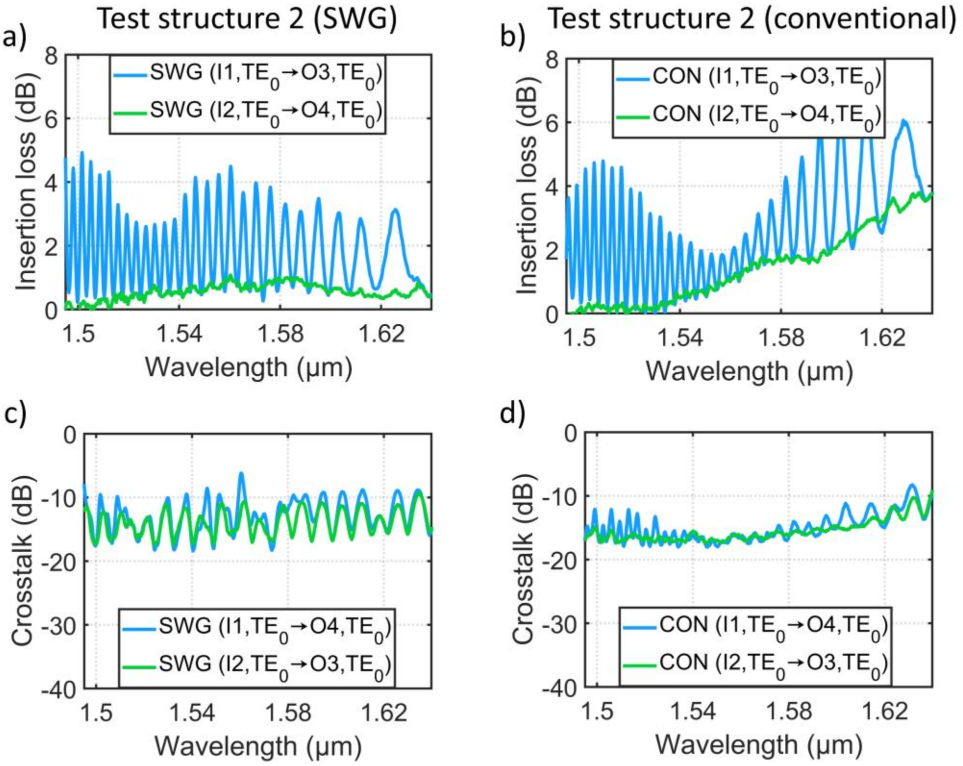

Figure 3.14. *Measured (a) insertion loss and (c) crosstalk of the complete MUX-DEMUX link composed of two mode converters and MUX/DEMUXs based on SWG structures. Measured (b) insertion loss and (d) crosstalk of an identical MUX-DEMUX link composed of two mode converters and MUX/DEMUXs based on conventional MMIs.*

To shed some light on the behaviour of the MUX-DEMUX link, all the design variations in the sample were carefully measured and two conclusions could be drawn:

- Since insertion loss measurements of both structures (SWG and conventional) present ripples for all the fabricated designs, it can be ruled out that the problem comes from the SWG MMI. Additionally, problems with the PS can also be discarded because this behaviour only occurs when the light is launched through the input port 1 and the fundamental mode is generated in the multimode waveguides. Therefore, the initial prediction points to a problem with the symmetric Y-junction and the tip that is generated due to the limited resolution of the fabrication process.

- The FSR measured from Fig. 3.14a and Fig. 3.14b is approximately 4.5 nm near the wavelength of 1.55 μm. This value is almost half the FSR originated from the beat between the fundamental and first-order modes in the 600-μm-long multimode waveguide designed in the previous subsection (see Eq. (3.26)). This means that another undesired higher-order mode is partially excited in the multimode waveguide and propagates together with the fundamental mode.

Additional 3D FDTD simulations of two symmetric Y-junctions in back-to-back configuration were carried out to verify this hypothesis. The schematic of the simulated structure is shown in Fig. 3.15a considering the same geometrical parameters as in subsection 3.3.3 and a 50 nm tip formed at the junction between the arms. The length of the multimode waveguide was selected to be $L_M = 14.6$ μm, since 3D FDTD simulations of a 600-μm-long structure using a nanometric scale mesh is impractical. The simulated field distribution is shown Fig. 3.15b when two in-phase TE_0 modes at the wavelength of 1.55 μm are simultaneously launched through the input ports 1 and 2. A spatial interference pattern appears in the multimode waveguide as a consequence of the beating between the fundamental mode and another higher-order mode, the second-order mode (TE_2). Group indexes of TE_0 and TE_2 modes in the 1-μm-wide multimode waveguide are $n_{g,0} \approx 3.88$ and $n_{g,2} \approx 5$ at $\lambda = 1.55$ μm, respectively. The calculation of the FSR due to the beating of both modes can be done by taking the Eq. (3.26) and replacing $n_{g,1}$ with $n_{g,2}$, obtaining an $\mathrm{FSR} = 3.6$ nm for the 600-μm-long multimode waveguide. This value is very similar to the FSR measured in Fig. 3.14a and 3.14b, indicating that the undesired TE_2 mode is excited due to fabrication constraints. It should be noted that small variations in the FSR value fall within the fabrication error.

The design of the symmetric Y-junction was optimized to avoid the propagation of the second-order mode along the multimode waveguide. The width of the multimode waveguide was varied until the TE_2 mode was not supported at the minimum wavelength of 1.495 μm, yielding a width of 700 nm. However, this width results in narrow waveguides, i.e. width of 350 nm, which can lead to high propagation losses [Morichetti'10]. On this account, a width of the Y-junction arms of $W_Y = 400$ nm was chosen as a compromise between propagation loss and a weak confinement of the TE_2 mode. Final verification was performed by simulating the excess losses of the structure depicted in Fig. 3.15a with a 50 nm tip and injecting two in-phase TE_0 modes through ports 1 and 2. Figure 3.15c shows that excess loss ripples from the original design (blue curve) are mitigated in the optimized design with $W_Y = 400$ nm (green curve). Furthermore, the amount of power transferred to the second-order mode in the multimode waveguide is reduced by more than 6 dB within the 1.495 – 1.64 µm wavelength range as shown in Fig. 3.15d.

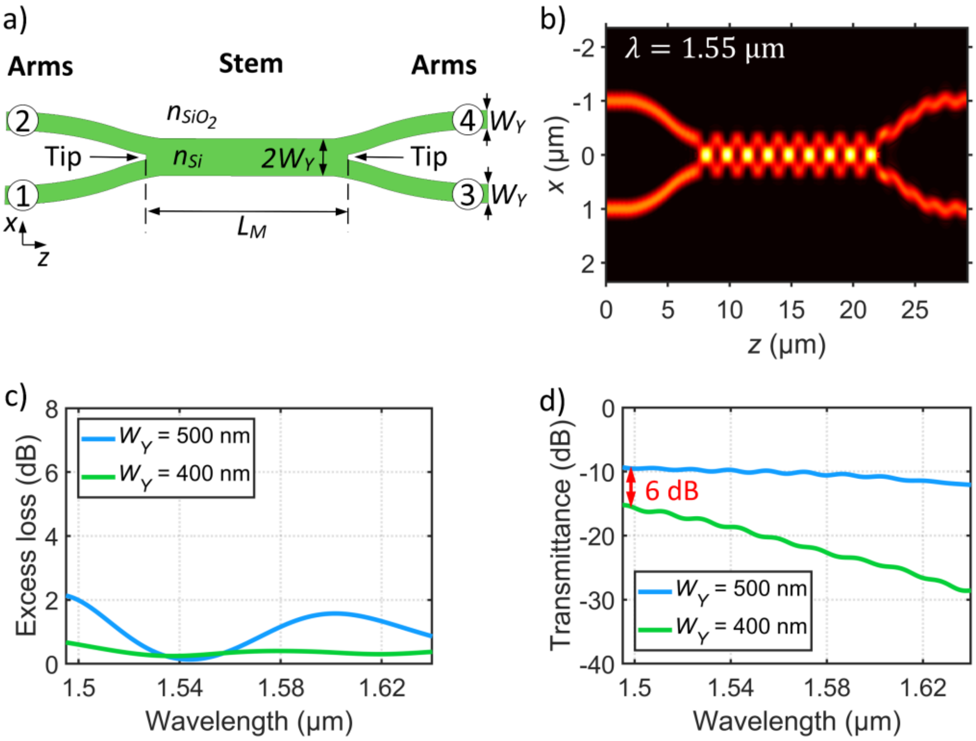

Figure 3.15. *(a) Schematic top view of two symmetric Y-junction in back-to-back configuration connected by a multimode waveguide of length* L_M*. A tip of 50 nm is considered in both Y-junctions in order to model the limited resolution of the fabrication process. (b) Simulated field distribution of the structure with* $W_Y = 500$ *nm when the fundamental mode is launched through ports 1 and 2 at the wavelength of 1.55 µm. (c) Simulated excess loss of the structure and (d) amount of power coupled to the* TE_2 *mode in the multimode calculated for* $W_Y = 500$ *nm (blue curves) and* $W_Y = 400$ *nm (green curves).*

3.5. Final characterization

According to the findings of section 3.4.2, geometry of the mode converter and MUX/DEMUX was minimally modified to avoid the excitation of the second-order mode in the multimode waveguide when two devices are connected in a MUX-DEMUX link. Two tapers were incorporated between the PS and the symmetric Y-junction with a length $L_R = 2$ µm to adiabatically reduce the width of the Y-junction arms from $W_I = 500$ nm to $W_Y = 400$ nm. The schematic of the optimized mode converter and MUX/DEMUX based on SWG structures is represented in Fig. 3.16 for the convenience of the reader.

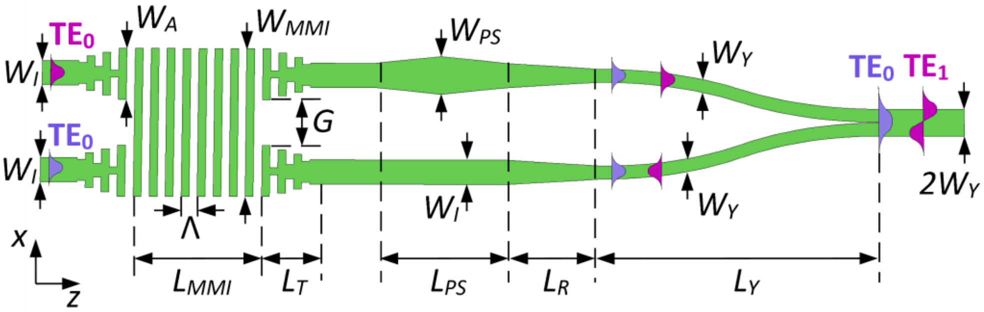

Figure 3.16. *Schematic of the optimized mode converter and MUX/DEMUX. Adiabatic tapers of length* L_R *are included to decrease the width of the Y-junction arms from* W_I *to* W_Y*.*

A second fabrication run was performed thanks to the collaboration with Alcyon Photonics S.L. The same tools as described in subsection 3.4.1 were used to draw the mask and identical test structures were included to characterize the device although updated with the optimized design. Due to economic and technical reasons (chip size, possibility of deep trenches, minimum feature size and short delivery time), fabrication was carried out in a commercial foundry [AppliedNanotools'19] using standard SOI wafers with 220-nm-thick silicon layer and a 2-µm-thick BOX. Patterns were defined using e-beam lithography (100 keV) and etching was performed through anisotropic reactive ion etching process with an inductively coupled plasma etcher (ICP-RIE). SEM images were taken before cladding deposition (see Fig. 3.17) and the tip of the symmetric Y-junction was measured, yielding an approximate value of 48 nm (close to the value used for the symmetric Y-junction optimization in the previous section). Finally, a 2.2-µm-thick SiO_2 cladding was deposited by chemical vapour deposition (CVD). Table 3.2 summarizes the final geometrical parameter of the fabricated mode converter and MUX/DEMUX based on an SWG MMI. All values were the same as in the first fabrication run, except for the Y-junction arm and stem widths. Furthermore, the best performance was attained for an SWG MMI with 77 periods and a PS length of 3.41 µm, being the overall footprint as small as 38.6 × 3.7 µm^2.

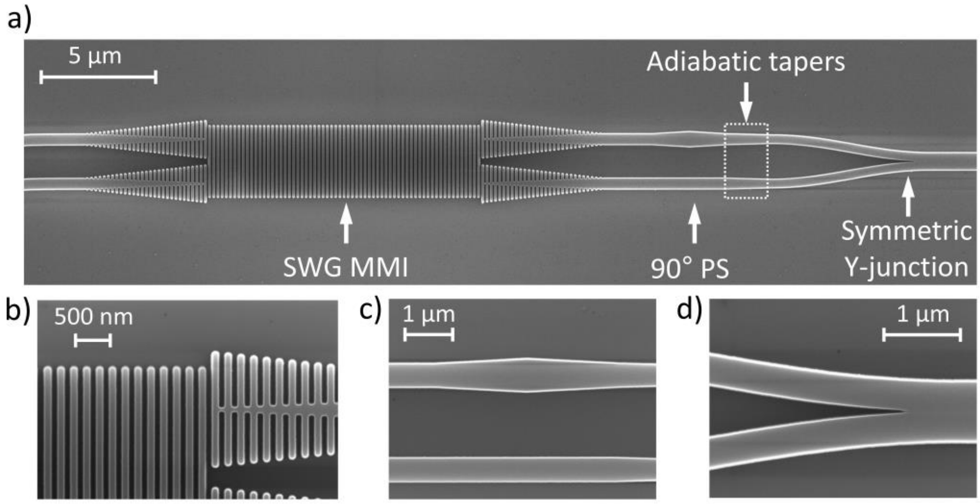

Figure 3.17. *Scanning electron microscope images of (a) the optimized mode converter and MUX/DEMUX and zoomed-in images of (b) the SWG MMI, (c) the 90° PS and (d) the symmetric Y-junction.*

Table 3.2. *Geometrical parameters of the optimized mode converter and MUX/DEMUX based on SWG structures that was fabricated in the second fabrication run.*

Component	Parameter	Definition	Value
SWG MMI	Λ	Period	190 nm
	DC	Duty cycle	50%
	W_I	Input width	500 nm
	W_A	Access width	1.7 µm
	W_{MMI}	MMI width	3.25 µm
	G	Gap	300 nm
	L_T	Taper length	5.7 µm (30 periods)
	L_{MMI}	MMI length	14.63 µm (77 periods)

90° Phase Shifter	W_{PS}	PS width	700 nm
	L_{PS}	PS length	3.41 µm
Symmetric Y-junction	W_Y	Y-junction arm width	400 nm
	$2W_Y$	Y-junction stem width	800 nm
	L_R	Y-junction taper length	2 µm
	L_Y	Y-junction arm length	7.14 µm

The fabricated PICs were measured in collaboration with Alcyon Photonics S.L. and the UMA in the laboratories of the latter. In this case, Alcyon Photonics S.L. contributed by measuring part of the designs included in the chip, whereas the other part was measured by the author of this thesis. The same setup was used as for the characterization of the first fabricated PICs (see Fig. 3.12) and the results obtained for a complete MUX-DEMUX link are shown in Fig. 3.18. The response of the insertion losses no longer exhibits the ripples when injecting light through the input port 1, confirming that the problem in the first fabrication run was the excitation of the second-order mode in the multimode waveguide as a consequence of the tip generated between the arms of the symmetric Y-junctions. When the fundamental mode is injected through input port 1 (Fig. 3.18a, blue curve), insertion loss is lower than 1.3 dB for the complete MUX-DEMUX link within a broad bandwidth of 145 nm (1.495 – 1.64 µm). In addition, when the fundamental mode is injected through port 2 (Fig. 3.18a, green curve) insertion loss decrease up to 1 dB within the same wavelength range. In other words, a single mode converter and MUX/DEMUX exhibits insertion loss as low as 0.65 dB and 0.5 dB for TE_0 and TE_1 modes, respectively, over the measured 145 wavelength range. On the other hand, the measured crosstalk of the MUX-DEMUX link is better than -15.3 dB and -15.4 dB when the fundamental mode is injected through port 1 (Fig. 3.18b, blue curve) and port 2 (Fig. 3.18b, green curve), respectively. These values of the MUX-DEMUX link are improved when the wavelength range is limited to 120 nm (1.52 – 1.64 µm). In this case, insertion losses as low as 1.1 dB and 0.84 dB are attained when the fundamental mode is injected through input ports 1 and 2, respectively. The crosstalk values improve almost 4 dB within the same wavelength range, yielding -19.1 dB and -19.7 dB for light coupled to the ports 1 and 2, respectively.

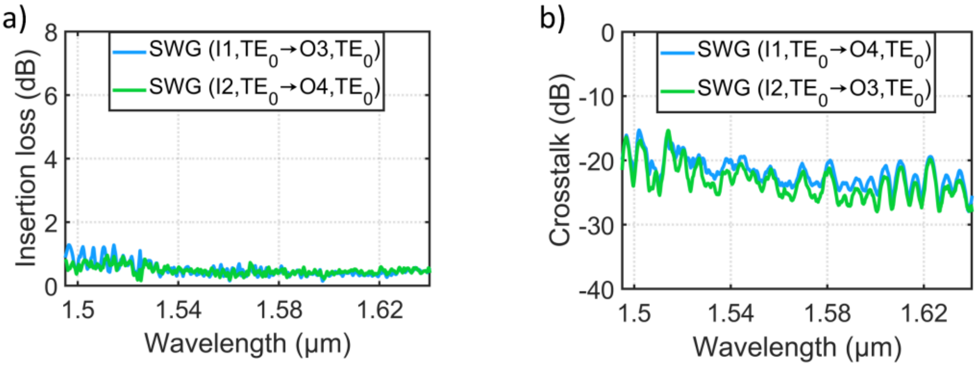

Figure 3.18. *Measured (a) insertion loss and (c) crosstalk of the complete MUX-DEMUX link composed of two optimized mode converters and MUX/DEMUXs based on SWG structures.*

The experimental results obtained are shown in Table 3.3 along with the performance and footprints of other state-of-the-art passive mode converters and MUX/DEMUXs. The proposed mode converter and MUX/DEMUX is the one of the most compact devices (apart from those based on inverse design), exhibiting an excellent compromise between insertion loss, crosstalk and operating bandwidth.

This final characterization experimentally verifies the concept proposed in this chapter, i.e. reducing the insertion loss of the MDM architecture based on a conventional MMI, a 90° PS and a symmetric Y-junction by replacing the conventional MMI with an SWG MMI. Although the light source of the measurement setup partially limited the characterization to longer wavelengths, it can be observed that the performance in terms of crosstalk is now restricted by the phase errors introduced by the PS. A possible improvement would be to replace it with another PS with a broader response. It is important to mention that the chips and the results of this second fabrication run are the property of Alcyon Photonics S.L., and therefore, the measurements (in terms of wavelength range) were carried out according to their criteria.

Table 3.3. *Comparison of state-of-the-art passive mode converters and MUX/DEMUXs fabricated on the SOI platform.*

Reference	Architecture	IL (dB)	XT (dB)	BW (nm)	Length (µm)
[Dai’13]	Asymmetric directional coupler	< 1	< -23	20	~ 100
[Ding’13]	Tapered directional coupler	> 0.3	< -16	100	50

[Driscoll’13]	Asymmetric Y-junction	< 1.5	< -9	100	> 100
[Xing’13a]	Adiabatic tapers	~ 0.3	< -36	100	300
[Wang’15]	Tapered directional coupler	< 1	< -13	180	260
[Sun’16b]	Tapered-etched directional coupler	< 1.6	< -26	65	> 68
[Frellsen’16]	Inverse design	< 2.4	< -12	100	4.22
[Sun’16a]	Adiabatic tapers	~ 1	< -20	75	200
[Zhang’17]	Adiabatic tapers	< 1.5	< -19	90	181
[Guo’17]	Tapered directional coupler	< 1.1	< -24	100	150
[Li’17]	Tapered directional coupler	< 0.2	< -20	65	310
[Li’18c]	Asymmetric Y-junction	> 0.4	< 9.1	106	60
[Dai’18]	Tapered directional coupler	< 1.8	< -15	90	~500
[Chang’18b]	Inverse design	< 1	< -24	60	3
[Xu’19]	Adiabatic tapers	< 2.6	<-18.8	230	55
This work	MMI	< 1.3	<-15.3	145	38.6

3.6. Summary

In this chapter, mode-division multiplexing technology has been introduced along with the fundamental components required to handle and route higher-order modes in PICs. Mode converters and MUX/DEMUXs have been presented as fundamental constituents for MDM systems and the different architectures proposed to simultaneously perform mode conversion and multiplexing/demultiplexing have been reviewed.

Architectures based on MMIs couplers comprise several components, but their performance is usually restricted by the beat length of conventional MMIs. To overcome this constraint, a broadband and compact mode converter and MUX/DEMUX based on a subwavelength engineered MMI has been designed, fabricated and characterized for the SOI platform. In addition to the SWG MMI, this device consists of a 90° PS and a symmetric Y-junction. Simulation results predict insertion loss lower than 0.84 dB and crosstalk better than -20 dB over an unprecedented bandwidth of 300 nm (1.495 – 1.64 µm). However, the proposed device was fabricated and the characterization of a complete MUX-DEMUX link revealed, after a thorough analysis, that the second-order mode was excited in the multimode waveguide only for TE_0 mode conversion. The origin of this problem was the limited resolution of the fabrication process, which generates a tip of non-negligible dimensions between the arms of the symmetric Y-junction and degrades the performance. After a design optimization to reduce the width of the Y-junction arms, and subsequently, the width of the multimode waveguide, the optimized mode converter and MUX/DEMUX was fabricated again. This time, the complete MUX-DEMUX link was successfully demonstrated exhibiting insertion loss lower than 1.3 dB and crosstalk better than -15.3 dB for both multiplexed modes over a broad 145 nm wavelength range (1.495 – 1.64 µm). This flat low-loss response is achieved for a single MUX/DEMUX footprint of only 38.6 µm × 3.7 µm, being one of the demonstrated mode converters and MUX/DEMUXs with lowest insertion loss over a broad bandwidth enclosed in a compact footprint.

IV

Nanophotonic passive phase shifter

Optical phase shift between different signals constitutes one of the fundamental operations in many photonic systems. Passive phase shifters have barely evolved in recent decades although their presence is becoming increasingly important for applications like mode-division multiplexing and optical communications with arbitrary-ratio power splitters. This chapter presents a novel passive phase shifter based on SWG metamaterial waveguides with an ultra-broad bandwidth. Section 4.1 revisits the different active and passive mechanisms to perform on-chip phase shifting in the state of the art. The limitations of passive PSs with arms of the same length are discussed in section 4.2. The design of the proposed PS is explained in section 4.3. For the sake of comparison, the design of other conventional PSs can also be found in this section. Fabrication and characterization procedures are detailed in section 4.4. Finally, a summary of this chapter is briefly outlined in section 4.5.

4.1. Introduction to optical phase shifting

Optical phase shifting is a fundamental operation for most PICs aimed at disparate applications such as telecom [Hillerkuss'10], datacom [Doerr'10], microwave and terahertz photonics [Marpaung'19, Harter'18], sensing [Halir'13, Wangüemert-Pérez'19] and quantum information processing [Knill'01, Harris'16], to name a few. Optical PSs should not be confused with optical delay lines (ODLs). Although their operating principle is essentially the same, their practical purpose is quite different. Optical PSs provide an adjustment of the signal phase with respect to a reference signal of up to 360° (i.e. the spectral phase is varied with small changes in the optical path within the order of one optical wavelength). On the other side, ODLs perform an adjustment substantially larger, which is typically specified as a delay in the time domain [Wang'16b]. In order to induce a specific time delay between optical pulses, the change in the optical path must be considerably greater than one optical wavelength, and subsequently, the group index must be considered for ODLs calculations instead of the effective index of the guided modes [Velasco'13b], which is used for the design of PSs. This section focuses primarily on optical PSs and the main techniques used to induce spectral phase variations between the involved signals.

Optical PSs can be sorted into two different groups depending on whether their structure includes an active control element or not to change the optical path difference between two or more signals located in different physical positions. Active PSs enable to modify the optical path difference over time, resulting in an adjustable phase shift between signals [Harris'14]. Conversely, passive PSs have no active control elements and, thus, the optical path difference is stationary, which leads to a fixed phase shift between the signals [Morrissey'15]. Different approaches can be distinguished in both groups to carry out said phase shift.

4.1.1. Techniques for active phase shifting

The ability to tune the phase shift response for different wavelengths by means of active PSs has received continued attention from the silicon photonics community in recent years for the development of phased antenna arrays [Sun'13], tunable filters [Djordjevic'11, Orlandi'12], modulators [Reed'10], optical switches [Xiong'17, VanCampenhout'09] and polarization controllers [Sarmiento-Merenguel'15], among other devices.

One of the most adopted mechanisms to actively tune the phase shift response is the thermo-optic effect [Harris'14]. The relatively high thermo-optic material coefficient of silicon, i.e. $dn_{Si}/dT = 1.8 \times 10^{-4}\ \mathrm{K}^{-1}$ [Schmid'11], can be leveraged to modulate the refractive index of the waveguides and change its optical path length. In this regard, resistive micro-heaters are integrated on-chip near the waveguide (on top or on the side) to generate heat in its vicinity and maximize the overlap between the mode propagated along the waveguide and the heat flow. However, active PSs based on the thermo-optic effect require waveguides with a length of several hundred micrometers and a high-power consumption in order to induce large phase shifts [Xia'04]. Additionally, the thermal crosstalk between devices located near the thermo-optic PSs must be taken into consideration to prevent the malfunction of the complete system.

Another alternative for phase shifting widely used in silicon photonics relies on the free-carrier plasma dispersion effect, in which the change of the refractive index of the Si waveguide is performed by varying the concentration of free carriers (electrons and holes) [Soref'87]. Electric control of the carriers is performed via three different structures: carrier injection, carrier depletion and carrier accumulation [Debnath'18]. These PSs are often used in optical modulators due to the faster response times compared to thermo-optic PSs and the absence of the Pockels effect on the canonical silicon platform (on account of its centro-symmetric crystal structure) [Reed'10]. The main limitation of these PSs is given by the low efficiency of the plasma dispersion effect, resulting in high-power consumption and long PS lengths from a few hundred micrometers in forward-biased devices (i.e. in carrier injection structures) to several millimeters in reverse-biased devices (i.e. in carrier depletion structures) [Pfeifle'12]. This results in high propagation losses which are further emphasized by the absorption of free-carriers [Reed'08].

In order to cope with the high-power consumption of PSs based on thermo-optic and plasma dispersion effects, micro electromechanical systems (MEMS) have been implemented on-chip for phase shifting purposes [Sattari'19]. This approach is based on a suspended waveguide that moves when an electric field is applied to a mechanical actuator [Ikeda'10]. Therefore, low insertion loss and more compact footprints than the former counterparts are achieved at the cost of intricate designs and a slower response time compared to PSs based on plasma dispersion effect [Poot'14].

Other active mechanisms have also been proposed to perform radio frequency phase shifting [Chang'08, Burla'14, McKay'19] and to exploit the electro-optical effect by using an organic liquid crystal cladding [Pfeifle'12, Xing'15]. Notwithstanding, many applications simply require active PSs to tune the phase shift response for different wavelengths or to compensate for possible fabrication errors that result in deviations from the target phase shift, and therefore, they would benefit from a complexity reduction by suppressing active control elements.

4.1.2. Techniques for passive phase shifting

Integrated PSs with passive operation, i.e. without an active control element, are crucial devices for many complex PICs and subsystems such as mode converters [Leuthold'98, Pérez-Galacho'16], mode converters and MUX/DEMUXs [Li'14, González-Andrade'18], optical 90° hybrids [Jeong'09, Voigt'11], arbitrary-ratio power splitters [Saida'99, Cherchi'14, Li'19] and mode-insensitive power splitters [Ren'18], to name a few. Although most progress in the last decade has focused on active PSs, the search for a high-performance passive PS with a compact footprint and improved tolerances to fabrications errors has attracted increasing interest from the scientific community.

The most common structures used for passive phase shifting are depicted in Fig. 4.1, considering two parallel non-periodic waveguides as the simplest example. It should be noted that every waveguide induces its own phase relations between the input and output signals (as denoted in Eqs. (3.3) and (3.4) of the previous chapter), hence optical PSs are typically compared to a reference signal that propagates through an unmodified waveguide. In this way, the optical path length is altered by means of geometric variations to induce a static phase shift between the signals propagated through the different waveguides. This phase shift can be generated by a difference in the length of the physical path (see Fig. 4.1a) or by a difference in the effective indexes of the modes propagated along the waveguides, i.e. by changing the widths of the non-periodic waveguides (see Fig. 4.1b).

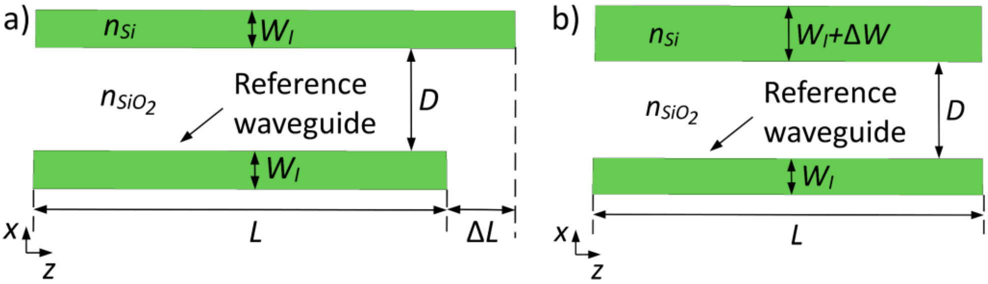

Figure 4.1. *Schematic of two passive phase shifting structures based on (a) two waveguides with dissimilar lengths (ΔL) and the same width (W_I), and (b) two waveguides with the same length (L) and different widths (ΔW).*

Most PICs that require passive PSs are based on building blocks with fixed relative position for their inputs and outputs. Therefore, PS alternatives with disparate waveguide lengths impose challenging layout constraints (Fig. 4.1a) that make alternatives based on disparate refractive index (Fig. 4.1b) a far more common choice [Leuthold'98, Saida'99, Jeong'09, Cherchi'14, Morrissey'15, Pérez-Galacho'16, González-Andrade'18, Ren'18]. On this account, the rest of the chapter will focus on the study of this type of PSs, covering from a theoretical analysis to show their bandwidth limitations to a novel proposal to improve their performance by replacing non-periodic waveguides with SWG waveguides.

4.2. Theoretical study of passive phase shifters

This section aims to analyse the bandwidth and fabrication constraints posed by passive PSs based on non-periodic waveguides of the same length. Thereafter, the additional degrees of freedom in the design provided by SWG metamaterial waveguides are leveraged to control both dispersion and anisotropy, mitigating the wavelength dependence of the phase shift response and also enhancing the resilience to fabrication errors.

4.2.1. Limitations of phase shifters based on non-periodic waveguides

For this theoretical study, we first consider the same structure as in the introductory section 4.1, that is, two waveguides of equal length and different widths. For convenience its geometrical variables have been renamed (see Fig. 4.2). The PS is composed of two parallel waveguides with a width W_U for the upper waveguide and a width W_L for the lower waveguide. The separation between both waveguides is D, which is assumed large enough to avoid interference between them, i.e. the power of one waveguide is not coupled to the adjacent one. The length of the PS is L_{PS} and the phase shift, as in the previous chapter, is considered between the lower and upper arms.

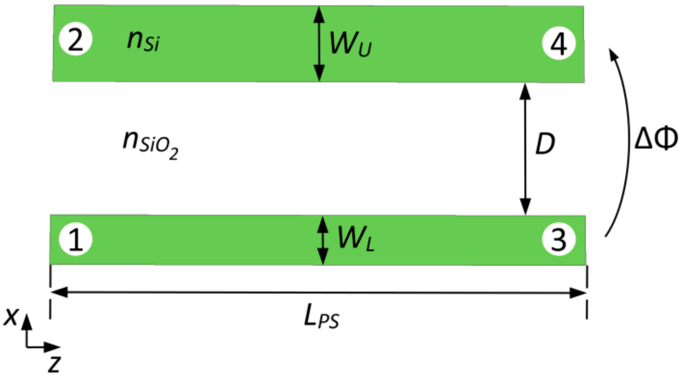

Figure 4.2. *Schematic top view of a passive PS consisting of two parallel waveguides with the same length (L_{PS}) and different widths (W_U and W_L). The waveguides are separated a distance D to avoid any power coupling.*

The phase shift induced by each waveguide is determined by:

$$\Phi_{42}(\lambda) = -\beta_U(\lambda) L_{PS}, \tag{4.1}$$

$$\Phi_{31}(\lambda) = -\beta_L(\lambda) L_{PS}, \tag{4.2}$$

where $\beta_U(\lambda)$ is the phase constant of the fundamental mode propagating through the upper arm of the PS, $\beta_L(\lambda)$ is the phase constant of the fundamental mode propagating through the lower arm of the PS, L_{PS} is the length of the phase shifter, and $\Delta\Phi_{ij}$ is the phase shift between ports i and j. The phase shift between the fundamental modes propagating along the lower and upper arms is therefore:

$$\Delta\Phi(\lambda) = \Phi_{31}(\lambda) - \Phi_{42}(\lambda) = \left[\beta_U(\lambda) - \beta_L(\lambda)\right] L_{PS}. \tag{4.3}$$

The expression of Eq. (4.3) can be rewritten in terms of the difference between the effective indexes of the fundamental modes propagating through each waveguide:

$$\Delta\Phi(\lambda) = \frac{2\pi}{\lambda} \Delta n_{eff}(\lambda) L_{PS}, \tag{4.4}$$

where $\Delta n_{eff}(\lambda) = n_{eff,r,U}(\lambda) - n_{eff,r,L}(\lambda)$. Here, $n_{eff,r,U}(\lambda)$ and $n_{eff,r,L}(\lambda)$ are the real part of the effective indexes of the fundamental modes supported by the upper and lower arms of the PS, respectively. Since passive PSs are designed to induce a specific nominal phase shift ($\Delta\Phi_0$) at the design wavelength (λ_0), the length of the PS can be computed as:

$$L_{PS} = \frac{\Delta\Phi_0 \lambda_0}{2\pi \Delta n_{eff}(\lambda_0)}. \tag{4.5}$$

By inserting Eq. 4.5 into Eq. 4.4, an alternative expression for the phase shift induced between the lower and upper PS arms is obtained:

$$\Delta\Phi(\lambda) = \frac{\Delta\Phi_0 \lambda_0}{\Delta n_{eff}(\lambda_0)} \cdot \frac{\Delta n_{eff}(\lambda)}{\lambda}. \tag{4.6}$$

It should be noted that the first term of Eq. 4.6 is a constant value, whereas the second terms gives the response of the PS with the wavelength.

The wavelength dependence can be studied by derivating Eq. 4.6:

$$\begin{aligned}\left.\frac{d\Delta\Phi(\lambda)}{d\lambda}\right|_{\lambda=\lambda_0} &= \frac{\Delta\Phi_0\lambda_0}{\Delta n_{eff}(\lambda_0)}\cdot\frac{d}{d\lambda}\left[\frac{\Delta n_{eff}(\lambda)}{\lambda}\right]= \\ &= \frac{\Delta\Phi_0\lambda_0}{\Delta n_{eff}(\lambda_0)}\left[\frac{\lambda_0\left(d\Delta n_{eff}(\lambda)/d\lambda\big|_{\lambda=\lambda_0}\right)-\Delta n_{eff}(\lambda_0)}{\lambda_0^2}\right]= \\ &= -\frac{\Delta\Phi_0}{\lambda_0}\left[1-\frac{\lambda_0\left(d\Delta n_{eff}(\lambda)/d\lambda\big|_{\lambda=\lambda_0}\right)}{\Delta n_{eff}(\lambda_0)}\right].\end{aligned} \tag{4.7}$$

At this point, Eq. (4.7) can be simplified by taking into account the definition of the group index, which is recalled below for the convenience of the reader:

$$n_g(\lambda)=n_{eff,r}(\lambda)-\lambda\frac{dn_{eff,r}(\lambda)}{d\lambda}, \tag{4.8}$$

$$\left.\frac{d\Delta\Phi(\lambda)}{d\lambda}\right|_{\lambda=\lambda_0}=-\frac{\Delta\Phi_0}{\lambda_0}\frac{\Delta n_g(\lambda_0)}{\Delta n_{eff}(\lambda_0)}, \tag{4.9}$$

where Δn_g is the difference between group indexes of the fundamental modes supported by each PS arm. From Eq. (4.9), it seems clear that a null wavelength dependence near the design wavelength can be achieved when the group indexes have the same value. Nevertheless, this condition can only be fulfilled for very narrow waveguides as shown in Fig. 4.3, where the group index of a Si wire waveguide is calculated at the typical telecom wavelength of $\lambda_0 = 1.55$ µm. This solution has a reduced applicability in practice, as explained hereunder:

- Any small variation in the waveguide widths considered for the design results in a large variation of the group index and the condition for wavelength independence is no longer fulfilled, i.e. $\Delta n_g \neq 0$.
- In addition, such narrow waveguides are not usually used for fabricated devices due to high propagation losses, exceeding 30 dB/cm waveguide widths below 400 nm [Dumon'04].

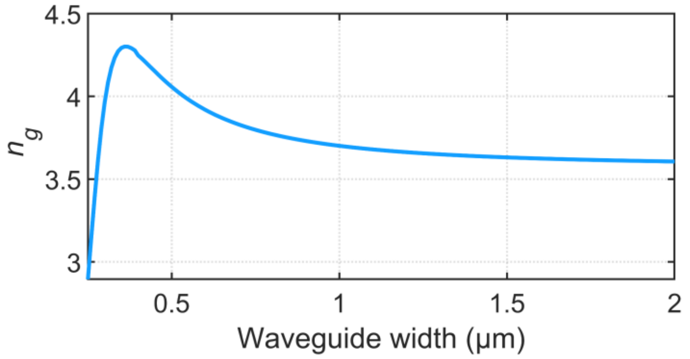

Figure 4.3. *Group index of the fundamental mode as a function of the waveguide width calculated at the wavelength of 1.55 µm for the SOI platform with a 220-nm-thick Si waveguide.*

On the contrary, tolerances to fabrication errors depend on the variation experienced by the real part of the effective indexes with respect to changes in width, i.e. $dn_{eff,r}/dW$. The slope of both waveguides acquires similar values for waveguides widths greater than 1 µm (see Fig. 4.4), resulting in an improved resilience to typical over- and under-etching errors that may arise during the fabrication process.

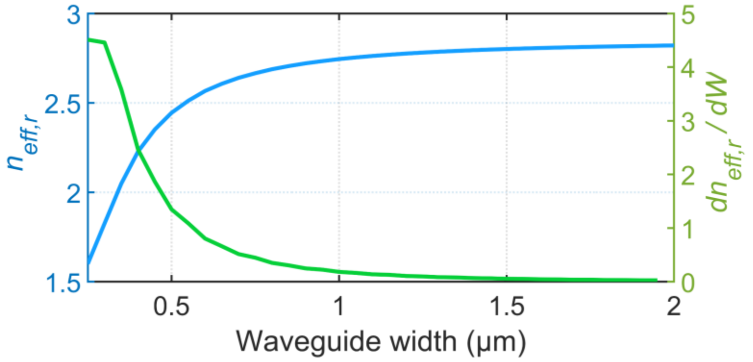

Figure 4.4. *Real part of the effective index (blue curve) as a function of the waveguide width calculated at the wavelength of 1.55 µm for the SOI platform with a 220-nm-thick Si waveguide. The green curve represents the slope of the real part of the effective index ($dn_{eff,r}/dW$).*

Additionally, for wide waveguides, Eq. (4.9) can be further simplified. Assuming the widths of the waveguides are sufficiently wide to hold paraxiality condition [Soldano'95], the propagation constant of the fundamental modes supported by these waveguides can be approximated as:

$$\beta(\lambda) \approx k_0 n_c - \frac{\pi\lambda}{4 n_c W_e^2}, \qquad \textbf{(4.10)}$$

where n_c represents the effective index of the equivalent 2D waveguide, k_0 stands for the wavenumber and W_e denotes the effective width of the waveguide. It is important to mention that the wavelength dependence of the effective waveguide width is much smaller than the physical waveguide width because modes are strongly confined in wide waveguides. Hence, W_e can be assumed to be invariant with the wavelength as in [Soldano'95, Halir'16]. From Eq. (4.10), the effective index is calculated straightforwardly:

$$n_{eff,r}(\lambda) \approx n_c - \frac{\lambda^2}{8 n_c W_e^2}. \qquad \textbf{(4.11)}$$

And the effective index difference of the modes propagated through both arms of the PS with wide arms is given by:

$$\Delta n_{eff}(\lambda) = \frac{\lambda^2}{8 n_c W_{e,L}^2} - \frac{\lambda^2}{8 n_c W_{e,U}^2}, \qquad \textbf{(4.12)}$$

with $W_{e,U}$ and $W_{e,L}$ being the effective width of the upper and lower arms, respectively. Taking the derivative of Eq. (4.12):

$$\frac{\Delta n_{eff}(\lambda)}{d\lambda} = \frac{\lambda}{4 n_c}\left(W_{e,L}^{-2} - W_{e,U}^{-2}\right). \qquad \textbf{(4.13)}$$

Finally, replacing Eqs. (4.12) and (4.13) in Eq. (4.7), the dependence on wavelength remains as:

$$\left.\frac{d\Delta\Phi(\lambda)}{d\lambda}\right|_{\lambda=\lambda_0} = \frac{\Delta\Phi_0}{\lambda_0}. \qquad \textbf{(4.14)}$$

A major conclusion that can be drawn for the theoretical analysis carried out in this subsection is that conventional PSs based on waveguides of equal lengths cannot be tolerant to fabrication deviations and have a wavelength-independent response simultaneously. Furthermore, the response of the phase shift error (defined in section 3.3.2 for the designed 90° PS) is approximately linear with a slope given by Eq. (4.14). By way of example, the same 90° PS designed in the previous chapter can be implemented by means of two parallel wide waveguides to improve the tolerances to fabrication errors; however, the phase slope would be $d\Delta\Phi(\lambda)/d\lambda \approx 58°/\mu\text{m}$ at the wavelength of 1.55 µm. Note that as the target phase shift increases so does the slope of the PS response.

4.2.2. Dispersion and anisotropy engineering using SWG waveguides

The performance of the PS studied in the previous subsection is intrinsically limited by the degrees of freedom in the design provided by non-periodic waveguides. To overcome this constraint, the extended design space of SWG waveguides can be leveraged to further improve the performance by means of anisotropy and dispersion engineering. Figure 4.5 shows a phase shifting section based on two SWG waveguides of equal length. Similar to the conventional counterpart, the widths of the upper and lower arms are W_U and W_L, respectively, whereas the pitch and the duty cycle have been selected to be the same for simplicity.

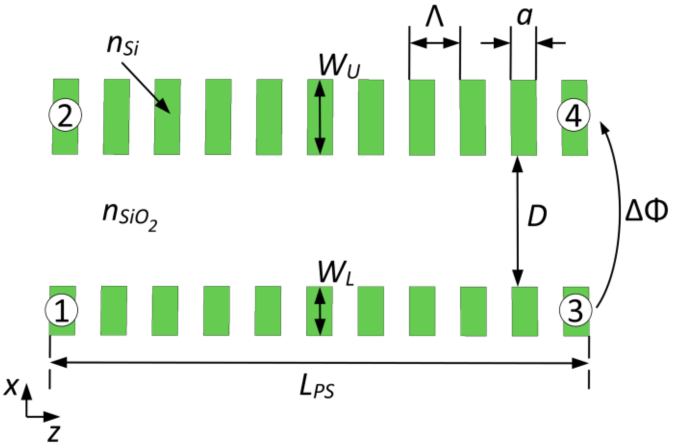

Figure 4.5. *Schematic top view of a passive PS consisting of two parallel SWG waveguides with the same length (L_{PS}), period (Λ) and duty cycle (a/Λ), and different widths (W_U and W_L). The waveguides are separated a distance D, which avoids any power coupling between them.*

The analytical study of this phase shifting structure is conducted by modelling SWG waveguides as equivalent 2D anisotropic media (see section 2.3.3 for a detailed explanation). In this case, the refractive index tensor is described as:

$$\mathbf{n}_{\mathbf{eq}} = \mathrm{diag}\left[n_{xx}, n_{zz}\right]. \tag{4.15}$$

In an anisotropic medium, the effective index of the fundamental Floquet-Bloch modes propagating through the SWG waveguides can be approximated to the following expression when the modes are well confined, i.e. for wide waveguides [Halir'16]:

$$n_{eff}(\lambda) \approx n_{xx} - \frac{\lambda^2 n_{xx}}{8W_e^2 n_{zz}^2}. \qquad \textbf{(4.16)}$$

The phase shift induced between the lower and upper arms is obtained by inserting the effective indexes of the corresponding Floquet-Bloch modes in Eq. (4.4):

$$\Delta\Phi_{SWG}(\lambda) \approx \frac{\pi\lambda n_{xx}}{4n_{zz}^2}\left(W_{e,L}^{-2} - W_{e,U}^{-2}\right)L_{PS}. \qquad \textbf{(4.17)}$$

The wavelength dependence of Eq. (4.17) can be mitigated by judiciously selecting the values of the pitch and duty cycle of the SWG waveguides in order to modify the values of the refractive index tensor. Following the same rationale as in [Halir'16], the term n_{xx}/n_{zz}^2 can be engineered to compensate wavelength variations and achieve an almost zero phase slope. Mathematically, the explanation is as follows. The variation with the wavelength of a PS composed of wide waveguides is given by Eq. (4.7), thereby it is first necessary to obtain the difference between the effective indexes of the Floquet-Bloch modes propagating along the upper and lower SWG arms:

$$\Delta n_{eff}(\lambda) \approx \frac{\lambda^2 n_{xx}}{8n_{zz}^2}\left(W_{e,L}^{-2} - W_{e,U}^{-2}\right). \qquad \textbf{(4.18)}$$

Since n_{zz}^2/n_{xx} is engineered to be proportional to λ, the term to $\lambda n_{xx}/n_{zz}^2$ can be approximated as a constant C, and Eq. (4.18) is simplified to:

$$\Delta n_{eff}(\lambda) \approx C\frac{\lambda}{8}\left(W_{e,L}^{-2} - W_{e,U}^{-2}\right). \qquad \textbf{(4.19)}$$

The derivative of the previous Eq. (4.19) can be straightforwardly calculated as:

$$\frac{\Delta n_{eff}(\lambda)}{d\lambda} \approx C\frac{1}{8}\left(W_{e,L}^{-2} - W_{e,U}^{-2}\right). \qquad \textbf{(4.20)}$$

And replacing Eqs. (4.19) and (4.20) in Eq. (4.7), the phase slope of the SWG PS yields an approximate value of zero:

$$\left.\frac{d\Delta\Phi_{SWG}(\lambda)}{d\lambda}\right|_{\lambda=\lambda_0} \approx -\frac{\Delta\Phi_0}{\lambda_0}\left[1 - \frac{C\frac{\lambda_0}{8}\left(\frac{1}{W_{e,L}^2} - \frac{1}{W_{e,U}^2}\right)}{C\frac{\lambda_0}{8}\left(\frac{1}{W_{e,L}^2} - \frac{1}{W_{e,U}^2}\right)}\right] \approx 0. \qquad \textbf{(4.21)}$$

The key aspect here is that the dependence with the wavelength can be mitigated regardless of whether it is a relative maximum, a relative minimum, an inflection point or a point at which the function is constant. The extension of this approximation depends on the values of Λ and DC selected, which modify the values of n_{xx} and n_{zz} [Halir'16]. This result will be subsequently verified by both simulation and experimental results.

4.3. Design of our proposed phase shifter and comparison with other passive alternatives

The design of the proposed passive PSs is described in this section considering an SOI platform with 220-nm-thick silicon waveguides surrounded by a SiO_2 upper and lower layers. A passive PS based on two back-to-back tapers was already designed in the previous chapter in order to induce a +90° phase shift between the lower and the upper arms for the proposed mode converter and MUX/DEMUX (see subsection 3.3.2). The geometrical parameters of this tapered PS will be taken as a reference in this section. Accordingly, interconnection waveguides with a typical width of $W_I = 500$ nm and a separation of $D = 1.5$ µm are selected. First, the design of the tapered PS is briefly revisited in the following subsection to show its performance and tolerance to fabrication errors within the 400 nm wavelength range (1.35 – 1.75 µm) considered for the design. Subsequently, the design of the asymmetric PS and the SWG asymmetric PS can be found for TE polarization. Finally, the performance and tolerances to fabrication errors of the three designed PSs are compared.

4.3.1. 90° tapered phase shifter

The scheme of the tapered PS is replicated in Fig. 4.6a for the convenience of the reader. The design is exactly the same as in section 3.3.2, achieving a +90° phase shift at design wavelength of 1.55 µm when the total length of the PS is $L_{PS} = 3.41$ µm and the taper width is $W_{PS} = 700$ µm.

To obtain the PSE as a function of the wavelength, a FEM simulator [FemSIM'19] was used to calculate the effective index of the fundamental mode for the different waveguide widths that make up the structure at different wavelengths covering from 1.35 µm to 1.75 µm. Over- and under-etching errors that usually occur during the fabrication process were modelled as absolute width variations of $\Delta\delta = \pm 20$ nm. The results obtained for the nominal and the biased structures are depicted in Fig. 4.6b.

Two important conclusions can be drawn from the simulation results. Firstly, as expected, PSE linearly increases when moving away from the central wavelength. Secondly, fabrication deviations result in a vertical offset of the PSE curve. A detailed analysis of the results will be carried out in section 4.3.3, in which the performance of the three designed PSs (tapered, asymmetric and SWG asymmetric PSs) will be compared.

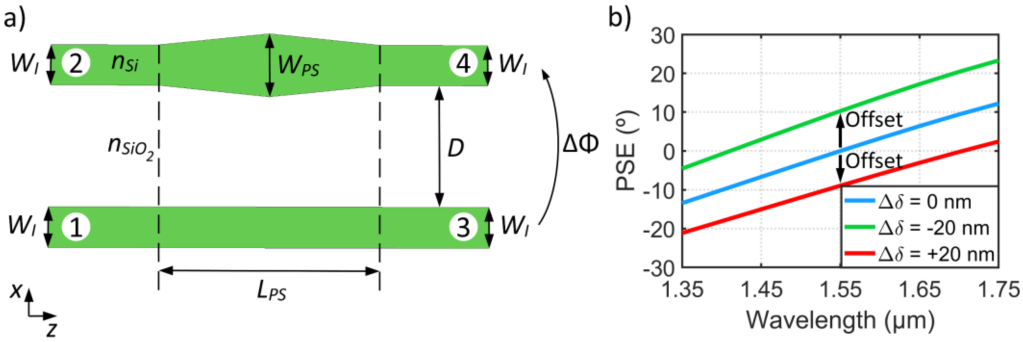

Figure 4.6. *(a) Schematic top view of a state-of-the-art 90° phase shifter based on two tapers in back-to-back configuration (upper arm) and a straight waveguide (lower arm). (b) Phase shift error of the designed PS as a function of the wavelength (blue curve). Width deviations of -20 nm (in green) and +20 nm (in red) are also represented, which result in a vertical offset of the PSE curve.*

4.3.2. 90° asymmetric phase shifter

The asymmetric PS shown in Fig. 4.7a relies on a phase shifting section formed by two parallel waveguides of different widths (W_U and W_L). In order to provide enhanced resilience against fabrication errors, the width of both waveguides must be wider than 1 µm as stated in Fig. 4.4. Therefore, a minimum width of $W_L = 1.6$ µm was selected for the lower arm. To maintain consistency with the design of the tapered PS, the width of the upper arm was chosen to be $W_U = 1.8$ µm, yielding a width difference of 200 nm between the upper and lower waveguides. Additionally, the asymmetric PS requires adiabatic tapers to connect the phase shifting section with the interconnection waveguides of width $W_I = 500$ nm. Two tapers in back-to-back configuration were simulated via 3D FDTD [FullWAVE'19] to obtain the minimum taper length that achieves negligible insertion loss and, at the same time, minimizes the phase shift introduced. A small length of only $L_T = 3$ µm was obtained at the design wavelength of 1.55 µm, ensuring that the minimum power transmitted is above 95% and the phase shift is below 4° for the pairs of tapers placed at the input or at the output. The small phase shift introduced by the tapers was taken into account to design the length of the phase shifting section, being subtracted from the target 90° phase shift. To this end, FEM calculations [FemSIM'19] were performed in a similar way to the tapered PS design, attaining a length of $L_{PS} = 36.19$ µm. The asymmetric PS has a total length of 42.19 µm to attain a +90° phase shift between the lower and upper arms at the wavelength of 1.55 µm.

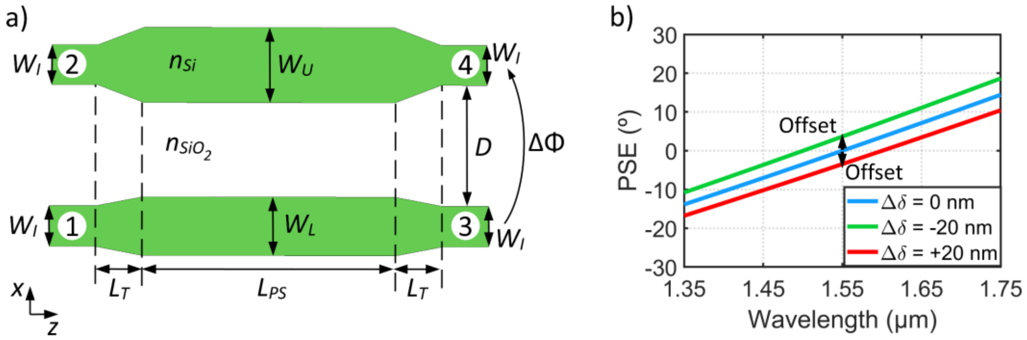

Figure 4.7. *(a) Schematic top view of a state-of-the-art 90° phase shifter based on two non-periodic waveguides of dissimilar widths. (b) Phase shift error of the designed PS as a function of the wavelength (blue curve). Width deviations of -20 nm (in green) and +20 nm (in red) are also represented, which result in a vertical offset of the PSE curve.*

Once the length of the structures was fixed, tolerances to fabrication errors of the complete structure (phase shifting section with input and output tapers) were simulated via FEM by introducing width variations of $\Delta\delta = \pm 20$ nm. The phase shift error as a function of the wavelength is depicted in Fig. 4.7b for the nominal design (blue curve), and width deviations of $\Delta\delta = -20$ nm (green curve) and $\Delta\delta = +20$ nm (red curve). As it can be observed from the simulation results, the vertical offset is indeed reduced compared to the tapered PS, proving that asymmetric PSs based on wide waveguides are more robust to fabrication errors than the tapered counterpart based on narrow waveguides. However, the wavelength response is still narrowband.

4.3.3. 90° asymmetric SWG phase shifter

In this thesis, we propose to leverage the extended design space provided by SWG waveguides to enhance simultaneously the narrow wavelength response and the tight fabrication tolerances presented by state-of-the art PSs. Conventional non-periodic waveguides of the phase shifting section are now replaced by SWG waveguides as shown in Fig. 4.8a. The proposed asymmetric SWG PS also comprises SWG tapers to perform an adiabatic transition between the non-periodic interconnection waveguides (width W_I) and the SWG waveguides (widths W_U and W_L).

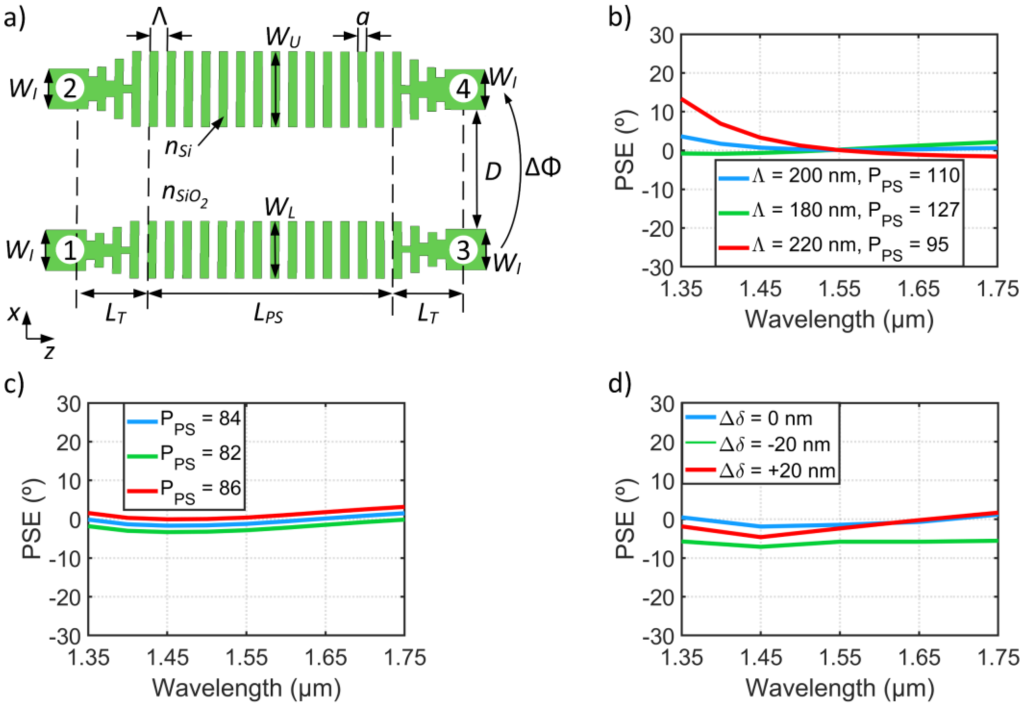

Figure 4.8. *(a) Schematic top view of the proposed 90° phase shifter based on two SWG waveguides of dissimilar widths. (b) Phase shift error of the two parallel SWG waveguides as a function of the wavelength (SWG tapers not included). The duty cycle is fixed at 50% and different pitchs were explored, each with an optimum number of periods ($L_{PS} = P_{PS}\cdot\Lambda$). (c) Phase shift error as a function of the wavelength of the complete asymmetric SWG PS (SWG tapers included). (d) 3D FDTD simulations for the nominal design (blue curve) and fabrication errors of $\Delta\delta = -20$ nm (green) and $\Delta\delta = +20$ nm (red).*

The design of this subwavelength engineered PS consists of three distinct parts, which are described in detail hereafter:

- First, the design of the parallel waveguides of width W_U and W_L is carried out by means of Floquet-Bloch calculations [Wangüemert-Pérez'14]. The same widths as for the asymmetric PS have been chosen, i.e. $W_U = 1.8$ μm and $W_L = 1.6$ μm, to maintain consistency and to be able to compare the performance of both designs at a later stage. The duty cycle was kept at 50% to maximize the minimum feature size contemplating the fabrication, and several pitch values were analyzed. For each pitch value, the number of periods P_{PS} needed to induce a +90° phase shift between the lower and upper arms was calculated at the design wavelength of 1.55 µm. As observed in Fig. 4.8b, a maximally flat PSE response can be achieved for $\Lambda = 200$ nm, ensuring 100 nm of minimum feature size and yielding a length of $L_{PS} = P_{PS} \cdot \Lambda = 22$ µm. It is important to mention that the length of the wide SWG waveguides must be shorter than 30 µm to avoid jitter problems [Ortega-Moñux'17]. In case the latter condition is not fulfilled, the difference in width between the upper and lower arms must be increased.

- Second, the SWG tapers are designed in order to perform an adiabatic transition between input/output non-periodic waveguides and wide SWG waveguides. 3D FDTD simulations [FullWAVE'19] of the tapers in back-to-back configuration were carried out to obtain insertion losses as a function of the length of the tapers L_T, yielding negligible losses for the same taper length as for the asymmetric PS, i.e. $L_T = 3$ µm. In order to obtain the PSE response of the complete SWG PS (see Fig. 4.8c), the phase shift introduced by SWG tapers (~20°) is deducted from the target 90° phase shift and the number of periods of the two SWG waveguides is recalculated. For the geometrical parameters chosen in the previous point, the resolution with which the PSE response can be adjusted is approximately 0.8° per period of the SWG waveguide at $\lambda_0 = 1.55$ µm. A PSE close to 0° is attained for $P_{PS} = 84$ periods, being the total length of the proposed SWG PS as small as 22.8 µm.
- Finally, the complete structure was simulated via 3D FDTD [FullWAVE'19] to perform a tolerance study. The differences between the Floquet-Bloch calculations (including the 3D FDTD response of the SWG tapers) shown in Fig. 4.8c and the 3D FDTD simulations of the complete SWG PS in Fig. 4.8d are minimal, demonstrating that Floquet-Bloch calculations are fast and suitable approach for the design of this type of structures. On the other hand, fabrication errors were modeled taking into account both variations in width and in the duty cycle (in the same way as was done for SWG MMI in section 3.3.4). Figure 4.8d shows that the flat response of the asymmetric SWG PS is maintained even for errors up to $\Delta\delta = \pm 20$ nm.

4.3.4. Performance comparison

In order to facilitate comparison between the PSs designed in the previous subsections, the simulated PSE for each device is shown in Fig. 4.9a as a function of the wavelength. One can immediately realise that the proposed asymmetric SWG PS yields an outstanding flat response compared to its conventional counterparts. The PSE of the subwavelength engineered PS (represented in blue) is practically zero in the entire 400 nm simulated bandwidth, with phase deviation of less than ±1.7°. On the contrary, PSs based on non-periodic waveguides present a similar PSE response, with a PSE $< \pm 14.4°$ for the asymmetric PS (green curve) and a PSE $< \pm 13.5°$ for the tapered PS (red curve). Near the design wavelength ($\lambda_0 = 1.55$ µm), the phase slope of both PSs is approximately the same as predicted by the theory set forth in subsection 4.2.1. In the wavelength range from 1.35 µm to 1.75 µm, the calculated phase slope is ~64°/µm and ~71°/µm for the tapered PS and the asymmetric PS, respectively.

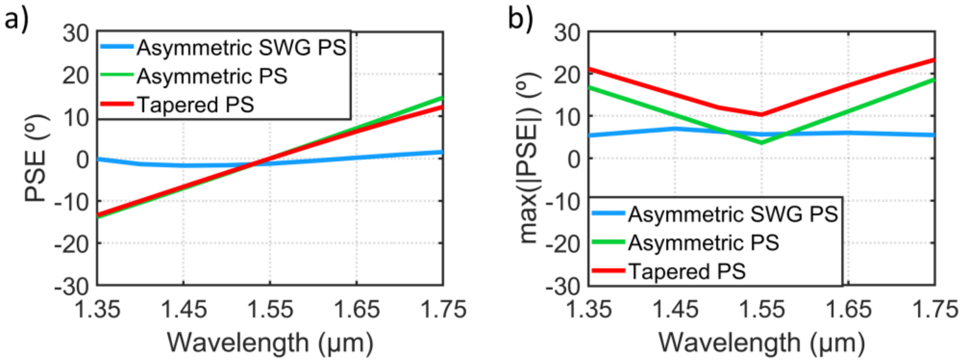

Figure 4.9. *(a) Comparison of the simulated PSE of the asymmetric SWG PS (blue curve), the asymmetric PS (green) and the tapered PS (red). (b) Worst PSE in absolute value between PSE(Δδ = +20 nm) and PSE(Δδ = -20 nm). Blue curve corresponds to the asymmetric SWG PS, green curve to the asymmetric PS and red curve to the tapered PS.*

Regarding the tolerances to fabrication errors, the two curves of each PS (i.e. $\Delta\delta = +20$ nm and $\Delta\delta = -20$ nm), have been unified into a single curve in Fig. 4.9b considering the worst case for each wavelength:

$$\max\left(\left|\mathrm{PSE}\right|\right) = \max\left[\left|\mathrm{PSE}\left(\Delta\delta = +20\,\mathrm{nm}\right)\right|, \left|\mathrm{PSE}\left(\Delta\delta = -20\,\mathrm{nm}\right)\right|\right]. \qquad \textbf{(4.22)}$$

As expected, the tapered PS presents the worst fabrication tolerances due to the narrow waveguides, yielding a maximum phase deviation of 23.3° within the simulated wavelength range. The asymmetric PS considerably improves the robustness at the center wavelength ($\lambda_0 = 1.55$ µm) but at the edge of the band the PSE increases up to 18.7°. Conversely, the proposed SWG PS exhibits a flat response with a phase deviation of only 7.1° within the 400 nm wavelength range. This entails a reduction of the PSE of more than two and a half times compared to the conventional PSs based on non-periodic waveguides.

4.4. Fabrication and experimental characterization

The fabrication of the proposed ultra-broadband SWG PS was carried out in close collaboration with the UMA and the NRC in the same commercial foundry in which the mode converter and MUX/DEMUX was fabricated for the second time [AppliedNanotools'19]. This section is intended to explain the test structures used for the characterization of the fabricated PSs and the procedure followed to perform the phase measurements.

4.4.1. Test structures

The characterization of the designed PSs is not straightforward, as measurements cannot be performed directly from the stand-alone fabricated devices, unlike in the field of microwaves, where this type of measurements is made by a vector network analyzer that requires directional couplers and precise calibration standards [Lewandowski'16]. Since there is no equivalent method in photonics to perform phase measurements to date, the phase difference induced by the PSs was extracted using a Mach-Zehnder interferometer (MZI) as a test structure. Only the proposed asymmetric SWG PS and the tapered PS were included in the masks due to space restrictions on the chip that was fabricated. Tapered PSs were considered instead of asymmetric PSs due to the fact that the former present a more compact footprint and slightly better bandwidth response, being a solution more commonly used for PICs.

The structure of the test MZI is schematically shown in Figs. 4.10a and 4.10b for the SWG PS and the tapered PS, respectively. This test structure comprises two beam splitters connected through 14 PSs. SWG MMIs were selected for the beam splitters in order to avoid limitations in terms of insertion loss, imbalance and phase error over the entire operating bandwidth of the PSs (see section 3.3.1). The principle of operation of the structure is as follows:

- The fundamental mode injected through port 1 is evenly divided in amplitude by the SWG MMI, but a phase difference is induced between the lower and upper arms, i.e. $\Delta\Phi_{\mathrm{AB}} = \Phi_{\mathrm{A}} - \Phi_{\mathrm{B}} = -90°$.
- Each of the PSs (either the SWG PS or the tapered PS) induce an additional 90° phase shift between the lower and upper arms. At this point, it is important to clarify that all the phase shifts are always calculated throughout this thesis between the lower and the upper arms and a change in the reference, i.e. calculated between the upper and lower arms, implies a change in the sign. Therefore, a total phase shift of 1260° is achieved by the 14 PSs,

which combined with the phase shift induced by the first SWG MMI results in $\Delta\Phi_{\mathrm{CD}} = \Phi_{\mathrm{C}} - \Phi_{\mathrm{D}} = 90°$ (wrapped to the interval 0 – 360°), being the fundamental mode coupled to the output port 3.

- Similarly, when the fundamental mode is injected through port 2, it is equally split by the first SWG MMI and the induced phase shift is $\Delta\Phi_{\mathrm{AB}} = \Phi_{\mathrm{A}} - \Phi_{\mathrm{B}} = 90°$. After the PSs' section the total phase shift is $\Delta\Phi_{\mathrm{CD}} = \Phi_{\mathrm{C}} - \Phi_{\mathrm{D}} = 270°$ (wrapped to the interval 0 – 360°) and the fundamental mode is extracted through output port 4.

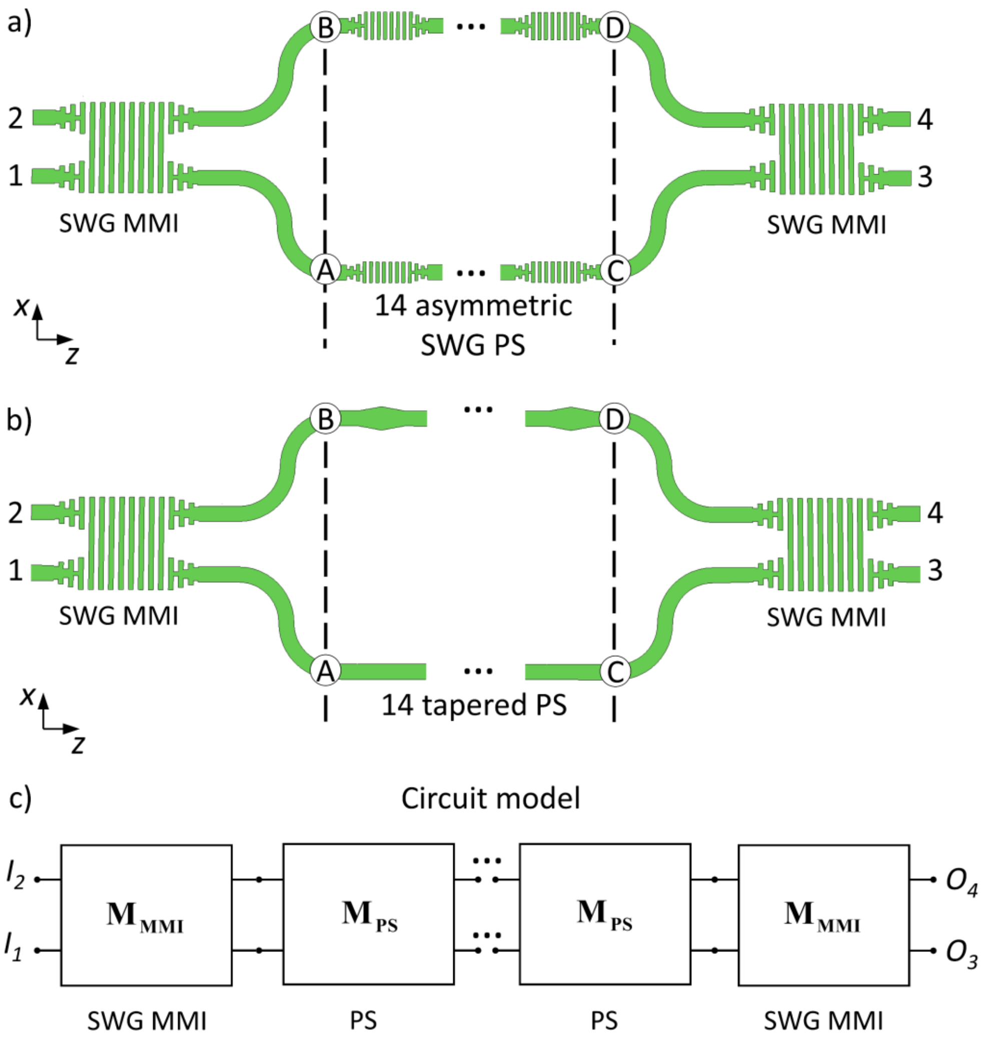

Figure 4.10. *Schematic top view of the test structures used for the characterization of (a) the proposed asymmetric SWG PS and (b) the conventional tapered PS. (c) Representation of the circuit model of the test structure using transmission parameters.*

The key concept of the MZI as test structure is that the intensity signal at the output is modulated based on the imbalance between the arms. Thereby, output power is maximized at port 3 when the fundamental mode is injected through port 1 at the design wavelength of $\lambda_0 = 1.55$ µm. As the wavelength deviates from λ_0, the PSE introduced by each PS is multiplied by 14 and the measured power starts to oscillate from the output port 3 to the output port 4. Therefore, the greater the phase slope of the PSs, the faster the power varies between output ports. On the contrary, a smaller slope of the PS implies that the variation of the wavelength must be larger to make the power to oscillate from output port 3 to 4.

Fabrication errors, on the other hand, introduce a vertical offset in the PS response without hardly varying its slope as illustrated in the previous section (see Figs. 4.6b and 4.7b). In the MZI, this effect leads to a change in the wavelength at which the maximum power exits through the corresponding port (i.e. the response of the MZI experiences a horizontal wavelength shift). These two concepts are fundamental to successfully model the MZI circuit and extract the phase difference induced by each of the PSs.

The detailed circuit model developed for this characterization can be found in Appendix B.

4.4.2. Fabrication and measurements

The mask containing the test structures presented in the previous section was drawn in AutoCAD using the same Visual Basic library that was employed for the mode converter and MUX/DEMUX (see subsection 3.4.1). Geometrical parameters of the asymmetric SWG PS and the tapered PS were taken as specified in the design sections 4.3.2 and 4.3.1, respectively. Regarding the SWG MMI, geometrical parameters were taken from the design of the mode converter and MUX/DEMUX (see section 3.5). Different designs of the test structures were included in the mask, varying the number of periods of the SWG MMI, the number of periods of the asymmetric SWG PS and the length of the tapered PS.

The devices were fabricated on a 220-nm-thick SOI platform with a 2-µm-thick BOX in the same commercial foundry in which the mode converter and MUX/DEMUX was fabricated for the second time [AppliedNanotools'19]. E-beam lithography was used to pattern the Si layer, and etching was performed through ICP-RIE process. SEM images of the fabricated SWG and tapered PSs are shown in Figs. 4.11a and 4.11b respectively. The period jitter of the SWG structure was measured from Fig. 4.11a, yielding almost negligible variations of 3 nm in the period. The length of the tapered PS was measured to be ~3.35 µm, showing a slight reduction from its nominal value. The 2.2-µm-thick SiO_2 upper cladding (same thickness as the one used for the mode converter and MUX/DEMUX in the second fabrication run) was deposited after taking the SEM images by CVD.

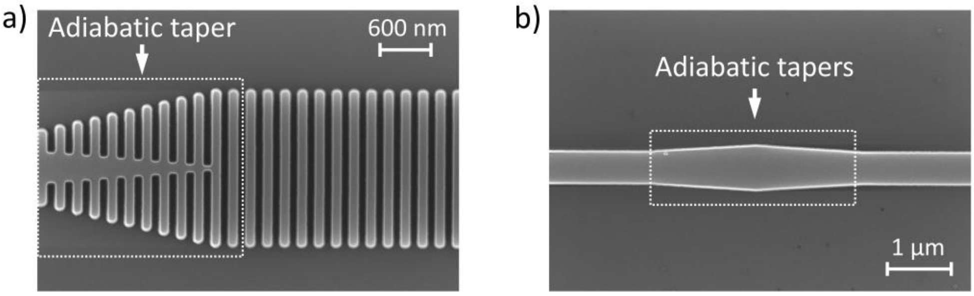

Figure 4.11. *Scanning electron microscope images of (a) the asymmetric SWG PS and (b) the tapered PS.*

The fabricated MZI test structures were characterized in the laboratories of the UMA using the same setup as described in subsection 3.4.2 of the previous chapter. The light was coupled into input port 1 and collected from output ports 3 and 4 sequentially via high-performance SWG fiber-chip couplers [Cheben'06, Cheben'10, Cheben'15]. The best performance was obtained for designs with geometric parameters close to the nominal design values, i.e. $L_{PS} = 3.41$ µm and $P_{PS} = 86$ periods.

The measured transmittance normalized with respect to the transmission of a reference waveguide is shown in Figs. 4.12a and 4.12b for the MZI composed of 14 SWG PSs and 14 tapered PSs, respectively. Theoretically the light coupled into input port 1 is expected to exit through output port 3 at the wavelength of 1.55 µm (i.e. the light blue curve should be at a maximum and the light green curve at a minimum). This behavior is not observed for any of the interferograms presented in Fig. 4.12, indicating that over- or under-etching errors occurred during the fabrication. Nevertheless, a fundamental point that can be inferred from both graphs is that the variation with the wavelength is smaller for the MZI based on 14 SWG PS compared to the MZI based on 14 tapered PS. This first assessment indicates that indeed the phase shift introduced by the SWG PSs has a lower wavelength dependence compared to tapered PSs.

In order to quantify this assessment, SWG MMIs were first measured yielding EL $<$ 0.6 dB, IB $<$ 1 dB and PE $<$ 5° within the measured 145 nm wavelength range of the measurement setup (1.495 – 1.64 µm). This data was incorporated to the transmission matrix of the SWG MMIs, whereas data from 3D FDTD simulations were used to build the transmission matrix of the PSs (Appendix B for details). Then, results obtained with the circuit model were fitted to the measured spectra by adjusting a variable error offset. The final result fit is represented in Fig. 4.12 with dark blue and dark green curves, being the phase shift introduced by fabrication determined to be 6° for the SWG PS and -6.5° for the tapered PS. The latter is in accordance with the shorter length measured in the SEM image.

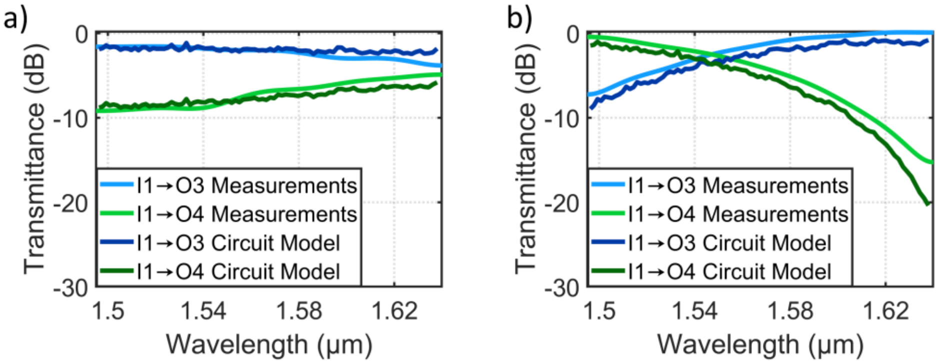

Figure 4.12. *Measured spectra of the MZI test structures with (a) 14 asymmetric SWG PSs and (b) 14 tapered PSs. The fitting of the developed circuit model is also shown by dark blue and dark green curves.*

The resulting PSEs extracted from the circuit model are shown in Fig. 4.13 for the SWG PS and the tapered PS (solid curves), showing a great agreement with the 3D FDTD simulation results (dotted curves). A phase slope of 63°/µm was measured for the tapered PS, very closely matching the 64°/µm obtained in the design section. Conversely, a phase slope of only 16°/µm was measured for the SWG PS, yielding a nearly four-fold reduction within the measured 145 nm wavelength range. Small ripples observed in the experimental curves are due to phase errors introduced by the SWG MMIs and the limitations of the method used for calculating the PSE, although their value is less than 0.5° for the case of the proposed SWG PS.

It should be noted that the response of the SWG PS is designed to be maximally flat in a 300 nm bandwidth, which does not impose a 0° value for the wavelength of 1.55 µm. Furthermore, owing to the measurement setup limitation, it was not possible to characterize the response for lower wavelengths and it would be interesting to verify that the flat PSE is maintained. Nevertheless, the results serve as experimental proof that the proposed PS mitigates wavelength dependence by means of anisotropy and dispersion engineering using SWG waveguides.

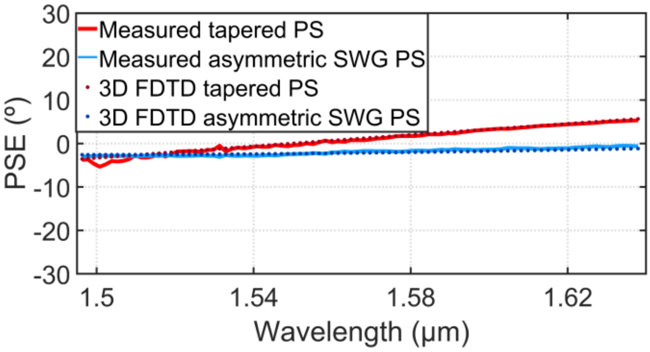

Figure 4.13. *Measured PSE of a single PS (solid lines) compared to simulated 3D FDTD results (dotted lines).*

Finally, the experimental results of the proposed SWG PS are shown in Table 4.1 by way of comparison with other state-of-the-art active and passive PSs. Even though, most passive PSs have not been experimentally demonstrated, the subwavelength engineered PS still exhibits a better measured performance than other state-of-the-art passive PS with minimal insertion losses and a compact footprint of less than 24 μm × 3.7 μm.

Table 4.1. *Comparison of state-of-the-art active (A) and passive (P) PSs fabricated using different technologies. Values with an asterisk correspond to experimental results.*

Reference	Structure/Technol.	IL (dB)	Phase (°)	PSE (°)	BW (nm)
[Harris'14]* (A)	Thermo-optic/SOI	0.23	–	–	–
[Ikeda'10]* (A)	MEMS/SOI	1	0–540	–	–
[Jeong'10] (P)	Tapered PS/GaInAsP	0.1*	45	< ±2	70
[González-Andrade'18] (P)	Tapered PS/SOI	–	90	< ±5	110
[Morrissey'15] (P)	MMI/InP	0.7	180	< ±10	100
[Morrissey'15] (P)	MMI/Si	1.25	90	< ±13	100
[Han'15] (P)	MMI/SOI	0.22	90	–	–
This work (simulated) (P)	SWG/SOI	0.15	90	< ±1.7	400
This work* (measured) (P)	SWG/SOI	0.2	90	< ±3	145

4.5. Summary

Although active PSs have focused most of the scientific attention in recent years, new emerging applications require high-performance passive PSs in order to avoid the complexity of active control elements and power driving constraints. Among the different options to perform passive phase shifting, the architecture based on waveguides of equal length was studied and it was found that its limitation arises from the lack of degrees of freedom in the design. We proposed SWG structures to provide an extended design space that can be leveraged to improve both bandwidth and manufacturing error tolerances.

Three different passive PSs (tapered, asymmetric and our novel asymmetric SWG PSs.) were designed to carry out a comparison. Simulation results showed that tapered and asymmetric PSs have a similar wavelength-dependent response, but fabrication tolerances are improved for the asymmetric PS due to its comparatively wider waveguide. The proposed SWG PS exploits the inherent anisotropy of SWG waveguides to engineer the dispersion and compensate the wavelength dependence, and at the same time provides enhanced fabrication tolerances due to the use of wide waveguides.

Tapered and asymmetric SWG PS were fabricated on an SOI platform and a method based on a circuit model was developed to perform phase measurements over a broad bandwidth of 145 nm (1.495 – 1.64 μm), limited by the available light source of the experimental setup. The phase slope was measured from experimental PSE, and an almost four-fold reduction was attained by the proposed subwavelength engineered PS with regard to the conventional solution. Compared with the state of the art, the proposed SWG PS is one of the passive PSs based on waveguides of equal length with broadest bandwidth ever reported.

V

Ultra-broadband dual-polarization beam splitters

Splitting and combining light beams is another fundamental operation in many photonic systems. Although a myriad of different architectures has been reported to perform beam splitting since the beginning of integrated optics, performance improvements are continuously required on account of emerging cutting-edge applications and ever increasing performance requirements. In this chapter, a novel design strategy to implement high-performance beam splitters is presented. Specifically, ultra-broadband beam splitters with polarization-independent behaviour and improved fabrication tolerances are designed, fabricated and characterized. Section 5.1 discusses the performance limitations of state-of-the art beam splitters. Section 5.2 presents the developed design strategy and section 5.3 shows the experimental results achieved for a beam splitter fabricated on the SOI platform. In section 5.4 the design and implementation of another beam splitter on the SiN platform is detailed. A summary is given in section 5.5.

5.1. Limitations of state-of-the-art beam splitters

Optical beam splitters are a cornerstone element for optical power distribution in PICs, regardless of their top-level purpose and application field. These devices, also named power splitters or power dividers, have been intensively studied by the scientific community since the beginning of integrated optics in 1969, which has resulted in a plethora of different architectures reported hitherto. In particular, optical beam splitters based on the SOI platform face some important challenges due to the high refractive index contrast between silicon waveguides and the materials used for the top cladding layer or the bottom layer (see Appendix A). This high refractive index contrast results in three main limitations for the development of high-performance silicon beam splitters, which are the following:

- Tight fabrication tolerances, since small geometric variations have a greater impact on guided waveguide modes with a high confinement factor.
- Narrow bandwidths as a result of the strong modal dispersion of SOI waveguides.
- Single-mode operation owing to the high birefringence between TE and TM polarizations.

Different approaches have been proposed to perform on-chip power splitting for the fundamental mode, although each solution presents its own strengths and limitations in terms of performance. Among these architectures, directional couplers were one of the most used beam splitters due to their design simplicity [Marcatili’69, Trinh’95, Yamada’05]. This structure relies on a coupling region formed by two parallel waveguides placed close to each other (see Fig. 5.1a). The fundamental mode injected through one of the coupler arms excites the even and odd supermodes of the coupling region. The beat length between even and odd supermodes depends directly on the wavelength and also on the real part of their effective index, as described in Chapter II (see Eq. 2.26). Therefore, a low loss 50/50 coupler can be designed simply by establishing the physical length of the device as half the beat length. Other splitting ratios can be implemented in a simple manner by changing the length of the coupling region. Nevertheless, this mode-beating operation principle intrinsically limits the operation bandwidth, inasmuch as the splitting ratio condition is only fulfilled at a specific wavelength. Apart from bandwidth restrictions, conventional directional couplers only operate for a single polarization and present tight fabrication tolerances. For this reason, other alternatives such as bent directional couplers shown in Fig. 5.1b have been explored to further increase the bandwidth response up to ~110 nm for both TE and TM polarizations [Chen'17].

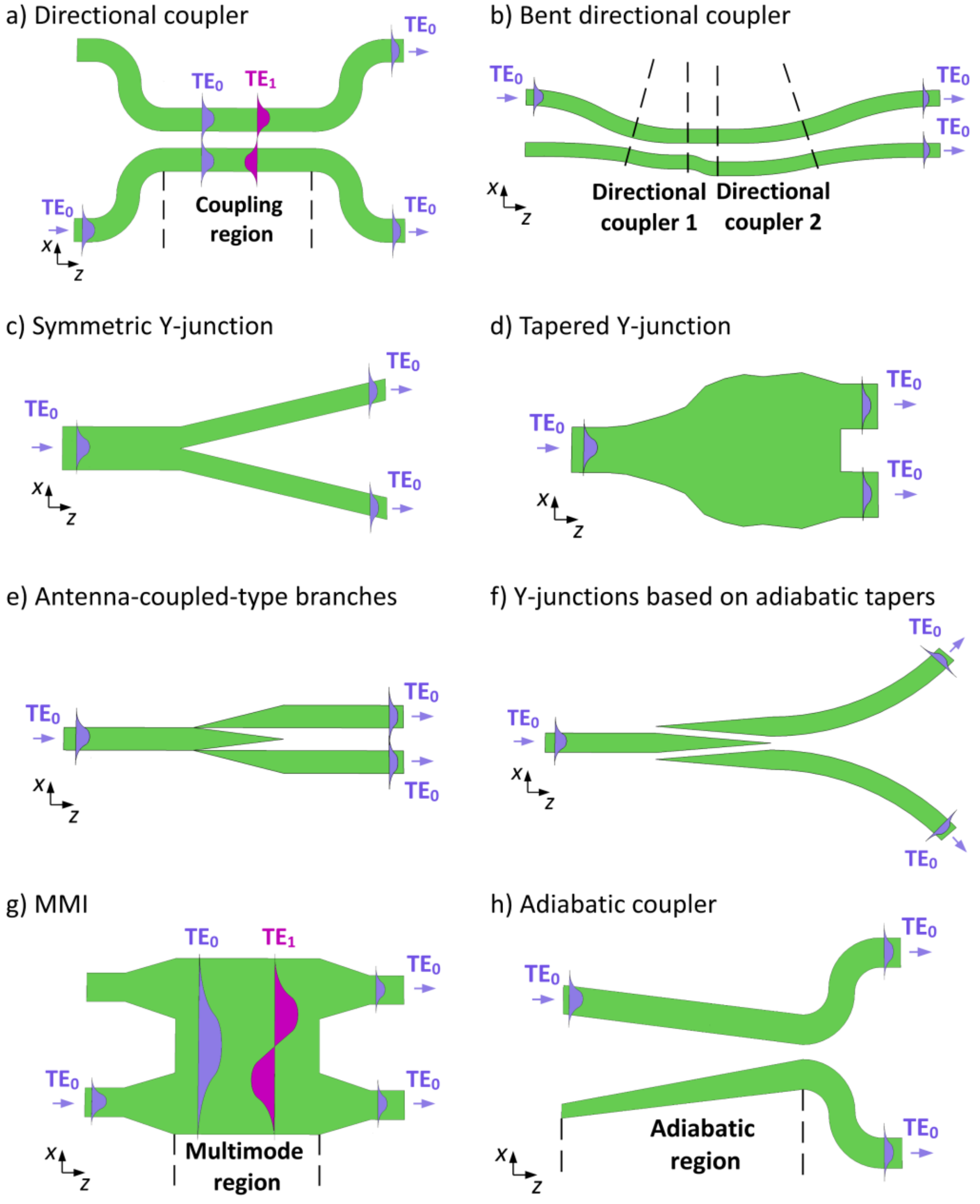

Figure 5.1. *Examples of state-of-the-art optical beam splitters. (a) Directional coupler, (b) bent directional coupler, (c) symmetric Y-junction, (d) tapered Y-junction, (e) antenna-coupled-type branches, (f) Y-junctions based on adiabatic tapers, (g) multimode interference coupler and (h) adiabatic splitter.*

Symmetric Y-junctions were intensively studied in the 1970s to overcome bandwidth and single-polarization operation of directional couplers [Yajima’73, Burns’75]. This architecture typically relies on a stem and two diverging arms as shown in Fig. 5.1c. The fundamental mode injected through the stem is equally divided into two fundamental modes of the arms due to the symmetry of the structure [Love’11]. Theoretically, the lack of beating between two or more modes results in low losses independently of the wavelength or polarization. However, the main limitations of this architecture arise when moving from theory to practice. The limited resolution of current fabrication processes results in a tip of finite dimensions between the junction of the arms as discussed in section 3.4.2. This abrupt discontinuity results in high insertion losses for the splitting of the fundamental mode. Different geometries have been proposed to circumvent this issue such as a tapered Y-junctions [Zhang’13], antenna-coupled-type branches [Sakai’02] and Y-junctions based on adiabatic tapers [Wang’16c] (see Figs. 5.1d, 5.1e and 5.1f).

More recently, MMI couplers have become mainstream in integrated optics to divide or recombine several light beams [Wei’01, Sheng’12, Yang’13]. This architecture is based on the Talbot effect or self-imaging principle, whereby the input field is reproduced in single or multiple images due to the beat between the fundamental and higher-order modes along the multimode section (see Fig. 5.1g) [Soldano’95]. A broader bandwidth and better fabrication tolerances can be achieved with MMI couplers compared to directional couplers, even though they typically operate for a single polarization. As stated in Chapter III, conventional MMIs based on non-periodic waveguides are also hampered by their mode-beating operation principle (see Eq. 3.1). In this case, self-images of the input field are formed in different positions of the multimode region for each different wavelength, which leads to significative performance degradation for bandwidths broader than ~150 nm.

SWG waveguides have been incorporated to directional couplers and MMIs in order to overcome the aforementioned bandwidth constraints. Dispersion and anisotropy can be engineered by judiciously selecting the values of the period and duty cycle of the SWG waveguides, mitigating the wavelength dependence as explained in sections 2.4.2 and 3.2 for the directional coupler and the SWG MMI, respectively. Experimental results show a low loss within a 100 nm wavelength range for the directional coupler [Wang’16a], whereas the SWG MMI presents an ultra-broadband behavior of 300 nm [Halir’16]. However, both devices operate only for a single polarization.

Other recently reported power splitters rely on adiabatic mode evolution of the even mode to avoid exciting the odd mode, or vice versa. A 2D schematic view of these devices is shown in Fig. 5.1h, where the adiabatic region tends to be hundreds of micrometers long to ensure an adiabatic transition. This solution has demonstrated slightly broader bandwidths than conventional MMIs for single- [Xing'13b, Tamazin'18] and dual-polarization operation [Yun'15, Xu'17] of up to ~160 nm at best. To reduce the length of conventional adiabatic couplers, SWG waveguides have been employed to design broadband single-polarization 3 dB couplers [Yun'16, Yun'18, Xu'18c].

Finally, architectures based on photonic crystal waveguides [Frandsen'04], star couplers [Rasigade'10] and inverse tapers [Li'13] have also been proposed but are limited either in terms of bandwidth or single-polarization operation. For example, the photonic crystal waveguide splitter [Frandsen'04] and the splitter based on inverse tapers [Li'13] exhibit low loss over a bandwidth of only 25 nm and 40 nm, respectively; whereas the star coupler beam splitter is a compact and robust solution but operates only for TE polarization [Rasigade'10]. Therefore, a fabrication-tolerant beam splitter with dual-polarization operation over an ultra-broad bandwidth is still sought for the next-generation of PICs.

5.2. Operation, design strategy and simulation results

5.2.1. Device operation and design

To overcome these limitations, a novel ultra-broadband and dual-polarization beam splitter (see Figure 5.2) was developed in collaboration with the C2N [González-Andrade'19]. The splitter is based on a modal- and symmetry-engineered single-mode slot waveguide (length L_S) that prevents any wavelength-dependent beating between fundamental and higher-order modes as occurs in directional couplers and MMIs. The device further comprises a strip-to-slot mode transformer (also named strip-to-slot mode converter), and a symmetric slot-to-strip splitting transition. The strip-to-slot mode transformer (length $L_A + L_B$) guarantees adiabaticity and converts the fundamental mode of the strip waveguide into the fundamental mode of the slot waveguide without hardly any losses; whereas the structural symmetry of the slot-to-strip transition (length L_T) equally splits the light propagating along the slot waveguide in a wavelength- and polarization-agnostic fashion, imitating the working principle of conventional symmetric Y-junctions.

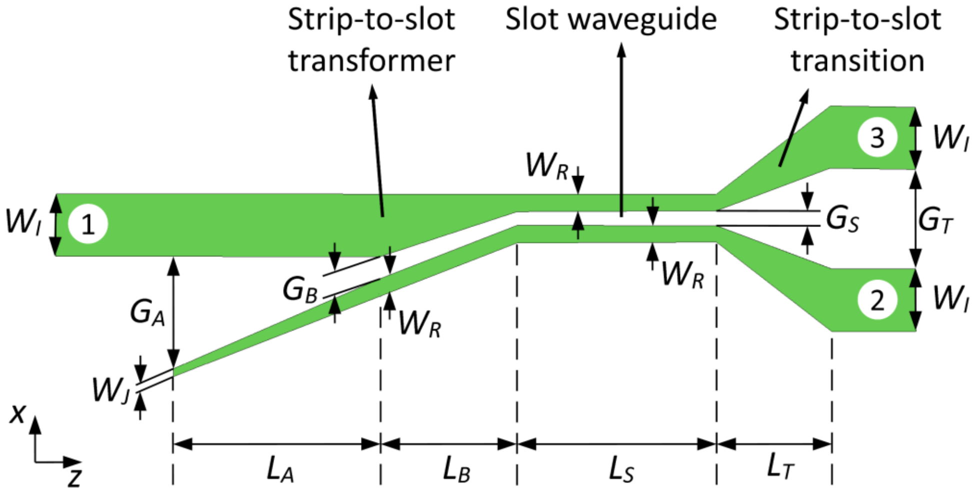

Figure 5.2. *Proposed ultra-broadband and dual-polarization beam splitter based on a strip-to-slot mode transformer (length L_A+L_B), a single-mode slot waveguide (L_S) and a symmetric slot-to-strip splitting transition (L_T).*

The aforementioned slot waveguide is formed by two waveguides with very narrow widths placed very close to each other [Almeida'04, Xu'04]. These two waveguides are typically called rails because a significant part of the optical power transported by the modes (especially for TE polarization) is propagated through the slot between them. In this way, the light is mostly confined in a low-index region, whose refractive index is given by the material used for the upper cladding layer. By applying this structure to power splitting, the proposed architecture avoids any abrupt discontinuity between the two arms of the splitting transition (i.e. the tip). Furthermore, it should be noted that typical over- and under-etching errors do not break the symmetry of the slot waveguide and this output splitting transition, thus maintaining a low imbalance between the output ports.

The procedure to design this device is described in this section, considering 220-nm-thick silicon wire waveguides deposited on a 2 µm BOX layer and covered by a PMMA upper cladding. In this case, PMMA was used for the cladding instead of SiO_2 mainly because it has a refractive index similar to SiO_2 and was the material being used at the facilities of the C2N at the moment of fabrication. A further extension of this architecture to the SiN platform is presented in section 5.4. A width of the input and output strip waveguides of $W_I = 450$ nm was considered for interconnection waveguides, and the bandwidth considered for the design ranges from 1.2 µm to 1.7 µm. The electric field intensity profile of the fundamental modes supported by the waveguide and their effective refractive indexes can be found in Appendix A. This work was mainly carried out during a research stay at C2N in collaboration with the NRC.

Modal engineering is the cornerstone of the slot waveguide design in order to ensure that only the fundamental TE mode or the fundamental TM mode is propagated, and all other higher-order modes are cut off. To fulfill single-mode condition of the slot waveguide within the target 500 nm bandwidth, the width of the rails and the slot are set to $W_R = 150$ nm and $G_S = 100$ nm, respectively. Figure 5.3a shows the real part of the effective index of the modes supported by the designed slot waveguide as a function of the wavelength. These results were obtained via a finite difference eigenmode (FDE) solver [MODE'20], taking into consideration material dispersion for Si and SiO_2 [Palik'98]. As it can be observed, the slot waveguide is single mode within the 1.2 – 1.7 μm wavelength range and all other higher-order modes are below the cut-off condition.

Next, the transition between the strip and the slot waveguides is designed to perform an adiabatic mode conversion [Feng'07, Palmer'13]. A narrow waveguide of width $W_J = 100$ nm, which is within the minimum feature size of e-beam lithography, is placed next to the input strip waveguide at a distance $G_A = 850$ nm to avoid any power coupling between them. This narrow waveguide is gradually transformed into the lower rail of the slot waveguide of width $W_R = 150$ nm, while approaching to the strip waveguide. The size of the intermediate gap is $G_B = W_R + G_S = 250$ nm to adiabatically adjust the sizes of the initial gap G_A and the slot G_S along the entire section of lengths $L_A + L_B$. The complete strip-to-slot mode transformer was simulated in back-to-back configuration using a commercial 3D eigenmode expansion (EME) solver [MODE'20]. Insertion losses were first calculated by sweeping the length L_A and L_B separately, whereas the length of the part that remained fixed in each case (i.e. L_B or L_A, respectively) was selected long enough not to introduce additional losses. Results are shown in Fig. 5.3b for TE (blue curves) and TM (green curves) polarizations at $\lambda_0 = 1.55$ μm. Negligible losses under 0.02 dB can be achieved for lengths longer than 10 μm.

We set a 2:1 ratio between L_A and L_B to maintain the same slope with respect to the optical axis between the upper and lower tapers. Figure 5.3c shows the insertion loss as a function of the total length of the strip-to-slot mode transformer when the 2:1 ratio is maintained. In this case, insertion losses as low as 0.005 dB can be obtained for both polarizations when the length is longer than 100 μm. Hence, a total length of 120 μm is finally chosen, being $L_A = 80$ μm and $L_B = 40$ μm.

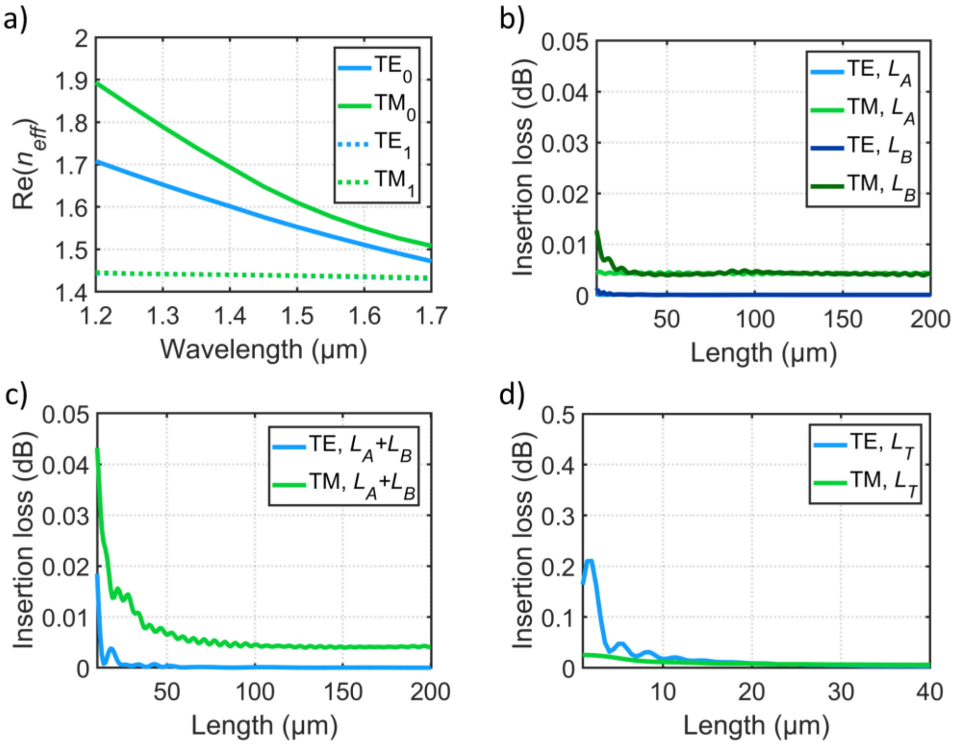

Figure 5.3. *(a) Real part of the effective index of the fundamental TE (solid blue line) and TM (solid green line) modes as a function of the wavelength calculated for an SOI slot waveguide with* W_R*=150 nm and* G_S*=100 nm. First-order TE (dotted blue line) and TM (dotted green line) are under the cutoff condition. (b) Simulated insertion loss as a function of the lengths* L_A *(light blue and green curves) and* L_B *(dark blue and green curves). (c) Simulated insertion loss of the complete strip-to-slot transformer length when a ratio 2:1 is maintained between* L_A *and* L_B*, respectively. (d) Simulated insertion loss as a function of the taper length* L_T *of the slot-to-strip splitting transition. All the simulations of the design of the tapers were carried out at the design wavelength of 1.55 μm.*

Imperfections in the tapers of the strip-to-slot mode transformer may produce some radiated light that might be coupled back into the output strip waveguides. In order to minimize the possibility of reinjection of any residual light radiated in the output tapers, the length of the single-mode slot waveguide must be a few tens of microns to spatially separate the strip-to-slot mode transformer and the output strip waveguides. Therefore, a slot waveguide length of $L_S = 60$ μm was selected for this purpose.

Finally, the slot-to-strip transition is designed. Two adiabatic tapers are connected to each of the rails to transform the slot waveguide into two conventional waveguides of width $W_I = 450$ nm. Additionally, the separation between both strip waveguides is increased up to $G_T = 350$ nm. Similar to the design of the strip-to-slot mode transformer, the length of the output tapers was swept via 3D EME [MODE'20] at the design wavelength of $\lambda_0 = 1.55$ µm. As it can be observed from Fig. 5.3d, negligible losses can be obtaining by selecting $L_T = 20$ µm. It is important to highlight that the separation between output waveguides was increased in the fabricated device up to 1.75 µm by means of cosine-type bends.

5.2.2. Simulation results of the complete device

The final performance of the proposed beam splitter was also obtained by means of the 3D EME solver. The same figures of merit as for the symmetric Y-junction in Chapter III were used to quantify the performance of this device (i.e. excess loss and imbalance). For the convenience of the reader, the mathematical expression of excess loss and imbalance are rewritten hereunder using scattering parameters:

$$\mathrm{EL_S} = -10\log\left(\left|S_{21}\right|^2 + \left|S_{31}\right|^2\right), \tag{5.1}$$

$$\mathrm{IB_S} = 10\log\left(\left|S_{21}\right|^2 \big/ \left|S_{31}\right|^2\right). \tag{5.2}$$

Simulations were carried out for the nominal design and for width deviations of ±25 nm, mimicking typical over- and under-etching errors. It is worth mentioning that both the waveguide widths and the gaps were varied in opposite ways. That is, for over-etching errors, the waveguide width shrinks $\Delta\delta$ while the gaps widen $\Delta\delta$. Conversely, for under-etching errors, the waveguide widths widen $\Delta\delta$, whereas the gap sizes are reduced a factor $\Delta\delta$.

Simulated excess loss and imbalance are shown in Fig. 5.4 for TE (left column) and TM (right column) polarizations. Our nominal design achieves low excess loss and imbalance of 0.2 dB and ±0.1 dB, respectively, for the entire simulated bandwidth (a remarkable 500 nm range) and for both polarizations. Regarding excess losses, negative fabrication deviations (i.e. $\Delta\delta = -25$ nm) lead to an increase of the losses at longer wavelengths. The main reason is that TE and TM fundamental modes are very close to the cutoff condition and are radiated from the slot waveguide. On the other hand, when the fabrication deviations are positive (i.e. $\Delta\delta = +25$ nm), excess losses decrease but the imbalance begins to increase since higher-order modes are supported in the slot waveguide and a wavelength-dependent beating occurs between higher-order and fundamental modes. However, these results show that the design of the splitter carried out is tolerant of fabrication errors of ±25 nm without significantly degrading its performance. Additionally, return losses (i.e. the amount of power reflected to the input port) were computed for nominal and biased designs, yielding values as low as -50 dB and -70 dB for TE and TM polarizations.

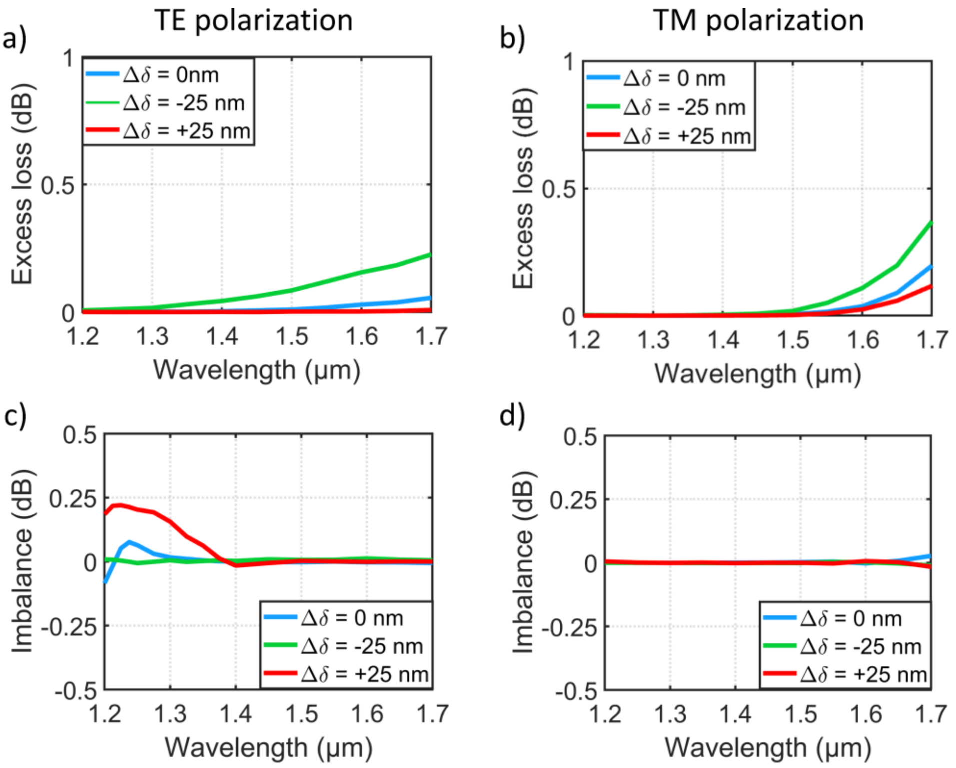

Figure 5.4. *Simulated excess loss of the proposed beam splitter for (a) TE and (b) TM polarizations as a function of the wavelength. Simulated imbalance of the proposed beam splitter for (c) TE and (d) TM polarizations as a function of wavelength. In all cases the nominal design is represented with blue curves, whereas width deviations of +25 nm and -25 nm are represented with red and green curves, respectively.*

5.3. Device characterization

The fabrication of the proposed ultra-broadband polarization-independent beam splitter was carried out at the facilities of the C2N [C2N'20] using SOI wafers with a silicon thickness of 220 nm and a BOX layer of 2 μm. In this case, patterns were drawn by e-beam lithography and transferred to the silicon layer via dry etching with sulphur hexafluoride (SF_6) gas as an inductively coupled plasma etcher. SEM images were taken prior the deposition of the 1-μm-thick upper PMMA cladding layer. The different test structures used to fully characterize the fabricated devices are described in the following subsections, in which the experimental results are also presented.

5.3.1. Mach-Zehnder interferometer

As shown in the previous chapter, MZIs are a very interesting test structure in order to extract the power imbalance from the measured extinction ratio (as performed for the SWG MMIs in Appendix B). The fabricated MZI is composed of two equal beam splitters whose geometrical parameters were taken from the design subsection 5.2.1. The imbalance between the arms is 40 μm to achieve virtually insignificant losses between the two arms. Figure 5.5a shows a SEM image of the fabricated MZI test structure. Zoomed-in images of the strip-to-slot mode converter, the slot waveguide and the slot-to-strip splitting transition are also shown in Figs. 5.5b, 5.5c and 5.5d, respectively.

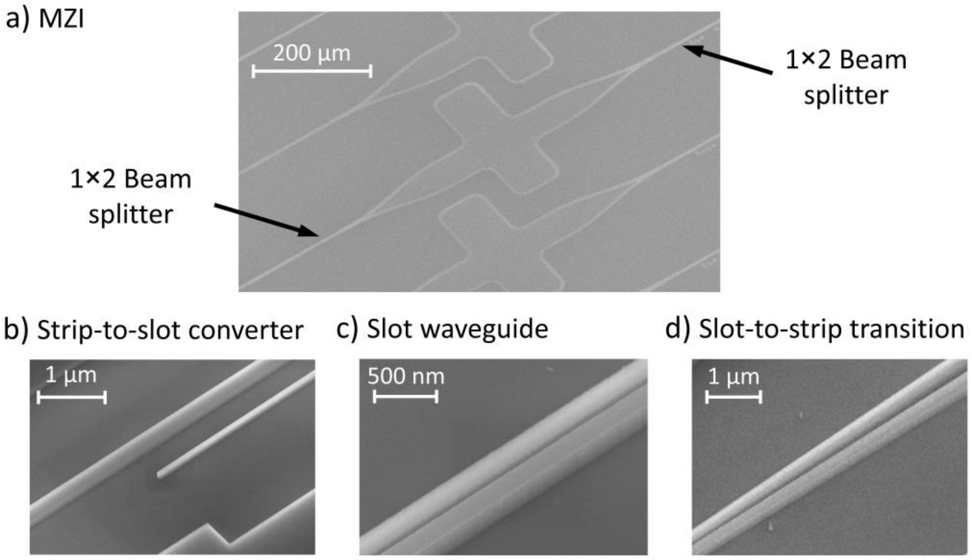

Figure 5.5. *Scanning electron microscope images of the (a) MZI test structure and zoomed-in images of (b) the strip-to-slot mode converter, (c) the slot waveguide and (d) the symmetric slot-to-strip transition.*

Measurements of the MZI test structure were carried out in the laboratories of the C2N using three tunable lasers from the former Yenista Optics to cover a combined wavelength range of up to 390 nm (i.e. from 1.26 μm to 1.65 μm). The polarization of the light at the output of each of the lasers was controlled by means of a 3-paddle polarization controller, and all of them were connected to an optical component tester (Yenista CT400) to perform measurements over the entire wavelength range in an automated manner. After the CT400, light polarization was selected with a fiber bench polarization controller kit using a rotating quarter-waveplate and a linear polarizer. A lensed PMF and 3-µm-wide tapers were used to couple the light into the chip regardless wavelength and polarization. At the output, the light was collected with a microscope objective, filtered and directed to the photodetector of the CT400.

The measured raw results of the MZI and the reference waveguide were normalized with respect to the setup response. The resulting transmittances are depicted in Figs. 5.6a and 5.6b for TE and TM polarizations, respectively.

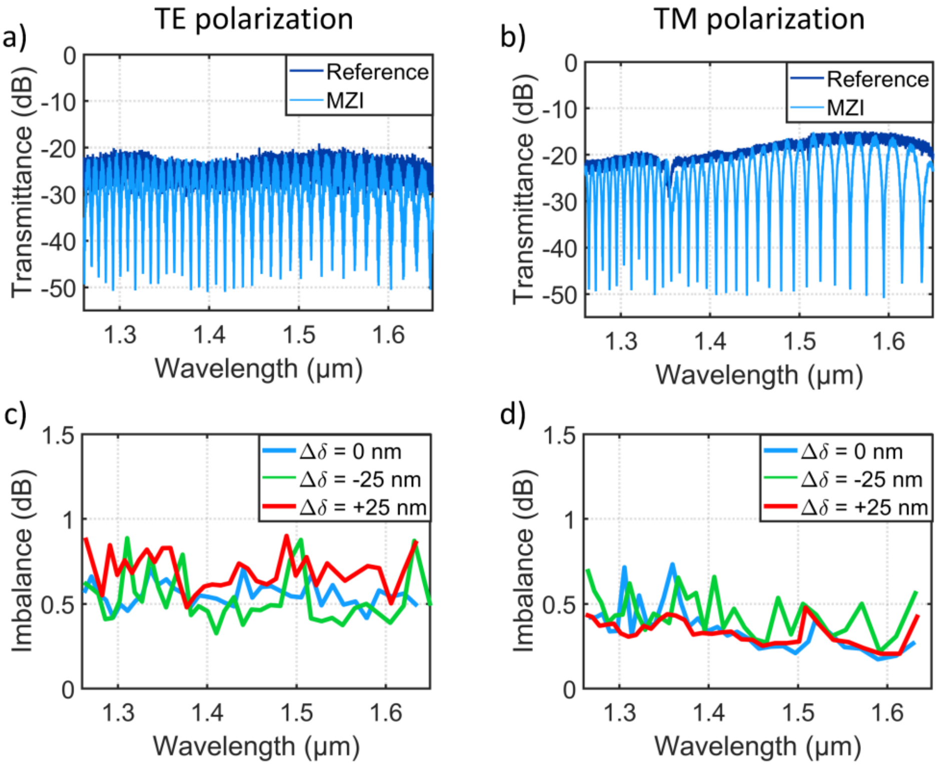

Figure 5.6. *Measured spectra of the MZI test structure formed by two nominal beam splitters for (a) TE and (b) TM polarizations. Transmittance of a reference waveguide is also represented for comparison purposes. Imbalance as a function of the wavelength obtained from the measured ER for (c) TE and (d) TM polarizations.*

Maxima of the MZI response fit perfectly with the response of the reference waveguide, evidencing the low losses of the fabricated beam splitter. Moreover, the measured ER values are better than 20 dB over the entire measured bandwidth for both TE and TM polarizations. The imbalance can be obtained using the method described in [Wang'16a], particularized for our 1×2 beam splitter. In this case the expression to calculate the measured coupling coefficient ($\kappa^2_{\mathrm{Measured}}$) is the same:

$$\kappa^2_{\mathrm{Measured}} = 0.5 \pm 0.5\sqrt{\frac{1}{10^{\mathrm{ER}/10}}}. \tag{5.3}$$

And the measured imbalance can be straightforwardly derived using Eq. 5.3:

$$\mathrm{IB}_{\mathrm{Measured}} = \pm 10\log\left(\frac{0.5 + 0.5\sqrt{\frac{1}{10^{\mathrm{ER}/10}}}}{0.5 - 0.5\sqrt{\frac{1}{10^{\mathrm{ER}/10}}}}\right). \tag{5.4}$$

Therefore, an imbalance below ±0.9 dB in the whole range is calculated using Eq. (5.4) for TE and TM polarizations.

In addition to the MZI consisting of two nominal beam splitters, other MZIs including biased splitters were also fabricated with width/gap deviations of $\Delta\delta = \pm 25$ nm. Experimental results for nominal and biased designs are shown in Figs. 5.6c and 5.6d for TE and TM polarizations, respectively. The curves represented in red correspond to the imbalance measured for the structure with $\Delta\delta = +25$ nm, whereas the green curves correspond to the structure with $\Delta\delta = -25$ nm. It is remarkable that in all these cases an imbalance of less than ±0.9 dB is observed for both polarizations within an unprecedented 390 nm wavelength range, which demonstrates the resilience of our proposed device to typical etching errors.

5.3.2. Cascaded beam splitters

One of the main limitations of the MZI test structure used in the previous subsection is the inaccuracy to estimate the losses of the beam splitter. It should be noted that the measured MZI response is the combination of the losses of the Mach-Zehnder structure and the chip coupling. Small defects in the input and output facets of the chip cause non-uniform coupling that prevents accurate measurement of the beam splitters' excess loss. To correctly characterize the low losses of our proposed device, five beam splitters were connected in series as shown in Fig. 5.7.

In this test structure, one of the arms of the beam splitters is routed to the output facet whereas the other is used for the connection with the following beam splitter. In this way, losses of a beam splitter can be estimated by measuring the transmission level at each stage and performing a linear regression fitting. Similar to the previous MZI test structure, nominal and biased designs with $\Delta\delta = \pm 25$ nm were fabricated to show the resilience of our device to fabrication errors.

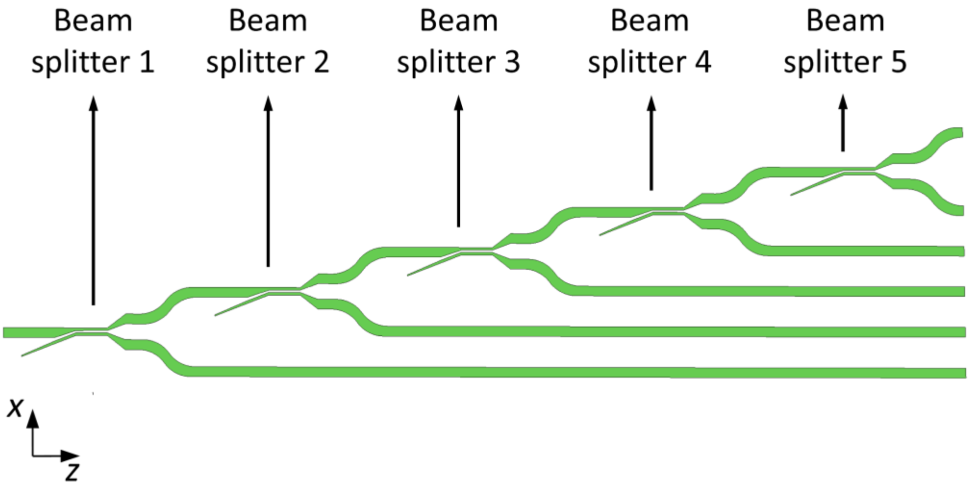

Figure 5.7. *Schematic top view of the five cascaded beam splitters (i.e. connected in series) used to perform accurate measurements of the excess loss.*

The one-arm splitter transmittance was retrieved by measuring all the outputs of the test structure shown in Fig. 5.7 and estimating the slope of the transmission as a function of the number of couplers. The ideal transmittance for one of the output arms of our 1×2 beam splitter is -3 dB. Figures 5.8a and 5.8b show that the measured transmittance for the nominal splitter (blue curve) is in very good agreement with the ideal response. Deviations are as low as ±0.5 dB within the 390 nm bandwidth for both TE and TM polarizations. This outstanding performance is maintained for the artificially introduced fabrication errors, represented in green and red for width deviations of $\Delta\delta = -25$ nm and $\Delta\delta = +25$ nm, respectively.

The deviation from the ideal -3 dB transmittance is the combination of both excess loss and imbalance. Although these two effects are difficult to separate, it is possible to make a worst-case estimation of the excess loss by taking the less favorable imbalance value. The transmittance (in dB) in one of the arms of the splitter can be expressed as:

$$\mathrm{T}[dB] = -3[dB] - \mathrm{IL}[dB] \pm \mathrm{IB}/2[dB] \tag{5.5}$$

Therefore, the experimental excess loss can be calculated from the transmittance of the cascaded splitters and taking into account the worst imbalance from the MZI experiment. Estimated excess losses for the worst case are represented in Figs. 5.8c and 5.8d for TE and TM polarizations, respectively. Both the nominal and biased designs exhibit losses well below 1 dB within the entire measured wavelength range for both polarizations. For example, losses less than 0.5 dB are achieved in the wavelength range from 1.35 μm to 1.64 μm for the proposed nominal design for TE polarization, while for TM polarization the losses are slightly above 0.5 dB within the same wavelength range. It should be noted that the differences between measured and simulated excess losses have its origin in the sidewall roughness (i.e. small variations in the width of the waveguides that result in scattering losses) [Wang'18]. These fabrication imperfections were not taken into account for the simulations performed in section 5.2 and constitute an additional source of loss in the fabricated devices.

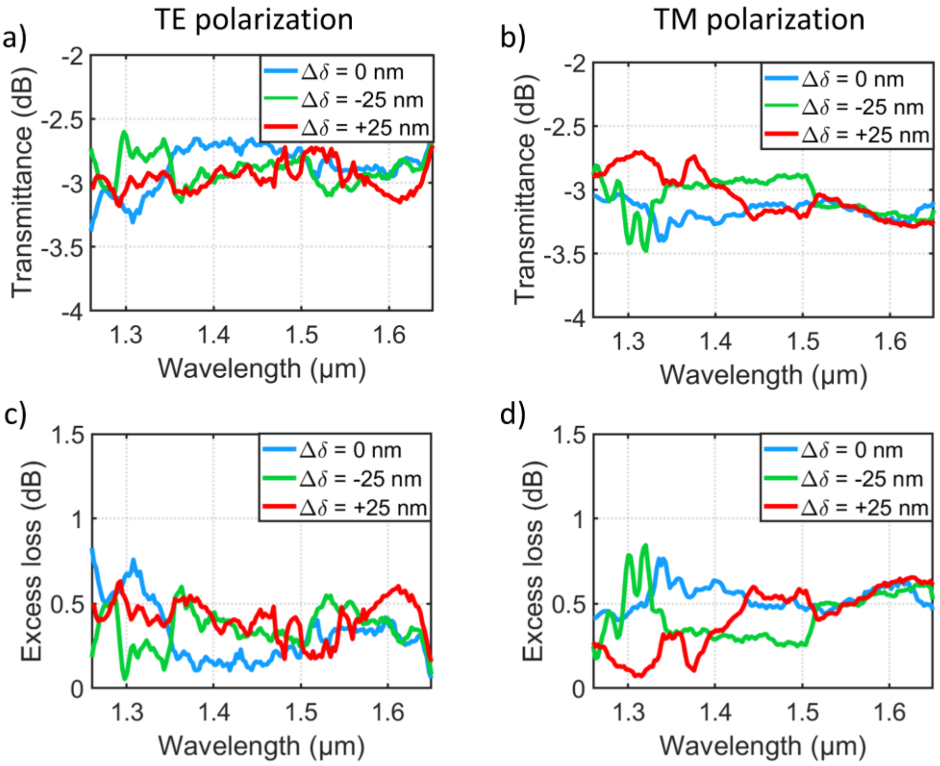

Figure 5.8. *Measured one-arm splitter transmittance for (a) TE and (b) TM polarizations, obtained through linear regression fitting from the measurements performed for the five beam splitters connected in series. Excess loss of single beam splitter for (a) TE and (b) TM polarizations.*

Finally, power reflections of the fabricated beam splitters were studied by means of the minimum phase technique [Halir'09]. Thus, the measured power transmittances of the reference waveguide and the beam splitter can be transformed into the minimum phase impulse response (i.e. into the spatial domain). Figures 5.9a and 5.9b shows the impulse response as a function of the physical length for TE and TM polarizations, respectively. The first peak at 0 mm corresponds to the direct transmission at the input facet, whereas the second peak at 9 mm shows the facet reflection since the length of the chip is 9 millimeters. As the splitter is placed at a distance of 7 millimeters from the input facet, any backward reflection would be evinced as a peak near that distance. No peak can be observed neither for TE nor TM polarizations, verifying that our proposed beam splitter presents very low return losses.

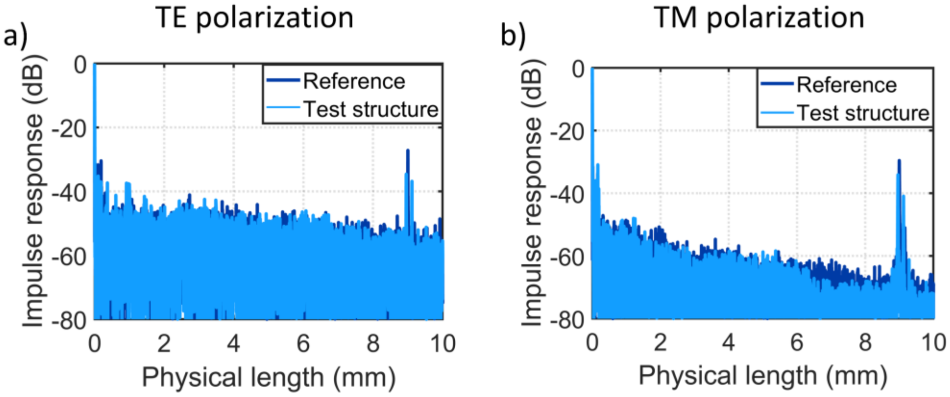

Figure 5.9. *Measured phase impulse response as a function of the physical length for (a) TE and (b) TM polarizations of a nominal beam splitter. The length of the chip is 9 millimeters, and the splitter is placed at a distance of ~7 mm from the input facet.*

5.4. Migration to the silicon nitride platform

The SiN platform has increasingly attracted attention due to its lower refractive index contrast compared to SOI, improving tolerances to fabrication errors and reducing both scattering losses and the birefringence between TE and TM polarizations. In addition to all these advantages, the transparency window of SiN reaches wavelengths from the visible range up to the mid-IR (see Appendix A for detailed information of this material platform). Many applications have emerged in recent years exploiting these virtues such as sensing [Liu’13], quantum photonics [Mohanty’17], supercontinuum generation [Zhao’15] and absorption spectroscopy [Nie’17], to name a few.

Contrary to what happens in SOI, only a few beam splitters have been reported to date on the SiN platform. The most relevant devices are ring resonators [Spencer’12], directional coupler [Poot’16], multimode interference devices [Mu’14Mu’14Mu’14, Poulton’17b, Romero-García’13], wavelength-stabilized directional couplers [Guerber’18a], adiabatic tapers [Yuan’18] and asymmetric directional couplers [Sharma’19]. Among all of them, only the wavelength-stabilized directional couplers have been experimentally demonstrated with a bandwidth of 100 nm operating for TE polarization [Guerber'18a]. This section aims to apply our design strategy based on modal and symmetry engineering to the SiN platform, in order to implement an ultra-broadband and polarization-independent beam splitter.

5.4.1. Revised design

The beam splitter was redesigned considering a SiN film with a thickness of 600 nm surrounded by a SiO_2 upper and lower cladding layers. In this case, the structure was slightly modified for an even simpler design. Figure 5.10 shows the minor changes that have been made to the structure. The width of the intermediate gap is now equal to the slot width (i.e. $G_B = G_S$), whereas the narrow waveguide placed next to the strip waveguide has the same width as the rails of the slot waveguide (i.e. $W_J = W_R$). The rest of the design geometry is exactly the same as in the Si beam splitter, as is the targeted wavelength range (1.2 µm to 1.7 µm). However, owing to the lower refractive index contrast and more restrictive minimum feature size (200 nm) of the SiN platform, the splitter geometrical parameters were completely redesigned.

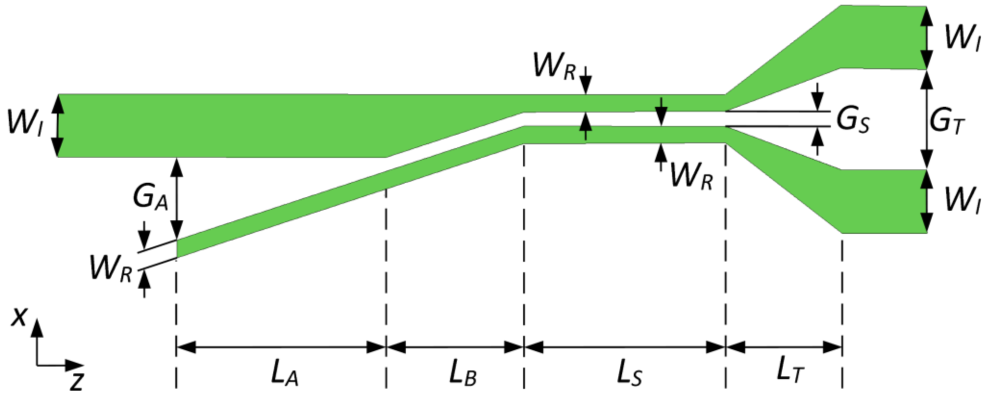

Figure 5.10. *Proposed ultra-broadband and dual-polarization SiN beam splitter based on a strip-to-slot mode transformer (length L_A+L_B), a single-mode slot waveguide (L_S) and a symmetric slot-to-strip splitting transition (L_T).*

Modal engineering was first applied to the slot waveguide to ensure that single-mode condition is fulfilled over the complete design bandwidth. The real part of the effective indexes of the slot modes were calculate via a commercial FDE solver [MODE'20]. In this way, the widths of the rails and the slot were judiciously selected in order to satisfy the monomode condition, obtaining $W_R = 200$ nm and $G_S = 200$ nm. Figure 5.11a shows that both fundamental TE and TM modes are supported by the designed SiN slot waveguide, whereas the next higher-order modes are under cutoff condition for the entire 500 nm bandwidth.

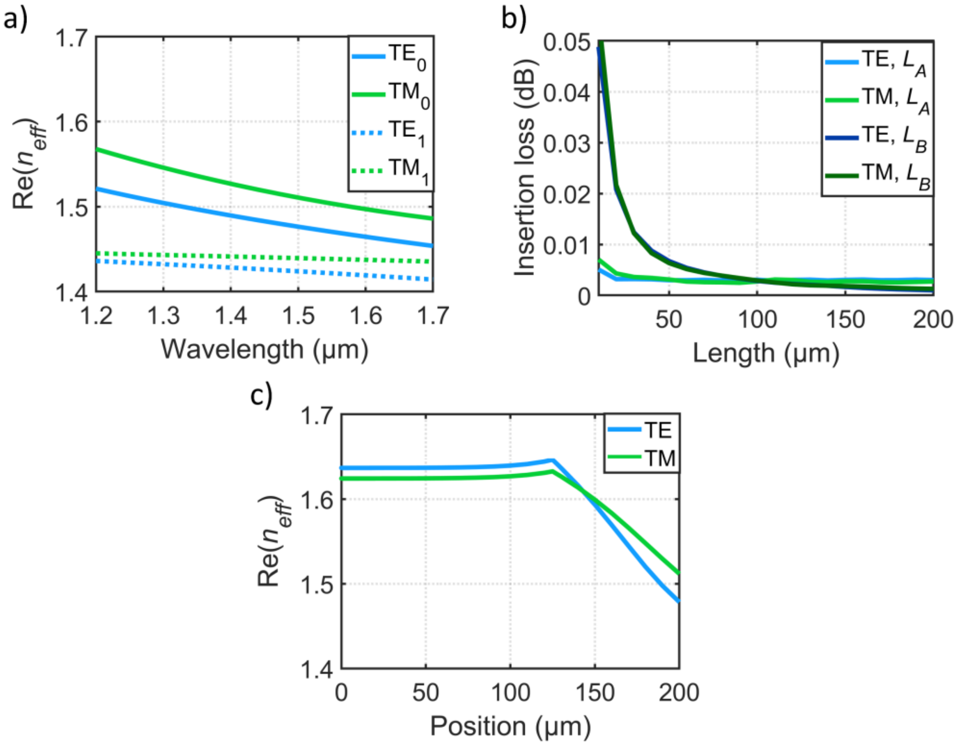

Figure 5.11. *(a) Real part of the effective index of the fundamental TE (solid blue line) and TM (solid green line) modes as a function of the wavelength calculated for a SiN slot waveguide with* W_R*=200 nm and* G_S*=200 nm. First-order TE (dotted blue line) and TM (dotted green line) are under the cutoff condition. (b) Simulated insertion loss as a function of the lengths* L_A *(light blue and green curves) and* L_B *(dark blue and green curves). (c) Real part of the effective index along the strip-to-slot mode transformer for TE (blue curve) and TM (green curve). Simulations in (b) and (c) were carried out at the design wavelength of 1.55 µm.*

The strip-to-slot mode transformer was then designed to perform an adiabatic conversion between the mode propagated through the 700-nm-wide interconnection waveguide and the slot waveguide. To this end, the mode transformer was simulated in back-to-back configuration using the 3D EME solver at the design wavelength of $\lambda_0 = 1.55$ µm [MODE'20]. Similar to the design of the Si beam splitter, the length of the sections L_A and L_B were varied independently as shown in Fig. 5.11b. The final lengths were selected to be $L_A = 120$ µm and $L_B = 80$ µm, ensuring that an adiabatic mode conversion is performed. Furthermore, FDE simulations were performed at $\lambda_0 =$ 1.55 µm in order to obtain the real part of the effective indexes of TE$_0$ and TM$_0$ modes along the strip-to-slot mode transformer (see Fig. 5.11c). The slope for the fundamental TE and TM modes is as low as $2.2 \cdot 10^{-3}$ μm^{-1} and $1.61 \cdot 10^{-3}$ μm^{-1}, respectively, proving that the designed transition is performed in an adiabatic way. To physically separate the strip-to-slot mode converter from the output tapers and prevent radiated power (caused by fabrication imperfections) from coupling between both sections, the length of the slot waveguide was maintained at $L_S = 60$ µm, similar to our the previous design.

Finally, symmetry engineering is applied to the slot-to-strip output section to equally divide the fundamental TE or TM modes propagating along the slot waveguide. Two trapezoidal tapers were connected to each of the rails to transform the slot waveguide into two conventional waveguides of width $W_I = 700$ nm. We fixed the separation of the two output waveguides to $G_T = 1.5$ µm, and found that a length of $L_T = 60$ µm results in insignificant losses for the slot-to-strip transition for both TE and TM polarizations.

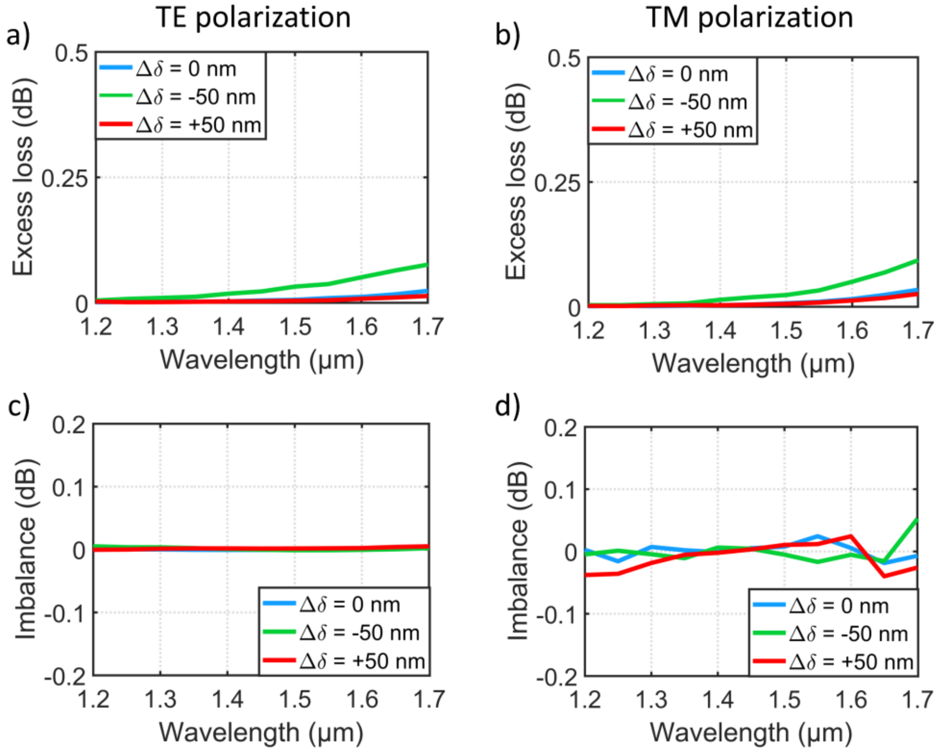

Figure 5.12. *Simulated excess loss of the proposed SiN beam splitter for (a) TE and (b) TM polarizations as a function of the wavelength. Simulated imbalance of the proposed SiN beam splitter for (c) TE and (d) TM polarizations as a function of wavelength. In all cases the nominal design is represented with blue curves, whereas width deviations of +50 nm and -50 nm are represented with red and green curves, respectively.*

By way of verification of the design carried out, the complete SiN beam splitter was simulated by means of a 3D EME solver [MODE’20]. Figures 5.12a and 5.12b represent the simulated excess losses for TE and TM polarizations, respectively. In addition to the nominal design (represented with blue curves), fabrication tolerances were also studied by incorporating biased design with width variations of $\Delta\delta = \pm 50$ nm. Note that width variations were updated according to the fabrication process used for the SiN platform (i.e. based on deep-UV photolithography). Simulated excess losses are below 0.1 dB in all the cases within the 500 nm wavelength range and for TE and TM polarizations. Similar to what happened with the Si beam splitter, excess losses begin to grow at longer wavelengths as a result of the modes approaching the cutoff condition. This effect is observed mainly for negative fabrication errors (i.e. $\Delta\delta = -50$ nm) when over-etching occurs. On the other hand, the imbalance is depicted in Figs. 5.12c and 5.12d for TE and TM polarizations, respectively. Values better than ±0.05 dB are achieved even for the biased designs, demonstrating again the resilience of the proposed architecture.

5.4.2. Measurements

The proposed SiN beam splitter was fabricated in collaboration with the C2N and STMicroelectronics in ST Crolles using their 300 mm silicon photonics platform [Guerber’18b]. Owing to space limitations on the chip, only the MZI test structure including nominal beam splitters with an arm imbalance of 50 μm was fabricated. A SiN layer with a thickness of 600 nm (the same as considered in the previous subsection for simulations) was deposited onto the SiO_2 lower layer via plasma enhanced chemical vapour deposition (PECVD). The patterns were drawn in the SiN layer using 248 nm deep-UV photolithography and etching was performed by means of a dry etching process. SEM images of the splitter were taken before encapsulation with a 1.5-μm-thick SiO_2 layer (see Fig. 5.13).

The fabricated MZI was measured in the laboratories of the C2N using a similar setup to the one described in subsection 5.3.1 for the Si beam splitter, that is, three tunable lasers from the former Yenista Optics were used to cover a combined wavelength range of up to 420 nm, with a 3-paddle polarization controller and a CT400. Identical fiber-chip grating couplers were used as input and output interfaces between the SiN chip and the cleaved single-mode fibers, and tilt angles of the fibers were adjusted between the different wavelength scans. Measured transmittance spectra of the MZI and the reference waveguide were normalized by the response of the input and output fiber-chip grating couplers.

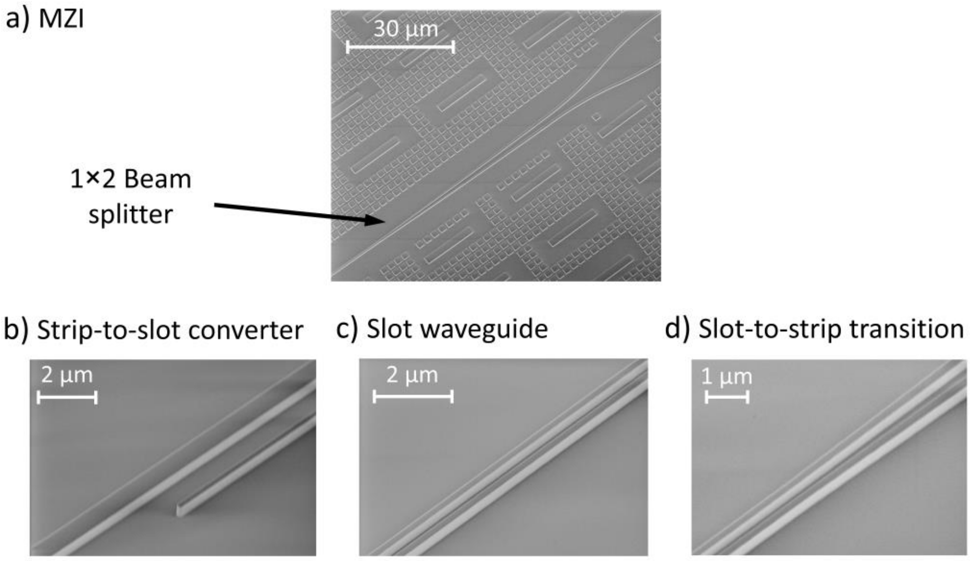

Figure 5.13. *Scanning electron microscope images of the (a) fabricated SiN beam splitter in an MZI. Zoomed-in images of (b) the strip-to-slot mode converter, (c) the slot waveguide and (d) the symmetric slot-to-strip transition.*

Figures 5.14a and 5.14b show the response of the MZI and the reference waveguide for TE and TM polarizations, respectively. Extinction ratios better than 23.5 dB and 23.3 dB were measured within the 420 nm for TE and TM polarizations, respectively. Power imbalances were obtained using Eq. (5.4) together with the measured extinction ratios. As shown in Figs. 5.14c and 5.14d, values better than 0.6 dB were attained for both polarizations within the entire measured bandwidth.

Although MZIs are somewhat inaccurate for studying excess loss, a first estimate was carried out for the SiN beam splitter using this structure. Excess losses were calculated by halving the difference between the transmissions of the MZI and the reference waveguide (both without normalization). Figures. 5.14e and 5.14f show the estimated excess loss of a single beam splitter (dotted curves) and the corresponding linear fitting (solid curves). The proposed SiN beam splitter exhibits low losses of 0.62 dB and 0.57 dB within the 1.26 – 1.68 µm wavelength range for TE and TM polarizations, respectively. Furthermore, the linear curve fitting shows that the simulation trend is met and, for longer wavelengths, the losses slightly increased.

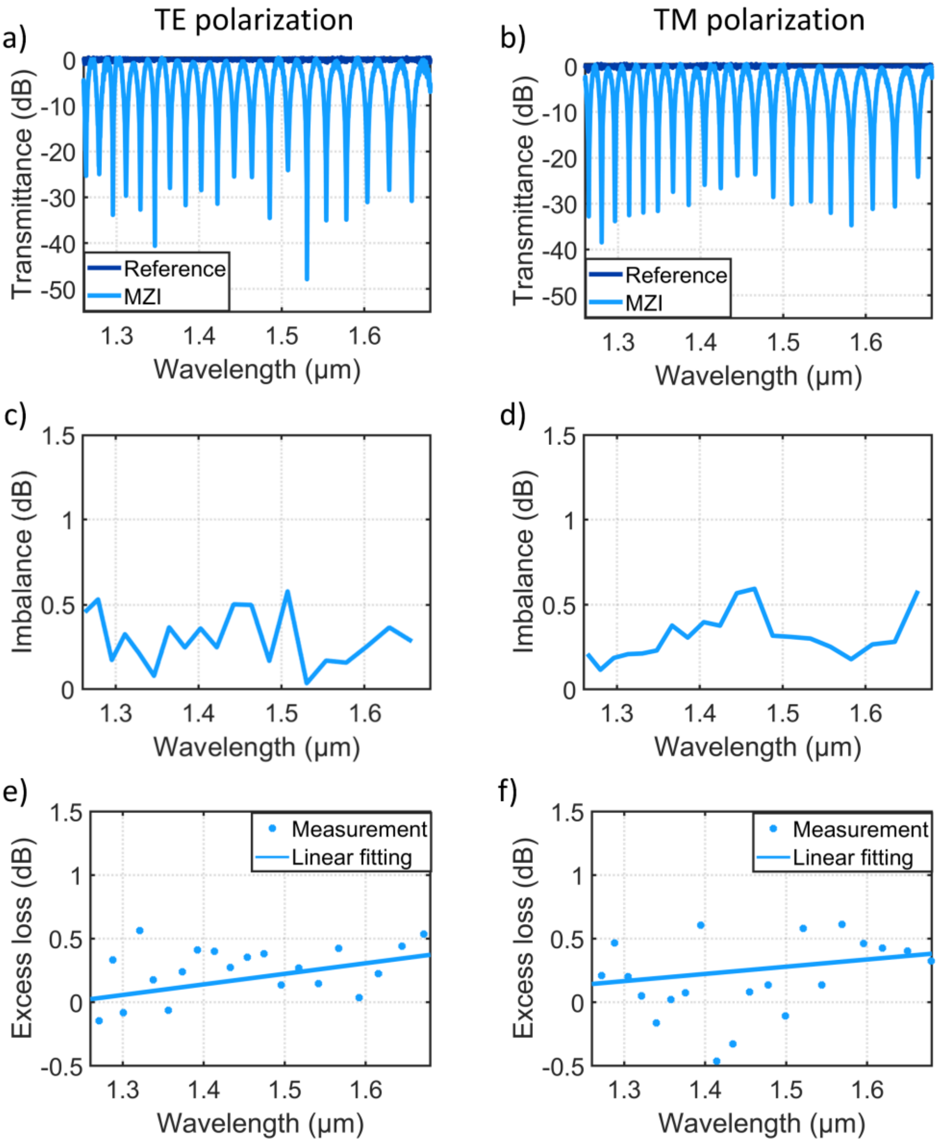

Figure 5.14. *Measured spectra of the MZI test structure formed by two nominal beam splitters for (a) TE and (b) TM polarizations. Transmittance of a reference waveguide is also represented for comparison purposes. All spectra are normalized by the fiber-chip grating coupler response. Imbalance as a function of the wavelength obtained from the measured ER for (c) TE and (d) TM polarizations. Excess loss as a function of the wavelength obtained from the MZI response (dotted curve) and its linear fitting (solid curve) for (e) TE and (f) TM polarizations.*

5.5. Summary

Optical beam splitters are essential building blocks in integrated photonics that have been intensively investigated by the scientific community over the years. Several different architectures have been proposed in the SOI platform, such as directional couplers, symmetric Y-junctions and MMIs; but a high-performance dual-polarization beam splitter is still sough-after for the next-generation of PICs aimed at cutting-edge applications.

In this chapter, a novel design strategy has been proposed based on modal- and symmetry-engineered slot waveguides. The single-mode slot waveguide prevents any mode-beating behaviour that limits the operation of other conventional beam splitters such as directional couplers and MMIs, whereas the symmetric output transition ensures equal power splitting in a polarization- and wavelength-agnostic fashion. The design of an ultra-broadband and polarization-independent beam splitter was carried out for the SOI platform using this approach. Simulation results show low losses and imbalance for both TE and TM polarizations over an ultra-broad bandwidth of 390 nm bandwidth. This performance is maintained even for typical over- and under-etching errors of ±25 nm.

Experimental characterization was carried out using two different test structures: an MZI to determine the power imbalance and five cascaded beam splitters to estimate the losses. The fabricated Si beam splitter yields excess loss and imbalance below 1 dB for both polarizations over a measured bandwidth of 390 nm. Moreover, this remarkable performance was also measured for the biased beam splitters, demonstrating the robustness to fabrication errors of the design.

Additionally, the proposed design strategy was also applied to design a high-performance beam splitter on the SiN platform. This device was fabricated at the facilities of ST Crolles with an excess loss and imbalance below 0.62 dB and 0.6 dB, respectively, for both TE and TM polarization in an outstanding 420 nm wavelength range.

The experimental results obtained for the two beam splitters demonstrated in this chapter are shown in Table 5.1, along with the performance of other state-of-the-art beam splitters for the SOI and SiN platforms.

Table 5.1. *Comparison of state-of-the-art beam splitters fabricated on the SOI and SiN platforms. Worst performance between TE and TM polarizations is considered for polarization-independent beam splitters*

Reference	Architecture	SOI/SiN	EL (dB)	IB (dB)	BW (nm)	Length (µm)	TE/TM
[Xing’13b]	Adiabatic splitter	SOI	< 0.31	< 0.2	100	300	TE
[Yun’18]	SWG-assisted coupler	SOI	< 0.11	< 0.3	185	35	TE
[Zhang’13]	Y-junction	SOI	< 0.28	< 0.02	80	2	TE
[Halir’16]	SWG MMI	SOI	< 1	< 1	325	25.4	TE
[Li’13]	Inverse tapers	SOI	< 0.4	< 0.68	40	12.5	TE
[Rasigade’10]	Star coupler	SOI	< 1	< 1	90	0.75	TE
[Frandsen’04]	Photonic crystal	SOI	< 0.25	< 0.58	30	20	TE
[Chen’17]	Bent directional coupler	SOI	< 1	< 0.87	80	< 50	TE/TM
[Xu’17]	Adiabatic coupler	SOI	–	< 0.7	100	185	TE/TM
[Tamazin’18]	Y-branch variation	SOI	< 0.19	< 0.47	70	20	TE/TM
This work	Slot waveguide	SOI	< 1	< 1	390	200	TE/TM
[Poot’16]	Directional coupler	SiN	< 0.06	< 0.01	–	< 50	TE
[Guerber’18a]	Wavelength-stabilized directional coupler	SiN	–	< 1.05	100	–	TE
[Spencer’12]	Ring resonator	SiN	< 0.9	< 0.4	–	> 9800	TE
[Poulton’17b]	MMI	SiN	< 0.1	–	100	33.7	TE
[Romero-García’13]	MMI	SiN	< 0.32	< 0.87	–	73.7	TE
This work	Slot waveguide	SiN	< 0.62	< 0.6	420	320	TE/TM

VI

Conclusions

In this thesis, the design and characterization of several original photonic devices has been carried out. This closing chapter overviews the contributions made in this field, their prospects and the impact generated. Specifically, section 6.1 summarizes the achievements made for each proposed device. The ongoing work and future lines of research are reviewed in section 6.2. Finally, the impact and the outcomes garnered from the development of the thesis are listed in section 6.3.

6.1. Conclusions

The work conducted in this thesis is primarily focused on the design, implementation and experimental characterization of highly-efficient building blocks for next-generation PICs. Novel structures based on nano-scale features, i.e. SWG metamaterial structures and slot waveguides, have been reported showing significant advances in the field of mode-division multiplexing, passive phase shifting and optical beam splitting.

6.1.1. Broadband mode converter and multiplexer/demultiplexer

A novel mode converter and MUX/DEMUX based on a subwavelength engineered MMI has been implemented for the first time in the SOI platform. Mode-division multiplexing technology is becoming established as an encouraging way to expand the capacity of optical interconnects in data centers. This technology requires the handling and conversion of fundamental and higher-order modes, being the mode converter and MUX/DEMUX a key constituent of the MDM system. Although different approaches have been proposed for mode conversion and multiplexing, reported devices are experimentally hampered either by narrow bandwidths, high transmission losses or large footprints.

In addition to the SWG MMI, our proposed architecture is composed of a 90° phase shifter and a symmetric Y-junction. By engineering the dispersion and anisotropy in the SWG MMI, the insertion loss and the footprint of the entire mode converter and MUX/DEMUX are reduced compared to its counterpart based on a conventional MMI. Simulations results predict a flat low-loss response over a 300 nm bandwidth. A complete MUX-DEMUX link was successfully demonstrated with insertion loss as low as 1.3 dB and 1 dB for TE_0 and TE_1 modes, respectively, over a 145 nm wavelength range (1.495 – 1.64 µm). Crosstalk values were below -15.3 dB for TE_0 mode and -15.4 dB for TE_1 mode within the same wavelength range. This remarkable low-loss performance was attained for a single MUX/DEMUX footprint of 38.6 µm × 3.7 µm, making it one of mode MUX/DEMUX with lowest insertion loss over a broad bandwidth without sacrificing compactness.

The device concept was proposed by the author of this thesis and the design was performed in collaboration with the UMA. A first fabrication run was carried out in collaboration with the NRC at the University of Washington. The subsequent characterization in the laboratories of the UMA demonstrated the correct operation of a MUX, but uncovered a problem in the MUX-DEMUX link related to the excitation of higher-order modes in the multimode waveguide. Insertion losses presented ripples with a maximum amplitude of ~5 dB for TE_0 mode conversion (i.e. the fundamental mode was generated in the multimode waveguide). Thus, in collaboration with Alcyon Photonics S.L., the device was refabricated in a commercial foundry (Applied Nanotools Inc.) after reducing the width of the Y-junction arms to prevent the excitation of undesired higher-order modes. In this case, an almost flat spectral response in terms of insertion losses was achieved. The theoretical design of the broadband mode converter and MUX/DEMUX based on subwavelength structures was published in [González-Andrade'18]. The experimental demonstration is currently under review in another Q1 peer-reviewed journal.

6.1.2. Ultra-broadband nanophotonic phase shifter

In this thesis, the unique properties of SWG metamaterial waveguides have been leveraged to substantially improve both the performance and the fabrication tolerances of passive PSs based on equal-length waveguides. Phase shifting is considered a fundamental operation in many photonic systems targeting dissimilar applications, such as sensing or datacom. In recent years, most research efforts have focused on active PSs and minor advances has been made in passive ones.

In order to contextualize the design, a theoretical study has been carried out to show the limitations of state-of-the-art PSs, i.e. tapered and asymmetric PSs based on non-periodic waveguides. To overcome these constraints, additional degrees of freedom in the design of PSs are required. In this way, an anisotropy- and dispersion engineered asymmetric SWG PS was proposed. A simulated phase shift error < ±1.7° was attained over an unprecedented 400 nm wavelength range (1.35 – 1.75 µm). This is an eight-fold improvement compared to conventional PSs. Furthermore, this flat spectral response is maintained for over- and under-etching errors of ±20 nm. The device was fabricated at the same commercial foundry as the mode MUX/DEMUX and measurements were carried out showing an excellent agreement with simulations predictions. A phase slope of 63°/µm was measured over a 145 nm bandwidth (1.495 – 1.64 µm) for tapered PSs, whereas the proposed asymmetric SWG PS yielded an almost flat phase slope of only 16°/µm within the same bandwidth. This constitutes, to the best of the author's knowledge, the most broadband silicon passive PS reported to date.

The SWG PS concept was proposed by the author of this thesis and the design, fabrication and characterization was performed in collaboration with the UMA and the

NRC. The related scientific paper has been recently publishe in Photonics Research [González-Andrade'20a].

6.1.3. Ultra-broadband dual-polarization beam splitter

One of the contributions of this thesis has been the development of a design strategy to implement high-performance beam splitters regardless of the material platform considered. Optical beam splitters are also critical constituents for many high-end applications, such as optical communications and absorption spectroscopy. The high refractive index contrast of the SOI platform severely limits the performance of beam splitters in terms of bandwidth, single-polarization operation and stringent fabrication tolerances. Despite the large number of beam splitters reported for the SOI platform, the research around these devices continues inasmuch as higher yields are required. On the contrary, only a few proposals have been demonstrated for the SiN platform with operating bandwidths < 100 nm.

To circumvent these shortcomings, we have proposed an ultra-broadband dual-polarization beam splitter with improved fabrication tolerances for the SOI and the SiN platforms. The key to the design lies in a modal engineered slot waveguide that avoids the excitation of higher-order modes and a symmetric slot-to-strip transition that ensures equal power splitting. The beam splitter implemented on the SOI platform showed measured insertion loss and imbalance lower than 1 dB for TE and TM polarizations within a remarkable bandwidth of 390 nm (1.26 – 1.65 μm), being the first dual-polarization beam splitter with a measured bandwidth in excess of 300 nm. In addition, this device has also proved to be tolerant to fabrication errors of ±25 nm. Following the same design strategy, another splitter based on the SiN platform was designed and fabricated. In this case, insertion loss and imbalance lower than 0.6 dB was demonstrated for both TE and TM polarizations covering all the telecommunications bands (1.26 – 1.68 μm).

The design, fabrication and characterization of the beam splitter for the SOI platform was carried out during a short research stay of three months in the MINAPHOT (micro and nano-photonics devices on silicon platform) group of the C2N and in collaboration with the NRC. The activities related to the design and device measurement were carried out by the author of the thesis, while the fabrication was performed by other members of the MINAPHOT group who had access to the cleanroom. These results were published in [González-Andrade'19]. The collaboration with the MINAPHOT group continued resulting in the design and fabrication of the SiN splitter. This design was performed by the author of this thesis at the IO, whereas the sample was fabricated in STMicroelectronics thanks to the collaboration with the C2N. Finally, the SiN beam splitter was characterized in the laboratories of the C2N during a second research stay, being the corresponding scientific paper recently accepted in Optics Letters journal [González-Andrade’20b].

6.2. Applications and future work

The devices developed in this thesis present a high performance that allow their use in demanding applications such as high capacity optical interconnects, microwave and terahertz photonics, microspectrometers, quantum computing, LIDAR and biochemical sensing.

Given the enormous potential of the developed devices, it is intended to continue studying improvements and variants of all of them in the near future, therefore proposed future lines of research for each device are indicated below.

Improvement of the mode multiplexer/demultiplexer

The demonstrated mode MUX/DEMUX shows a high performance in terms of low losses, broad bandwidth and compactness, being a promising candidate for the implementation of integrated MDM transceivers for broadband telecom and datacom applications. Although crosstalk values are within the state of the art, it is still possible to improve them. It should be noted that the conventional MMI was responsible for the high losses of the complete mode MUX/DEMUX, but once replaced by an SWG MMI, crosstalk is mainly limited by the narrow spectral response of the tapered PS. Since in this thesis an ultra-broadband PS has been demonstrated, the next step will be to replace the tapered PS of the MUX/DEMUX architecture with the proposed ultra-broadband PS based on SWG metamaterial waveguides in order to achieve a flat and low crosstalk. Additionally, another line of future work that is planned to be carried out in collaboration with Alcyon Photonics S.L. is to expand the number of multiplexed modes, building upon our core architecture (i.e. based on MMIs, PSs and symmetric Y-junctions).

Phase shifters based on subwavelength metamaterial waveguides

Apart from the integration of the SWG PS into more complex photonic systems such as the mode MUX/DEMUX mentioned above, the near future prospects for the ultra-broadband phase shifter focus on studying anisotropy to achieve a polarization-independent behaviour. Similar to the zero-birefringent waveguides introduced in section 2.4.3, it would be necessary to rotate the segments of the SWG waveguides to achieve the same phase shift for both TE and TM polarizations [Luque-González'18, Herrero-Bermello'19b]. In a longer term, it would be interesting to outline a path to make the PS tunable. A first approach could be to leverage the high thermo-optic coefficient of silicon waveguides [Schmid'11].Finally, the proposed SWG PS could find potential applications in coherent communications, polarimetry, quantum photonics, sensing and high-performance MDM transceivers.

Integration and optimization of the beam splitters

Due to the potential demonstrated by the beam splitters proposed in this thesis, these devices are currently being integrated into an SHFT microspectrometer for the SiN platform consisting of 16 spatially distributed interferometers. In addition to spectroscopy, the proposed beam splitters open new venues for telecom, datacom, sensing, and modulation and switching applications. Furthermore, the length of the proposed beam splitter could be further optimized, given the very conservative selection of the taper sections in our current design. According to the simulations these lengths can be further reduced without significantly degrading the performance. Moreover, there is another attractive option to reduce the length of the beam splitter: to replace the linear taper of the strip-to-slot transition by a logarithmic one [Palmer'13].

6.3. Impact of the present work

During the development of the present thesis significant advances have been reported in the fields of mode-division multiplexing, passive phase shifting and optical beam splitting with the implementation of essential building blocks for the next generation of photonic integrated circuits. These achievements pave the way for applications demanding higher capacities and energy-efficient consumption such as optical communications and interconnects, spectroscopy or quantum computing.

The results of this work have led to five high-impact-factor publications (see Appendix C), and 19 contributions to international conferences, 13 of which were invited presentations. The international nature of the work was promoted through research secondments in the University of Malaga, the Centre de Nanosciences et de Nanotechnologies and McGill University, and collaborations with the National Research Council of Canada, STMicroelectronics and Alcyon Photonics S.L.

These outcomes have already resulted in one Spanish patent application (P201731166ES) for the integrated mode converter and multiplexer. An international extension under the patent cooperation treaty (PCT) has already been filed (PCT/EP2018/075753). Because this patent covers in addition to the mode MUX/DEMUX, the phase shifter and other architectures to increase the number of multiplexed modes, in the near future a divisional patent application is expected for the phase shifter based on subwavelength metamaterial waveguides. Moreover, the aforementioned patent application was a key asset in the creation of the spin-off company Alcyon Photonics S.L., devoted to the development of high-end multipurpose photonic building blocks, which currently holds the license for its commercial exploitation.

Appendix A

Geometry and material platforms for silicon photonics

There is a wide range of material platforms and waveguide geometries currently available for the development of silicon-based PICs. This appendix, far from reviewing all of them, intends to introduce the geometry and materials used in this thesis, the motivation to use each material platform and the main differences between them.

One of the simplest and most widely used geometry in integrated optics is the strip waveguide, schematically shown in Fig. A.1. This structure is composed of a core or guiding layer (refractive index n_1) where the light is mostly confined and two surrounding upper and lower layers (refractive index n_2 and n_3). The thickness of each layer is defined during the manufacturing process. At a given wavelength (λ), the transverse dimensions of the guiding layer (height and width) determine whether the waveguide is single mode (only the fundamental mode is supported) or multimode (several modes are supported). In this architecture, it is important to note that the structure of each layer is invariant along the longitudinal section through which the light propagates (z axis).

The difference between refractive indexes of the materials used for the guiding and the cladding layers determines whether the platform is low contrast or high contrast. In this thesis, the main material platform for the design and fabrication of photonic integrated devices is the SOI platform. Nevertheless, the SiN platform has been additionally explored for one of the designs developed in the thesis as it is postulated as a promising candidate to complement the SOI platform in a wide range of applications.

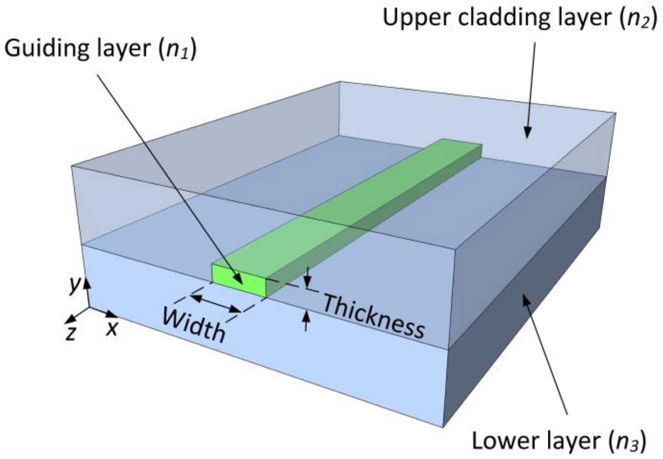

Figure A.1. *Schematic of a strip waveguide consisting of a guiding layer with refractive index* n_1 *(in green), an upper cladding layer with refractive index* n_2 *and a lower layer* n_3.

The silicon-on-insulator platform [Kurdi'88] emerged as a promising solution for cost-effective integration of numerous photonic devices into a single substrate enabled by the high refractive index contrast ($\Delta n \sim 2$) between the silicon waveguide and the buried oxide (BOX) or cladding layers. Since then, the SOI platform has mainly driven the evolution of silicon photonics due to its transparency window covering the 1.1 µm to 3.7 µm wavelength range. Note that the lower bound is limited by the silicon bandgap whereas the upper bound is limited by SiO_2 absorption [Baets'16]. Most of the devices developed in this thesis were fabricated using standard SOI wafers with 220-nm-thick silicon guiding layer and 2-µm-thick BOX layer. The upper cladding thickness and material, either SiO_2 or polymethyl methacrylate (PMMA), depend on each particular device and is mentioned in the corresponding chapter of the thesis. For this waveguide geometry, single-mode condition is given by a silicon waveguide width of 450 nm at the wavelength of 1.55 µm. At the same wavelength, the refractive indexes of Si, SiO_2 and PMMA are $n_{Si} = 3.476$, $n_{SiO_2} = 1.444$ and $n_{PMMA} = 1.481$, respectively [Palik'98, Beadie'15].

As an example, the electric field intensity profile of the fundamental TE and TM modes are shown in Figs. A.2a and A.2b, respectively, at the wavelength of 1.55 µm for a waveguide width of 450 nm and a SiO_2 upper cladding. The effective refractive indexes of both TE and TM modes are also shown in Fig. A.2c for a wavelength range from 1.2 µm to 1.8 µm. These results (i.e. electric field intensity profile and effective refractive indexes) are also depicted in Figs. A.2d, A.2e and A.2 for a 450-nm-wide Si waveguide with a PMMA upper cladding. The modal birefringence is defined as the difference between the effective refractive indexes of the modes with TE and TM polarizations, i.e. $b = n_{TE} - n_{TM}$ [Ye'05]. Owing to the high refractive index contrast, SOI waveguides present a high birefringence and, subsequently, most SOI-based devices operate in a single-polarization state, either TE or TM polarization. In addition, the high modal confinement provides enhanced light-matter interactions, but also results in narrowband devices with a strong sensitivity to fabrication errors.

To relax these limitations, the SiN platform has been proposed as a prominent candidate to complement the SOI platform with a transparency window reaching most of the visible range up to a wavelength of 400 nm [Blumenthal'18]. In this case, the material for the guiding layer is Si_3N_4, whereas SiO_2 is employed for the upper and lower layers. The refractive index of Si_3N_4 is $n_{SiN} = 1.95$ at the wavelength of 1.55 µm [Baudot'17], reducing the contrast of the platform to $\Delta n \sim 0.5$. The lower refractive index contrast of the SiN platform compared to SOI results in an improved robustness against geometrical deviations and lower scattering losses as the modes are less confined in the waveguide and sidewall roughness effect is mitigated. Furthermore, the low thermo-optic coefficient and modal birefringence of SiN waveguides enables the design of polarization-independent devices with low thermal sensitivity [Mikkelsen'18, Durán-Valdeiglesias'19]. One of the devices developed in this thesis was designed and fabricated for the SiN platform with a 600-nm-thick SiN layer deposited onto a 1.4-µm-thick SiO_2 layer and covered by a 1.5-µm-thick SiO_2 upper cladding. Figures A.2g and A.2h show the electric field intensity for fundamental TE- and TM-polarized modes, respectively, when a single-mode waveguide width of 700 nm is considered as an example. The low birefringence between TE and TM modes is shown in Fig. A.2i.

Geometric parameters and performance of single-mode waveguides for both material platforms are shown in Table A.1. The main restriction of the SiN platform is caused by the reduced refractive index contrast compared to SOI, resulting in larger devices, and subsequently, in a lower integration density of PICs. As mentioned earlier, the propagation losses of SiN waveguides are much lower than SOI-based waveguides. However, unless the waveguide length is really long for a particular PIC design (see spatial heterodyne FT spectrometer as an example [Velasco'13b]), the difference between propagation losses of both platforms is barely noticeable at chip scale. Additionally, the high thermo-optic coefficient of the SOI platform is typically leveraged to modify the waveguide refractive index in active devices such as phase shifters, modulators and switches.

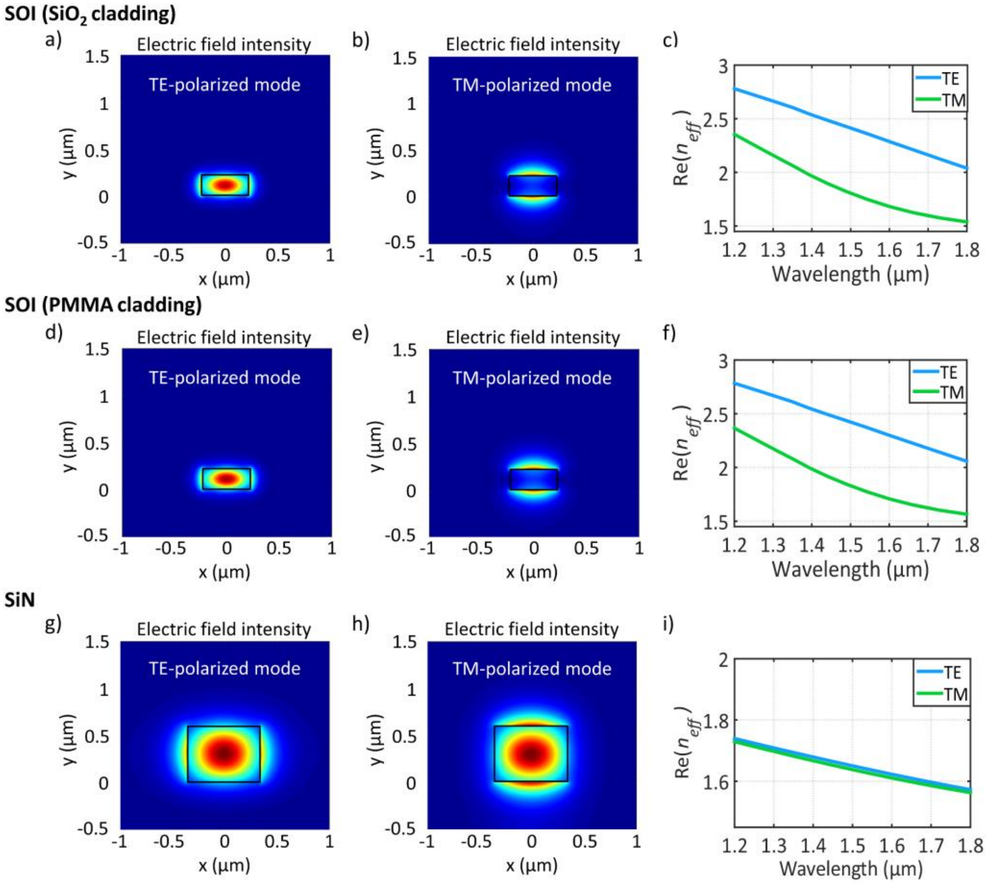

Figure A.2. Electric field intensity of (a) TE and (b) TM modes of a 220-nm-thick by 450-nm-wide SOI strip waveguide with SiO$_2$ upper cladding (black contour) at the wavelength of 1.55 µm. (c) Real part of the effective refractive index of the fundamental TE (in blue) and TM (in green) modes as a function of the wavelength calculated for the same SOI strip waveguide. Electric field intensity of (d) TE and (e) TM modes of a 220-nm-thick by 450-nm-wide SOI strip waveguide with PMMA upper cladding (black contour) at the wavelength of 1.55 µm. (f) Real part of the effective refractive index of the fundamental TE (in blue) and TM (in green) modes as a function of the wavelength calculated for the same SOI strip waveguide. Electric field intensity of (g) quasi-TE and (h) quasi-TM modes in a 600-nm-thick by 700-nm-wide SiN strip waveguide (black contour) at the wavelength of 1.55 µm. (i) Real part of the effective refractive index of the fundamental TE (in blue) and TM (in green) modes as a function of the wavelength calculated for the same SiN strip waveguide.

Table A.1. *Comparison between the material platforms used in this thesis: SOI and SiN. The table presents typical geometric parameters for single-mode interconnection waveguides (waveguide thickness and width), propagation losses, minimum feature size and thermo-optic coefficient. Note: single-mode widths are obtained for the wavelength of 1.55 µm.*

Material platform	Thickness	Single-mode width	Propagation loss	Minimum feature size	Thermo-optic coefficient
SOI	220 nm	450 nm	< 2.4 dB/cm	100 nm	$1.8 \cdot 10^{-4}$ K^{-1}
SiN	600 nm	700 nm	< 0.8 dB/cm	200 nm	$3.5 \cdot 10^{-5}$ K^{-1}

Appendix B

Circuit model for the characterization of phase shifters

This appendix presents the circuit model developed for the characterization of the phase shifters of Chapter IV. The circuit model is based on the transmission matrices of each component of the test MZI in order to simulate the response of the complete test structure as depicted in Fig. B.1c. The transmission matrix of the MZI, **T**, can be obtained by multiplying the matrices of the constituents as follows:

$$\mathbf{T} = \mathbf{M_{MMI}} \left(\mathbf{M_{PS}}\right)^{14} \mathbf{M_{MMI}}, \tag{B.1}$$

where $\mathbf{M_{MMI}}$ and $\mathbf{M_{PS}}$ are the transmission matrices of the SWG MMI and the PSs, respectively.

In order to perform precise simulations of the MZIs depicted in Fig. B.1, additional test structures were included in the mask to fully characterize the SWG MMIs. To this end, two SWG MMIs in an MZI were used with an optical path difference induced by arms of different lengths (instead of the 14 PSs). In this way the matrix $\mathbf{M_{MMI}}$ matrix can be reconstructed using the measured EL, IB and PE:

$$\mathbf{M_{MMI}} = \begin{bmatrix} \eta\sqrt{1-\kappa^2} & \eta\sqrt{\kappa^2}\, e^{j\left(\frac{\pi}{2}+\Delta\varphi\right)} \\ \eta\sqrt{\kappa^2}\, e^{j\left(\frac{\pi}{2}+\Delta\varphi\right)} & \eta\sqrt{1-\kappa^2} \end{bmatrix}, \tag{B.2}$$

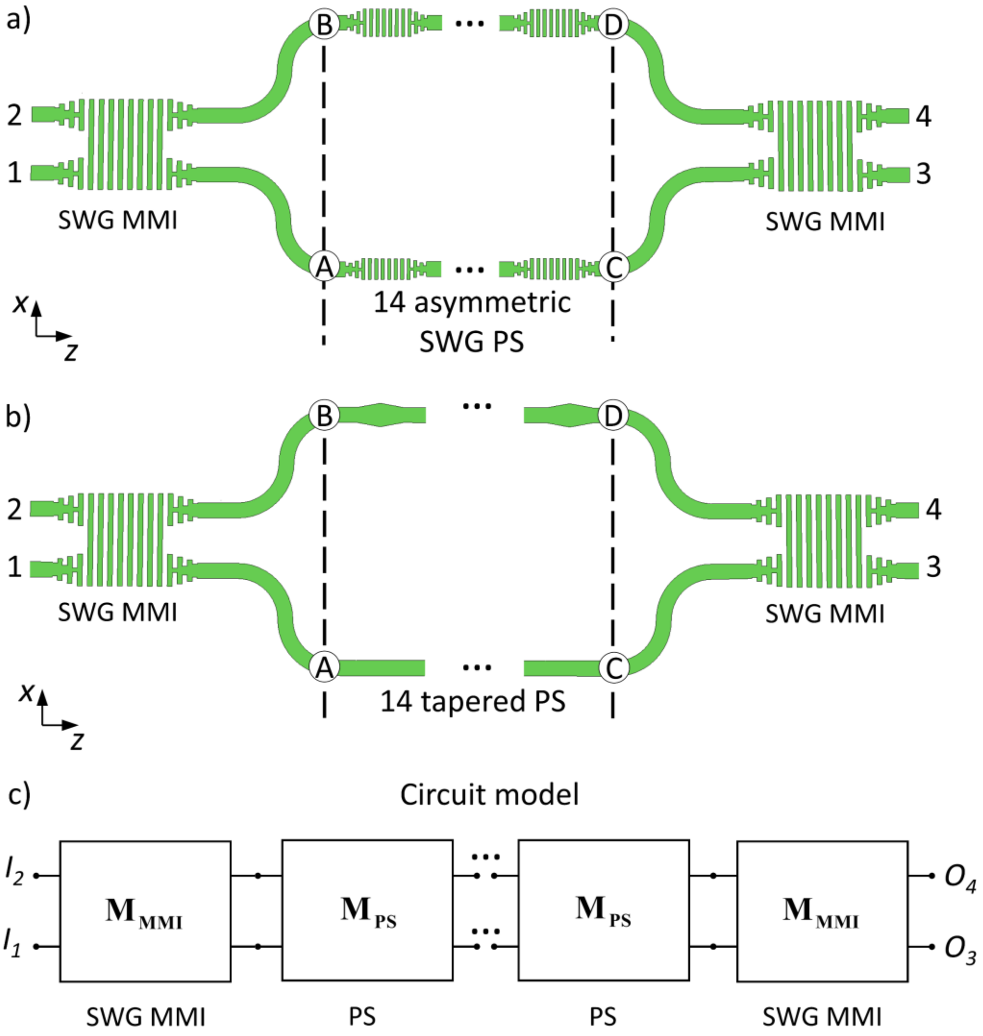

Figure B.1. *Schematic top view of the test structures used for the characterization of (a) the proposed asymmetric SWG PS and (b) the conventional tapered PS. (c) Representation of the circuit model of the test structure using transmission parameters.*

where η is the transmittance obtained from the total EL; κ is the coupling coefficient obtained from the extinction ratio (ER), i.e. difference between adjacent maxima and minima of the spectrum [Wang'16a], and $\Delta\varphi$ is the PE in radians [Voigt'12]:

$$\eta = \sqrt{10^{(\mathrm{EL}/2)/10}}, \tag{B.3}$$

$$\kappa^2 = 0.5 \pm 0.5\sqrt{\frac{1}{10^{\mathrm{ER}/10}}}, \tag{B.4}$$

$$\Delta\varphi = \frac{\pi\left(\lambda_{\mathrm{min,O3}} - \lambda_{\mathrm{min,O4}}\right)}{\mathrm{FSR}} + \frac{\pi}{2}. \tag{B.5}$$

Note that $\lambda_{\mathrm{min,O3}}$ and $\lambda_{\mathrm{min,O4}}$ are the wavelength of the transmission minima at output ports 3 and 4, and FSR is the free spectral range.

On the other hand, the transmission matrix of the PSs is given by:

$$\mathbf{M_{PS}} = \begin{bmatrix} 1 & 0 \\ 0 & e^{j\left(\Delta\Phi_{\mathrm{SIM}}(\lambda) + error\right)} \end{bmatrix}, \tag{B.6}$$

here, $\Delta\Phi_{\mathrm{SIM}}(\lambda)$ is the phase difference of the PSs simulated via 3D FDTD and $error$ is the phase offset introduced by fabrication deviations. Since the only variable undetermined in the circuit model is $error$, its value can be computed through an iterative method until the curves of the circuit model match the measured MZI transmittance. Moreover, the phase shift response of each fabricated PS, $\mathrm{PSE}_{\mathrm{EXP}}(\lambda)$, can be obtained by solving the matrix system for each wavelength when the following transmission matrix is considered:

$$\mathbf{M}^{'}_{\mathbf{PS}} = \begin{bmatrix} 1 & 0 \\ 0 & e^{j\left(\frac{\pi}{2} + \mathrm{PSE}_{\mathrm{EXP}}(\lambda)\right)} \end{bmatrix}. \tag{B.7}$$

Finally, it is necessary to subtract the offset introduced by the fabrication errors in order to compare the PSE with the simulation results:

$$\mathrm{PSE}^{'}_{\mathrm{EXP}} = \mathrm{PSE}_{\mathrm{EXP}}(\lambda) - error, \tag{B.8}$$

where $\mathrm{PSE}'_{\mathrm{EXP}}$ is the wavelength dependence of the PSs without the phase error introduced by the fabrication errors.

Appendix C

Scientific and technological production

International journal papers

1. D. González-Andrade, A. Dias, J. G. Wangüemert-Pérez, A. Ortega-Moñux, A. Herrero-Bermello, Í. Molina-Fernández, R. Halir, P. Cheben, and A. V. Velasco, "Experimental demonstration of a broadband mode multiplexer based on metamaterial waveguides" (Under review).
2. D. González-Andrade, J. M. Luque-González, J. G. Wangüemert-Pérez, A. Ortega-Moñux, P. Cheben, Í. Molina-Fernández, and A. V. Velasco, "Ultra-broadband nanophotonic phase shifter based on subwavelength metamaterial waveguies" *Photon. Res.* **8**, 359 (2020).
3. D. González-Andrade, S. Guerber, E. Durán-Valdeiglesias, D. Pérez-Galacho, X. Le Roux, N. Vulliet, S. Cremer, S. Monfray, E. Cassan, D. Marris-Morini, F. Boeuf, P. Cheben, L. Vivien, A. V. Velasco, and C. Alonso-Ramos, "Ultra-wideband dual-polarization silicon nitride power splitter based on modal engineered slot waveguides," *Opt. Lett.* **45**, 527 (2020).
4. D. González-Andrade, C. Lafforgue, E. Durán-Valdeiglesias, X. Le Roux, M. Berciano, E. Cassan, D. Marris-Morini, A. V. Velasco, P. Cheben, L. Vivien, and C. Alonso-Ramos, "Polarization- and wavelength-agnostic nanophotonic beam splitter", *Sci. Reports* **9**, 3604 (2019).
5. D. González-Andrade, J. G. Wangüemert-Pérez, A. V. Velasco, A. Ortega-Moñux, A. Herrero-Bermello, I. Molina-Fernández, R. Halir, and P. Cheben,

"Ultra-broadband mode converter and multiplexer based on sub-wavelength structures", *IEEE Photonics J.* **10**, 2201010 (2018).

International conferences

1. P. Cheben*, J. H. Schmid, R. Halir, C. Alonso-Ramos, D. Benedikovic, A. Sánchez-Postigo, J. M. Luque-González, D. González-Andrade, D. Pereira-Martín, J. Čtyroký, D. Melati,Y. Grinberg, A. Ortega-Moñux, J. G. Wangüemert-Pérez, I. Molina-Fernández, A. V. Velasco, A. Herrero-Bermello, J. Lapointe, S. Janz, D.-X. Xu, R. Cheriton, M. Kamandar Dezfouli, S. Wang, M. Vachon, L. Vivien, W. N. Ye, J. Litvík and M. Dado, "Recent advances in metamaterial integrated photonics," *IEEE Photonics Conference (IPC)*, San Antonio (United States), September 2019. (Invited)
2. R. Halir*, J. M. Luque-González, A. Sánchez-Postigo, A. Herrero-Bermello, D. González-Andrade, A. Hadij-El-Houati, J. Leuermann, D. Pereira-Martín, A. Ortega-Moñux, J. Čtyroký, G. Wangüemert-Pérez, A. V. Velasco, M. Sánchez-Rodríguez, J. de-Oliva-Rubio, J. H. Schmid, J. Soler Penadés, M. Nedeljkovic, G. Z. Mashanovich, P. Cheben, and Í. Molina-Fernández, "Practical metamaterial photonics," *IEEE 16th International Conference on Group IV Photonics (GFP)*, Singapore (Singapore), August 2019. (Invited)
3. D. González-Andrade*, C. Lafforgue, E. Durán-Valdeiglesias, X. Le Roux, M. Berciano, E. Cassan, D. Marris-Morini, A. V. Velasco, P. Cheben, L. Vivien, and C. Alonso-Ramos, "Ultra-broadband polarization-independent silicon beam splitter based on modal and symmetry engineering," *IEEE 16th International Conference on Group IV Photonics (GFP)*, Singapore (Singapore), August 2019. (Oral)
4. P. Cheben*, C. Alonso-Ramos, R. Halir, J. H. Schmid, J. Čtyroký, D. Benedikovic, A. Ortega-Moñux, A. Sánchez-Postigo, D. González-Andrade, J. G. Wangüemert-Pérez, I. Molina-Fernández, A. V. Velasco, A. Herrero-Bermello, J. M. Luque-González, D. Pereira-Martín, J. Lapointe, S. Janz, D.-X. Xu, D. Melati, Y. Grinberg, S. Wang, M. Vachon, M. Kamandar Dezfouli, R. Cheriton, V. Vakarin, M. Dado, D. Oser, F. Mazeas, D. Pérez-Galacho, X. Le Roux, E. Durán-Valdeiglesias, L. Labonte, S. Tanzilli, E. Cassan, D. Marris-Morini, W. N. Ye, and L. Vivien, "Subwavelength metamaterial nanophotonic waveguide devices," *Photonic Networks and Devices*, Burlingame (United States), July 2019. (Invited)
5. P. Cheben*, C. Alonso-Ramos, R. Halir, J. Schmid, J Ctyroky, D. Benedikovic, A. Ortega-Monux, A. Sanchez-Postigo, D. Gonzalez-Andrade, G. Wangüemert-

Pérez, I. Molina-Fernandez, Aitor V. Velasco, A. Herrero-Bermello, J. M. Luque-Gonzalez, D. Pereira-Martin, J. Lapointe, S. Janz, D.-X. Xu, D. Melati, Y. Grinberg, S. Wang, M. Vachon, M. Kamandar Dezfouli, R. Cheriton, V. Vakarin, M. Dado, D. Oser, and F. Mazeas, "Recent advances in subwavelength metamaterial silicon photonics," *International Conference on Metamaterials, Photonic Crystals and Plasmonics (META)*, Lisbon (Portugal), July 2019. (Invited)

6. R. Halir*, J. M. Luque-González, A. Sánchez-Postigo, A. Herrero-Bermello, D. González-Andrade, A. Hadij-El-Houati, J. Leuermann, D. Pereira-Martín, A. Ortega-Moñux, J. Čtyroký, G. Wangüemert-Pérez, A. V. Velasco, M. Sánchez-Rodríguez, J. de-Oliva-Rubio, J. H. Schmid, J. Soler-Penadés, M. Nedeljkovic, G. Z. Mashanovich, P. Cheben, and Í. Molina-Fernández, "High-performance silicon photonic devices based on practical metamaterials," *OptoElectronics and Communications Conference (OECC/PSC)*, Fukuoka (Japan), July 2019. (Invited)
7. D. González-Andrade, C. Lafforgue, E. Durán-Valdeiglesias, X. Le Roux, M. Berciano, E. Cassan, D. Marris-Morini, A. V. Velasco, P. Cheben, L. Vivien, and C. Alonso-Ramos*, "Ultra-broadband dual-polarization beam splitter based on modal engineered slot waveguides," *Photonics & Electromagnetics Research Symposium (PIERS)*, Rome (Italy), June 2019. (Oral)
8. C. Alonso-Ramos*, P. Cheben, R. Halir, J. H. Schmid, J. Čtyroký, D. Benedikovic, A. Ortega-Moñux, A. Sánchez-Postigo, D. González-Andrade, J. G. Wangüemert-Pérez, I. Molina-Fernández, A. V. Velasco, A. Herrero-Bermello5, J. M. Luque-González, D. Pereira-Martín, J. Lapointe, S. Janz, D.-X. Xu, D. Melati, Y. Grinberg, S. Wang, M. Vachon, M. Kamandar Dezfouli, R. Cheriton, V. Vakarin, M. Dado, D. Oser, F. Mazeas, D. Pérez-Galacho, X. Le Roux, E. Durán-Valdeiglesias, L. Labonte, S. Tanzilli, E. Cassan, D. Marris-Morini, and L. Vivien, "Recent advances on nanostructures metamaterial silicon photonics," *Photonics & Electromagnetics Research Symposium (PIERS)*, Rome (Italy), June 2019. (Invited)
9. P. Cheben*, J. H. Schmid, R. Halir, A. Ortega-Moñux, J. G. Wangüemert-Pérez, I. Molina-Fernández, A. Sánchez-Postigo, J M. Luque-González, D. Pereira-Martín, J. Čtyroký, D. González-Andrade, A. V. Velasco, A. Herrero-Bermello, C. Alonso-Ramos, D. Benedikovic, J. Lapointe, S Janz, D.-X. Xu, D. Melati, Y. Grinberg, M. Kamandar Dezfouli, S. Wang, M. Vachon, V. Vakarin, L. Vivien, J. Litvík, and M. Dado, "Metamarerial integrated photonics," *Photonics North*, Québec (Canada), May 2019. (Invited)

10. D. González-Andrade, C. Lafforgue, E. Durán-Valdeiglesias, X. Le Roux, M. Berciano, E. Cassan, D. Marris-Morini, A. V. Velasco, P. Cheben, L. Vivien, and C. Alonso-Ramos*, "Dual-polarization Ultra-wideband Nanophotonic Beam Splitter," *European Conference on Integrated Optics (ECIO),* Ghent (Belgium), April 2019. (Oral)
11. A. V. Velasco*, D. González-Andrade, A. Herrero-Bermello, A. Dias-Ponte, J. G. Wangüemert-Pérez, A. Ortega-Moñux, I. Molina-Fernández, R. Halir, J. M. Luque-González, and P. Cheben, "Subwavelength silicon photonic metamaterials for mode multiplexing and polarization control," *Photonics West*, San Francisco (United States), February 2019. (Invited)
12. P. Cheben*, R. Halir, J. H. Schmid, J. Čtyroký, D. Benedikovic, C. Alonso-Ramos, A. Ortega-Moñux, A. Sánchez-Postigo, D. González-Andrade, J. G. Wangüemert-Pérez, I. Molina-Fernández, A. V. Velasco, A. Herrero-Bermello, J. M. Luque-González, D. Pereira-Martín, J. Lapointe, S. Janz, D.-X. Xu, D. Melati, Y. Grinberg, S. Wang, M. Vachon, V. Vakarin, J. Litvík, M. Dado, and J. Müllerová, "Subwavelength Silicon Photonics," *Photonics West*, San Francisco, (United States), February 2019. (Invited)
13. J. G. Wangüemert-Pérez*, A. Sánchez-Postigo, A. Hadif-ElHouati, D. Pereira-Martín, J. M. Luque-González, J. Leuermann, A. Ortega-Moñux, R. Halir, I. Molina-Fernández, P. Cheben, D.-X. Xu, J. H. Schmid, J. Ctyroky, J. Litvík, J. Soler-Penades, M. Nedeljkovic, G. Z. Mashanovich, D. González-Andrade, and A. V. Velasco, "Subwavelength metamaterial for communications and sensing," *SPIE/COS Photonics Asia*, Beijing (China), October 2018. (Invited)
14. R. Halir*, J. M. Luque-González, A. Herrero-Bermello, D. González-Andrade, A. Sánchez-Postigo, J. G. Wangüemert-Pérez, J. Ctyroky, A. V. Velasco, I. Molina-Fernández, J. H. Schmid, J. Soler-Penades, M. Nedeljkovic, G. Mashanovich, A. Ortega-Moñux, "Designing high performance devices with silicon subwavelength structures," *European Optical Society Biennial Meeting (EOSAM),* Delft (Netherlands), October 2018. (Invited)
15. P. Cheben, R. Halir, J. H. Schmid, J. Ctyroky, D. Benedikovic, C. Alonso-Ramos, A. Ortega-Moñux, A. Sánchez-Postigo, D. González-Andrade, J. G. Wangüemert-Pérez, I. Molina-Fernández, A. V. Velasco, A. Herrero-Bermello, J. M. Luque-González, D. Pereira-Martín, J. Lapointe, S. Janz, D.-X. Xu, D. Melati, Y. Grinberg, S. Wang, M. Vachon, V. Vakarin, L. Vivien, J. Litvík, J. Müllerová, and M. Dado, "Subwavelength Silicon Photonic Metamaterial Waveguide

Devices," *European Conference on Optical Communications (ECOC)*, Rome (Italy), September 2018. (Invited)

16. D. González-Andrade, J. G. Wangüemert-Pérez, A. V. Velasco, A. Ortega-Moñux, A. Herrero-Bermello, R. Halir, P. Cheben and I. Molina-Fernández*, "Ultra-Broadband Converter and Multiplexer Using a Sub-Wavelength Metamaterial," *European Conference on Optical Communications (ECOC)*, Rome (Italy), September 2018. (Oral)
17. D. González-Andrade*, J. G. Wangüemert-Pérez, A. V. Velasco, A. Ortega-Moñux, A. Herrero-Bermello, R. Halir, and P. Cheben, "Sub-wavelength engineered ultra-broadband mode multiplexer," *SPIE Photonics Europe*, Strasbourg (France), April 2018. (Oral)
18. D. González-Andrade*, A. V. Velasco, J. G. Wangüemert-Pérez, A. Ortega-Moñux, R. Halir, and P. Cheben, "Ultra-broadband mode (de)multiplexer based on a sub-wavelength engineered MMI coupler," *IEEE Photonics Conference (IPC)*, Orlando (United States), October 2018. (Oral)
19. J. G. Wangüemert-Pérez*, A. Sánchez-Postigo, J. M. Luque-González, J. D. Sarmiento-Merenguel, R. Halir, A. Ortega-Moñux, I. Molina-Fernández, P. Cheben, D.-X. Xu, J. Schmid, J. Soler-Penades, M. Nedeljkovic, G. Z. Mashanovich, C. Alonso-Ramos, D. Pérez-Galacho, D. González-Andrade, and A. V. Velasco, "Subwavelength metamaterial structures for silicon photonics," *Photonics North*, Ottawa (Canada), June 2017. (Invited)

Patent applications

1. D. González-Andrade, A. V. Velasco, I. Molina-Fernández, P. Corredera-Guillén, R. Halir, A. Ortega-Moñux, and J. G. Wangüemert-Pérez, "Integrated mode converter and multiplexer," **P201731166ES** (September 2017).

   Licensed to Alcyon Photonics as part of the spin-off company foundation.

2. D. González-Andrade, A. V. Velasco, I. Molina-Fernández, P. Corredera-Guillén, R. Halir, A. Ortega-Moñux, and J. G. Wangüemert-Pérez, "Integrated mode converter and multiplexer," **PCTES2018075753** (September 2018).

   Licensed to Alcyon Photonics.

Bibliography

[Aboketaf’10] A. A. Aboketaf, A. W. Elshaari, and S. F. Preble, “Optical time division multiplexer on silicon chip,” *Opt. Express* **18**, 13529 (2010).

[Almeida’04] V. R. Almeida, Q. Xu, C. A. Barrios, and M. Lipson, “Guiding and confining light in void nanostructures,” *Opt. Lett.* **29**, 1209 (2004).

[Alonso-Ramos’14] C. Alonso-Ramos, P. Cheben, A Ortega-Moñux, J. H. Schmid, D.-X. Xu, and I. Molina-Fernández, “Fiber-chip grating coupler based on interleaved trenches with directionality exceeding 95%,” *Opt. Lett.* **39**, 5351 (2014).

[Alonso-Ramos’19] C. Alonso-Ramos, X. Le Roux, J. Zhang, D. Benedikovic, V. Vakarin, E. Durán-Valdeiglesias, D. Oser, D. Pérez-Galacho, F. Mazeas, L. Labonté, S. Tanzilli, E. Cassan, D. Marris-Morini, P. Cheben, and L. Vivien, “Diffraction-less propagation beyond the sub-wavelength regime: a new type of nanophotonic waveguide,” *Sci. Rep.* **9**, 5347 (2019).

[AppliedNanotools’19] Applied Nanotools Inc., “NanoSOI fabrication process,” https://www.appliednt.com/nanosoi/ (2019).

[Baets’16] R. Baets, A. Z. Subramanian, S. Clemmen, B. Kuyken, P. Bienstman, N. Le Thomas, G. Roelkens, D. Van Thourhout, P. Helin, and S. Severi, “Silicon photonics: silicon nitride versus silicon-on-insulator,” in *Optical Fiber Communication Conference (OFC)*, p. Th3J.1, Anaheim (USA), Mar 2016.

[Baets’19] R. Baets and B. Kuyken, “High speed phase modulators for silicon photonic integrated circuits: a role for lithium niobate?,” *Adv. Photon.* **1**, 030502 (2019).

[Bagheri’09] S. Bagheri and W. M. Green, “Silicon-on-insulator mode-selective add-drop unit for on-chip mode-division multiplexing,” in *IEEE 6th International Conference on Group IV Photonics (GFP),* p. ThP19, San Francisco (USA), Sep 2009.

[Barwicz’16] T. Barwicz, Y. Taira, T. W. Lichoulas, N. Boyer, Y. Martin, H. Numata, J.-W. Nah, S. Takenobu, A. Janta-Polczynski, E. L. Kimbrell, R. Leidy, M. H. Khater, S. Kamlapurkar, S. Engelmann, Y. A. Vlasov, and P. Fortier, “A novel approach to photonic packaging leveraging existing high-throughput microelectronic facilities,” *IEEE J. Sel. Top. Quantum Electron.* **22**, 8200712 (2016).

[Baudot’17] C. Baudot, M. Douix, S. Guerber, S. Crémer, N. Vulliet, J. Planchot, R. Blanc, L. Babaud, C. Alonso-Ramos, D. Benedikovic, D. Pérez-Galacho, S. Messaoudène, S. Kerdiles, P. Acosta-Alba, C. Euvrard-Colnat, E. Cassan, D. Marris-Morini, L. Vivien, and F. Boeuf, “Developments in 300mm silicon photonics using traditional CMOS fabrication methods and materials,” in *2017 IEEE International Electron Devices Meeting (IEDM)*, p. 34.3, San Francisco (USA), Dec 2017.

[Beadie’15] G. Beadie, M. Brindza, R. A. Flynn, A. Rosenberg, and J. S. Shrik, “Refractive inex measurements of poly(methyl methacrylate) (PMMA) from 0.4-1.6 µm,” *Appl. Opt.* **54**, F139 (2015).

[Benedikovic’15] D. Benedikovic, P. Cheben, J. H. Schmid, D.-X. Xu, B. Lamontagne, S. Wang, J. Lapointe, R. Halir, A. Ortega-Moñux, S. Janz, and M. Dado, “Subwavelength index engineered surface grating coupler with sub-decibel efficiency for 220-nm silicon-on-insulator waveguides,” *Opt. Express* **23**, 22628 (2015).

[Benedikovic’17] D. Benedikovic, C. Alonso-Ramos, D. Pérez-Galacho, S. Guerber, V. Vakarin, G. Marcaud, X. Le Roux, E.

Cassan, D. Marris-Morini, P. Cheben, F. Boeuf, C. Baudot and L. Vivien, “L-shaped fiber-chip grating couplers with high directionality and low reflectivity fabricated with deep-UV lithography,” *Opt. Lett.* **42**, 3439 (2017).

[Berdagué’82] S. Berdagué and P. Facq, “Mode division multiplexing in optical fibers,” *Appl. Opt.* **21**, 1950 (1982).

[Birner’01] A. Birner, R. B. Wehrspohn, U. M. Gösele, and K. Busch, “Silicon-based photonic crystals,” *Adv. Mater.* **13**, 377 (2001).

[Bloch’28] F. Bloch, “Über die quantenmechanik der elektronen in kristallgittern,” *Z. Phys.* **52**, 555 (1928).

[Blumenthal’18] D. J. Blumenthal, R. Heideman, D. Geuzebroek, A. Leinse, and C. Roeloffzen, “Silicon nitride in silicon photonics,” *Proc. IEEE* **106**, 2209 (2018).

[Bock’10] P. J. Bock, P. Cheben, J. H. Schmid, J. Lapointe, A. Delâge D.-X. Xu, S. Janz, A. Densmore, and T. J. Hall, “Subwavelength grating crossings for silicon wire waveguides,” *Opt. Express* **18**, 16146 (2010).

[Boeuf’15] F. Boeuf, S. Crémer, E. Temporiti, M. Ferè, M. Shaw, C. Baudot, N. Vulliet, T. Pinguet, A. Mekis, G. Masini, H. Petiton, P. Le Maitre, M. Traldi, and L. Maggi, “Silicon photonics R&D and manufacturing on 300-nm wafer platform,” *J. Lightwave Technol.* **34**, 286 (2015).

[Bragg’13] W. H. Bragg and W. L. Bragg, “The reflection of X-rays by crystals,” *Proc. R. Soc. Lond. A* **88**, 428 (1913).

[Burla’14] M. Burla, L. Romero-Cortés, M. Li, X. Wang, L. Chrostowski, and J. Azaña, “On-chip programmable ultra-wideband microwave photonic phase shifter and true time delay unit,” *Opt. Lett.* **39**, 6181 (2014).

[Burns'75] W. K. Burns and A. F. Milton, "Mode conversion in planar-dielectric separating waveguides," *IEEE J. Quantum Electron.* **11**, 32 (1975).

[C2N'20] C2N facility, "The technology facility of C2N," https://www.c2n.universite-paris-saclay.fr/en/platforms/technology-facility/ (2020).

[Camacho-Aguilera'12] R. E. Camacho-Aguilera, Y. Cai, N. Patel, J. T. Bessette, M. Romagnoli, L. C. Kimerling, and J. Michel, "An electrically pumped germanium laser," *Opt. Express* **20**, 11316 (2012).

[Cassedy'63] E. S. Cassedy and A. A. Oliner, "Dispersion relations in time-space periodic media: Part I – Stable interactions," *Proc. IEEE* **51**, 1342 (1963).

[Chaganti'06] K. Chaganti, I. Salakhutdinov, I. Avrutsky, and G. W. Auner, "A simple miniature optical spectrometer with a planar waveguide grating coupler in combination with a plano-convex lens," *Opt. Express* **14**, 4064 (2006).

[Chang'08] Q. Chang, Q. Li, Z. Zhang, M. Qiu, T. Ye, and Y. Su, "A tunable broadband photonic RF phase shifter based on a silicon microring resonator," *IEEE Photon. Technol. Lett.* **21**, 60 (2008).

[Chang'18a] W. Chang, X. Ren, Y. Ao, L. Lu, M. Cheng, L. Deng, D. Liu, and M. Zhang, "Inverse design and demonstration of and ultracompact broadband dual-mode 3 dB power splitter," *Opt. Express* **26**, 24135 (2018).

[Chang'18b] W. Chang, L. Lu, X. Ren, D. Li, Z. Pan, M. Cheng, D. Liu, and M. Zhang, "Ultra-compact mode (de) multiplexer base on subwavelength asymmetric Y-junction," *Opt. Express* **26**, 8162 (2018).

[Cheben'06] P. Cheben, D.-X. Xu, S. Janz, and A. Densmore, "Subwavelength waveguide grating for mode conversion and light coupling in integrated optics," *Opt. Express* **14**, 4695 (2006).

[Cheben'10] P. Cheben, P. J. Bock, J. H. Schmid, J. Lapointe, S. Janz, D.-X. Xu, A. Densmore, A. Delâge, B. Lamontagne, and T. J. Hall, "Refractive index engineering with subwavelength gratings for efficient microphotonic couplers and planar waveguide multiplexers," *Opt. Lett.* **35**, 2526 (2010).

[Cheben'15] P. Cheben, J. H. Schmid, S. Wang, D.-X. Xu, M. Vachon, S. Janz, J. Lapointe, Y. Painchaud, and M.-J. Picard, "Broadband polarization independent nanophotonic coupler for silicon waveguides with ultra-high efficiency," *Opt. Express.* **23**, 22553 (2015).

[Cheben'18] P. Cheben, R. Halir, J. H. Schmid, H. A. Atwater, and D. R. Smith, "Subwavelength integrated photonics," *Nature* **560**, 565 (2018).

[Chen'15a] S. Chen, Y. Shi, S. He, and D. Dai, "Compact monolithically-integrated hybrid (de)multiplexer based on silicon-on-insulator nanowires for PDM-WDM systems," *Opt. Express* **23**, 12840 (2015).

[Chen'15b] D. Chen, X. Xiao, L. Wang, Y. Yu, W. Liu, and Q. Yang, "Low-loss and fabrication tolerant silicon mode-order converters based on novel compact tapers," *Opt. Express* **23**, 11152 (2015).

[Chen'17] X. Chen, W. Liu, Y. Zhang, and Y. Shi, "Polarization-insensitive broadband 2×2 3 dB power splitter based on silicon-bent directional couplers," *Opt. Lett.* **42**, 3738 (2017).

[Chen'18] X. Chen, M. M. Milosevic, S. Stanković, S. Reynolds, T. Domínguez-Bucio, K. Li, D. J. Thomson, F. Gardes, and G. T. Reed, "The emergence of silicon photonics as a flexible technology platform," *Proc. IEEE* **106**, 2101 (2018).

[Cheng’18] Q. Cheng, M. Bahadori, M. Glick, S. Rumbley, and K. Bergman, “Recent advances in optical technologies for data centers: a review,” *Optica* **5**, 1354 (2018).

[Cherchi’14] M. Cherchi, S. Ylinen, M. Harjanne, M. Kapulainen, T. Vehmas, and T. Aalto, “Unconstrained splitting ratios in compact double-MMI couplers,” *Opt. Express* **22**, 9245 (2014).

[Chrostowski’15] L. Chrostowski and M. Hochberg, *Silicon photonics design: from devices to systems* (Cambridge University Press, 2015).

[Cisco’18] C. G. C. Index, “Cisco global cloud index: forecast and methodology, 2016-2021,” *Cisco White Paper* (2018).

[Čtyroký’18] J. Čtyroký, J. G. Wangüemert-Pérez, P. Kwiecien, I. Richter, J. Litvik, J. H. Schmid, Í. Molina-Fernández, A. Ortega-Moñux, M. Dado, and P. Cheben, “Design of narrowband Bragg spectral filters in subwavelength grating metamaterial waveguides,” *Opt. Express* **26**, 179 (2018).

[DAgostino’15] D. D’Agostino, G. Carnicella, C. Ciminelli, P. Thijs, P. J. Veldhoven, H. Ambrosius, and M. Smit, “Low-loss passive waveguides in a generic InP foundry process via local diffusion of zinc,” *Opt. Express* **23**, 25143 (2015).

[Dai’13] D. Dai, J. Wang, and Y. Shi, “Silicon mode (de)multiplexer enabling high capacity networks-on-chip with a single-wavelength-carrier light,” *Opt. Lett.* **38**, 1422 (2013).

[Dai’14] D. Dai and J. E. Bowers, “Silicon-based on-chip multiplexing technologies and devices for Peta-bit optical interconnects,” *Nanophotonics* **3**, 283 (2014).

[Dai’18] D. Dai, C. Li, S. Wang, H. Wu, Y. Shi, Z. Wu, S. Gao, T. Dai, H. Yu, and H.-K. Tsang, “10-channel mode (de)multiplexer with dual polarizations," *Laser Photon. Rev.* **12**, 1700109 (2018).

[Dändliker'00] R. Dändliker, "Concept of modes in optics and photonics," in *Sixth International Conference on Education and Training in Optics and Photonics (ETOP'99)*, vol. **3831**, p. 193-198, Cancun (Mexico), Jun 2010.

[Davison'96] S. G. Davison and M. Stęślicka, *Basic Theory of Surface States* (Oxfotd University Press, 1996).

[Debnath'18] K. Debnath, D. J. Thomson, W. Zhang, A. Z. Khokhar, C. Littlejohns, J. Byers, L. Mastronardi, M. K. Husain, K. Ibukuro, F. Y. Gardes, G. T. Reed, and S. Saito, "All-silicon carrier accumulation modulator based on a lateral metal-oxide-semiconductor capacitor," *Photon. Res.* **6**, 373 (2018).

[DeMiguel'18] J. L. De Miguel, J Galindo-Santos, C. Pulido de Torres, P. Salgado, A. V. Velasco, and P. Corredera, "Experimental demonstration of low-uncertainty calibration methods for Bragg grating interrogators," *Sensors* **18**, 1895 (2018).

[Ding'11] Y. Ding, H. Hu, M. Galili, J. Xu, L. Liu, M. Pu, H. C. H. Mulvad, L. K. Oxenløwe, C. Peucheret, P. Jeppesen, X. Zhang, D. Huang, and H. Ou, "Generation of a 640 Gbits/s NRZ OTDM signal using a silicon microring resonator," *Opt. Express* **19**, 6471 (2011).

[Ding'13] Y. Ding, J. Xu, F. Da Ros, B. Huang, H. Ou, and C. Peucheret, "On-chip two-mode division multiplexing using tapered directional coupler-based mode multiplexer and demultiplexer," *Opt. Express* **21**, 10376 (2013).

[Djordjevic'11] S. S. Djordjevic, L. W. Luo, S. Ibrahim, N. K. Fontaine, C. B. Poitras, B. Guan, L. Zhou, K. Okamoto, Z. Ding, M. Lipson, and S. J. B. Yoo, "Fully reconfigurable silicon photonic lattice filters with four cascaded unit cells," *IEEE Photon. Technol. Lett.* **23**, 42 (2011).

[Doerr'10] C. R. Doerr, P. J. Winzer, Y.-K. Chen, S. Chandrasekhar, M. S. Rasras, L. Chen, T.-Y. Liow, K.-W. Ang, and G.-Q. Lo, "Monolithic polarization and phase diversity coherent receiver in silicon," *J. Lightwave Technol.* **28**, 520 (2010).

[Dong'12] P. Dong, C. Xie, L. Chen, L. L. Buhl, and Y.-K. Chen, "112-Gb/s monolithic PDM-QPSK modulator in silicon," *Opt. Express.* **20**, B624 (2012).

[Dong'13] P. Dong, X. Liu, S. Chandrasekhar, L. L. Buhl, R. Aroca, Y. Baeyens, and Y.-K. Chen, "224-Gb/s PDM-16-QAM modulator and receiver based on silicon photonic integrated circuits," in *Optical Fiber Communication Conference and Exposition and the National Fiber Optic Engineers Conference (OFC/NFOEC)*, p. PDP5C.6, Anaheim (USA), Mar 2013.

[Dong'14] P. Dong, X. Liu, S. Chandrasekhar, L. L. Buhl, R. Aroca, and Y.-K. Chen, "Monolithic silicon photonic integrated circuits for compact 100^{+} Gb/s coherent optical receivers and transmitters," *IEEE J. Sel. Top. Quantum Electron.* **20**, 6100108 (2013).

[Dorin'14] B. A. Dorin and N. Y. Winnie, "Two-mode division multiplexing in a silicon-on-insulator ring resonator," *Opt. Express* **22**, 4547 (2014).

[Driscoll'13] J. B. Driscoll, R. R. Grote, B. Souhan, J. I. Dadap, M. Lu, and R. M. Osgood, Jr., "Asymmetric Y junctions in silicon waveguides for on-chip mode-division multiplexing," *Opt. Lett.* **38**, 1854 (2013).

[Driscoll'18] J. B. Driscoll, P. Doussiere, S. Islam, R. Narayan, W. Lin, H. Mahalingam, J. S. Park, Y. Lin, K. Nguyen, K. Roelofs, A. Dahal, R. Venables, L. Liao, R. Jones, D. Zhu, S. Priyadarshi, B. Parthasarathy, and Y. Akulova, "First 400G 8-channel CWDM silicon photonic integrated transmitter," in *IEEE 15th International Conference on Group IV Photonics (GFP)*, Cancun (Mexico), Aug. 2018.

[Dumon'04] P. Dumon, W. Bogaerts, J. Van Campenhout, V. Wiaux, J. Wouters, S. Becks, and R. Baets, "Low-loss photonic wires and compact ring resonators in silicon-on-insulator," in *Photonic Crystal Materials and Nanostructures (SPIE Photonics Europe)*, Strasbourg (France), Sep. 2004.

[Durán-Valdeiglesias'19] E. Durán-Valdeiglesias, S. Guerber, D. Oser, X. Le Roux, D. Benedikovic, D. Pérez-Galacho, N. Vulliet, S. Cremer, S. Monfray, E. Cassan, D. Marris-Morini, C. Baudot, F. Boeuf, L Vivien, and C. Alonso-Ramos, "Dual-polarization silicon nitride Bragg filters with low thermal sensitivity," *Opt. Lett.* **44**, 4578 (2019).

[Estevez'12] M. C. Estevez, M. Alvarez, and L. M. Lechuga, "Integrated optical devices for lab-on-a-chip biosensing applications," *Laser Photon. Rev.* **6**, 463 (2012).

[FemSIM'19] FemSIM, "RSoft FEM generalized mode solver," https://www.synopsys.com/photonic-solutions/rsoft-photonic-device-tools/passive-device-femsim.html (2019).

[Feng'07] N.-N. Feng, R. Sung, L. C. Kimerling, and J. Michel, "Lossless strip-to-slot waveguide transformer," *Opt. Lett.* **32**, 1250 (2007).

[Feng'13] D. Feng, W. Qiang, H. Liang, B. J. Luff, and M. Asghari, "High-speed receiver technology on the SOI platform," *IEEE J. Sel. Top. Quantum Electron.* **19**, 3800108 (2013).

[Field'49] L. M. Field, "Some slow-wave structures for travelling wave tubes," *Proc. IRE* **37**, 34 (1949).

[Flanders’74] D. C. Flanders, H. Kogelnik, R. V. Schmidt, and C. V. Shank, “Grating filter for thin film optical waveguides,” *Appl. Phys. Lett.* **24**, 194 (1974).

[Floquet’83] M. G. Floquet, “Sur les équations différentielles linéaires a coefficients périodiques,” *Ann. Sci. Éc. Norm. Supér.* **12**, 47 (1883).

[Florjańczyk’07] M. Florjańczyk, P. Cheben, S. Janz, A. Scott, B. Solheim, and D.-X. Xu, “Multiaperture planar waveguide spectrometer formed by arrayed Mach-Zehnder interferometers,” *Opt. Express* **15**, 18176 (2007).

[Flueckiger’16] J. Flueckiger, S. Schmidt, V. Donzella, A. Sherwali, D. M. Ratner, L. Chrostowski, and K. C. Cheung, “Sub-wavelength grating for enhanced ring resonator biosensor,” *Opt. Express* **24**, 15672 (2016).

[Frandsen’04] L. H. Frandsen, P. I. Borel, Y. X. Zhuang, A. Harpøth, M. Thorhauge, M. Kristensen, W. Bogaerts, P. Dumon, R. Baets, V. Wiaux, J. Wouters, and S. Beckx, “Ultralow-loss 3-dB photonic crystal waveguide splitter,” *Opt. Lett.* **29**, 1623 (2004).

[Frellsen’16] L. F. Frellsen, Y. Ding, O. Sigmund, and L. H. Frandsen, “Topology optimized mode multiplexing in silicon-on-insulator photonic wire waveguides,” *Opt. Express* **24**, 16866 (2016).

[FullWAVE’19] FullWAVE, “RSoft FDTD simulation software for photonic structures,” https://www.synopsys.com/photonic-solutions/rsoft-photonic-device-tools/passive-device-fullwave.html (2019).

[Gabrielli’12] L. H. Gabrielli, D. Liu, S. G. Johnson, and M. Lipson, “On-chip transformation optics for multimode waveguide bends,” *Nat. Commun.* **3**, 1217 (2012).

[Gaeta’19]	A. L. Gaeta, M. Lipson, and T. J. Kippenberg, “Photonic-chip-based frequency combs,” *Nat. Photonics* **13**, 158 (2019).
[González-Andrade’18]	D. González-Andrade, J. G. Wangüemert-Pérez, A. V. Velasco, A. Ortega-Moñux, A. Herrero-Bermello, I. Molina-Fernández, R. Halir, and P. Cheben, “Ultra-broadband mode converter and multiplexer based on sub-wavelength structures,” *IEEE Photonics J.* **10**, 2201010 (2018).
[González-Andrade’19]	D. González-Andrade, C. Lafforgue, E. Durán-Valdeiglesias, X. Le Roux, M. Berciano, E. Cassan, D. Marris-Morini, A. V. Velasco, P. Cheben, L. Vivien, and C. Alonso-Ramos, “Polarization- and wavelength-agnostic nanophotonic beam splitter,” *Sci. Rep.* **9**, 3604 (2019).
[González-Andrade’20a]	D. González-Andrade, J. M. Luque-González, J. G. Wangüemert-Pérez, A. Ortega-Moñux, P. Cheben, Í. Molina-Fernández, and A. V. Velasco, “Ultra-broadband nanophotonic phase shifter based on subwavelength metamaterial waveguies”, *Photon. Res.* **8**, 359 (2020).
[González-Andrade’20b]	D. González-Andrade, S. Guerber, E. Durán-Valdeiglesias, D. Pérez-Galacho, X. Le Roux, N. Vulliet, S. Cremer, S. Monfray, E. Cassan, D. Marris-Morini, F. Boeuf, P. Cheben, L. Vivien, A. V. Velasco, and C. Alonso-Ramos, “Ultra-wideband dual-polarization silicon nitride power splitter based on modal engineered slot waveguides,” *Opt. Lett.* **45**, 527 (2020).
[Greenberg’05]	M. Greenberg and M. Orenstein, “Multimode add-drop multiplexing by adiabatic linearly tapered coupling,” *Opt. Express* **13**, 9381 (2005).
[Gu’96]	C. Gu and P. Yeh, “Form birefringence dispersion in periodic layered media,” *Opt. Lett.* **21**, 504 (1996).

[Guerber'18a] S. Guerber, C. Alonso-Ramos, D. Benedikovic, D. Perez-Galacho, X. Le Roux, N. Vulliet, S. Crémer, L. Babaud, J. Planchot, D. Benoit, P. Chantraine, F. Leverd, D. Ristoiu, P. Grosse, D. Marris-Morini, L. Vivien, C. Baudot, and F. Boeuf, "Integrated SiN on SOI dual photonic devices for advanced datacom solutions," in *Silicon Photonics: From Fundamental Research To Manufacturing (SPIE Photonics Europe)*, vol. **10686**, p. 106860W, Strasbourg (France), May 2018.

[Guerber'18b] S. Guerber, C. Alonso-Ramos, D. Benedikovic, E. Durán-Valdeiglesias, X. Le Roux, N. Vulliet, E. Cassan, D. Marris-Morini, C. Baudot, F. Boeuf, and L. Vivien, "Broadband polarization beam splitter on a silicon nitride platform for O-band operation," *IEEE Photon. Technol. Lett.* **30**, 1679 (2018).

[Guo'17] D. Guo and T. Chu, "Silicon mode (de)multiplexers with parameters optimized using shortcuts to adiabaticity," *Opt. Express* **25**, 9160 (2017).

[Haggans'93] C. W. Haggans, L. Li, and R. K. Kostuk, "Effective-medium theory of zeroth-order lamellar gratings in conical mountings," *J. Opt. Soc. Am. A* **10**, 2217 (1993).

[Halir'09] R. Halir, Í. Molina-Fernández, J. G. Wangüemert-Pérez, A. Ortega-Moñux, J. de-Oliva-Rubio, and P. Cheben, "Characterization of integrated photonic devices with minimum phase technique," *Opt. Express* **17**, 8349 (2009).

[Halir'10] R. Halir, P. Cheben, J. H. Schmid, R. Ma, D. Bedard, S. Janz, D.-X. Xu, A Densmore, J. Lapointe, and Í. Molina-Fernández, "Continuously apodized fiber-to-chip surface grating coupler with refractive index engineered subwavelength structure," *Opt. Lett.* **35**, 3243 (2010).

[Halir'12] R. Halir, A. Maese-Novo, A. Ortega-Moñux, I. Molina-Fernández, J. G. Wangüemert-Pérez, P. Cheben, D.-X. Xu, J. H. Schmid, and S. Janz, "Colorless directional coupler with engineered sub-wavelength structure," *Opt. Lett.* **20**, 13470 (2012).

[Halir'13] R. Halir, L. Vivien, X. Le Roux, D.-X. Xu, and P. Cheben, "Direct and sensitive phase readout for integrated waveguide sensors," *IEEE Photonics J.* **5**, 6800906 (2013).

[Halir'15] R. Halir, P. J. Bock, P. Cheben, A. Ortega-Moñux, C. Alonso-Ramos, J. H. Schmid, J. Lapointe, D.-X. Xu, J. G. Wangüemert-Pérez, Í. Molina-Fernández, and S. Janz, "Waveguide sub-wavelength structures: a review of principles and applications," *Laser Photon. Rev.* **9**, 25 (2015).

[Halir'16] R. Halir, P. Cheben, J. M. Luque-González, J. D. Sarmiento-Merenguel, J. H. Schmid, G. Wangüemert-Pérez, D.-X. Xu, S. Wang, A. Ortega-Moñux, and Í. Molina-Fernández, "Ultra-broadband nanophotonic beamsplitter using an anisotropic sub-wavelength metamaterial," *Laser Photon. Rev.* **10**, 1039 (2016).

[Halir'18] R. Halir, A. Ortega-Moñux, D. Benedikovic, G. Z. Mashanovic, J. G. Wangümert-Pérez, J. H. Schmid, Í. Molina-Fernández, and P. Cheben, "Subwavelength-grating metamaterial structures for silicon photonic devices," *Proc. IEEE* **106**, 2144 (2018).

[Han'15] L. Han, S. Liang, H. Zhu, L. Qiao, J. Xu, and W. Wang, "Two-mode de/multiplexer based on multimode interference couplers with a tilted joint as phase shifter," *Opt. Lett.* **40**, 518 (2015).

[Harris'72] J. H. Harris, R. K. Winn, and D. G. Dalgoutte, "Theory and design of periodic couplers," *Appl. Opt.* **11**, 2234 (1972).

[Harris'14] N. C. Harris, Y. Ma, J. Mower, T. Baehr-Jones, D. Englund, M. Hochberg, and C. Galland, "Efficient, compact and low loss thermo-optic phase shifter in silicon," *Opt. Express* **22**, 10487 (2014).

[Harris'16] N. C. Harris, D. Bunandar, M. Pant, G. R. Steinbrecher, J. Mower, M. Prabhu, T. Baehr-Jones, M Hochberg, and D. Englund, "Large-scale quantum photonic circuits in silicon," *Nanophotonics* **5**, 456 (2016).

[Harter'18] T. Harter, S. Muehlbrandt, S. Ummethala A. Schmid, S. Nellen, L. Hahn, W. Freude, and C. Koos, "Silicon-plasmonic integrated circuits for terahertz signal generation and coherent detection," *Nat. Photonics* **12**, 625 (2018).

[Herrero-Bermello'17] A. Herrero-Bermello, A. V. Velasco, h. Podmore, P. Cheben, J. H. Schmid, S. Janz, M. L. Calvo, D.-X. Xu, A. Scott, and P. Corredera, "Temperature dependence mitigation in stationary Fourier-transform on-chip spectrometers," *Opt. Lett.* **42**, 2239 (2017).

[Herrero-Bermello'19a] A. Herrero-Bermello, J. M. Luque-González, A. V. Velasco, A. Ortega-Moñux, P. Cheben and R. Halir, "Design of a broadband polarization splitter based on anisotropy-engineered tilted subwavelength gratings," *IEEE Photonics J.* **11**, 6601508 (2019).

[Herrero-Bermello'19b] A. Herrero-Bermello, J. M. Luque-González, R. Halir, P. Cheben, A. Ortega-Moñux, I. Molina-Fernández, and A. V. Velasco, "Zero-birefringence silicon waveguides based on tilted subwavelength metamaterials," *IEEE Photonics J.* **11**, 2700308 (2019).

[Hertz'88] H. Hertz, "Ueber Strahlen electrisher Kraft," *Wiedemanns Ann.* **36**, 769 (1888).

[Hillerkuss'10] D. Hillerkuss, M. Winter, M. Teschke, A. Marculescu, J. Li, G. Sigurdsson, K. Worms, S. Ben Ezra, N. Narkiss, W. Freude, and J. Leuthold, "Simple all-optical FFT scheme enabling Tbit/s real-time signal processing," *Opt. Express* **18**, 9324 (2010).

[Ikeda’10] T. Ikeda, K. Takahashi, Y. Kanamori, and K. Hane, “Phase-shifter using submicron silicon waveguide couplers with ultra-small electro-mechanical actuator,” *Opt. Express* **18**, 7031 (2010).

[Jafari’17] Z. Jafari, A. Zarifkar, and M. Miri, “Compact fabrication-tolerant subwavelength-grating-based two-mode division (de)multiplexer,” *Appl. Opt.* **56**, 7311 (2017).

[Jalali’06] B. Jalali and S. Fathpour, “Silicon photonics,” *J. Lightwave Technol.* **24**, 4600 (2006).

[Jeong’09] S.-H. Jeong and K. Morito, “Optical 90° hybrid with broad operating bandwidth of 94 nm,” *Opt. Lett.* **34**, 3505 (2009).

[Jeong’10] S.-H. Jeong and K. Morito, “Novel optical 90° hybrid consisting of a paired interference based 2×4 MMI coupler, a phase shifter and a 2×2 MMI coupler,” *J. Lightwave Technol.* **28**, 1323 (2010).

[Jeong’13] S.-H. Jeong, D. Shimura, T. Simoyama, M. Seki, N. Yokoyama, M. Ohtsuka, K. Koshino, T. Horikawa, Y. Tanaka, and K. Morito, “Low-loss, flat-topped and spectrally uniform silicon-nanowire-based 5th-order CROW fabricated by ArF-immersion lithography process on a 300-mm SOI wafer,” *Opt. Express* **21**, 30163 (2013).

[Ji’10] H. Ji, M. Galili, H. Hu, M. Pu, L. K. Oxenløwe, K. Yvind, J. M. Hvam, and P. Jeppesen, “1.28-Tb/s demultiplexing of an OTDM DPSK data signal using a silicon waveguide,” *IEEE Photon. Technol. Lett.* **22**, 1762 (2010).

[Juan-Colás’16] J. Juan-Colás, A. Parkin, K. E. Dunn, M. G. Scullion, T. F. Krauss, and S. D. Johnson, “The electrophotonic silicon biosensor,” *Nat. Commun.* **7**, 12769 (2016).

[Kao’66]	K. C. Kao and G. A. Hockham, “Dielectric-fibre surface waveguides for optical frequencies,” *Proc. IEE* **113**, 1151 (1966).
[Kawaguchi’02]	Y. Kawaguchi and K. Tsutsumi, “Mode multiplexing and demultiplexing devices using multimode interference couplers,” *Electron. Lett.* **38**, 1701 (2002).
[Kippenberg’11]	T. J. Kippenberg, R. Holzwarth, and S. A. Diddams, “Microresonator-based optical frequency combs,” *Science* **332**, 555 (2011).
[Knill’01]	E. Knill, R. Laflamme, and G. J. Milburn, “A scheme for efficient quantum computation with linear optics,” *Nature* **409**, 46 (2001).
[Kuhn’71]	L. Kuhn, P. F. Heidrich, and E. G. Lean, “Optical guided wave mode conversion by an acoustic surface wave,” *Appl Phys. Lett.* **19**, 428 (1971).
[Kurdi’88]	B. N. Kurdi and D. G. Hall, “Optical waveguides in oxygen-implanted buried-oxide silicon-on-insulator structures,” *Opt. Lett.* **13**, 175 (1988).
[Lam’16]	C. F. Lam, “Fiber to the home: getting beyond 10 Gb/s,” *Opt. Photonics News* **27**, 22 (2016).
[Lee’03]	B.-T. Lee and S.-Y. Shin, “Mode-order converter in a multimode waveguide,” *Opt. Lett.* **28**, 1660 (2003).
[Lee’08]	B. G. Lee, X. Chen, A. Biberman, X. Liu, I.-W. Hsieh, C.-Y. Chou, J. I. Dadap, F. Xia, W. M. J. Green, L. Sekaric, Y. A. Vlasov, R. M. Osgood, and K. Bergman, “Ultrahigh-bandwidth silicon photonic nanowire waveguides for on-chip networks,” *IEEE Photon. Technol. Lett.* **20**, 398 (2008).
[Leuthold’98]	J. Leuthold, J. Eckner, E. Gamper, P. A. Besse, and H. Melchior, “Multimode interference couplers for the

conversion and combining of zero- and first-order modes," *J. Lightwave Technol.* **16**, 1228 (1998).

[Leuthold'10] J. Leuthold, C. Koos, and W. Freude, "Nonlinear silicon photonics," *Nat. Photonics* **4**, 535 (2010).

[Lewandowski'16] A. Lewandowski, W. Wiatr, D. Gu, N. D. Orloff, and J. Booth, "A multireflect-thru method of vector network analyser calibration," *IEEE Trans. Microw. Theory Tech.* **65**, 905 (2016).

[Li'13] X. Li, H. Xu, X. Xiao, Z. Li, J. Yu, and Y. Yu, "Compact and low-loss silicon power splitter based on inverse tapers," *Opt. Lett.* **38**, 4220 (2013).

[Li'14] Y. Li, C. Li, C. Li, B. Cheng, and C. Xue, "Compact two-mode (de)multiplexer based on symmetric Y-junction and multimode interference waveguides," *Opt. Express* **22**, 5781 (2014).

[Li'17] C. Li and D. Dai, "Low-loss and low-crosstalk multi-channel mode (de)multiplexer with ultrathin silicon waveguides," *Opt. Lett.* **42**, 2370 (2017).

[Li'18a] C. Li, D. Liu, and D. Dai, "Multimode silicon photonics," *Nanophotonics* **8**, 227 (2018).

[Li'18b] S. Li, Y. Zhou, J. Dong, X. Zhang, E. Cassan, J. Hou, C. Yang, S. Chen, D. Gao, and H. Chen, "Universal multimode waveguide crossing based on transformation optics," *Optica* **5**, 1549 (2018).

[Li'18c] H. Li, P. Wang, T. Yang, T. Dai, G. Wang, S. Li, W. Chen, and J. Yang, "Experimental demonstration of a broadband two-mode multi/demultiplexer based on asymmetric Y-junctions," *Opt. Laser Technol.* **100**, 7 (2018).

[Li'19] Z. Li, Y. Liu, H. Guan, W. Han, and Z. Li, "Ultra-compact low-loss 1×4 optical power splitter with splitting ratio of 1:2:4:8 based on two-stage cascaded MMI couplers," *Opt. Lett.* **44**, 5622 (2019).

[Liang'16] D. Liang, X. Huang, G. Kurczveil, M. Fiorentino, and R. G. Beausoleil, "Integrated finely tunable microring laser on silicon," *Nat. Photonics* **10**, 719 (2016).

[Linh'19] H. D. T. Linh, T. C. Dung, K. Tanizawa, D. D. Thang, and N .T. Hung, "Arbitrary $TE_0/TE_1/TE_2/TE_3$ mode converter using 1×4 Y-junction and 4×4 MMI couplers," *IEEE J. Sel. Top. Quantum Electron.* **26**, 8300708 (2019).

[Liu'08] J. Liu, M. Beals, A. Pomerene, S. Bernardis, R. Sun, J. Cheng, L. C. Kimerling, and J. Michel, "Waveguide-integrated ultralow-energy GeSi electro-absorption modulators," *Nat. Photonics* **2**, 433 (2008).

[Liu'10] H. Liu, C. F. Lam, and C. Johnson, "Scaling optical interconnects in datacentre networks opportunities and challenges for WDM," in *18th IEEE Symposium on High Performance Interconnects*, p. 113-116, Mountain View (USA), Aug 2010.

[Liu'13] Q. Liu, X. Tu, K. W. Kim, J. S. Kee, Y. Shin, K. Han, Y.-J. Yoon, G.-Q. Lo, and M. K. Park, "Highly sensitive Mach-Zehnder interferometer biosensor based on silicon nitride slot waveguide," *Sens. Actuators B Chem.* **188**, 681 (2013).

[Liu'19a] Z. Liu, J. Zhang, X. Li, L. Wang, J. Li, C. Xue, J. An, and B. Cheng, "25 × 50 Gbps wavelength division multiplexing silicon photonics receiver chip based on a silicon nanowire-arrayed waveguide grating," *Photon. Res.* **7**, 659 (2019).

[Liu'19b] Y. Liu, K. Xu, S. Wang, W. Shen, H. Xie, Y. Wang, S. Xiao, Y. Yao, J. Du, Z. He, and Q. Song, "Arbitrarily routed mode-division multiplexed photonic circuits for dense integration," *Nat. Commun.* **10**, 3263 (2019).

[Loewen'97] E. G. Loewen and E. Popov, *Diffraction gratings and applications* (Marcel Dekker, New York, 1997).

[Love'11] J. D. Love and N. Riesen, "Single-, few-, and multimode Y-junctions,"*J. Lightwave Technol.* **30**, 304 (2011).

[Luo'14] L.-W. Luo, N. Ophir, C. P. Chen, L. H. Gabrielli, C. B. Poitras, K. Bergmen, and M. Lipson, "WDM-compatible mode-division multiplexing on a silicon chip," *Nat. Commun.* **5**, 3069 (2014).

[Luo'16] Y. Luo, Y. Yu, M. Ye, C. Sun, and X. Zhang, "Integrated dual-mode 3 dB power coupler based on tapered directional coupler," *Sci. Rep.* **6**, 23516 (2016).

[Luque-González'18] J. M. Luque-González, A. Herrero-Bermello, A. Ortega-Moñux, Í. Molina-Fernández, A. V. Velasco, P. Cheben, J. H. Schmid, S. Wang, and R. Halir, "Tilted subwavelength gratings: controlling anisotropy in metamaterial nanophotonic waveguides," *Opt. Lett.* **43**, 4691 (2018).

[Maiman'60] T. H. Maiman, "Stimulated optical radiation in ruby," *Nature* **187**, 493 (1960).

[Malinauskas'16] M. Malinauskas, A. Žukauskas, S. Hasegawa, Y. Hayasaki, V. Mizeikis, R. Buividas, and S. Juodkazis, "Ultrafast laser processing of materials: from science to industry," *Light: Sci. Appl.* **5**, e16133 (2016).

[Marcatili'69] E. A. J. Marcatili, "Dielectric rectangular waveguide and directional coupler for integrated optics," *Bell Syst. Tech. J.* **48**, 2071 (1969).

[Marpaung'19] D. Marpaung, J. Yao, and J. Capmany, "Integrated microwave photonics," *Nat. Photonics* **13**, 80 (2019).

[Martínez-Garaot'14] S. Martínez-Garaot, S. Tseng, and J. G. Muga, "Compact and high conversion efficiency mode-sorting asymmetric

Y junction using shortcuts to adiabaticity," *Opt. Lett.* **39**, 2306 (2014).

[McKay'19] L. McKay, M. Merklein, A. Casas-Bedoya, A. Choudhary, M. Jenkins, C. Middleton, A. Cramer, J. Devenport, A. Klee, R. DeSalvo, and B. J. Eggleton, "Brillouin-based phase shifter in a silicon waveguide," *Optica* **6**, 907 (2019).

[Mikkelsen'18] J. C. Mikkelsen, A. Bois, T. Lordello, D. Mahgerefteh, S. Menezo, and J. K. S. Poon, "Polarization-insensitive silicon nitride Mach-Zehnder lattice wavelength demultiplexers for CWDM in the O-band," *Opt. Express* **26**, 30076 (2018).

[Miller'69] S. E. Miller, "Integrated optics: an introduction," *Bell Syst. Tech. J.* **48**, 2059 (1969).

[Miller'09] D. A. B. Miller, "Device requirements for optical interconnects to silicon chips," *Proc. IEEE* **97**, 1166 (2009).

[Miller'17] D. A. B. Miller, "Attojoule optoelectronics for low-energy information processing and communications," *J. Lightwave Technol.* **35**, 346 (2017).

[MODE'20] MODE Solutions, "Lumerical MODE simulator," https://www.lumerical.com/products/mode/ (2020).

[Mohanty'17] A. Mohanty, M. Zhang, A. Dutt, S. Ramelow, P. Nussenzveig, an M. Lipson, "Quantum interference between transverse spatial waveguide modes," *Nat. Commun.* **8**, 14010 (2007).

[Morgner'00] U. Morgner, W. Drexler, F. X. Kärtner, X. D. Li, C. Pitris, E. P. Ippen, and J. G. Fujimoto, "Spectroscopic optical coherence tomography," *Opt. Lett.* **25**, 111 (2000).

[Morichetti'10] F. Morichetti, A. Canciamilla, C. Ferrari, M. Torregiani, A Melloni, an M. Martinelli, "Roughness induced backscattering in optical silicon waveguides," *Phys. Rev. Lett.* **104**, 033902 (2010).

[Morrissey'15] P. E. Morrissey and F. H. Peters, "Multimode interference couplers as compact and robust static optical phase shifters," *Opt. Commun.* **345**, 1 (2015).

[Mu'14] J. Mu, P.-T. Lin, L. Zhang, X. Duan, L. C. Kimerling, and A. M. Agarwal, "Silicon nitride 1×8 power splitter for mid-infrared applications," in *Laser Science*, p. JW3A.26, Tucson (United States), October 2014.

[Muchmore'48] R. B. Muchmore, "Optimum band width for two layer anti-reflection films," *J. Opt. Soc. Am.* **38**, 20 (1948).

[Nie'17] X. Nie, E. Ryckeboer, G. Roelkens, and R. Baets, "CMOS-compatible broadband co-propagative stationary Fourier transform spectrometer integrated on a silicon nitride photonics platform," *Opt. Express* **25**, A409 (2017).

[Ohana'14] D. Ohana and U. Levy, "Mode conversion based on dielectric metamaterial in silicon," *Opt. Express* **22**, 27617 (2014).

[Oliner'59] A. A. Oliner and W. Rotman, "Periodic structures in trough waveguide," *IEEE Trans. Microw. Theory Techn.* **7**, 134 (1959).

[Orlandi'12] P. Orlandi, C. Ferrari, M. J. Strain, A. Canciamilla, F. Morichetti, M. Sorel, P. Bassi, and A. Melloni, "Continuously tunable bandwidth filter in SOI," *Opt. Lett.* **37**, 3669 (2012).

[Ortega-Moñux'17] A. Ortega-Moñux, J. Čtyroký, P. Cheben, J. H. Schmid, S. Wang, Í. Molina-Fernández, and R. Halir, "Disorder effects in subwavelength grating metamaterial waveguides," *Opt. Express* **25**, 12222 (2017).

[Oser'19] D. Oser, F. Mazeas, X. Le Roux, D. Pérez-Galacho, O. Alibart, S. Tanzilli, L. Labonté, D. Marris-Morini, L.

Vivien, E. Cassan, and C. Alonso-Ramos, “Coherency-broken bragg filters: overcoming on-chip rejection limitations,” *Laser Photon. Rev.* **13**, 1800226 (2019).

[Palik’98] E. D. Palik, *Handbook of optical constants of solids* (Academic Press, vol. 3, 1998).

[Palmer’13] R. Palmer, L. Alloatti, D. Korn, W. Heni, P. C. Schindler, J. Bolten, M. Kari, M Waldow, T. Wahlbrink, W. Freude, and J. Leuthold, “Low-loss silicon strip-to-slot mode converters,” *IEEE Sens. J.* **5**, 2200409 (2013).

[Pan’15] T.-H. Pan and S.-Y. Tseng, “Short and robust silicon mode (de)multiplexers using shortcuts to adiabaticity,” *Opt. Express* **23**, 10405 (2015).

[Passaro’08] V. M. Passaro, R. Loiacono, G. D’Amico, and F. De Leonardis, “Design of Bragg grating sensors based on submicrometer optical rib waveguides,” *IEEE Sens. J.* **8**, 1603 (2008).

[Pérez-Galacho’15] D. Pérez-Galacho, D. Marris-Morini, A. Ortega-Moñux, J. G. Wangüemert-Pérez, and L. Vivien, “Add/drop mode-division multiplexer based on a Mach-Zehnder interferometer,” *IEEE Photonics J.* **7**, 7800907 (2015).

[Pérez-Galacho’16] D. Pérez-Galacho, C. A. Alonso-Ramos, D. Marris-Morini, V. Vakari, X. Le Roux, A. Ortega-Moñux, J. G. Wangüemert-Pérez, and L. Vivien, “Integrated mode converter for mode division multiplexing,” in *Silicon Photonics and Photonic Integrated Circuits V (SPIE Photonics Europe)*, vol. **9891**, p. 98910B, Brussels (Belgium), May 2016.

[Pérez-Galacho’17] D. Pérez-Galacho, C. Alonso-Ramos, F. Mazeas, X. Le Roux, D. Oser, W. Zhang, D. Marris-Morini, L. Labonté, S. Tanzilli, E. Cassan, and L. Vivien, “Optical pump-rejection filter based on silicon sub-wavelength engineered photonic structures,” *Opt. Lett.* **42**, 1468 (2017).

[Pfeifle’12] J. Pfeifle, L. Alloatti, W. Freude, J. Leuthold, and C. Koos, “Silicon-organic hybrid phase shifter based on a slot waveguide with liquid-crystal cladding,” *Opt. Express* **20**, 15359 (2012).

[Poberaj’12] G. Poberaj, H. Hu, W. Sohler, and P. Günter, “Lithium niobite on insulator (LNOI) for micro-photonic devices,” *Laser Photon. Rev.* **6**, 488 (2012).

[Polman’12] A. Polman and H. A. Atwater, “Photonic design principles for ultrahigh-efficiency photovoltaics,” *Nat. Mater.* **11**, 174 (2012).

[Poot’14] M. Poot and H. X. Tang, “Broadband nanoelectromechanical phase shifting of light on a chip,” *Appl. Phys. Lett.* **104**, 061101 (2014).

[Poot’16] M. Poot, C. Schuck, X. S. Ma, X. Guo, and H. X. Tang, “Design and characterization of integrated components for SiN photonic quantum circuits,” *Opt. Express* **24**, 6843 (2016).

[Poulton’17a] C. V. Poulton, A. Yaacobi, D. B. Cole, M. J. Byrd, M. Raval, D. Vermeulen, and M. R. Watts, “Coherent solid-state LIDAR with silicon photonic optical phased arrays,” *Opt. Lett.* **42**, 4091 (2017).

[Poulton’17b] C. V. Poulton, M. J. Byrd, M. Raval, Z. Su, N. Li, E. Timurdogan, D. Coolbaugh, D. Vermeulen, and M. R. Watts, “Large-scale silicon nitride nanophotonic phased arrays at infrared and visible wavelengths,” *Opt. Lett.* **42**, 21 (2017).

[Qiu’13] H. Qiu, H. Yu, T. Hu, G. Jiang, H. Shao, P. Yu, J. Yang, and X. Jiang, “Silicon mode multi/demultiplexer based on multimode grating-assisted couplers,” *Opt. Express* **21**, 17904 (2013).

[Rasigade’10] G. Rasigade, X. Le Roux, D. Marris-Morini, E. Cassan, and L. Vivien, “Compact wavelength-insensitive fabrication-tolerant silicon-on-insulator beam splitter," *Opt. Lett.* **35**, 3700 (2010).

[Rayleigh'87] J. W. S. Rayleigh, "On the maintenance of vibrations by forces of double frequency, and on the propagation of waves through a medium endowed with a periodic structure," *Phil. Mag.* **24**, 145 (1887).

[Reed'08] G. T. Reed, *Silicon photonics: the state of the art* (John Wiley & Sons, 2008).

[Reed'10] G. T. Reed, G. Mashanovich, F. Y. Gardes, and D. J. Thomson, "Silicon optical modulators," *Nat. Photonics* **4**, 518 (2010).

[Ren'18] F. Ren, W. Chen, T. Zhangsun, Y. Zhang, X. Fan, J. Wang, "Variable-ratio mode-insensitive 1×2 power splitter based on MMI couplers and phase shifters," *IEEE Photonics J.* **10**, 7104912 (2018).

[ReportsnReports'18] ReportsnReports, "Silicon photonics market by product, application, component, and geograpgy – global forecast to 2023," (2018).

[Riesen'12] N. Riesen and J. D. Love, "Design of mode-sorting asymmetric Y-junctions," *Appl. Opt.* **51**, 2778 (2012).

[Rodríguez-Barrios'10] F. Rodríguez-Barrios, S. Martín-López, A. Carrasco-Sanz, P. Corredera, J. D. Ania-Castañón, L. Thévenaz, and M. González-Herráez, "Distributed Brillouin fiber sensor assisted by first-order Raman amplification," *J. Lightwave. Technol.* **28**, 2162 (2010).

[Roelkens'07] G. Roelkens, D. Van Thourhout, and R. Baets, "Silicon-on-insulator ultra-compact duplexer based on a diffractive grating structure," *Opt. Express* **15**, 10091 (2007).

[Romero-García'13] S. Romero-García, F. Merget, F. Zhong, H. Finkelstein, and J. Witzens, "Silicon nitride CMOS-compatible platform for integrated photonics applications at visible wavelengths," *Opt. Express* **21**, 14036 (2013).

[Rytov'56] S. M. Rytov, "Electromagnetic properties of a finely stratified medium," *Sov. Phys. JETP* **2**, 466 (1956).

[Saida'99] T. Saida, A. Himeno, M. Okuno, A. Sugita, and K. Okamoto, "Silica-based 2×2 multimode interference coupler with arbitrary power splitting ratio," *Electron. Lett.* **35**, 2031 (1999).

[Sakai'02] A. Sakai, T. Fukazawa, and T. Baba, "Low loss ultra-small branches in a silicon photonic wire waveguide," *IEICE Trans. Electron.* **85**, 1033 (2002).

[Saleh'91] B. E. A. Saleh and M. C. Teich, *Fundamentals of photonics* (John Wiley & Sons, 1991).

[Sánchez-Postigo'16] A. Sánchez-Postigo, J. G. Wangüemert-Pérez, J. M. Luque-González, Í. Molina-Fernández, P. Cheben, C. A. Alonso-Ramos, R. Halir, J. H. Schmid, and A. Ortega-Moñux, "Broadband fiber-chip zero-order surface grating coupler with 0.4 dB efficiency," *Opt. Lett.* **41**, 3013 (2016).

[Sarmiento-Merenguel'15] J. D. Sarmiento-Merenguel, R. Halir, X. Le Roux, C. Alonso-Ramos, L. Vivien, P. Cheben, E. Durán-Valdeiglesias, I. Molina-Fernández, D. Marris-Morini, D.-X. Xu, J. H. Schmid, S. Janz, and A. Ortega-Moñux, "Demonstration of integrated polarization control with a 40 dB range in extinction ratio," *Optica* **2**, 1019 (2015).

[Sattari'19] H. Sattari, T. Graziosi, M. Kiss, T. J. Seok, S. Han, M. C. Wu, and N. Quack, "Silicon photonic MEMS phase-shifter," *Opt. Express* **27**, 18959 (2019).

[Schmid'07] J. H. Schmid, P. Cheben, S. Janz, J. Lapointe, E. Post, and D.-X. Xu, "Gradient-index antireflective subwavelength structures for planar waveguide facets," *Opt. Lett.* **32**, 1794 (2007).

[Schmid’11] J. H. Schmid, M. Ibrahim, P. Cheben, J. Lapointe, S. Janz, P. J. Bock, A. Densmore, B. Lamontagne, R. Ma, W. N. Ye, and D.-X. Xu, “Temperature-independent silicon subwavelength grating waveguides,” *Opt. Lett.* **36**, 2110 (2011).

[Sharma’19] B. Sharma, K. Kishor, S. Sharma, and R. Makkar, “Design and simulation of broadband beam splitter on a silicon nitride platform for optical coherence tomography,” *Fiber Integr. Opt.* **38**, 247 (2019).

[Sheng’12] Z. Sheng, Z. Wang, C. Qiu, L. Li, A. Pang, A. Wu, X. Wang, S. Zou, and F. Gan, “A compact and low-loss MMI coupler fabricated with CMOS technology,” *IEEE Photonics J.* **4**, 2272 (2012).

[Simon’13] S. H. Simon, *The Oxford Solid State Basics* (Oxford University Press, 2013).

[Snitzer’61] E. Snitzer, “Cylindrical dielectric waveguide modes,” *J. Opt. Soc. Am.* **51**, 491 (1961).

[Soldano’95] L. B. Soldano and E. C. M. Pennings, “Optical multi-mode interference devices based on self-imaging: principles and applications,” *J. Lightwave Technol.* **13**, 615 (1995).

[Song’15] W. Song, R. Gatdula, S. Abbaslou, M. Lu, A. Stein, W. Y.-C. Lai, J. Provine, R. F. W. Pease, D. N. Christodouliddes, and W. Jiang, “High-density waveguide superlattices with low crosstalk,” *Nat. Commun.* **6**, 7027 (2015).

[Soref’86] R. Soref and J. Larenzo, “All-silicon active and passive guided-wave components,” *IEEE J. Quantum Electron.* **22**, 873 (1986).

[Soref’87] R. A. Soref and B. R. Bennett, “Electrooptical effects in silicon,” *IEEE J. Quantum Electron.* **23**, 123 (1987).

[Soref’10] R. Soref, “Mid-infrared photonics in silicon and germanium,” *Nat. Photonics* **4**, 495 (2010).

[Spencer’12] D. T. Spencer, D. Dai, Y. Tang, M. J. Heck, and J. E. Bowers, “Realization of a novel 1×N power splitter with uniformly excited ports,” *IEEE Photon. Technol. Lett.* **25**, 36 (2012).

[Stern’15] B. Stern, X. Zhu, C. P. Chen, L. D. Tzuang, J. Cardenas, K. Bergman, and M. Lipson, “On-chip mode-division multiplexing switch,” *Optica* **2**, 530 (2015).

[Sun’13] J. Sun, E. Timurdogan, A. Yaacobi, E. S. Hosseini, and M. R. Watts, “Large-scale nanophotonic phased array,” *Nature* **493**, 195 (2013).

[Sun’16a] C. Sun, Y. Yu, M. Ye, G. Chen and X. Zhang, “An ultra-low crosstalk and broadband two-mode (de) multiplexer based on adiabatic couplers,” *Sci. Rep.* **6**, 38494 (2016).

[Sun’16b] Y. Sun, Y. Xiong and N. Y. Winnie, “Experimental demonstration of a two-mode (de)multiplexer based on a taper-etched directional coupler,” *Opt. Lett.* **41**, 3743 (2016).

[Sun’17] C. Sun, Y. Yu, G. Chen, and X. Zhang, “Ultra-compact bent multimode silicon waveguide with ultralow inter-mode crosstalk,” *Opt. Lett.* **42**, 3004 (2017).

[Sun’18] C. Sun, W. Wu, Y. Yu, G. Chen, X. Zhang, X. Chen, D. J. Thomson, and G. T. Reed, “De-multiplexing free on-chip low-loss multimode switch enabling reconfigurable inter-mode and inter-path routing,” *Nanophotonics* **7**, 1571 (2018).

[Taillaert’02] D. Taillaert, W. Bogaerts, P. Bientsman, T. F. Krauss, P. Van Daele, I. Moerman, S. Verstuyft, K. De Mesel, and R. Baets, “An out-of-plane grating coupler efficient butt-coupling between compact planar waveguides and single-mode fibers," *IEEE J. Quantum Electron.* **38**, 949 (2002).

[Tait'17] A. N. Tait, T. F. de Lima, E. Zhou, A. X. Wu, M. A. Nahmias, B. J. Shastri, and P. R. Prucnal, "Neuromorphic photonic networks using silicon photonic weight banks," *Sci. Rep.* **7**, 7430 (2017).

[Tamazin'18] H. Tamazin, E. El-Fiky, Y. Wang, Y. D'Mello, D. Patel, A. Kumar, and D. V. Plant, "Ultra-broadband compact adiabatic coupler in silicon-on-insulator for joint operation in the C- and O-bands," in *Conference on Lasers and Electro-Optics (CLEO)*, p. STh4B.4, San Jose (United States), May 2018.

[Tamir'77] T. Tamir and S. T. Pend, "Analysis and design of grating couplers," *Appl. Phys.* **14**, 235 (1977).

[Tang'09] Y. Tang, D. Dai, and S. He, "Proposal for a grating waveguide serving as both a polarization splitter and an efficient coupler for silicon-on-insulator nanophotonic circuits," *IEEE Photon. Technol. Lett.* **21**, 242 (2009).

[Tatum'15] J. A. Tatum, D. Gazula, L. A. Graham, J. K. Guenter, R. H. Johnson, J. King, C. Kocot, G. D. Landry, I. Lyubomirsky, A. N. MacInnes, E. M. Shaw, K. Balemarthy, R. Shubochkin, D. Vaidya, M. Yan, and F. Tang, "VCSEL-based interconnects for current and future data centers," *J. Lightwave Technol.* **33**, 727 (2015).

[Thomas'57] A. S. Thomas and F. J. Zucker, "Radiation from modulated surface wave structures - I," in *IRE Int. Conv. Rec.* vol. **5**, p. 153-160, New York (USA), 1957.

[Thomson'16] D. Thomson, A. Zilkie, J. E. Bowers, T. Komljenovic, G. T. Reed, L. Vivien, D. Marris-Morini, E. Cassan, L. Virot, and J.-M. Fédéli, "Roadmap on silicon photonics," *J. Opt.* **18**, 073003 (2016).

[Trinh’95] P. D. Trinh, S. Yegnanarayanan, and B. Jalali, “Integrated optical directional couplers in silicon-on-insulator,” *Electron. Lett.* **31**, 2097 (1995).

[Uematsu’12] T. Uematsu, Y. Ishizaka, Y. Kawaguchi, K. Saitoh, and M. Koshiba, “Design of a compact two-mode multi/demultiplexer consisting of multimode interference waveguides and a wavelength-insensitive phase shifter for mode-division multiplexing transmission,” *J. Lightwave Technol.* **30**, 2421 (2012).

[Vacondio’10] F. Vacondio, M. Mirshafiei, J. Basak, A. Liu, L. Liao, M. Paniccia, and L. A. Rusch, “A silicon modulator enabling RF over fiber for 802.11 OFDM signals,” *IEEE J. Sel. Top. Quantum Electro.* **16**, 141 (2010).

[VanCampenhout’09] J. Van Campenhout, W. M. J. Green, S. Assefa, and Y. A. Vlasov, “Low-power, 2×2 silicon electro-optic switch with 110-nm bandwidth for broadband reconfigurable optical networks,” *Opt. Express* **17**, 24020 (2009).

[Velasco’13a] A. V. Velasco, P. Cheben, M. Florjańczyk, J. H. Schmid, P. J. Bock, J. Lapointe, A. Delâge, S. Janz, M. Vachon, M. L. Calvo, D.-X. Xu, and Svatopluk Civiš, “Optical fiber interferometer array for scanless Fourier-transform spectroscopy,” *Opt. Lett.* **38**, 2262 (2013).

[Velasco’13b] A. V. Velasco, P. Cheben, P. J. Bock, A. Delâge, J. H. Schmid, J. Lapointe, S. Janz, M. L. Calvo, D.-X. Xu, M. Florjańczyk, and M. Vachon, “High-resolution Fourier-transfor spectrometer chip with microphotonic silicon spiral waveguides,” *Opt. Lett.* **38**, 706 (2013).

[Vivien’09] L. Vivien, J. Osmond, J.-M. Fédéli, D. Marris-Morini, P. Crozat, J.-F. Damlencourt, E. Cassan, Y. Lecunff, and S. Laval, “42 GHz p.i.n Germanium photodetector integrated in a silicon-on-insulator waveguide,” *Opt. Express* **17**, 6252 (2009).

[Vivien’16]	L. Vivien and L. Pavesi, *Handbook of silicon photonics* (Taylor & Francis, 2016).
[Vlasov’12]	Y. A. Vlasov, “Silicon CMOS-integrated nano-photonics for computer and data communications beyond 100G,” *IEEE Commun. Mag.* **50**, S67 (2012).
[Voigt’11]	K. Voigt, L. Zimmermann, G. Winzer, H. Tian, B. Tillack, and K. Petermann, “C-band optical 90° hybrids in silicon nanowaveguide tecnology,” *IEEE Photon. Technol. Lett.* **23**, 1769 (2011).
[Voigt’12]	K. Voigt, “Interferometric devices based on 4µm SOI material for application in optical telecommunications,” Ph.D. dissertation, Technische Universität Berlin (2012).
[Wagner’10]	C. Wagner and N. Harned, “EUV lithography: lithography gets extreme,” *Nat. Photonics* **4**, 24 (2010).
[Wang’74]	S. Wang, “Principles of distributed feedback and distributed Bragg-reflector lasers,” *IEEE J. Quantum Electron.* **10**, 413 (1974).
[Wang’14a]	J. Wang, Z. Yao, T. Lei, and A. W. Poon, “Silicon coupled-resonator optical-waveguide-based biosensors using light-scattering pattern recognition with pixelized mode-field-intensity distributions,” *Sci. Rep.* **4**, 7528 (2014).
[Wang’14b]	J. Wang, S. He, and D. Dai, “On-chip silicon 8-channel hybrid (de)multiplexer enabling simultaneous mode- and polarization-division-multiplexing,” *Laser Photon. Rev.* **8**, L18 (2014).
[Wang’15]	J. Wang, Y. Xuan, M. Qi, H. Huang, Y. Li, M. Li, X. Chen, Z. Sheng, A. Wu, W. Li, X. Wang, S. Zou, and F. Gan, “Broadband and fabrication-tolerant on-chip scalable mode-division multiplexing based on mode-evolution counter-tapered couplers,” *Opt. Lett.* **40**, 1956 (2015).

[Wang’16a] Y. Wang, Z. Lu, M. Ma, H. Yun, F. Zhang, N. A. Jaeger, and L. Chrostowski, “Compact broadband directional couplers using subwavelength gratings,” *IEEE Photonics J.* **8**, 7101408 (2016).

[Wang’16b] J. Wang, R. Ashrafi, R. Adams, I. Glesk, I. Gasulla, J. Capmany, and L. R. Chen, “Subwavelength grating enabled on-chip ultra-compact optical true time delay line,” *Sci. Rep.* **6**, 30235 (2016).

[Wang’16c] Y. Wang, S. Gao, K. Wang, and E. Skafidas, “Ultra-broadband and low-loss 3 dB optical power splitter based on adiabatic tapered silicon waveguides,” *Opt. Lett.* **41**, 2053 (2016).

[Wang’18] Y. Wang, M. Kong, Y. Xu, and Z. Zhou, “Analysis of scattering loss due to sidewall roughness in slot waveguides by variation of mode effective index,” *J. Opt.* **20**, 025801 (2018).

[Wangüemert-Pérez’14] J. G. Wangüemert-Pérez, P. Cheben, A. Ortega-Moñux, C. Alonso-Ramos, D. Pérez-Galacho, R. Halir, I. Molina-Fernández, D.-X. Xu, and J. H. Schmid, “Evanescent field waveguide sensing with subwavelength grating structures in silicon-on-insulator,” *Opt. Lett.* **39**, 4442 (2014).

[Wangüemert-Pérez’19] J. G. Wangüemert-Pérez, A. Hadij-ElHouati, A. Sánchez-Postigo, J. Leuermann, D.-X, Xu, P. Cheben, A. Ortega-Moñux, R. Halir, and Í. Molina-Fernández, “Subwavelength structures for silicon photonics biosensing,” *Opt. Laser Technol.* **109**, 437 (2019).

[Washington’19] University of Washington, “Washington nanofabrication facility electron beam lithography,” https://ebeam.wnf.uw.edu/ebeamweb/ (2019).

[Wei’01] H. Wei, J. Yu, X. Zhang, and Z. Liu, “Compact 3-dB tapered multimode interference coupler in silicon-on-insulator,” *Opt. Lett.* **26**, 878 (2001).

[Wei’08] X. Wei, C. Kang, M. Liscidini, G. Rong, S. T. Retterer, M. Patrini, J. E. Sipe, and S. M. Weiss, “Grating couplers on porous silicon planar waveguides for sensing applications,” *J. Appl. Phys.* **104**, 1231113 (2008).

[Williams’19] C. Williams, G. Zhang, R. Priti, G. Cowan, and O. Liboiron-Ladouceur, “Modal crosstalk in silicon photonic multimode interconnects,” *Opt. Express* **27**, 27712 (2019).

[Xia’04] J. Xia, J. Yu, Z. Wang, Z. Fan, and S. Chen, “Low power 2×2 thermo-optic SOI waveguide switch fabricated by anisotropy chemical etching,” *Opt. Commun.* **232**, 223 (2004).

[Xiao’18] H. Xiao, Z. Liu, X. Han, J. Yang, G. Ren, A. Mitchell, and Y. Tian, “On-chip reconfigurable and scalable optical mode multiplexer/demultiplexer based on three-waveguide-coupling structure,” *Opt. Express* **26**, 22366 (2018).

[Xing’13a] J. Xing, Z. Li, X. Xiao, J. Yu, and Y. Yu, “Two-mode multiplexer and demultiplexer based on adiabatic couplers,” *Opt. Lett.* **38**, 3468 (2013).

[Xing’13b] J. Xing, K. Xiong, H. Xu, Z. Li, X. Xiao, J. Yu, and Y. Yu, “Silicon-on-insulator-based adiabatic splitter with simultaneous tapering of velocity and coupling,” *Opt. Lett.* **38**, 2221 (2013).

[Xing’15] Y. Xing, T. Aki, J. P George, D. Korn, H. Yu, P. Verheyen, M. Pantouvaki, G. Lepage, P. Absil, A. Ruocco, C. Koos, J. Leuthold, K. Neyts, J. Beeckman, and W. Bogaerts, “Digitally controlled phase shifter using an SOI slot waveguide with liquid crystal infiltration,” *IEEE Photon. Technol. Lett.* **27**, 1269 (2015).

[Xiong’14] Y. Xiong, J. G. Wangüemert-Pérez, D.-X. Xu, J. H. Schmid, P. Cheben, and N. Y. Winnie, “Polarization splitter and rotator with subwavelength grating for enhanced fabrication tolerance," *Opt. Lett.* **39**, 6931 (2014).

[Xiong'17] Y. Xiong, R. B. Priti, and O. Liboiron-Ladouceur, "High-speed two-mode switch for mode-division multiplexing optical networks," *Optica* **4**, 1098 (2017).

[Xu'04] Q. Xu, V. R. Almeida, R. R. Panepucci, an M. Lipson, "Experimental demonstration of guiding and confining light in nanometer-size low-refractive-index material," *Opt. Lett.* **29**, 1626 (2004).

[Xu'16] H. Xu and Y. Shi, "Ultra-broadband dual-mode 3 dB power splitter based on a Y-junction assisted with mode converters," *Opt. Lett.* **41**, 5047 (2016).

[Xu'17] L. Xu, Y. Wang, D. Patel, E. El-Fiky, Z. Xing, R. Li, M. Ghulam-Saber, M. Jacques, and D. V. Plant, "Polarization independent adiabatic 3-dB coupler for silicon-on-insulator," in *Conference on Lasers and Electro-Optics (CLEO)*, p. SF1I.5, San Jose (United States), May 2017.

[Xu'18a] H. Xu and Y. Shi, "Ultra-sharp multi-mode waveguide bending assisted with metamaterial-based mode converters," *Laser Photon. Rev.* **12**, 1700240 (2018).

[Xu'18b] H. Xu and Y. Shi, "Metamaterial-based Maxwell's fisheye lens for multimode waveguide crossing," *Laser Photon. Rev.* **12**, 1800094 (2018).

[Xu'18c] L. Xu, Y. Wang, A. Kumar, E. El-Fiky, D. Mao, H. Tamazin, M. Jacques, Z. Xing, M. Ghulam-Saber, and D. V. Plant, "Compact high-performance adiabatic 3-dB coupler enabled by subwavelength grating slot in the silicon-on-insulator platform," *Opt. Express* **26**, 29873 (2018).

[Xu'19] L. Xu, Y. Wang, D. Mao, J. Zhang, Z. Xing, E. El-Fiky, M. Ghulam-Saber, A. Kumar, Y. D'Mello, M. Jacques, and D. V. Plant, “Ultra-broadband and compact two-mode multiplexer based on subwavelength-grating-slot-assisted adiabatic coupler for the silicon-on-insulator platform,” *J. Lightwave Technol.* **37**, 5790 (2019).

[Yajima’73] H. Yajima, “Dielectric thin-film optical branching waveguide,” *Appl. Phys. Lett.* **22**, 647 (1973).

[Yamada’05] H. Yamada, T. Chu, S. Ishida, and Y. Arakawa, “Optical directional coupler based on Si-wire waveguies,” *IEEE Photon. Technol. Lett.* **17**, 585 (2005).

[Yang’11] J. Yang, Z. Zhou, W. Zhou, X. Zhang, and H. Jia, “High efficient subwavelength binary blaze grating beam splitter via vertical coupling,” *IEEE Photon. Technol. Lett.* **23**, 896 (2011).

[Yang’13] W. Yang, M. Yin, Y. Li, X. Wang, and Z. Wang, “Ultra-compact optical 90° hybrid based on a wedge-shaped 2×4 MMI coupler and a 2×2 MMI coupler in silicon-on-insulator,” *Opt. Express* **21**, 28423 (2013).

[Yariv’77] A. Yariv and P. Yeh, “Electromagnetic propagation in periodic stratified media. II. Birefringence, phase matching, and x.ray lasers,” *J. Opt. Soc. Am.* **67**, 438 (1977).

[Ye’77] P. Yeh, A. Yariv, and C. S. Hong, “Electromagnetic propagation in periodic stratified media. I. General theory,” *J. Opt. Soc. Am.* **67**, 423 (1977).

[Ye’05] W. N. Ye, D.-X. Xu, S. Janz, P. Cheben, M.-J. Picard, B. Lamontagne, and N. G. Tarr, “Birefringence control using stress engineering in silicon-on-insulator (SOI) waveguides,” *J. Lightwave Technol.* **23**, 1308 (2005).

[Yi’14] Y. Li, C. Li, C. Li, B. Cheng, and C. Xue, “Compact two-mode (de)multiplexer based on symmetric Y-junction and multimode interference waveguides,” *Opt. Express* **22**, (2014).

[YoléDevelopment’16] Yolé Development, “Silicon photonics market & applications,” (2016).

[Yuan’18] Z. Yuan and K. Wang, “Ultra broadband, low loss and polarization independent silicon nitrite integrated optical power splitter,” in *Asia Communications and Photonics Conference (ACP)*, p. 1, Hangzhou (China), October 2018.

[Yun’15] H. Yun, Z. Lu, Y. Wang, W. Shi, L Chrostowski, and N. A. F. Jaeger, “2×2 broadband adiabatic 3-dB couplers on SOI strip waveguides for TE and TM modes,” in *Conference on Lasers and Electro-Optics (CLEO)*, p. STh1F.8, San Jose (United States), May 2015.

[Yun’16] H. Yun, Y. Wang, F. Zhang, Z. Lu, S. Lin, L. Chrostowski, and N. A. F. Jaeger, “Broadband 2×2 adiabatic 3 dB coupler using silicon-on-insulator sub-wavelength grating waveguides,” *Opt. Lett.* **41**, (2016).

[Yun’18] H. Yun, L. Chrostowski, and N. A. F. Jaeger, “Ultra-broadband 2×2 adiabatic 3 dB coupler using subwavelength-grating-assisted silicon-on-insulator strip waveguides,” *Opt. Lett.* **43**, (2018).

[Zhang’13] Y. Zhang, S. Yang A. E.-J. Lim, G.-Q. Lo, C. Galland, T. Baehr-Jones, and M. Hochberg, “A compact and low loss Y-junction for submicron silicon waveguide,” *Opt. Express* **21**, 1310 (2013).

[Zhang’17] Z. Zhang, Y. Yu, and S. Fu, “Broadband on-chip mode-division multiplexer based on adiabatic couplers and symmetric Y-junction,” *IEEE Photonics J.* **9**, 6600406 (2017).

[Zhang’18] W. Zhang and J. Yao, “A fully reconfigurable waveguide Bragg grating for programmable photonic signal processing,” *Nat. Commun.* **9**, 1396 (2018).

[Zhao'15] H. Zhao, B. Kuyken, S. Clemmen, F. Leo, A Subramanian, A. Dhakal, P. Helin, S. Severi, E. Brainis, G. Roelkens, and R. Baets, "Visible-to-near-infrared octave spanning supercontinuum generation in a silicon nitride waveguide," *Opt. Lett.* **40**, 2177 (2015).

[Zhao'19] H. Zhao, S. Pinna, F. Sang, B. Song, S. T. Š. Brunelli, L. A. Coldren, and J. Klamkin, "High-power indium phosphide photonic integrated circuits," *IEEE J. Sel. Top. Quantum Electron.* **25**, 4500410 (2019).

[Zhong'14] Q. Zhong, V. Veerasubramanian, Y. Wang, W. Shi, D. Patel, S. Ghosh, A. Samani, L. Chrostowski, R. Bojko, and D. V. Plant, "Focusing-curved subwavelength grating couplers for ultra-broadband silicon photonics optical interfaces," *Opt. Express* **22**, 18224 (2014).

[Zhou'19] D. Zhou, C. Sun, Y. Lai, Y. Yu, and X. Zhang, "Integrated silicon multifunctional mode-division multiplexing system," *Opt. Express* **27**, 10798 (2019).